Jordan Journal of Mechanical and Industrial Engineering (JJMIE)

JJMIE is a high-quality scientific journal devoted to fields of Mechanical and Industrial Engineering. It is published by Hashemite University in cooperation with the Jordanian Scientific Research and Innovation Support Fund, Ministry of Higher Education and Scientific Research.

EDITORIAL BOARD

THE INTERNATIONAL ADVISORY BOARD

EDITORIAL BOARD SUPPORT TEAM

SUBMISSION ADDRESS:

Prof. Moh'd Sami Ashhab, Editor-in-Chief
Jordan Journal of Mechanical & Industrial Engineering,
Hashemite University,
PO Box 330127, Zarqa, 13133 , Jordan
E-mail: jjmie@hu.edu.jo

Hashemite Kingdom of Jordan

Hashemite University

Jordan Journal of Mechanical and Industrial Engineering

JJMIE

An International Peer-Reviewed Scientific Journal

Financed by Scientific Research Support Fund

Volume 16 Number 1, January 2022

http://jjmie.hu.edu.jo/

ISSN 1995-6665

Jordan Journal of Mechanical and Industrial Engineering (JJMIE)

JJMIE is a high-quality scientific journal devoted to fields of Mechanical and Industrial Engineering. It is published by Hashemite University in cooperation with the Jordanian Scientific Research and Innovation Support Fund, Ministry of Higher Education and Scientific Research.

Introduction: The Editorial Board is very committed to build the Journal as one of the leading international journals in mechanical and industrial engineering sciences in the next few years. With the support of the Ministry of Higher Education and Scientific Research and Jordanian Universities, it is expected that a heavy resource to be channeled into the Journal to establish its international reputation. The Journal's reputation will be enhanced from arrangements with several organizers of international conferences in publishing selected best papers of the conference proceedings.

Aims and Scope: *Jordan Journal of Mechanical and Industrial Engineering* (JJMIE) is a refereed international journal to be of interest and use to all those concerned with research in various fields of, or closely related to, mechanical and industrial engineering disciplines. *Jordan Journal of Mechanical and Industrial Engineering* aims to provide a highly readable and valuable addition to the literature which will serve as an indispensable reference tool for years to come. The coverage of the journal includes all new theoretical and experimental findings in the fields of mechanical and industrial engineering or any closely related fields (Materials, Manufacturing, Management, Design, Thermal, Fluid, Energy, Control, Mechatronics, and Biomedical). The journal also encourages the submission of critical review articles covering advances in recent research of such fields as well as technical notes.

Guide for Authors

Manuscript Submission:
High-quality submissions to this new journal are welcome now and manuscripts may be either submitted online or email.

Online: For online and email submission upload one copy of the full paper including graphics and all figures at the online, submission site, accessed via http://jjmie.hu.edu.jo. The manuscript must be written in MS Word Format. All correspondence including notification of the Editor's decision and requests for revision, takes place by e-mail and via the Author's homepage, removing the need for a hard-copy paper trail

Submission address and contact :
Prof. Moh'd Sami Ashhab
Editor-in-Chief
Jordan Journal of Mechanical & Industrial Engineering, Hashemite University
PO Box 330127, Zarqa, 13115, Jordan
E-mail: jjmie@hu.edu.jo

Types of contributions*:* Original research papers and Technical reports

Corresponding author: Clearly indicate who is responsible for correspondence at all stages of refereeing and publication, including post-publication. Ensure that telephone and fax numbers (with country and area code) are provided in addition to the e-mail address and the complete postal address. Full postal addresses must be given for all co-authors.

Original material: Submission of an article implies that the work described has not been published previously (except in the form of itstan abstract or as part of a published lecture or academic thesis), that it is not under consideration for publication elsewhere, tha publication is approved by all authors and that, if accepted, it will not be published elsewhere in the same form, in English or in any other language, without the written consent of the Publisher. Authors found to be deliberately contravening the submission guidelines on originality and exclusivity shall not be considered for future publication in this journal.

Withdrawing: If the author chooses to withdraw his article after it has been assessed, he shall reimburse JJMIE with the cost of reviewing the paper.

Manuscript Preparation:

General: Editors reserve the right to adjust style to certain standards of uniformity. Original manuscripts are discarded after .publication unless the Publisher is asked to return original material after use. Please use MS Word for the text of your manuscript

Structure: Follow this order when typing manuscripts: Title, Authors, Authors title, Affiliations, Abstract, Keywords, Introduction, Main text, Conclusions, Acknowledgements, Appendix, References, Figure Captions, Figures and then Tables. Please supply figures imported into the text AND also separately as original graphics files. Collate acknowledgements in a separate section at the end of the article and do not include them on the title page, as a footnote to the title or otherwise.

Text Layout: Use 1.5 line spacing and wide (3 cm) margins. Ensure that each new paragraph is clearly indicated. Present tables and figure legends on separate pages at the end of the manuscript. If possible, consult a recent issue of the journal to become familiar with layout and conventions. All footnotes (except for table and corresponding author footnotes) should be identified with superscript Arabic numbers. To conserve space, authors are requested to mark the less important parts of the paper (such as records of experimental results) for printing in smaller type. For long papers (more than 4000 words) sections which could be deleted without destroying either the sense or the continuity of the paper should be indicated as a guide for the editor. Nomenclature should conform to that most frequently used in the scientific field concerned. Number all pages consecutively; use 12 or 10 pt font size and standard fonts.

Corresponding author: Clearly indicate who is responsible for correspondence at all stages of refereeing and publication, including post-publication. The corresponding author should be identified with an asterisk and footnote. Ensure that telephone and fax numbers (with country and area code) are provided in addition to the e-mail address and the complete postal address. Full postal addresses must be given for all co-authors. Please consult a recent journal paper for style if possible.

Abstract: A self-contained abstract outlining in a single paragraph the aims, scope and conclusions of the paper must be supplied.

Keywords: Immediately after the abstract, provide a maximum of six keywords (avoid, for example, 'and', 'of'). Be sparing with abbreviations: only abbreviations firmly established in the field may be eligible.

Symbols: All Greek letters and unusual symbols should be identified by name in the margin, the first time they are used.

Units: Follow internationally accepted rules and conventions: use the international system of units (SI). If other quantities are mentioned, give their equivalent quantities in SI

Maths: Number consecutively any equations that have to be displayed separately from the text (if referred to explicitly in the text).

References: All publications cited in the text should be presented in a list of references following the text of the manuscript.

Text: Indicate references by number(s) in square brackets in line with the text. The actual authors can be referred to, but the reference number(s) must always be given.

List: Number the references (numbers in square brackets) in the list in the order in which they appear in the text.

Examples:

Reference to a journal publication:

[1] M.S. Mohsen, B.A. Akash, "Evaluation of domestic solar water heating system in Jordan using analytic hierarchy process". Energy Conversion & Management, Vol. 38 (1997) No. 9, 1815-1822.

Reference to a book:

[2] Strunk Jr W, White EB. The elements of style. 3rd ed. New York: Macmillan; 1979.

Reference to a conference proceeding:

[3] B. Akash, S. Odeh, S. Nijmeh, "Modeling of solar-assisted double-tube evaporator heat pump system under local climate conditions". 5th Jordanian International Mechanical Engineering Conference, Amman, Jordan, 2004.

Reference to a chapter in an edited book:

[4] Mettam GR, Adams LB. How to prepare an electronic version of your article. In: Jones BS, Smith RZ, editors. Introduction to the electronic age, New York: E-Publishing Inc; 1999, p. 281-304

Free Online Color : If, together with your accepted article, you submit usable color and black/white figures then the journal will ensure that these figures will appear in color on the journal website electronic version.

Tables: Tables should be numbered consecutively and given suitable captions and each table should begin on a new page. No vertical rules should be used. Tables should not unnecessarily duplicate results presented elsewhere in the manuscript (for example, in graphs). Footnotes to tables should be typed below the table and should be referred to by superscript lowercase letters.

Notification: Authors will be notified of the acceptance of their paper by the editor. The Publisher will also send a notification of receipt of the paper in production.

Copyright: All authors must sign the Transfer of Copyright agreement before the article can be published. This transfer agreement enables Jordan Journal of Mechanical and Industrial Engineering to protect the copyrighted material for the authors, but does not relinquish the authors' proprietary rights. The copyright transfer covers the exclusive rights to reproduce and distribute the article, including reprints, photographic reproductions, microfilm or any other reproductions of similar nature and translations.

Proof Reading: One set of page proofs in MS Word format will be sent by e-mail to the corresponding author, to be checked for typesetting/editing. The corrections should be returned within 48 hours. No changes in, or additions to, the accepted (and subsequently edited) manuscript will be allowed at this stage. Proofreading is solely the author's responsibility. Any queries should be answered in full. Please correct factual errors only, or errors introduced by typesetting. Please note that once your paper has been proofed we publish the identical paper online as in print.

JJMIE

Volume 16, Number 1, January. 2022
ISSN 1995-6665

Jordan Journal of Mechanical and Industrial Engineering

PAGES	PAPERS
1 - 9	**Modeling and Analysis of Relationship Between Flow Characteristics and Efficiency of Reciprocating Porous Medium Burner** *Boxue Zhong, Weihua Li*
11 - 18	**Automatic Obstacle Avoidance Path Planning Method for Unmanned Ground Vehicle Based on Improved Bee Colony Algorithm** *Yan Ren, Jiayong Liu*
19– 29	**Interference Suppression Control Method for Aircraft Electromechanical Speed Control System** *Qian Zhang*
31– 40	**Gait Control System of Autonomous Mobile Robot Based on PMAC** *Guobin Si, Xiaofeng Jin, Chunxia Wang*
41– 51	**Optimal Control Method for Side Impact Safety of Vehicle Frame Structure** *Mingming Wu, Xueping Zhang*
53– 62	**Dynamic Response Analysis of the Impact Force of Steel Wheel on the Elastic Half-Space** *Zhipo Cao, Naixing Liang, Sheng Zeng, Xianshui Gang*
63– 72	**Application of Direction Vector Model of Multibody System Dynamics in Sports Posture Positioning** *Feng Liu*
73– 78	**Theoretical Research of Corn Orientation Device** *Liai Pan, Yanli Wu*
79–86	**Parallel Computing-Based Dynamics Model for Tracking Moving Targets** *Yugang Cui*
87–95	**Coordinated Gait Control of Snake Like Robot Based on Electromechanical Tracking** *Jianwei Guo, Yongbo Lv, Han Zhang*
97–104	**Trajectory Tracking Control Algorithm of Six Degrees of Freedom Industrial Robot** *Zhenhua Meng*
105–111	**Design of Multi Joint Integrated Control System for Non Driven Robot** *Qian Zhang*

JJMIE

Volume 16, Number 1, January. 2022
ISSN 1995-6665

Jordan Journal of Mechanical and Industrial Engineering

PAGES	PAPERS
113–121	**Temperature Field and Stress Field Distribution of Forged Steel Brake Disc for High Speed Train** *Ruoqi Suo, Xiaoling Shi*
123–131	**Mechanical Parts Pose Detection System Based on ORB Key Frame Matching Algorithm** *Chun Liang*
133–139	**Design of Visual Monitoring Software for Micro-Drive Debugging in Electromechanical System** *Qian Wang, Yuqing Zhao, Hongjun Shi*
141–152	**Design of Quantitative Risk Assessment System for Ship Longitudinal Motion Based on Analytic Hierarchy Process** *Lixiao Jia, Jiantao Wang, Lejun Rui, Jing Chu*
153–162	**Multi-Layer and Multi-Channel Welding Trajectory Control Method of Welding Robot** *Baiyang Zhao*

JJMIE

Volume 16, Number 1, January. 2022
ISSN 1995-6665
Pages 1 - 9

Jordan Journal of Mechanical and Industrial Engineering

Modeling and Analysis of Relationship Between Flow Characteristics and Efficiency of Reciprocating Porous Medium Burner

Boxue Zhong[1*], Weihua Li[2]

[1]Department of Safety Supervision, Preparatory Office, Datang Baoding Co-generation Power Plant, Baoding 071051, China
[2]School of Energy Power and Mechanical Engineering, North China Electric Power University, Baoding 071003, China

Received 14 July 2021 Accepted 29 December 2021

Abstract

When the relationship model between flow characteristics and efficiency of reciprocating porous medium burner is built by energy spectrum analysis method, it is disturbed by a large number of factors affecting combustion efficiency, so it is impossible to accurately analyze the relationship between flow characteristics and efficiency of the burner. A new relationship model between flow characteristics and efficiency of reciprocating porous medium burner is constructed. According to the symmetry of reciprocating porous medium burning system structure and the periodic exchange characteristics of internal gas flow, a physical model of reciprocating porous medium burning system is constructed. On this basis, a reciprocating porous medium burner is established. After giving the initial boundary conditions of the model equation, the finite volume method is used to discretize the model equation, boundary conditions and calculation area. The Gauss-Seidel iteration method is used to solve the mathematical model, and the relationship between the flow characteristics and efficiency of the reciprocating porous medium burner is analyzed. The experimental results show that the model can effectively analyze the relationship between flow characteristics, such as reversal half cycle, gas calorific value, secondary air ratio and efficiency in reciprocating porous medium burner, and the stability of the model is strong. The analysis time is less than 0.5 s.

Keywords: Reciprocating; Porous medium; Burner; Flow characteristics; Efficiency; Modeling analysis;

1. Introduction

With the development of society and economy, energy crisis and environmental pollution are becoming more and more serious. People's voice for energy conservation and environmental protection is getting higher and higher [1]. The development of clean energy and the efficient use of energy play an important role in promoting and guaranteeing the sustained, rapid and healthy development of the national economy, improving the environment and the quality of people's lives. Controlling the use of highly polluted energy, developing the utilization of clean energy, and improving the effect of energy conservation are to greatly increase the use of energy, which has become one of the researches focuses of energy researchers since the 1990s [2, 3].

Environment is the source of human life and survival. However, with the development of the world economy, environmental problems are becoming more and more serious, threatening the survival and development of mankind. Nowadays, human beings are faced with three major environmental problems: acid rain, greenhouse effect and ozone layer damage. The harm of acid rain is getting worse and worse, and almost all over the world [4, 5]. According to a survey conducted by the Economic Commission for Europe (UNECE) and the United Nations Environment Programme in 1989, acid rain has been harmful to 28 countries in Europe, and 50 million hectares of 110 million hectares of forests in Europe have become fragile and withered due to acid rain; In the United States, according to Environmental Protection Agency (EPA) estimates, acid rain has corroded up to 5 billion United States (US) dollars in 17 states since 1985. In China, acid rain has been the trend of development, and the acidity of rainfall has been increasing from south to north. The economic losses caused by acid rain are also increasing year by year. Soil in some areas is gradually increasing. Acidification is a serious pollution problem in agriculture. According to rough estimates, the area of farmland polluted by acid rain in the mid-1980s has reached 40 million mu, resulting in economic losses of more than 1.5 billion yuan per year. In addition, some parts of China also suffer from forest and water hazards, which seriously threaten the ecological balance of [6-10].

Reciprocating porous medium combustion has higher advantages than other combustion technologies in improving combustion efficiency, expanding flammability limit, saving fuel, improving environment and disposing of all kinds of garbage and waste [11-14]. It is a combustion technology with high combustion efficiency and low pollution emission. This combustion technology is an effective and practical combustion method in enhancing combustion and emission control. Therefore, the relationship between flow characteristics and efficiency of

* Corresponding author e-mail: boxuezhong@126.com.

reciprocating porous medium burner is analyzed by modeling in order to improve fuel efficiency and reduce environmental pollution.

2. Modeling and Analysis of Relationship Between Flow Characteristics and Efficiency of Reciprocating Porous Medium Burner

2.1. Establishment of physical model

According to the symmetry of the structure of reciprocating porous medium burner and the periodic interchangeability of the gas flow direction in the system, the burner is simplified [15-18]. The physical model shown in Figure 1 is established, which is divided into combustion zone and regeneration zone. The combustion zone and regeneration zone are cylinders, and the burner zone are foam ceramic tile with high porosity, the regenerator area is a regenerative sphere or honeycomb regenerator with low void ratio, and the length of the combustion heat transfer area is x_e; The gas flow area [19] on the outside of the two ends of porous medium is one-twentieth of the length of the porous medium area, and the total length is L. In order to prevent the burner from tempering, a heat dissipation aluminium ring jacket with a length of 40 mm is installed outside the burner at the entrance of some premixed gases [20-22]. The igniter is located at 2/3 of the burner length.

During the first half period t_{hp1}, some premixed gas enters the burner from upstream of the burner at a flow rate of u_1 and initial temperature of T_0. At the same time, the heated secondary air enters the burner at a flow rate of u_2 and a temperature of T_2. It joins the primary air and combusts after ignition by the igniter. The combustion product passes through heat storage. The downstream of the regenerator is excluded [23, 24]. The solid line in the figure shows the direction of gas flow in the first half cycle. In the second half cycle t_{hp2}, the premixed gas stops supplying. The secondary air enters from the downstream of the regenerator at a flow rate of u_2 and an initial temperature of T_0. After heating in the regenerator area and the porous medium combustion area, it flows out of the middle cross-pipe mouth. It can also be seen in the figure that the distance between the premixed gas inlet upstream of the burner and the connecting point of the middle cross-pipe is relatively small compared with the whole burner, and the proportion of the premixed gas inlet in the whole calculation area is relatively small [25]. The influence of the incoming flow of the fresh premixed gas and the heated secondary air in this section can be neglected. Therefore, in the first half of the model processing, it can be considered that the primary and secondary air has been premixed before entering the system from the premixed gas inlet upstream of the burner [26]. Similarly, in the second half of the cycle, the outflow of secondary air can also be considered as outflow from the upstream middle cross-pipe of the burner. In this way, the physical model can be simplified to one-dimensional problem in the first and second half cycle.

2.2. Establishment of mathematical model

2.2.1. Establishment of model equation

According to the results of the physical model built in Section 2.1, an axial coordinate system x is established. As shown in Figure 1, for the combustion reaction process of reciprocating porous burner in the first half cycle, a micro-element is selected in the calculation area of physical model [27, 28]. Considering the non-thermal equilibrium between gas and solid phases, and according to the mass conservation and energy in the micro-element body, the conservation law is used to establish the one-dimensional double temperature control equation for gas solid two phase.

The continuity equation is:

$$\frac{\partial(\varepsilon\rho_g)}{\partial t}+\frac{\partial(\varepsilon\rho_g)}{\partial x}=0 \tag{1}$$

The energy equation of mixed gases is:

$$\varepsilon\frac{\partial(C_{pg}\rho_g T_g)}{\partial t}+\varepsilon\frac{\partial(C_{pg}\rho_g uT)}{\partial x}=\varepsilon\frac{\partial}{\partial x}\left(\lambda_g\frac{\partial T_g}{\partial x}\right)+\varepsilon h_0 W-h_v(T_g-T_s) \tag{2}$$

The energy equation for porous medium is:

$$(1-\varepsilon)\frac{\partial(C_{ps}\rho_s T_s)}{\partial t}=\frac{\partial}{\partial x}\left(\lambda_s\frac{\partial T_s}{\partial x}\right)-\frac{\partial q_r}{\partial x}+h_v(T_g-T_s)-\xi(T_s-T_0) \tag{3}$$

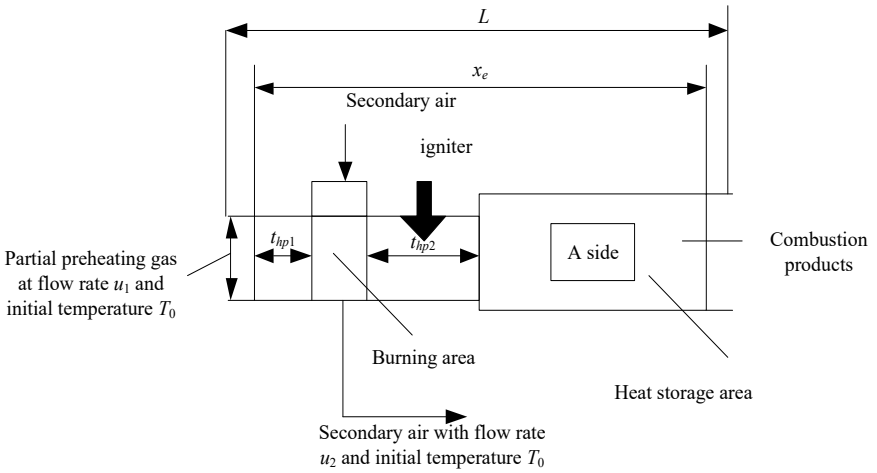

Figure 1. Physical model of reciprocating porous medium combustion system

The composition equation of the product is:

$$\frac{\partial(\rho_g Y)}{\partial t}+\frac{\partial(\rho_g u Y)}{\partial x}=\frac{\partial}{\partial x}\left(D\rho_g\frac{\partial Y}{\partial x}\right)+W \tag{4}$$

In the above equations, the porosity is ε; T is temperature; Y is product component; h_0 is low calorific value of fuel per unit mass; W is chemical reaction rate; λ_g is gas thermal conductivity; D is diffusion coefficient; C_{pg} is gas specific heat; C_{ps} is specific heat of porous medium; q_r is the radiation of porous medium; ξ is wall heat loss coefficient of combustion system; The subscripts is a porous medium, and the subscript g indicates gas.

λ_s is the thermal conductivity of solid, and it can be obtained by the following empirical equation.

$$\lambda_s=(1-\varepsilon)(0.561-0.855\log(T_s)) \tag{5}$$

h_v is the volumetric heat transfer coefficient, which is mainly obtained from the Nusselt number of dimensionless volume as following Equation (6):

$$Nu_{v,1}=\frac{h_v d_m^2}{\lambda_s} \tag{6}$$

The Nusselt number of dimensionless volume can be obtained by the following Equation (7):

$$Nu_{v,1}=\left(0.0426+\frac{1.236 d_m}{X_e}\right)/\mathrm{Re}_{dm} \tag{7}$$

The average pore size d_m and Reynolds number of aperture Re_{dm} is are obtained through the following Equation (8):

$$d_m=\sqrt{4\phi/\pi}\,/\,ppc;\mathrm{Re}_{dm}=\frac{u d_m^2}{\upsilon} \tag{8}$$

where ppc is the number of holes in porous medium in a centimeter unit length.

Similarly, the second half cycle is a heating process in which the secondary air flows backward from the downstream of the regenerator into the system. There is no combustion reaction, but a simple gas-solid two-phase heat transfer process [29]. Therefore, the model equation in the second half cycle can be further simplified as follows:

The continuity equation is:

$$\frac{\partial(\varepsilon\rho_g)}{\partial t}+\frac{\partial(\varepsilon\rho_g u_2)}{\partial x}=0 \tag{9}$$

The energy equation of mixed gases is:

$$\varepsilon\frac{\partial(C_{pg}\rho_g T_g)}{\partial t}+\varepsilon\frac{\partial(C_p\rho_g u_2 T_g)}{\partial x}=$$
$$\varepsilon\frac{\partial}{\partial x}\left(\lambda_g\frac{\partial T_g}{\partial x}\right)-h_v(T_g-T_s) \tag{10}$$

The energy equation for porous medium is:

$$(1-\varepsilon)\frac{\partial(C_{ps}\rho_s T_s)}{\partial t}=\frac{\partial}{\partial x}\left(\lambda_s\frac{\partial T_s}{\partial x}\right)-$$
$$\frac{\partial q_r}{\partial x}+h_v(T_g-T_s)-\xi(T_s-T_0) \tag{11}$$

2.2.2. Treatment of chemical reaction source term

The combustion reaction is a very rapid exothermic reaction. Natural gas is used as combustion gas, the main component is methane, the content of which is up to 90%. Because it combusts with a large amount of air to form a lean gas, the proportion of other components is smaller [30]. Therefore, the combustion of other components can be neglected and only the chemical reaction of methane combustion can be considered. The stoichiometric equation of chemical reaction can be expressed as follows:

$$CH_4+2\phi^{-1}(O_2+3.762N_2)\rightarrow$$
$$CO_2+2H_2O+2(\phi^{-1}-1)O_2+2\phi^{-1}3.76N_2 \tag{12}$$

The experimental analysis shows that the oxygen concentration in the gas is very high and the combustion efficiency is very high when combustion is carried out in a reciprocating porous medium burner, especially for lean gas fuel with low calorific value. Therefore, in the model calculation, the combustion reaction is considered to be complete [31, 32]. In addition, the purpose of chemical reaction item treatment is the main one. The effect of thermal effect caused by combustion reaction on temperature field is considered. According to Arrehnius law, the thermal effect caused by one-step reaction is the same as that caused by detailed reaction. Therefore, the overall one-step irreversible reaction can be used to simplify the combustion reaction. Since the combustion reaction is assumed to follow Arrehnius law, the chemical reaction rate equation is as follows:

$$W=A_f\rho_R(1-Y)\exp(-E/RT_R) \tag{13}$$

where, the chemical reaction frequency factor $A_f=2.6\times10^8 s^{-1}$, activation energy $E=130kJ/mol$.

Therefore, in combustion reaction, only the molar fraction of reactants and biomass components exists. Therefore, when the biomass component $Y<1$ or not equal to 1 in numerical simulation, it can be confirmed that combustion reaction can not proceed steadily.

2.2.3. Treatment of radiation source term

On the one hand, natural gas becomes a gas fuel with low calorific value after mixing with air, and the proportion of combustible gas component is relatively small [33]. Therefore, the proportion of triatomic radiative gases such as CO_2 and H_2O in the product is relatively small, and the radiation ability is greatly reduced. On the other hand, compared with the radiation effect of porous medium, the radiation effect of gas is much less than that of porous medium. The radiation effect of gas can be neglected. Only the radiation effect of solids is considered. At the same time, the radiation coefficient of foam ceramic medium and the phase function parameter fluctuate less with wavelength variation [34], so the wavelength effect can be considered as smaller, the wavelength is treated as gray body. For the micro-elements in the physical model area, the radiation energy transfer is established as follows:

$$\frac{\partial q_r(\tau)}{\partial x}=-2\pi k\Big[I_0E_2(\tau)+$$
$$I_e E_2(\tau_e-\tau)-2I_b(\tau)+\int_0^{\tau_e}I_b(\tau')E(|\tau-\tau'|)d\tau'\Big] \tag{14}$$

where, $I_b(\tau)$ and $E_n(\tau)$ respectively denote black body radiation intensity and n-order exponential integral function, as shown in Equation (15):

$$I_b(\tau)=\frac{\sigma T^4}{\pi};E_n(\tau)=\int_0^1\xi^{n-2}\exp(-\tau/\zeta)d\zeta \tag{15}$$

Porous ceramic foam is composed of a network framework with twelve sides interpenetrating. It has high randomness, uncertainty and complex structure. It can be treated as a continuous medium, and the combustion of porous medium makes the temperature distribution in the combustion chamber more uniform. The gap is much smaller, so that radiation mainly comes from the adjacent point, and the radiation energy far away has been greatly attenuated before reaching the micro-element [35]. Therefore, the radiation energy can be treated by the diffusion approximation method based on the optical thickness assumption, and the Rosseland diffusion equation can be obtained as follows:

$$q_r(x) = -\frac{16}{3}\frac{\sigma T^3}{k}\frac{dT}{dx} \tag{16}$$

The Stephen-Boltzmann constant $\sigma = 5.67\times10^{-8} W/m^2\cdot K$ and k is the radiation attenuation coefficient.

By incorporating the above equations into the energy equation of porous medium and combining them, the expression (17) of energy diffusion equation of porous medium can be obtained:

$$(1-\varepsilon)\frac{\partial(C_{ps}\rho_s T_s)}{\partial t} = \frac{\partial}{\partial x}(\lambda_{ss})\frac{\partial T_s}{\partial x} + h_v(T_g - T_s) \tag{17}$$

where

$$\lambda_{ss} = \lambda_s + \frac{16}{3}\frac{\sigma T_s^3}{k} \tag{18}$$

where, λ_{ss} is the effective conversion coefficient of heat conduction.

2.2.4. Establishment of ignition model

The reciprocating porous medium burner is ignited by an igniter. The ignition process is regarded as a uniform exothermic process with constant flow [36]. The uniform heat release rate is limited to the combustion area of porous medium, and the heat source range is 1/50 of the whole porous medium area. The corresponding model equation is simplified as the relative heat transfer between gas and solid with constant internal heat source [37]. The temperature at which the ignition is stabilized is the initial value of the ignition combustion as the mixed gas.

2.2.5. Initial boundary condition

1. Initial condition

When $t = 0, -0.05x_e < x \le L$, then:

$$T_g = T_s = T_{i0}; Y = 0; u = u_1 + u_2 \tag{19}$$

2. Boundary condition

The first half cycle $0 \le t \le t_{hp}, u > 0$, when $x = -0.05x_e$, then:

$$T_g = (1-\alpha)T_0 + \alpha T_{g2}; Y_{in} = 0; u = u_1 + u_2 \tag{20}$$

If $X = L$, there is:

$$\frac{\partial T_g}{\partial x} = \frac{\partial Y}{\partial x} = 0; u = u_1 + u_2 \tag{21}$$

If $x = 0$ and $x = 0$, there is:

$$(1-\varepsilon)\lambda_s\frac{\partial T_s}{\partial x} = -\alpha_s(T_g - T_s)\big|_{x=0} \tag{22}$$

α_s is the convection heat transfer coefficient, $\alpha_s = h_v / 169.4\,ppc$, and ppc is the number of hole per cm unit length.

The second half cycle $t_{tp} \le t \le 2t_{hp}, u < 0$, if $x = L$:

$$T_g = T_0; Y_{in} = 0; u = u_2 \tag{23}$$

If $x = -0.05x_e$, there is:

$$\frac{\partial T_g}{\partial x} = 0; u = u_2 \tag{24}$$

At $x = 0$ and $x = x_e$, there is:

$$(1-\varepsilon)\lambda_s\frac{\partial T_s}{\partial x} = -\alpha_s(T_g - T_s)\big|_{x=x_e} \tag{25}$$

3. Solid wall boundary

In order to prevent backfire, a cooling aluminium ring with a length of 40 mm is installed at the inlet of the premixed gas upstream of the burner. The heat loss coefficient ξ_1 is treated according to the unit length uniform heat sink, and 1 200 is selected through the comparison of the test results. Other avoiding areas adopt better thermal insulation measures in the test process, with less heat loss, according to adiabatic heat treatment.

2.2.6. Solution of mathematical model

Aiming at the established mathematical model equation, variable of that dimension is 1 and parameter of that dimension is 1 are introduced. The model equation and boundary conditions are transformed into two dimension 1 forms. The finite volume method is used to discretize the model equation, boundary condition and calculation area. The model equation is solved by Gauss-Seidel iteration method, and the combustion efficiency is obtained. The calculation results of the rate can effectively analyze the relationship between flow characteristics and efficiency of the reciprocating porous medium burner.

Firstly, ignition simulation is carried out. Given constant heat source h_0, the gas-solid two-phase energy equation of constant internal heat source is solved. The obtained temperature distribution field is taken as the initial ignition temperature, and then the numerical simulation of system combustion is carried out. Secondly, the position of the flame is not predetermined, but by the energy balance of the system itself.

$$\begin{aligned}
&X = x/x_e, \theta = T/T_0, \beta = ut/x_0, \tau_e = kx,\\
&\beta_{hp} = ut_{hp}/x_e, M_2 = x_e^{2\xi}/\lambda_g, \mathrm{Re} = ux_e v, \gamma_e = \lambda_s/\lambda_g\\
&\mathrm{Pr} = \rho_g v c_p/\lambda_g, Le = \rho_g c_p D/\lambda_g, hr = \rho_s C_s/\rho_g C_s,\\
&E_a = E/RT_0, R_s = A_f x_e/v, M = x_e^2 h_v\lambda_g, H_0 = h_0/c_p T_0,\\
&Nr = k\lambda_g/4\sigma T_0^3, Nu = \alpha_s x_e/(\lambda_s + 16\sigma T_s^3/3k)
\end{aligned} \tag{26}$$

In the above equation, X is the coordinate of that dimension is 1; E_a is the activation energy; θ is the temperature; Le is Levis number; D is diffusion coefficient; M is the convective heat transfer coefficient; v is motion viscosity.

3. Results

In order to verify the validity of the model of the relationship between flow characteristics and efficiency of reciprocating porous medium burner constructed in this paper, the application effect of the model is empirically

analyzed. The main characteristic of porous medium combustion is "superenthalpy combustion". The reciprocating thermal cycle porous medium combustion system is also based on porous medium combustion. Periodic reversing combustion achieves normal and stable operation. Therefore, in the steady combustion process of reciprocating porous medium burner system, there is also the phenomenon of "superenthalpy combustion". Superenthalpy combustion has the characteristics of high thermal efficiency and high combustion rate. The experiment will start from the flow characteristics of the burner, such as reversal half cycle, gas calorific value, secondary air ratio and so on to analyze the validity of the model.

The following characteristics are explained below. Relative to superenthalpy θ_r, a characteristic quantity used to represent the "superenthalpy" combustion program of a combustion system is defined by Hanamura, as shown in Equation (27):

$$\theta_r = \frac{\theta_{\max} - 1}{\theta_{th} - 1} \tag{27}$$

where, $\theta_{\max}$ represents the maximum temperature of reciprocating porous medium burner and θ_{th} represents the theoretical adiabatic temperature of gas. In the reaction model, only the products and reactants can be distinguished. Therefore, combustion efficiency η is directly represented by the biomass components calculated in the model. It should be pointed out that the model in this paper uses an irreversible reaction to approximate the combustion reaction effect of the system. The reaction model is relatively simple, only a simple qualitative analysis.

3.1. Impact analysis of commutation half cycle

In Figure 2, Reynolds number $\mathrm{Re} = 10321$, gas calorific value $H_0 = 3.48$, secondary air ratio $a = 0.2$, porosity in the left end burner is ε_1, and porosity in the right end burneris $\varepsilon_2 = 0.51$. When the heat loss coefficient in left end is 1200, the influence of commutation half cycle on relative enthalpy and combustion efficiency is analyzed by the proposed model. As shown in the figure, for the relative superenthalpy, the relative superenthalpy increases and the combustion efficiency increases with the increase of the commutation half cycle. It increases to the maximum at half cycle $\beta_{hp} = 40$ and then decreases gradually. This is because when the calorific value of the gas is the same, the maximum adiabatic theoretical combustion temperature remains unchanged. From the analysis of Figure 2, it can be seen that with the increase of half cycle, the maximum peak combustion temperature is relatively small at the beginning, relatively high at half cycle $\beta_{hp} = 40$, and then gradually decreases.

Generally speaking, the effect of commutation half cycle on relative superenthalpy is relatively small, it is equivalent to that of commutation half cycle on combustion efficiency of reciprocating porous medium burner, which is between 1.0 and 1.06. This is because when the calorific value of premixed gas is fixed, the heat released from combustion is fixed. Under normal combustion conditions, the change of commutation half cycle is only an external factor to change the maximum temperature of premixed gas combustion, not an internal factor, so the influence is relatively small.

For combustion efficiency, at half cycle $\beta_{hp} = 5$, it is relatively small, less than 0.9, and then increases rapidly, reaching a higher level after $\beta_{hp} = 40$, then decreases slightly, but the decrease is very small. Overall, except for the small commutation half cycle, the combustion efficiency is relatively low, and the overall combustion efficiency remains at a higher level. Therefore, the model can effectively analyze the relationship between commutation half cycle and combustion efficiency.

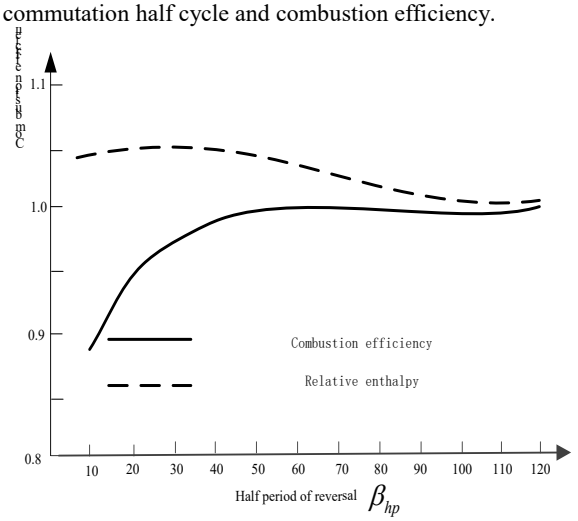

Figure 2. Effect of half-period of commutation on the combustion characteristics and efficiency of superenthalpy

3.2. Impact analysis of gas calorific value

Figure 3 shows the effect of gas calorific value on relative superenthalpy and combustion efficiency when Reynolds number $\mathrm{Re} = 10321$, half cycle $\beta_{hp} = 40$, secondary air ratio $a = 0.2$, porosity in the left end burner is $\varepsilon_1 = 0.85$, porosity in the right end burner is $\varepsilon_2 = 0.51$ in and heat loss coefficient in left end is 1200, the influence of gas calorific value on the relative super-energy and combustion efficiency is obtained from the model analysis in this paper. As shown in the figure, for the relative superenthalpy, the relative superenthalpy decreases rapidly with the increase of the calorific value of the gas. When the calorific value of the gas is $H_0 = 3.48$, the relative superenthalpy basically approaches 1, and the hyperbolic trend is obvious. The results show that with the increase of calorific value of gas, the characteristic of "superenthalpy combustion" decreases gradually, and the lower the calorific value of gas is, the more obvious the phenomenon of "superenthalpy combustion" is.

For combustion efficiency, with the increase of calorific value of gas, combustion efficiency gradually increases, and overall, combustion efficiency remains at a high level. This is because when the calorific value of the gas $H_0 = 0.8$, the peak value of the maximum combustion temperature is smaller, the temperature distribution presents an inverted "V" distribution, the burner has been in the extreme lean combustion state, and the combustion efficiency is relatively low; With the increase of the calorific value, the overall temperature level in the system increases, the peak temperature gradually increases, and the combustion efficiency gradually increases. Therefore, this model can

effectively analyze the relationship between gas calorific value and combustion efficiency.

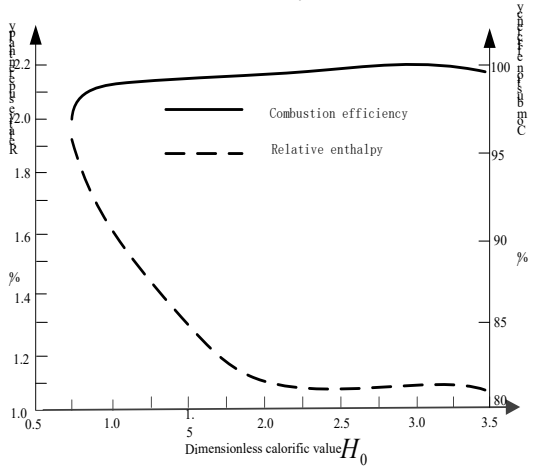

Figure 3. Influence of gas calorific value on superenthalpy combustion characteristics and combustion efficiency

3.3. Impact analysis of the secondary air ratio

Figure 4 shows the effect of secondary air ratio on relative superenthalpy and combustion efficiency when Reynolds number is $\mathrm{Re} = 10321$, gas calorific value is $H_0 = 2.27$, half cycle is $\beta_{hp} = 40$, porosity in the left end burner is $\varepsilon_1 = 0.85$, porosity in the right end burner is $\varepsilon_2 = 0.51$ and heat loss coefficient in left burner is 1200. As shown in the figure, for the relative superenthalpy, the relative superenthalpy is lower when the secondary air ratio is $a = 0.1$. When $a = 0.2$, the relative superenthalpy is higher, then decreases gradually. With the increase of the secondary air ratio, the maximum combustion peak temperature is higher when the secondary air ratio is $a = 0.2$, then decreases gradually, while the adiabatic theoretical combustion temperature of gas combustion is fixed. Therefore, the variation of relative superenthalpy is similar to that of maximum combustion peak temperature. At the beginning, the secondary air ratio is relatively high when $a = 0.2$, and then decreases gradually.

For combustion efficiency, similar to the relative enthalpy, it is relatively small when the secondary air ratio is a = 3 and relatively high when the secondary air ratio is a = 1, and then gradually decreases. The main reason is the analysis of the influence of the two wind ratio on the combustion temperature distribution. Therefore, this model can effectively analyze the relationship between the two air ratio and combustion efficiency.

For combustion efficiency, similar to the relative superenthalpy, it is relatively small when the secondary air ratio is $a = 0.1$ and relatively high when the secondary air ratio is $a = 0.2$, and then gradually decreases. The main reason is the analysis of the influence of the secondary air ratio on the combustion temperature distribution. Therefore, this model can effectively analyze the relationship between the secondary air ratio and combustion efficiency.

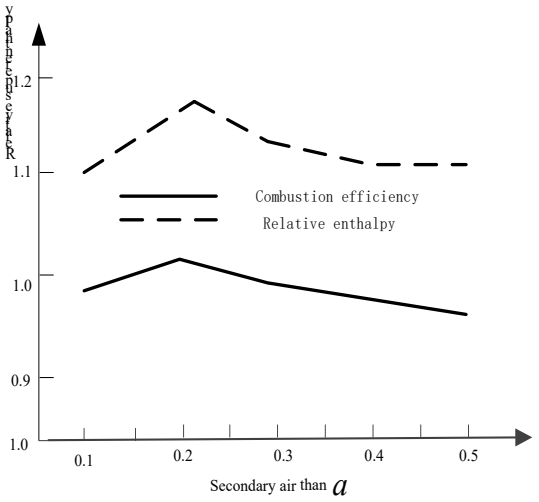

Figure 4. Influence of secondary air ratio on combustion characteristics and combustion efficiency

3.4. Influence analysis of reynolds number

Figure 5 shows the effect of Reynolds number on relative superenthalpy and combustion efficiency of the burner system when the calorific value of gas is $H_0 = 13.4$, half cycle is $\beta_{hp} = 40$, secondary air ratio is $a = 0.2$, porosity in the left burner is $\varepsilon_1 = 0.85$, porosity in the right burner is $\varepsilon_2 = 0.51$ and heat loss coefficient is 1200 in the left. As shown in the figure, with the increase of Reynolds number, the relative superenthalpy increases obviously and shows a linear distribution relationship. The main reason is that when the calorific value of the gas is constant, the adiabatic theoretical combustion temperature of the gas remains unchanged. With the increase of Reynolds number, the combustion load of the system increases correspondingly, the maximum peak temperature increases gradually, and the relative enthalpy increases gradually, showing an approximate linear relationship.

For the combustion efficiency, similar to the relative superenthalpy, the combustion efficiency increases slightly with the increase of Reynolds number, and overall, the change is relatively small. With the increase of Reynolds number, the maximum combustion temperature and preheating zone temperature gradually increase, the preheating effect of fresh gas gradually increases, the combustion effect in high temperature zone increases, and the combustion efficiency gradually increases. Overall, the combustor combustion efficiency is very high, basically maintained at more than 98%.

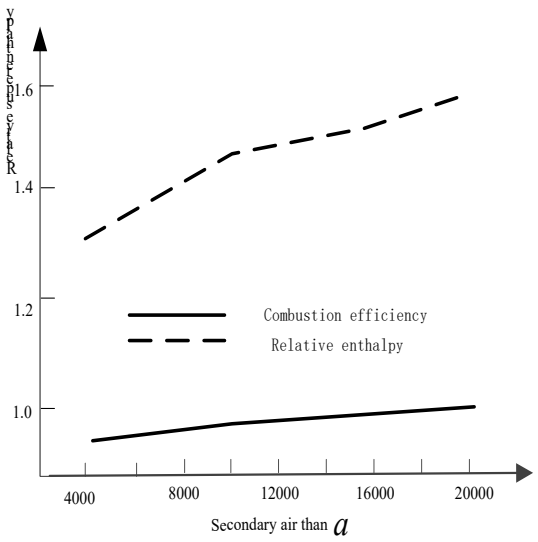

Figure 5. Effects of reynolds number on combustion characteristics and efficiency of superenthalpy

3.5. Comparison analysis of time-consuming

In order to verify the efficiency and stability of the model, the results of the flow characteristics and efficiency relationship model of reciprocating porous medium burner based on energy spectrum analysis are compared. The time-consuming results of analyzing the relationship between reversal half-cycle, gas calorific value, secondary air ratio and Reynolds number and combustion efficiency by the two models are compared. The time-consuming results of analyzing the relationship between flow characteristics and combustion efficiency of reciprocating porous medium burner by using the present model and the model based on energy spectrum analysis are shown in Tables 1 and 2, respectively.

Table 1. Results for the model in this article (s)

	Half period of reversal	Gas calorific value effect	Secondary air than	Reynolds number
1	0.36	0.42	0.41	0.42
2	0.42	0.35	0.47	0.5
3	0.35	0.36	0.4	0.39
4	0.47	0.42	0.42	0.39
5	0.52	0.36	0.43	0.42
6	0.32	0.33	0.44	0.45
7	0.25	0.36	0.45	0.44
8	0.36	0.36	0.48	0.35
9	0.35	0.38	0.26	0.32
10	0.41	0.35	0.41	0.31
11	0.47	0.41	0.35	0.36
12	0.45	0.4	0.38	0.28
13	0.43	0.37	0.36	0.35
14	0.42	0.38	0.24	0.41
15	0.41	0.38	0.35	0.26

The results of Table 1 show that the overall analysis of the relationship between flow characteristics and efficiency of reciprocating porous medium burner in the proposed model takes less time than 0.5 s, the stability of this model is strong according to the results of many measurements, and the difference between the measurements is small.

Table 2. Time-use results of flow characteristic and efficiency model of reciprocating porous medium burner based on energy spectrum analysis (s)

	Half period of reversal	Gas calorific value effect	Secondary air than	Reynolds number
1	3.25	3.26	3.46	2.25
2	3.24	3.26	4.25	2.54
3	5.24	2.35	4.25	2.45
4	2.31	2.36	4.36	2.65
5	1.35	2.47	4.36	2.15
6	2.56	2.58	4.28	2.35
7	1.24	2.65	2.57	2.65
8	1.35	2.64	2.56	2.58
9	2.55	2.35	2.68	2.57
10	2.65	3.16	2.69	2.65
11	2.24	3.25	2.34	2.45
12	2.73	3.16	2.65	2.35
13	2.71	3.25	2.58	2.35
14	2.67	3.28	2.26	2.45
15	3.26	3.26	2.34	2.65

From the data in Table 2, it can be seen that the relationship between flow characteristics and efficiency of reciprocating porous medium burner based on energy spectrum analysis takes longer time to analyze the relationship between flow characteristics and efficiency of reciprocating porous medium burner than that of the model in this paper. The stability of the model can be seen from many measurements. The difference between two adjacent analyses is relatively high. Therefore, the results of Tables 1 and 2 show that the model presented in this paper has strong stability and high efficiency in analyzing the relationship between flow characteristics and efficiency of reciprocating porous medium.

Comprehensive analysis of experimental results shows that the model can effectively analyze the relationship between flow characteristics and efficiency of reciprocating porous medium burner, and the stability and efficiency of the model is high, which has strong practicability.

4. Discussion

For the application of new combustion technology, a large number of experimental studies are needed, and the combustion mechanism and flow characteristics should be analyzed so that it can be applied to industry. The premixed combustion of porous medium gas should be further studied in the following aspects.

1. Gas adaptability: It is not difficult to find that the existing research results are mainly focused on the numerical simulation and experiment of a single gas source. Most of them are natural gas, a small part is liquefied petroleum gas, and the combustion stability of artificial gas with high tempering tendency in porous medium. Qualitative research on combustion

characteristics has not been reported. Only the numerical simulation of the effect of hydrogen addition on Methane combustion in porous medium has been made. The results show that the lean combustion limit is enlarged and the combustion speed is doubled after hydrogenation, but the results are not validated by experiments.

2. Theoretical study of porous medium gas combustion-heat transfer combined device with built-in cold source: When heat exchanger is installed in the combustor, the combustion stability of the high combination device is new and different from that of the combustor only, and the research results of foreign scholars are quite inconsistent. Scholars in China have not done any detailed research in this respect. Therefore, it is necessary for us to study the feasibility and reliable common stable working range of using multiple gas sources according to the characteristics of gas supply in China.

Academically, through research, we can deepen our understanding of the complex physical and chemical phenomena of porous medium combustion after the built-in cold source, and clarify the combustion characteristics of porous medium, including flame stability. The influence of pollutant emission promotes the interdisciplinary integration of porous medium combustion, radiation heat transfer, chemical reaction dynamics and other disciplines, and innovates while tracking the international academic frontiers.

3. Equipment development: Taking porous medium combustion device without or without built-in cold source as object, a lot of research has been carried out from theory to experiment, such as the mechanism and characteristics of heat transfer enhancement, combustion stability, pollutant emission, etc., so as to develop ultra-miniaturized gas combustion equipment or combustion heat transfer combination device.

5. Conclusions

In this paper, a new model to study the relationship between flow characteristics and efficiency of reciprocating porous medium burner is presented. Based on the structural symmetry of reciprocating porous medium burning system and the periodic exchange of internal gas flow, the physical model of reciprocating thermal cycle porous medium burning system is determined. On this basis, the reciprocating porous medium burning system is constructed. The mathematical model of flow characteristics and efficiency of medium burner is established, and the normalization and solution of the model are designed. The relationship between flow characteristics and efficiency of reciprocating porous medium burner is analyzed effectively. From the experimental results, it can be concluded that the model can better analyze the relationship between the communication half cycle, gas calorific value, secondary air ratio and Reynolds number and combustion efficiency and combustion rate in reciprocating porous medium burner. The model also changes below 0.5 s when used. The reciprocating porous medium burner flow based on energy spectrum analysis is adopted. The relationship model between dynamic characteristics and efficiency is used to analyze the relationship between flow characteristics and efficiency of reciprocating porous medium burner. The time consumed in this model is more than 2 seconds longer than that in the proposed model. It shows that the proposed model has high analysis efficiency and practicability.

References

[1] Losi, G.; Arnone, D.; Correra, S. Modelling and statistical analysis of high viscosity oil/air slug flow characteristics in a small diameter horizontal pipe. Chemical Engineering Science, 2016, 148: 190-202.

[2] Hunt, J.E.A.; Stodart, C.; Ferguson, R.A. The influence of participant characteristics on the relationship between cuff pressure and level of blood flow restriction. European Journal of Applied Physiology, 2016, 116: 1421-1432.

[3] Liu, Y.; Mutailipu, M.; Jiang, L. Interfacial tension and contact angle measurements for the evaluation of CO2-brine two-phase flow characteristics in porous media. Environmental Progress & Sustainable Energy, 2016, 34: 1756-1762.

[4] Akselsen, A.H. Characteristic methods and Roe's method for the incompressible two-fluid model for stratified pipe flow. International Journal of Multiphase Flow, 2017, 89: 81-91

[5] Xie, P.; Lu, X.; Yang, X. Characteristics of liquid flow in a rotating packed bed for CO_2, capture: A CFD analysis. Chemical Engineering Science, 2017, 172: 216-229.

[6] Nam, J.S.; Lee, M.Y.; Seo, J.H. Numerical analysis on the electrical and thermal flow characteristics of Ar-N 2. Inductively Coupled Plasma Torch System. Journal of the Korean Physical Society, 2018, 72: 755-764.

[7] Wang, Y.; Cao, L.; Hu, P.; Li, B.; Li, Y. Model establishment and performance evaluation of a modified regenerative system for a 660 MW supercritical unit running at the IPT-setting mode. Energy, 2019, 179: 890-915.

[8] Wen, B.Z.; Yong, Y.; Yong, R.Y. Measurement of flow characteristics in a bubbling fluidized bed using electrostatic sensor arrays. IEEE Transactions on Instrumentation and Measurement, 2016, 65: 703-712.

[9] Wang, C.; Zheng, D.; Zhang, Y. Relationship between lightning activity and vertical airflow characteristics in thunderstorms. Atmospheric Research, 2017, 191: 12-19.

[10] Łukasz, A. Influence of geometrical parameters on the flow characteristics of multi-pipe earth-to-air heat exchangers-experimental and CFD investigations. Applied Energy, 2018, 226: 849-861.

[11] Yu, S.; Wang, J.; Yan, M. Experimental and numerical study on single-phase flow characteristics of natural circulation system with heated narrow rectangular channel under rolling motion condition. Annals of Nuclear Energy, 2017, 103: 97-113.

[12] Wang, G.; Wang, F.; Shen, F.; Jiang, T.; Chen, Z.; Hu, P. Experimental and optical performances of a solar CPV device using a linear Fresnel reflector concentrator. Renewable Energy, 2020, 146: 2351-2361.

[13] Sun, F.; Yao, Y.; Li, X. The flow and heat transfer characteristics of superheated steam in offshore wells and analysis of superheated steam performance. Computers & Chemical Engineering, 2017, 100: 80-93.

[14] Zoca, S.M.; Shafii, B.; Price, W.J. Use of principal component analysis to evaluate variability in CASA and flow cytometer sperm characteristics. Animal Reproduction Science, 2018, 194: e20-e21.

[15] Wang, Y.; Shukla, A.; Liu, S. A state of art review on methodologies for heat transfer and energy flow characteristics of the active building envelopes. Renewable & Sustainable Energy Reviews, 2017, 78: 1102-1116.

[16] Wan Mahari, W.A.; Chong, C.T.; Cheng, C.K.; Lee, C.L.; Hendrata, K.; Yek, P.N.Y.; Ma, N.L.; Lam, S.S. Production of

value-added liquid fuel via microwave co-pyrolysis of used frying oil and plastic waste. Energy, 2018, 162: 309-317.

[17] Zalucky, J.; Claußnitzer, T.; Schubert, M. Pulse flow in solid foam packed reactors: Analysis of morphology and key characteristics. Chemical Engineering Journal, 2017, 307: 339-352.

[18] Romero, G.; Panzalis, R.; Ruegg, P. Relationship of goat milk flow emission variables with milking routine, milking parameters, milking machine characteristics and goat physiology. Animal, 2017, 11: 1-6.

[19] Jin, Z.J.; Chen, F.Q.; Qian, J.Y. Numerical analysis of flow and temperature characteristics in a high multi-stage pressur14e reducing valve for hydrogen refueling station. International Journal of Hydrogen Energy, 2016, 41: 5559-5570.

[20] Parziale, N.; Adhikari, R. Model and sensitivity analysis of the reciprocating biomass conversion reactor (RBCR). International Journal of Heat and Mass Transfer, 2020, 147: 118988.

[21] Batista, M.R.; Mota, J. Monotone iterative method of upper and lower solutions applied to a multilayer combustion model in porous media. Nonlinear Analysis Real World Applications, 2021, 58(3): 103223.

[22] Quaye, E.K.; Pan, J.; Zhang, Y.; Lu, Q.; Alubokin, A.A. Effects of influencing factors on premixed CH4-O2 combustion in a cylindrical porous media combustor. Chemical Engineering and Processing, 2021, 161(5-6): 108320.

[23] Devi, S.; Sahoo, N.; Muthukumar, P. Effect of combustion zone material on the thermal performance of a biogas-fuelled porous media burner: Experimental studies. Biomass Conversion and Biorefinery, 2020, 175: 1-9.

[24] Dowd, C.S.; Meadows, J.W. Thermoacoustic instability model with porous media: linear stability analysis and the impact of porous media. Journal of Engineering for Gas Turbines and Power, 2019, 141(4): 041017.

[25] Bai, X. Eight energy and material flow characteristics of urban ecosystems. Ambio, 2016, 45: 819-830.

[26] Cebral, J.R.; Duan, X.; Gade, P.S. Regional mapping of flow and wall characteristics of intracranial aneurysms. Annals of Biomedical Engineering, 2016, 44: 1-15.

[27] Alzoubi, K. Parametric study for a reciprocating screw blow injection molding process using design of experiments tools. Jordan Journal of Mechanical and Industrial Engineering, 2016, 10(4): 279-284.

[28] Yang, S.; Cahyadi, A.; Wang, J. DEM study of granular flow characteristics in the active and passive regions of a three-dimensional rotating drum. Aiche Journal, 2016, 62: 3874-3888.

[29] Zhang, B.; Ren, Z.; Shi, S. Numerical analysis of gasification and emission characteristics of a two-stage entrained flow gasifier. Chemical Engineering Science, 2016, 152: 227-238.

[30] Jiang, Y.; He, M.H.; Yu, C.L. Modeling and analysis of deceptive jamming signal based on phase quantization DRFM. Journal of China Academy of Electronics and Information Technology, 2015, 10: 361-366.

[31] Xu, J.Z.; Zhao, C.Y.; Ji, Y.K. Research on modelling and fast simulation of cascaded two-level converter. Journal of Power Supply, 2015, 13: 101-109.

[32] Ravi Kumar, S. The effect of the couple stress fluid flow on MHD peristaltic motion with uniform porous medium in the presence of slip effect. Jordan Journal of Mechanical and Industrial Engineering, 2015, 9(4): 269-278.

[33] Zhou, H.D.; Zhang, D.Z.; Gong, H. Analyzing and modeling for charging/discharging process of substation battery. Chinese Journal of Power Sources, 2015, 39: 536-538.

[34] Zhang, S.J. The Research on mathematical modeling education contest based on IT technology. Automation & Instrumentation, 2016, (4): 126-127.

[35] Peng, F.S. Basketball player overtraining modeling and simulation to elbow knee joint injury. Computer Simulation, 2015, 32: 382-385.

[36] Cheng, Y.W.; Ng, K.H.; Lam, S.S.; Lim, J.W.; Wongsakulphasatch, S.; Witoon, T.; Cheng, C.K. Syngas from catalytic steam reforming of palm oil mill effluent: An optimization study. International Journal of Hydrogen Energy, 2019, 44: 9220-9236.

[37] Shahirah, M.N.N.; Gimbun, J.; Lam, S.S.; Ng, Y.H.; Cheng, C.K. Synthesis and characterization of a La-Ni/alpha-Al2O3 catalyst and its use in pyrolysis of glycerol to syngas. Renewable Energy, 2019, 132: 1389-1401.

JJMIE

Volume 16, Number 1, January. 2022
ISSN 1995-6665
Pages 11 - 18

Jordan Journal of Mechanical and Industrial Engineering

Automatic Obstacle Avoidance Path Planning Method for Unmanned Ground Vehicle Based on Improved Bee Colony Algorithm

Yan Ren[1*], Jiayong Liu[2]

[1]Henan Polytechnic Institute, Nanyang 473000, China
[2]Department of Technical Education and Training, Machinery Industry Education Development Center, Beijing 100055, China

Received 14 July 2021 Accepted 22 December 2021

Abstract

In order to solve the problems of low accuracy and long time-consuming of traditional obstacle avoidance path planning methods for unmanned ground vehicle (UGV), an automatic obstacle avoidance path planning method based on improved bee colony algorithm is proposed. Based on the analysis of the working principle of the bee colony algorithm, the differential evolution algorithm is used to improve the local search ability of the bee colony algorithm; the kinematics model of the UGV is constructed, and the improved bee colony algorithm is used to optimize the obstacle avoidance path planning of the UGV. On this basis, the obstacles in the path planning are extracted by the multi-objective optimization algorithm. Finally, the obstacle avoidance path automatic planning of UGV based on improved bee colony algorithm is completed. The simulation results show that the maximum error of the proposed method is about 2%, and the planning time is short, so it has certain research value.

Keywords: Improved bee colony algorithm; Sub evolutionary algorithm; Local search; Kinematics model; Improved bee colony algorithm; Multi-objective optimization;

1. Introduction

With the continuous development of science and technology, vehicle engineering technology has been developing rapidly. UGV has emerged to meet the needs of social development. UGV is applied in various working conditions, which saves manpower and material resources and creates certain economic benefits [1]. Obstacle avoidance path planning is a key point in the research of UGV. Obstacle avoidance path refers to that after receiving effective environmental information, the UGV evades obstacles, selects the shortest route and saves time, and plans a shortest and optimal path at the starting point. Therefore, it is of great significance to study the automatic planning of obstacle avoidance path for UGV. The bee colony algorithm is applied to the obstacle avoidance path planning of UGV to improve the working efficiency of UGV. Bee colony algorithm is artificial bee colony algorithm, referred to as ABC algorithm, which has certain swarm intelligence [2]. By simulating the behavior of bee colony evolution, the algorithm optimizes the problems existing in the process of its movement. However, with the increasing complexity of the solution space dimension and multi-objective search, the disadvantages of the algorithm are also exposed. The convergence speed of the algorithm is slower and slower, and the precision of local optimal search is lower. The algorithm is good at finding problems, but it is poor in dealing with the problems found. Therefore, the artificial bee colony algorithm is improved and applied to the obstacle avoidance path planning of UGV, so as to improve the working efficiency of UGV. Therefore, researchers in this field have done a lot of research.

Reference [3] proposed a convex approximation obstacle avoidance path planning model prediction method for unmanned vehicles. This method analyzes the convex approximation principle of obstacle avoidance, optimizes the selection point of obstacle reference point, and expands the range of obstacle avoidance path. Through the improvement of the method, with the help of model predictive control and curvilinear coordinate system, the external conditions of UGV, the geometric constraints of the Road, the structural constraints of vehicles, the shortest obstacle avoidance path and the lateral speed of vehicles are taken into account proportion, complete the path planning of vehicles under the influence of complex obstacles. This method can obtain a reasonable and smooth path and avoid obstacles in the vehicle path. However, this method is easy to be affected by external factors when comprehensively analyzing vehicle factors and road factors, resulting in low accuracy of obstacle path planning, which is not conducive to universal application. In Reference [4], a dynamic obstacle avoidance oriented rolling time domain path planning method for intelligent vehicles is proposed. Aiming at the problem of vehicle avoiding obstacle path planning in low speed environment, the vehicle lane is divided according to certain rules, and the boundary of vehicle road is fitted by cubic Lagrange interpolation method. The dynamic traffic scene is simulated with the help of regional virtual force according to the divided lane area, the vehicle kinematics model is constructed, the obstacle model is predicted, the vehicle and obstacle are

* Corresponding author e-mail: shuifang5218@163.com.

avoided, the control input of vehicle model, state variables and other dynamic constraints are integrated, and the multi-objective rolling time domain controller is established to obtain the control value of vehicle front wheel angle and avoid obstacles. This method can effectively avoid obstacles, control the vehicle moving forward target, and ensure the effective planning of vehicle obstacle avoidance path. However, this method takes a long time to plan the path in the process of model building and vehicle virtual force field, and has certain limitations. Reference [5] proposed a path planning method for unmanned vehicles based on improved RRT algorithm. In this method, two RRT trees are generated at the beginning and the end at the same time, and the parallel multiple paths are calculated. The evaluation function is used to select the optimal path, and the path is optimized and smoothed. The algorithm efficiency of this method is high, but the method is simple, and the factors considered are less, and the planning accuracy is not good.

Based on the above problems, this paper proposes an automatic obstacle avoidance path planning method based on improved bee colony algorithm. Based on the analysis of the working principle of the bee colony algorithm, the differential evolution algorithm is used to improve the local search ability of the bee colony algorithm; the kinematics model of the UGV is constructed, and the improved bee colony algorithm is used to optimize the obstacle avoidance path planning of the UGV, and the automatic obstacle avoidance path planning of the UGV based on the improved bee colony algorithm is completed. The technical route of this paper is as follows.

1. The basic working principle of bee colony algorithm is analyzed, and the differential evolution algorithm is used to improve the bee colony algorithm;
2. The kinematics model of UGV is constructed, and the operation mode of UGV is analyzed;
3. The improved bee colony algorithm is used to optimize the obstacle avoidance path planning of the UGV. The obstacles in the path planning are extracted and optimized by the multi-objective optimization algorithm. The obstacle avoidance path planning of the UGV based on the improved bee colony algorithm is completed.
4. Experimental analysis.
5. Conclusion and future prospects.

2. Bee Colony Algorithm and Its Improvement

Artificial bee colony algorithm is an optimization method proposed by imitating the behavior of bees. It is a specific application of the idea of cluster intelligence. Its main feature is that it does not need to know the special information of the problem, and realizes the optimal bee colony based on the calculated probability solution. The solution only needs to compare the pros and cons of the problem. Through the local optimization behavior of each artificial bee individual, the global optimal value is finally brought out in the group, with a faster convergence rate.

2.1. Working principle of artificial bee colony algorithm

Artificial bee colony algorithm is a kind of intelligent optimization algorithm based on honeybee's honey collecting behavior. In the process of optimization, the algorithm takes into account the exploitation and search of food sources, to a certain extent, surpasses the local optimum and finds the global optimum with the maximum probability [6]. In each search process, the bee colony follows the forerunner to find the target and the optimal path solution. If the food source is found to fall into the local optimum, he will choose to explore other food sources. The artificial bee colony algorithm uses the fitness value guidance method for global optimization. The fitness function is used to explore the minimum value optimization:

$$sy_i = \begin{cases} \dfrac{1}{1+y_i} & y_i \geq 0 \\ 1+abs(y_i) & y_i < 0 \end{cases} \tag{1}$$

In the formula, y_i represents the global objective function to be processed.

In the process of global optimization, artificial bee colony algorithm needs to determine the population, the number of iterations and the control factors. In the search space, multiple initial solutions are generated randomly.

Suppose ψ represents the number of food sources, the number of each food source is N, and each optimal solution $x_i(i=1,2,3...N)$ is a multidimensional vector η, which is the number of parameters to be optimized.

On the basis of the above analysis, the subsequent wasps search the optimal solution effectively. Each member of the bee colony searches to produce a new candidate food source [7], namely:

$$\chi_{ic} = x_{ic} + \vartheta_{ic}(x_{ic} - x_{dc}) \tag{2}$$

In the formula, $d \in 1,2,3...N$, $c \in (1,2,3...\eta)$, ϑ_{ic} any number in the range of [0,1], and $d \neq c$, a new fitness function is obtained and evaluated:

$$sx_{ic} = \begin{cases} \dfrac{d}{1+x_{ic}} \\ 1+abs(x_{ic})\ d \end{cases} \tag{3}$$

After the bee colony completes the search of the optimal food source, it will share the final high-quality information with its peers [8, 9]. The probability of the bee colony to select the food source is as follows:

$$G_i = \frac{sy_i}{\sum_{d=1}^{N} sx_{ic}} \quad or\ G_i = \frac{sy_i}{\max(sx_{ic})} \tag{4}$$

According to the probability solution obtained by the above calculation, if the solution is greater than any number between [0,1], then it means that the bee colony has not obtained the optimal solution and continues to calculate. If the solution exceeds the range, it indicates that the optimal solution is obtained. Therefore, the solution can be retained and the optimal solution can be obtained by continuous search.

2.2. Improvement of artificial bee colony algorithm based on differential evolution algorithm

In the artificial bee colony algorithm, when searching the optimal solution, the bee colony search will only randomly select a food source nearby, and can not obtain more food sources with the help of other information, which will lead to the food quality guarantee, resulting in the weak

search function of the bee colony algorithm. Therefore, this paper uses differential evolution algorithm multi artificial bee colony algorithm to improve the global search ability of bee colony algorithm [10].

Set the individual optimal value to p, the improved artificial bee colony algorithm is improved by considering other interference factors:

$$q_{ic} = x_{ic} + \varpi_{l1}(p_c - x_{ic}) + \varpi_{l2}(x_{icd} - x_{icd2}) \tag{5}$$

In the formula, l_1, l_2 represents a different source of food, ϖ represents a factor that interferes with a colony's search for food. When the difference between the food source found by the bee colony and its corresponding fitness is large, interference individuals will be generated in its search process. These individuals have strong interference ability, which will affect the direction of the bee colony algorithm, affect the global optimization, and otherwise affect the convergence of the algorithm [11]. Therefore, considering that the bee colony can get the best food as soon as possible, the selection probability is optimized, that is:

$$G_i = (\frac{sy_i}{\max sy_i}) \times 10\% + 0.9 \tag{6}$$

In the formula, $\max sy_i$ represents the maximum fitness value of the food source.

3. Obstacle Avoidance Path Planning of Unmanned Ground Vehicle Based on Improved Bee Colony Algorithm

3.1. Kinematics model construction of unmanned ground vehicle

In order to realize the automatic path planning of the UGV, it is necessary to analyze the operation mode of the UGV. In this paper, the kinematics model of UGV is constructed, and the operation mode of UGV is analyzed.

Suppose the coordinate system of the outer body of the UGV is aob, its inertial coordinate system is AOB, the a axis of the outer body of the UGV overlaps with the main shaft of the vehicle, they're all UGV, its A axis is on the right side of the unmanned vehicle, and its inertial coordinate system a-axis keeps the same direction with the vehicle's moving direction, and its b axis is on the right side of the vehicle's driving direction [12]. The motion model of the UGV is shown in Figure 1.

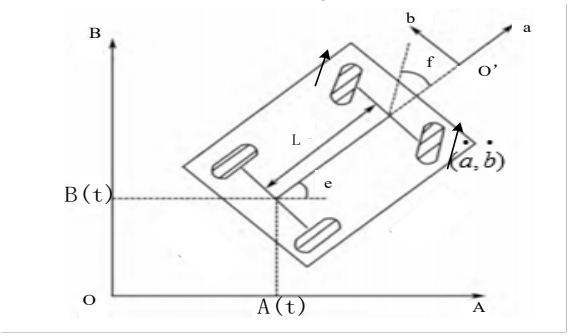

Figure 1. Motion model of unmanned ground vehicle

In Figure 1, $(A(t), B(t))$ represents coordinates in the axis coordinate system of the rear wheel of an UGV, t represents the operating time of the UGV, e represents the yaw angle of the UGV, f represents the angle of rotation of the front tire of the unmanned floor, L represents the distance between the front and rear axle of an UGV, $(\dot{a}, \dot{b})$ represents the longitudinal and transverse running speed of the vehicle in the coordinates of the UGV. According to the operation model of the UGV, the kinematic model of the UGV is constructed as follows:

$$\begin{cases} A(t) = a(t)\cos e(t) + b\sin e(t) \\ B(t) = a\sin e(t) + b\cos e(t) \\ f(t) = \dfrac{a\tan f(t)}{L} \end{cases} \tag{7}$$

3.2. Obstacle avoidance path planning of UGV based on improved bee colony algorithm

In the improved bee colony algorithm, its fitness function is the key factor of obstacle avoidance path planning [13]. The UGV must successfully avoid obstacles and arrive at the destination with the shortest time and shortest path, so as to improve the working efficiency of the UGV. In the obstacle avoidance path planning, the safety and length of UGV are regarded as the key points of path planning. Obstacles cannot overlap with the driving path of UGV [14-16].

Assuming that the penalty function H_{punish} of an obstacle free path is not greater than the barrier free distance W_{safe} of the UGV, the punishment intensity of the path increases according to the shortest distance between the obstacle and the UGV H_{punish} is:

$$H_{punish} = \begin{cases} \tau_{safe}, 0 \le \tau_{safe} \le W_{safe} \\ 0, \tau_{safe} > W_{safe} \end{cases} \tag{8}$$

$$W_{safe} = \min_{c\forall\sigma} \min_{\mu\in[1,1]} \sqrt{(a(\mu)-o_a)^2 + (b(\mu)-o_b)^2} \tag{9}$$

In the formula, $a(\mu)$, $b(\mu)$ represents the coordinates of each point when the UGV is running, o_a, o_b representing the center of an obstacle in an UGV 's path, σ represents the total set of obstacles in the route.

When the minimum distance between the driving route and the obstacles is greater than the safe distance, the distance of the driving route of the UGV needs to be analyzed. Among them, the minimum length of the shortest distance traveled through the obstacle [17, 18], and the penalty function of the minimum length of the driving path of the UGV is:

$$K_i = \int_0^1 \sqrt{(a'(\mu))^2 + (b'(\mu))^2 d\vartheta} \tag{10}$$

According to the judgment of the distance between the UGV (UGV) and the obstacles, the objective function of its travel path is designed, and the automatic planning of the obstacle avoidance path of the UGV is completed:

$$R = \upsilon_1 H_{punish} + \upsilon_2 w_{safe} \tag{11}$$

In the formula, υ_1, υ_2 for the specific gravity coefficient, the path length of UGV and the proportion of obstacles in path planning are adjusted by specific gravity coefficient.

On the basis of the above obstacle avoidance path planning, it is necessary to further optimize the extraction of multiple obstacles in the planning path. Therefore, the multi-objective optimization algorithm is used to optimize the planned obstacle avoidance path [19, 20]. In the actual operation process of UGV the diversity index of obstacles can obtain the uniformity degree of planned route distribution, which is expressed by the following formula:

$$\Delta = \frac{m_f + m_k + \sum_{i=1}^{n} \left| m_i - \overline{m} \right|}{m_f + m_k (n-1)m} \tag{12}$$

In the formula, m_f represents the extreme value of the route planning, m_k represents the Euclidean distance of the boundary solution of the route, n represents the number of planned routes for obstacle avoidance paths, $\overline{m}$ represents the average value of Euclidean distance m_i. Of which:

$$\overline{m} = \frac{\sum_{i=1}^{n} m_i}{n-1} \tag{13}$$

When calculating the maximum distance between the two farthest obstacles, it is necessary to consider the maximum coverage of obstacles in the path:

$$F = \sqrt{\frac{1}{z} \left\{ \sum_{j=1}^{h} \frac{\min(V_i^{\max}, \lambda_i^{\max}) - \max(V_i^{\min}, \lambda_i^{\min})}{V_i^{\max} - \lambda_i^{\min}} \right\}} \tag{14}$$

In the formula, $V_i^{\max}$ and $V_i^{\min}$ represents the maximum and minimum of the actual obstacle coverage. In this case, the larger the value, the larger the coverage.

The width of obstacles is an important factor affecting the normal passage of UGV [21]. The distribution range of obstacle target space can be calculated by the following formula, namely:

$$\Re = \sqrt{\sum_{j=1}^{h} \max(V_i) - \min(V_i)} \tag{15}$$

In the formula, h represents the number of obstruction targets, $\max(V_i)$ represents the maximum objective function of an obstacle in route planning, $\min(V_i)$ represents the minimum value of the objective function of an obstacle in route planning [22].

The automatic path planning flow of UGV based on improved bee colony algorithm is shown in Figure 2.

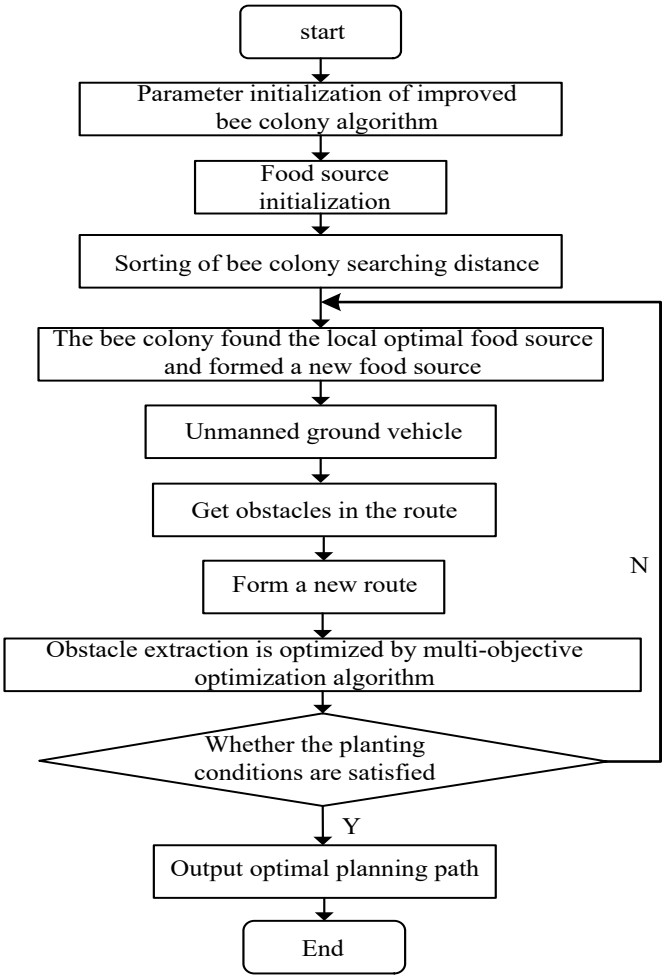

Figure 2. Automatic path planning process of UGV based on improved bee colony algorithm

4. Experimental Analysis

4.1. Experimental environment

In order to verify the scientific effectiveness of this method, simulation experiments are carried out. Methods [3] and [4] were used as experimental comparison methods. The experiment was carried out in the laboratory. The experiment is carried out in MATLAB 7 0 platform. The operating system of the experiment is windows 10 system, with 8GB memory and 3.6ghz CPU. Simulate UGV driving and obstacle avoidance path planning. The specific experimental environment is shown in Figure 3.

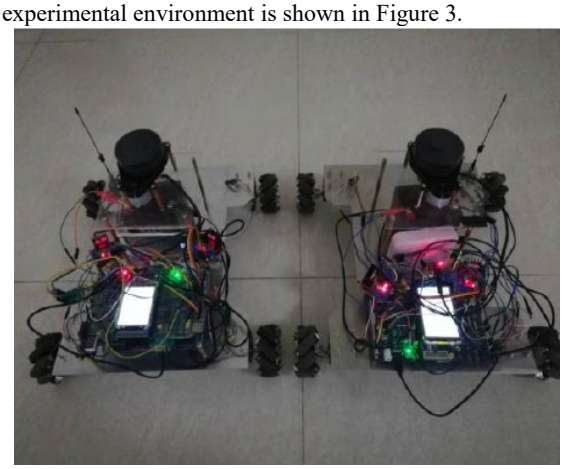

(a) Simulation of UGV

(b) Obstacle avoidance of unmanned ground vehicle

Figure 3 Real-time experiment

4.2. Experimental parameters

The experimental parameters are shown in Table 1.

Table 1 Experimental parameters

Parameter	Value
Number of obstacles/piece	10
Vehicle speed/M/S	5
Number of lanes	4
Iterations/times	10
Running time/min	60

4.3. Experimental indicators

Under the above experimental parameters design, the simulation experiment analysis is carried out. The error of obstacle avoidance path planning, the planning time and the effect of path planning are taken as the experimental indexes for experimental analysis.

1. Obstacle avoidance path planning error: obstacle avoidance path planning error is an important indicator to measure the proposed method. The lower the planning error is, the better the effectiveness of the method is.
2. Time consuming for obstacle avoidance path planning: the shorter the time required, the more efficient the vehicle can be.
3. Obstacle avoidance path planning effect: in the obstacle avoidance path planning of UGV, the search of obstacle free path is the key factor to improve its operation efficiency, which can improve the effect of path planning.

4.4. Experimental results

4.4.1. Error analysis of obstacle avoidance path planning with different methods

In order to verify the scientific effectiveness of the proposed method, the errors of the proposed method, the method in Reference [3] and the method in Reference [4] are analyzed experimentally. The lower the planning error is, the stronger the usability of the method is. The experimental results are shown in Figure 4.

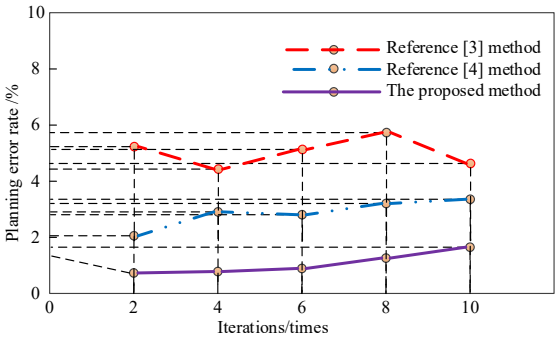

Figure 4. Comparison of path planning errors of different obstacle avoidance methods

It can be seen from the analysis in Figure 4 that there is a certain gap in the errors of the proposed method, the method in Reference [3] and the method in Reference [4] under the same experimental environment. The maximum error of the proposed obstacle avoidance path planning method is about 2%, and the planning errors of the methods in References [3] and [4] are higher than those of the proposed method. This is because the proposed method improves the artificial bee colony algorithm and constructs the motion model of UGV. According to the motion model, the obstacle avoidance path planning accuracy of the method is improved, the path planning error of the method is reduced, and the scientific effectiveness of the method is verified.

4.4.2. Time consuming analysis of different obstacle avoidance path planning methods

In order to verify the reliability of the proposed method, the time consumption of the proposed method, the method in Reference [3] and the method in Reference [4] are analyzed experimentally. Among them, the shortest time-consuming method of obstacle avoidance path planning is better. The experimental results are shown in Figure 5.

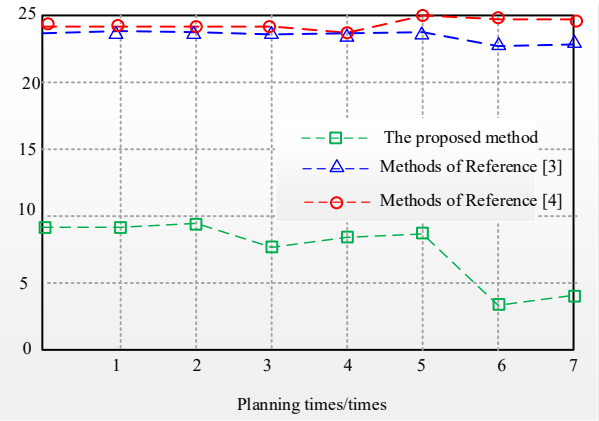

Figure 5. Time consumption comparison of different methods for obstacle avoidance path planning

From the analysis of Figure 5, it can be seen that there is a big difference in the time consumption of the proposed method, the method in Reference [3] and the method in Reference [4] for obstacle avoidance path planning of UGV. When the number of iterations is 3, the planning time of the proposed method is about 8 s, the planning time of Reference [3] method and Reference [4] method is about 22 s and 23 s respectively; when the iteration number is 7, the planning time of the proposed method reaches the minimum value, which is about 4 s, and the planning time of the method in Reference [3] and Reference [4] is about 23 s and 24 s, respectively; In contrast, the proposed method takes much less time than the other two methods. This is because the proposed method can evaluate the penalty function of obstacles through the motion model of UGV, which improves the planning speed and verifies the scientific effectiveness of the proposed method.

4.4.3. Effect analysis of different methods for obstacle avoidance path planning

In order to further verify the scientific effectiveness of the proposed method, the effect analysis of the proposed method, the method of Reference [3] and the method of Reference [4] in obstacle avoidance path planning are analyzed experimentally. The experimental results are shown in Figure 6.

It can be seen from the analysis in Figure 6 that there are some differences in the effects of the proposed method, the method in Reference [3] and the obstacle avoidance path planning method in Reference [4]. Among them, the obstacle avoidance path planning of this method is relatively stable, the shortest path can be found, and there are no obstacles to successfully reach the destination. The Reference [3] method has poor obstacle avoidance effect. When encountering obstacles, the selected path is long, and the planned path is not the optimal path. Because the robot will change the direction at a fixed angle, the path obtained in the real-time implementation process is not smooth. Referring to [4], the obstacle avoidance method can effectively judge the location of obstacles, but the planned path distance is long and the planning effect is poor. In contrast, this method can effectively avoid obstacles and reach the destination smoothly, which verifies the comprehensive effectiveness of this method.

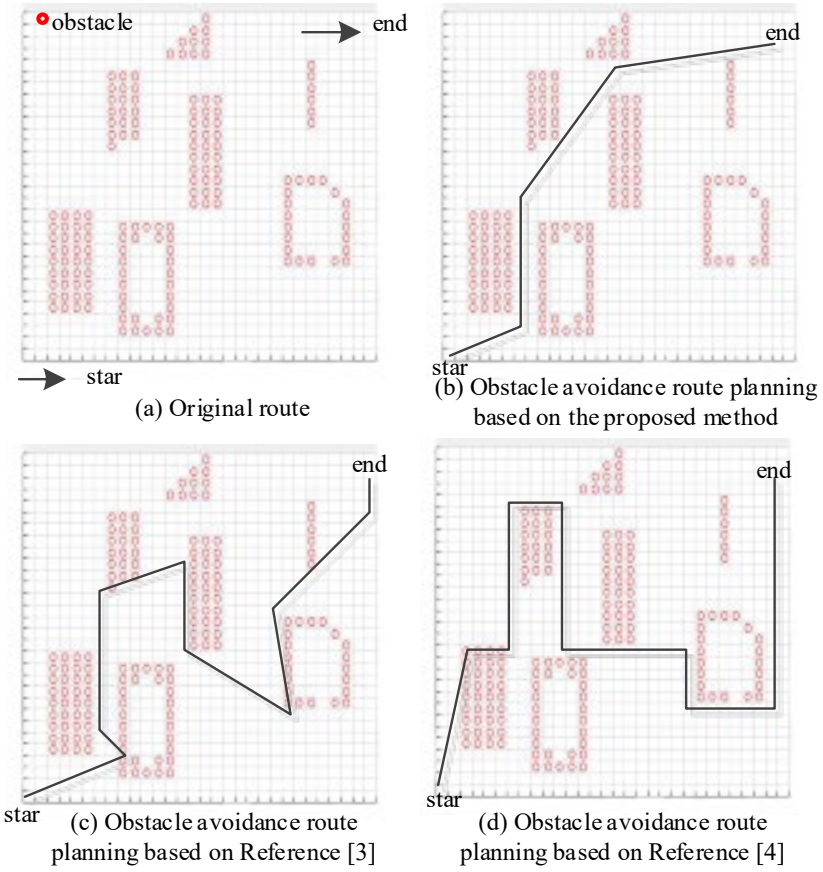

Figure 6. Comparison of different obstacle avoidance path planning methods

5. Conclusion

The obstacle avoidance path planning of UGV is a complex planning problem. In order to avoid the collision between UGV and obstacles, it is necessary to ensure the optimal route of obstacle avoidance path for UGV. Based on this, this paper proposes an automatic obstacle avoidance path planning method based on improved bee colony algorithm. This paper analyzes the working principle of the bee colony algorithm, as to improve the bee colony algorithm with differential evolution algorithm in order to enhance the local search ability of the bee colony algorithm. The study constructs the kinematics model of the UGV, and uses the improved bee colony algorithm to optimize the obstacle avoidance path planning of the UGV, and completes the automatic obstacle avoidance path planning of the UGV based on the improved bee colony algorithm. Compared with traditional methods, the proposed method has the following advantages:

1. The error of obstacle avoidance path planning using the proposed method is low, the lowest is about 2%, which verifies the accuracy of the proposed method;
2. When the proposed method is used for obstacle avoidance path planning, the shortest time is about 4 s, which verifies the efficiency of the proposed method;
3. In the experiment of obstacle avoidance path planning, the path planning of the proposed method is the best and the effect is good.

Although this paper has achieved some research results at this stage, there are still many deficiencies. In the future, it will be improved in the following aspects:

1. When improving the bee colony algorithm, we should pay more attention to the global optimization to avoid the defect of local optimization;
2. In the path planning of obstacle avoidance, the kinematic model of multiple parts of UGV should be considered when constructing the kinematics model of UGV, so as to improve the planning accuracy of obstacle avoidance path.

Acknowledgement

The research is supported by: 2021 school level young backbone teacher training plan, Project No.:202102, Project name: Research on polishing system of industrial robot based on visual perception; 2020 Development project of Jiangsu Key Laboratory of Advanced Robotics, Project No.:KJS2026, Project name: Research on Key Technologies of industrial robot polishing system based on visual perception.

References

[1] Cui, B.X., Song, J.R. Obstacle avoidance and dynamic target tracking of robot in unknown environment. Journal of Shenyang University of Technology, 2018, 40(3): 55-61

[2] Jin, X.F., Wang, H., Zong, W.J., Wang, P.C., Wang, C. Transducer and microsystem technologies. Computer Applications and Software, 2018, 37(5): 12-16.

[3] Yu, C.F., Sun, J.H. A real-time obstacle avoidance system for multi-rotor unmanned aerial vehicle based on optical flow sensor. Computer Applications and Software, 2018, 35(1): 206-210.

[4] Li, L.Y., Chang, Q., Wang, Y.L. Simulation on the target obstacles avoidance path optimization of indoor robot service. Computer Simulation, 2018, 35(1): 301-305.

[5] Zhang, Y., Meng, Q.Y., Yang, X.X. Obstacle avoidance algorithm for UAV based on bi-rotation Lyapunov vector fields. Control and Decision, 2018, 33(8): 173-181.

[6] Pei, H.L. Method of path planning and tracking for intelligent vehicle obstacle avoidance by lane changing. China Safety Science Journal, 2018, 28(9): 26-32.

[7] Li, D.F., Li, K.W., Deng, H.B., Pan, Z.H., Wei, Y.R., Wang, C. The 2D aquatic obstacle avoidance control algorithm of the snake-like robot based on artificial potential field and IB-LBM. Robot, 2018, 40(3): 346-359.

[8] Ayyappan, S., Kalaimathi, M., Venkatachalam, G. Multi-objective optimization of process parameters for electrochemical machining of 6061al/ 10%wt Al2O3/ 5%wt SiC composite using hybrid Fuzzy-Artificial bee colony algorithm. Jordan Journal of Mechanical and Industrial Engineering, 2014, 8(5): 323-331.

[9] Liu, B., Luo, X., Zhu, J. Research on simulation of planning obstacle avoidance path for automated vehicles. Computer Simulation, 2018, 35(2): 105-110.

[10] Zhang, W., Ma, Y., Zhao, H.D., Zhang, L., Li, Y., Li, X.D. Obstacle avoidance path planning of intelligent mobile based on improved fireworks-ant colony hybrid algorithm. Control and Decision, 2019, 34(2): 114-122.

[11] Kong, L., Zhang, G.F., Su, Z.P., Jiang, J.G. Ambulance emergency rescue routing planning for improved ant colony algorithm. Computer Engineering and Applications, 2018, 54(13): 153-159.

[12] Li, Y.P. Design of path tracking control system for UAV based on adaptive preview method. Jordan Journal of Mechanical and Industrial Engineering, 2020, 14(1): 101-108.

[13] Xi, A.X., Zhao, J., Zhou, T., Hu, Q.X. Target searching and global path planning in UAV/UGV cooperative systems. Application of Electronic Technique, 2019, 45(1): 5-9.

[14] Liu, E.H., Yao, X.F., Liu, M., Jin, H. AGV path planning based on improved grey wolf optimization algorithm and its implementation prototype platform. Computer Integrated Manufacturing Systems, 2018, 24(11): 2779-2791.

[15] Shan, Y.X., Guo, X.M., Long, J.Y., Cai, B.B., Li, B.J. Asymptotically sampling-based algorithm with applications to autonomous urban driving on structured road. China Journal of Highway and Transport, 2018, 31(4): 196-205.

[16] Wei, Y.L., Jin, W.Y. Intelligent vehicle path planning based on neural network Q-learning algorithm. Fire Control & Command Control, 2019, 44(2): 48-51.

[17] Zhong, M.S., Yang, Y.S., Zhou, Y.M. Free-conflict AGV path planning in automated terminals based on speed control. Computer Science, 2019, 46(7): 308-314.

[18] Pei, H.L. Method of path planning and tracking for intelligent vehicle obstacle avoidance by lane changing. China Safety Science Journal, 2018, 28(9): 26-32.

[19] Hu, L., Zhong, Y.X., Huang, J., Du, R.H., Zhang, X. Optimal path programming algorithm with consideration

of signalized intersection delay. Automotive Engineering, 2018, 40(10): 103-109+133.

[20] Hang, P., Chen, X.B., Zhang, B., Shi, P.F., Tang, T.J. Path planning and tracking control for collision avoidance of a 4WIS-4WID electric vehicle. Automotive Engineering, 2019, 41(2): 170-176.

[21] Zheng, Z.G., Ren, X.H., Cheng, Y.J., Chang, Z.W. Monocular vision mobile robot path planning in unknown environment. Computer Engineering and Applications, 2018, 54(3): 255-258,264.

[22] Xi, F.F., Zeng, X., Ji, S.M., Chen, G.D., Cai, C.P. Path planning of mobile robot based on PG-RRT algorithm. Computer Science, 2019, 46(4): 247-253.

JJMIE

Volume 16, Number 1, January. 2022
ISSN 1995-6665
Pages 19 - 29

Jordan Journal of Mechanical and Industrial Engineering

Interference Suppression Control Method for Aircraft Electromechanical Speed Control System

Qian Zhang

Department of Computer Science, Guangdong University of Education, Guangzhou 510303, China

Received 14 July 2021 *Accepted 23 December 2021*

Abstract

In order to improve the stability and dynamic performance of the aircraft electromechanical speed control system, the interference suppression control method is proposed. Firstly, the interference factors of the speed regulation system are analyzed in detail, and then the chaotic mutation attractor is introduced into the quantum particle swarm optimization algorithm by using intelligent optimization method. The nonlinear model of the aircraft electromechanical control system is established to realize the tracking and identification of the parameters of the aircraft electromechanical speed regulation system. Accordingly, the PID control method is improved, and the interference suppression of aircraft electromechanical speed regulation system is realized. The simulation results show that the control method has high control accuracy, good dynamic and static characteristics, and also has good performance in resisting disturbance. The purpose of improving the transient stability of power system is realized.

Keywords: Aircraft electromechanical; Speed control system; Quantum particle swarm optimization algorithm; Interference suppression;

1. Introduction

The scale and complexity of modern power system is increasing day by day. It has become a large-scale dynamic system with strong nonlinearity, changeable structure and a large number of disturbances [1]. For aircraft electromechanical system, improving its stability and dynamic performance has become an important topic [2]. The control of aircraft electromechanical speed control system is one of the most effective and economical means to improve the stability and dynamic performance of power system with large disturbance. In recent 20 years, with the development of modern control theory, various control strategies, such as linear optimal control, robust control and nonlinear control, have been applied to aircraft electromechanical speed control system. Among them, Fang and Shi put forward a differential geometric control method based on feedback linearization, which successfully solved the problem of decentralized stabilization of multi-machines [3]. This control method can effectively improve the stability of the system. However, this method relies heavily on the accurate mathematical model. However, in the actual power system, there are various uncertain factors, such as interference and measurement error, which makes it difficult to accurately model it. So and Jin introduced the nonlinear robust control method into the design of speed controller [4]. The disadvantage of this method is that the control law obtained is aimed at the system after feedback linearization, which does not have strict robustness for the original nonlinear system.

PID (proportional integral differential) control algorithm is a control algorithm combining proportional, integral and differential [5]. It is the most mature and widely used control algorithm in continuous system. The essence of PID control is to operate according to the function relationship of proportional, integral and differential according to the input deviation value, and the operation results are used to control the output.

Based on this, an interference suppression control method for aircraft electromechanical speed control system is proposed. Based on the detailed analysis of the interference factors of the speed regulation system, the intelligent optimization method is used to optimize the quantum particle swarm optimization algorithm, and the parameters of the aircraft electromechanical speed control system are tracked and identified. Based on the tracking and identification results, the PID is improved to improve the stability and dynamics of the aircraft electromechanical speed control system State performance objectives.

* Corresponding author e-mail: zhqian020@126.com.

2. Interference Analysis of Aircraft Electromechanical Speed Control System

2.1. Electromagnetic interference sources

In the aircraft electromechanical speed control system, the high voltage change rate and current change rate produced by IGBT (Insulated Gate Bipolar Transistor) devices in the switching process are the source of EMI (Electromagnetic Interference). For conducted electromagnetic interference, according to the provisions of GB 12668.3 on electromagnetic compatibility of speed regulating electric drive system [6], the frequency range of conducted electromagnetic interference is 150 kHz~30 MHz. In this paper, the transient process of IGBT is analyzed carefully when the conducted EMI of speed control system is analyzed accurately.

Considering that the research object of this paper is the aircraft electromechanical speed control system, the double pulse experiment is used to analyze the on-off characteristics of IGBT [7], and the circuit schematic diagram shown in Figure 1.

$C_{res}=C_{cg}$ is the transfer capacitance (Miller capacitor), $C_{oes}=C_{ce}+C_{cg}$ is the equivalent output capacitance, $C_{ies}=C_{cg}+C_{ge}$ is the equivalent input capacitance, and C_{ip} is the radiator parasitic capacitance. The equivalent circuit of on and off is shown in Figure 2.

The transient diagram of voltage and current is analyzed in the process of turn on and turn off, as shown in Figure 3.

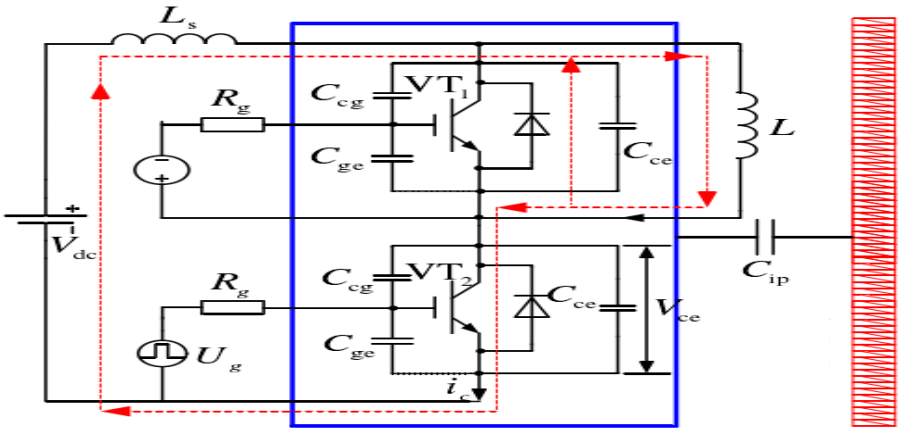

Figure 1. PID device circuit diagram

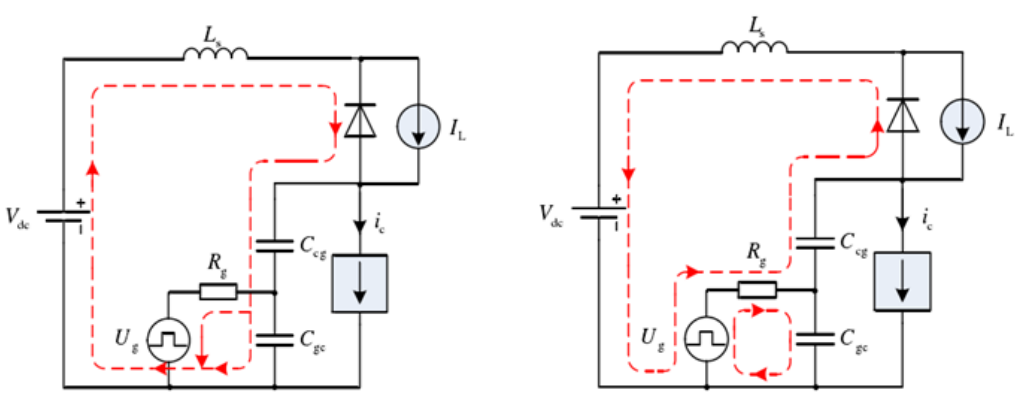

(a) Turn on equivalent circuit (b) Close equivalent circuit

Figure 2. Equivalent circuit diagram of switching process

It can be seen from Figure 3 that the current or charge of the field source will produce electromagnetic radiation with time. The intensity of electromagnetic radiation depends on the frequency. The higher the frequency, the greater the intensity of electromagnetic radiation. According to the types of interference, radiated electromagnetic interference can be divided into differential mode radiated interference and common mode radiated interference. Among them, the differential-mode radiation interference mainly refers to the electromagnetic radiation caused by the high-frequency signal loop. Common-mode radiation interference is mainly electromagnetic radiation caused by common-mode interference current flowing through cables or other long conductors.

2.2. Electromagnetic interference coupling path analysis

In the analysis of electromagnetic interference, mainly from the perspective of three elements of electromagnetic interference: (1) interference source; (2) coupling path; (3) sensitive equipment. The coupling path is the propagation channel between the interference source and the sensitive equipment of the speed control system.

These two aspects are also considered in the analysis of conducted EMI path. The common mode interference is mainly due to the high voltage change rate of the power switching device when switching, which acts on the parasitic capacitance of some main components to the ground; the differential mode interference is mainly due to the high current change rate of the power switching device when switching, which acts on the parasitic inductance of some main components. The conducted EMI path is shown in Figure 4.

According to the analysis in Figure 4, there are two common mode interference propagation paths of the speed regulation system studied in this paper: one mainly propagates at the rectifier side and the other mainly propagates at the inverter side. The analysis of radiated EMI also needs to start from three aspects: interference source, propagation path and sensitive equipment. The propagation path of electromagnetic radiation interference is shown in Figure 5.

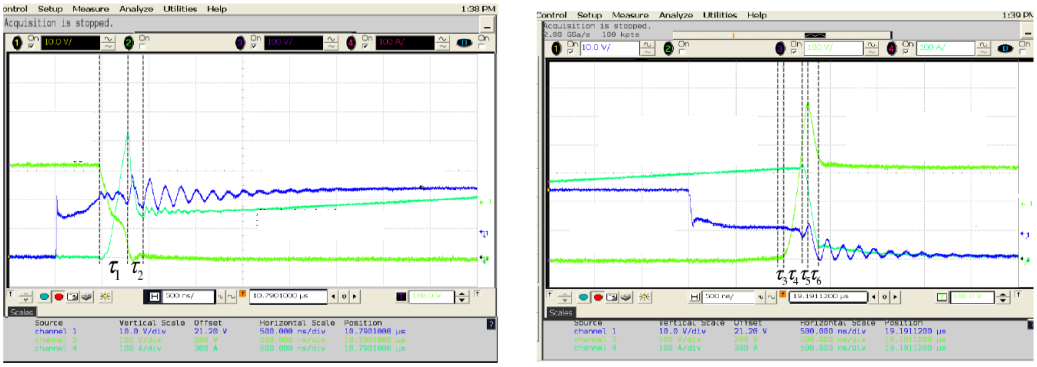

(b) Current and voltage waveforms during turn off

Figure 3. Transient diagram of voltage and current during turn on and turn off

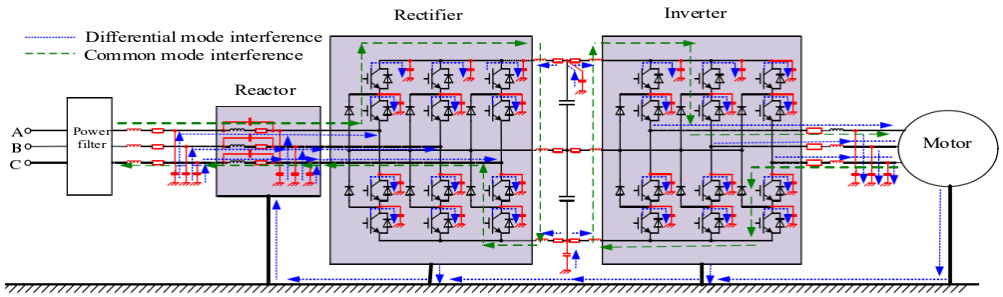

Figure 4. Interference path

In Figure 5, the frequency converter and the internal wires of the system are the main radiation sources, while the motor and other equipment around it is the main sensitive equipment. The electromagnetic wave emitted by the radiation source acts on the motor through space propagation. After the electromagnetic radiation is coupled into the circuit, the motor continues to radiate to the outer space and acts on other sensitive equipment around the motor. Through the above analysis, there are many types of radiation transmission forms in the aircraft electromechanical speed control system studied in this topic. In the speed control system, all components are connected by wires, so the high-frequency current flowing through the wires will make the wires become the main radiation interference. According to the analysis of interference, it also points out the direction of interference suppression. How to accurately track and identify the parameters of aircraft electromechanical speed control system and provide the basis for its interference suppression control is the focus of this paper.

3. Parameter Tracking and Identification of Aircraft Electromechanical Speed Control System Based on Intelligent Optimization

Aircraft electromechanical speed control system is characterized by nonlinear structure, and it is easy to seriously affect the dynamic characteristics of the system under large disturbance, which leads to discontinuous output of the system. Therefore, chaos mutation is introduced into quantum particle swarm optimization algorithm, and an improved quantum particle swarm optimization algorithm is proposed, which realizes parameter tracking and identification of aircraft electromechanical speed control system.

3.1. Parameter tracking and identification of aircraft electromechanical speed control system based on improved quantum particle swarm optimization algorithm

Accurate aircraft electromechanical speed control system is not only the basis of governor controller design, but also has important value for dynamic analysis of speed control system. Due to the complex nonlinear characteristics of aircraft electromechanical system, the current intelligent identification method is only limited to black box modeling, which is difficult to be applied to parameter tracking identification of aircraft electromechanical control system. The intelligent optimization algorithm is not only suitable for linear system parameter tracking identification, but also suitable for solving complex nonlinear system parameter tracking identification. Aiming at the slow convergence speed in parameter identification of nonlinear aircraft electromechanical regulation system, an improved quantum particle swarm optimization algorithm is proposed.

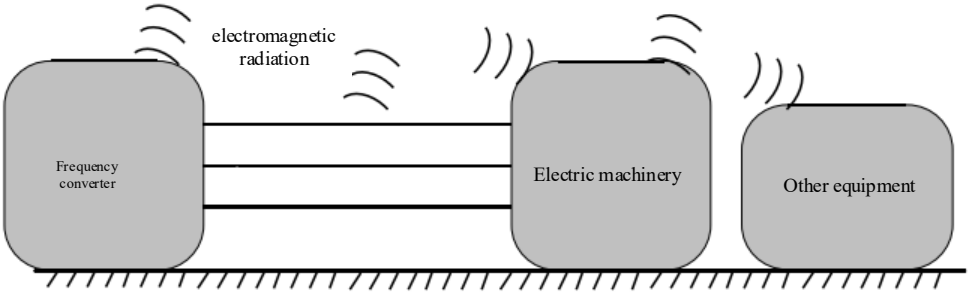

Figure 5. Radiation interference mode

In order to avoid premature convergence of the algorithm and improve the global search performance, chaotic mutation attractor is introduced into the algorithm. According to a certain probability, the population will generate mutation operation and generate population attractor to improve the diversity of the population. The mutation operation is as follows:

$$\begin{cases} y_1(t) = \mathrm{mod}[y_1(t-1)] \\ y_2(t) = \cos(2\pi y_1(t-1) + e - 1 y_2(t-1)) \end{cases} \quad (1)$$

The local attractor of the population is:

$$\begin{aligned} &if \\ &r > P_m(t) \\ &then \\ &J = \frac{\varphi_1(t)}{\varphi_1(t)+\varphi_2(t)} gbest + \frac{\varphi_2(t)}{\varphi_1(t)+\varphi_2(t)} pbest \quad (2) \\ &else \\ &J = \beta_1 gbest + \beta_2 pbest \end{aligned}$$

where $\varphi_1(t)$ and $\varphi_2(t)$ is the distance between $y_1(t)$ and $y_2(t)$ with the attractor, P_m is the rated output power, r is the actual output power, and β_1, β_2 is the contraction coefficient.

According to the above equation, the particle state update equation in the improved quantum particle swarm optimization algorithm is as follows:

$$t_{i,j}^{k+1} = J + \beta \left| gbest_{i,j}^{k+1} - t_{i,j}^{k} \right| \ln(\frac{r}{P_m}) \quad (3)$$

To sum up, the calculation steps of the improved quantum particle swarm optimization algorithm are as follows:

1. Initializing the population;
2. The creation coefficient decreases linearly from 1.0 to 0.5 with the number of iterations;
3. Calculate the average best position of the population;
4. The fitness value of each particle is compared with the best position of the particle individual, and if the former is better, it is regarded as the best position of the current individual;
5. Comparing the fitness value of each particle with the global best position, and if the former is better, taking it as the global best position;
6. Refreshing the new position of particles;
7. Calculate the variance of population fitness. If the variance is less than the value of C (judging whether the population falls into premature convergence or not, the value of C depends on the specific situation), conduct chaotic search for N times to obtain the optimal solution vector and the corresponding fitness value. If the fitness value is less than the global optimal fitness value, this is the global best position;
8. If the termination condition is not met, return to (2); Otherwise, the algorithm ends.

The pseudo code of the algorithm is as follows:

```
procedure PSO
    for each particle i
        Initialize velocity Vi and position Xi for
    particle i
        Evaluate particle i and set pBesti = Xi
    end for
    gBest = min{pBesti}
    while not stop
        for i=1 to N
            Update the velocity and position of
        particle i
            Evaluate particle i
            if fit (Xi) < fit (pBesti)
                pBesti = Xi;
            if fit(pBesti) < fit (gBest)
                gBest = pBesti;
        end for
    end while
    print gBest
end procedure
```

3.2. Parameter tracking and identification of aircraft electromechanical speed control system

The basic idea of the nonlinear model based on intelligent optimization algorithm is to transform the parameter tracking identification problem into the optimization problem of solving the extreme value of fitness function [8]. Set the physical parameters to be identified as the particles of the population, establish the fitness function according to the output response of the identification model, and continuously adjust the particles of the population according to the evolution strategy of the intelligent optimization algorithm. When the fitness function exceeds a certain threshold or the evolution algebra reaches the set value, that is to say, the globally optimal particle is considered to be the solution of the extremum problem [9]. Based on this, the nonlinear model of aircraft electromechanical control system as shown in Figure 6 is established.

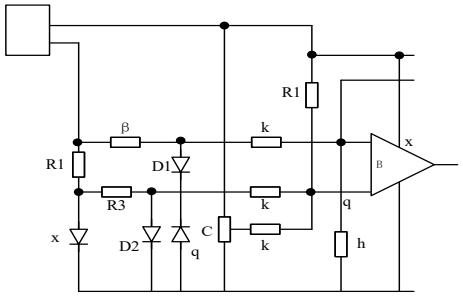

Figure 6. Nonlinear model of aircraft electromechanical control system

Considering that different parameter combinations may correspond to the same system output, unit speed, transmission distance and main receiver stroke are selected as system outputs, and the degree of fitness function evaluation and identification model approaching the original model is evaluated as follows,

$$fitness = \frac{1}{N}\left(\sum_{i=1}^{N}\left(x_i - \hat{x}_i\right)^2 + \sum_{i=1}^{N}\left(m_i - \hat{m}_i\right)^2 + \sum_{i=1}^{N}\left(y_i - \hat{y}_i\right)^2\right) \quad (4)$$

where x_i, m_i, y_i is the i sampling value of the original system output unit speed, transmission distance and main receiver stroke, and $\hat{x}_i, \hat{m}_i, \hat{y}_i$ is the i sampling value of the identification model output unit speed, transmission distance and main receiver stroke.

The system input and output data required for identification are generated by simulation test. The simulation test of turbine governing system includes no-load disturbance test and load disturbance test. The simulation test time is 10 s, the sampling frequency is 1000 Hz, the maximum iterations of the algorithm is 30 times, and the independent operation is 12 times. The experimental results are shown in Figure 7.

It can be seen from the middle Figure 7 that the error between the system response of the identification parameter mean value and the dynamic response of the aircraft electromechanical regulation system under the set parameters is very small, so it is difficult to distinguish the difference between the identified system response and the dynamic response of the aircraft electromechanical regulation system under the set parameters.

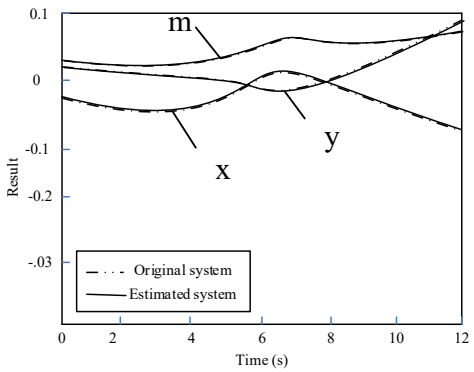

Figure 7. Parameter tracking and recognition effect

4. Interference Suppression Control of Aircraft Electromechanical Speed Control System

The essence of classical PID control is to eliminate the error based on error information. It is a kind of adjustment method that directly uses the information of set value and output value to determine the size of control force. It is a weighted combination of proportional, integral and derivative links of error. These three links represent the estimation of the "present", "past" and "future" information of the error respectively. Since PID only needs to know the input and output information of the controlled system, its algorithm is simple, adaptable and reliable, so it is widely used in industrial control system. One of the important reasons that PID can be widely used is that it only needs the expected value and the actual output value of the system to complete the control [10, 11]. In fact, it is not necessarily reasonable to directly take the error between the expected value and the output value. Sometimes, it will cause excessive instantaneous control force, which will lead to overshoot of the system and even damage the system hardware. In addition, in practical application, and because of the complex electromagnetic environment, ordinary differentiator cannot effectively filter, so that the differential link cannot be used, only PI control law can be used, which further reduces the control performance of PID. Moreover, even if the differential link can be used, the efficiency of the weighted combination of PID proportional, integral and differential link is not

high. Therefore, on the basis of realizing the accurate parameter tracking and identification of aircraft electromechanical speed control system, an improved PID control strategy based on the results of tracking and identifying the parameters of the speed control system is proposed [12].

The function of current loop in the whole control system is not only to quickly track the output command of the speed loop, but also to limit the maximum current [13, 14]; As the outer loop, the speed regulator should track the input command quickly and accurately, and play an anti-interference role. Therefore, the current regulator in this paper only needs the traditional PI regulator, while the relatively important speed regulator adopts the improved PID strategy, so as to minimize the complexity of the control system and greatly improve the dynamic and static characteristics of the speed control system [15, 16].

The design method of PID can be carried out as follows:

The first step is to establish the second-order approximate speed mathematical model of aircraft electromechanical system [17]. In general, the cut-off frequency of the current loop is higher than that of the speed loop and the response speed is faster. The given value $^{*}I_q$ of the q-axis current is approximately regarded as the actual current I_q of the q-axis. In fact, the given current $^{*}I_q$ of the q-axis is not always the same as the actual current I_q of the q-axis. There are always large or small errors before reaching the steady-state, but the second-order interference suppression controller can effectively compensate for this influence. The second order motion equation of generator in rotating coordinate system is as equation 5.

Among them, ω is the rotor angle; $Kr = k\text{-}1$ is the minimum value of angular velocity deviation; $K_0=2\pi K_r$ is the standard value of rotor angular velocity; P_m is the minimum value of input mechanical power; m, t represents damping coefficient, generator moment of inertia and generator operating time constant respectively; and (ω_s, 0, P_{ms}) is the balance point of the system.

Secondly, the structure of PID is determined. The structure block diagram of the speed controller based on the second-order improved active disturbance rejection control is shown in Figure 8.

The third step is to design the parameters of PID controller according to the model. When parameter disturbance exists in the system model, the motion equation $H(x)$ can be modified to obtain the desired control effect function as follows

$$H(x)' = \frac{1}{2}H(x) - \frac{1}{2}\left[P_m(\omega - \omega_s)\right] \quad (6)$$

In order to make the control law independent of the accurate balance point of the system, the system equilibrium point (ω_s, 0, P_{ms}) is regarded as the parameter to be estimated, d is the parameter adaptive coefficient.

$$Q = \left[\int_0^t K_0 K_r^{\,2} dt - \omega_s\right] - \frac{1}{2}d(P_m - P_{ms}) \quad (7)$$

$$H(\omega, K_r, P_m) = \frac{1}{2}MK_0K_r^{\,2} - \left[P_m(\omega - \omega_s)\right] + \frac{1}{2}(P_m - P_{ms}) + J\left(\frac{(^{*}I_q - I_q)}{U_q} + \frac{(^{*}I_d - I_d)}{U_q}\right) \quad (5)$$

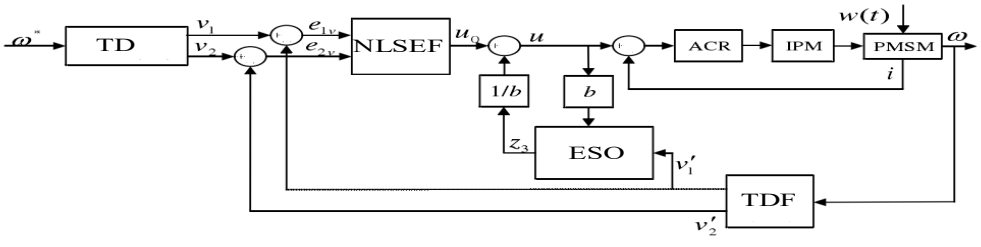

Figure 8. Second order PDI speed controller

The third step is to design the parameters of PID controller according to the model. When parameter disturbance exists in the system model, the motion equation *H(x)* can be modified to obtain the desired control effect function as follows

$$H(x)' = \frac{1}{2}H(x) - \frac{1}{2}\left[P_m(\omega - \omega_s)\right] \quad (6)$$

In order to make the control law independent of the accurate balance point of the system, the system equilibrium point (ω_s, 0, P_{ms}) is regarded as the parameter to be estimated, *d* is the parameter adaptive coefficient.

$$Q = \left[\int_0^t K_0 K_r^{\,2} dt - \omega_s\right] - \frac{1}{2}d(P_m - P_{ms}) \quad (7)$$

5. System Simulation

As an example to verify the effectiveness of the proposed method, the simulation experiment is divided into two parts: the dynamic and static characteristics of the proposed improved PID and NRC (nonlinear robust controller) are compared; the simulation results of the improved PID and ADRC are compared to illustrate the advantages of PID in anti-interference. Using Matlab/Simulink joint simulation method, the parameters of aircraft electromechanical system are shown in Table 1.

Table 1. Simulation parameters of aircraft electromechanical system

Parameter	Numerical value	Parameter	Numerical value
Rotor flux linkage	0.79263 wb	Rated power	1.0 kW
Moment of inertia	$8*10^{-4}$ kg.m^2	Rated speed	1*103 rpm
Pole pairs	2	Rated Voltage	220 V
AC-DC axis inductance	$4.35*10^{-3}$ H	Rated torque	10 N*m
Stator resistance	0.9 Ω	Friction coefficient	0

The population size is 100, the mutation probability is 0.05, the self factor is 2.0, the global factor is 2.0, the number of particles is 80, the maximum number of iterations is 1500, and the historical best fitness value is 54.041. The sampling period of PID is 0.1 s, the proportional gain is 1, and the integral time constant is 1.5.

1. Control effect comparison

When the given speed is set at 600 rpm, the simulation results show that the control effect of the inverter under NRC and improved PID control is shown in Figure 9 and Figure 10.

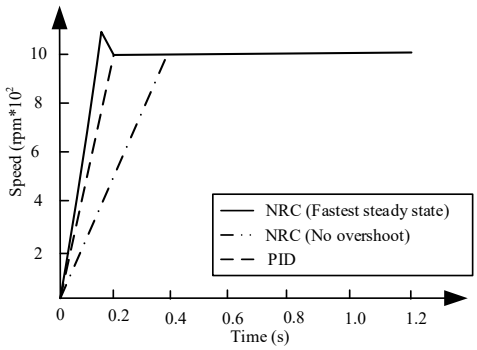

Figure 9. Control effect under given start condition

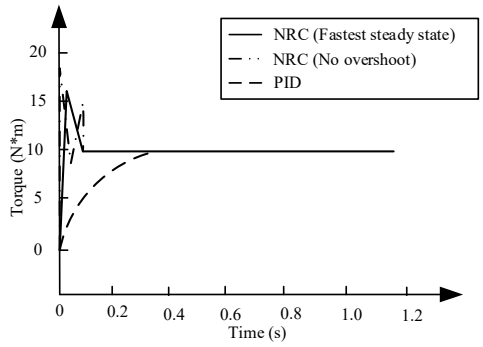

Figure 10. Torque curve during start-up

It can be seen from Figure 9 that the fastest time for NRC to reach steady state is almost the same as that of improved PID, both of which are 0.2 s. However, the speed curve of NRC speed regulator at this time has overshoot, while the whole speed regulation process of improved PID has no overshoot phenomenon and control force mutation. When the parameters are selected to make it reach the steady state in the way of no overshoot and the shortest time, the time to reach the steady state is about 0.4 s; no matter how the NRC parameters are adjusted, if the dynamic process of the speed is to be as small as possible, it will take a long time to reach the target value, and to reach the steady state as soon as possible, the speed will inevitably overshoot, which is the overshoot and fast in NRC controller There is an inherent contradiction between the two, and the improved PID is a good solution to this contradiction.

It can be seen from Figure 10 that under all NRC parameters, the torque curve will directly climb to the maximum of the current limit at the beginning, and then rapidly decline under the control of the controller. The torque of the improved PID controller has almost no sudden change in the whole transition process. In the actual speed control system, the sudden change of control force will cause the output current mutation of three-phase inverter, which will lead to motor heating and spark, which not only wastes electric energy, causes motor howling, pollutes electromagnetic environment, but also greatly reduces the service life and stability of motor. In the running process of the motor, it is often necessary to deal with the interference caused by the load with different torque. The anti-interference performance of the speed control system can be detected by suddenly adding load. The given speed is 1000 rpm and the load torque is 1 n. When the system reaches steady state, when t = 1 s, the load torque of 5 N is suddenly applied. The response curve under NRC and improved PID control is shown in Figure 11.

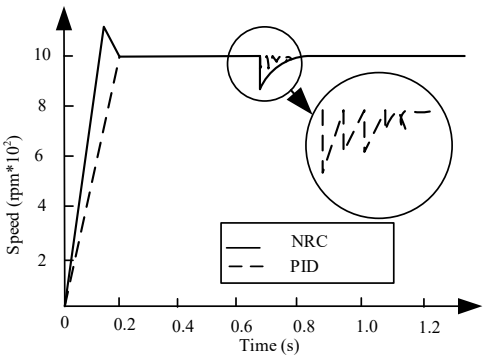

Figure 11. Speed response curve under the condition of increasing load

It can be seen from Figure 11 that the system controlled by NRC has a large dynamic drop in speed and a long dynamic recovery process; in contrast, the dynamic drop of the system under the improved PID control is very small, and the dynamic recovery process is also very short. It can be seen that the system has good robustness and can stabilize the speed in a short time when disturbance occurs

2. Comparison of control effect between improved PID and NRC under disturbance

In order to verify the superiority of the improved PID in dealing with high-frequency disturbance, the white noise module in Simulink is used to generate white noise, which is superimposed on the speed feedback link to simulate the high-frequency interference of the speed feedback link. The white noise is shown in Figure 12.

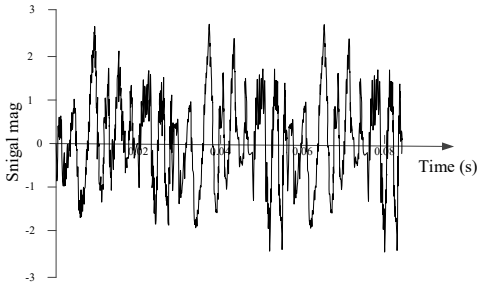

Figure 12. Adding noise information

It can be seen from Figure 12 that the amplitude of the noise is about 3V. Since the white noise is generated by the random number of normal distribution, the noise content of each frequency band is relatively large. The simulation results after adding white noise are shown in Figure 13.

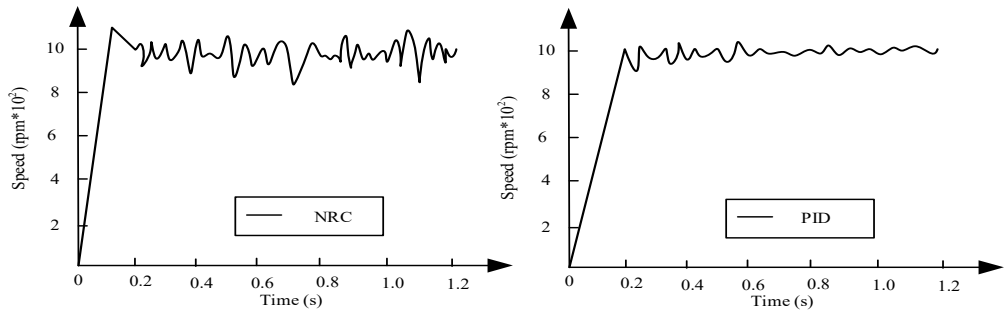

Figure 13. Speed response curve under disturbance

It can be seen from Figure 13 that for the same noise interference, the improved PID can better follow the given value. In the whole process, the speed has little fluctuation, the dynamic characteristics are good, and the control precision is high. However, the speed curve under the traditional NRC control has a large fluctuation, which is because the white noise contains large differential information, if it cannot accurately and effectively control the speed curve, it is necessary to improve the performance of the system If it is tracked and identified, it will enter the control system directly, which will inevitably lead to the fluctuation of the controller and affect the control effect.

6. Conclusion

In this paper, the aircraft electromechanical speed control system control, through the comprehensive analysis of the interference factors, get the interference source and interference mode, through the intelligent optimization algorithm to optimize the quantum particle swarm optimization algorithm, and then realize the accurate tracking and identification of aircraft electromechanical speed control system parameters, provide reliable basis for control, and improve the original PID based on the tracking identification results. The results show that the improved PID has better dynamic and static characteristics than NRC, and is better than NRC in resisting high frequency disturbance.

Due to the time relationship, coupled with my limited knowledge and ability, there is still room for further optimization. The current control software needs to correct the initial phase error. In the follow-up work, the function of self-correction can be achieved by programming. The rotor position of the hardware platform is measured by the photoelectric encoder. The method of no position sensor can be introduced to improve the system, so as to reduce the investment of hardware.

Acknowledgement

The research is supported by: Computer Experimental Teaching Demonstrating Center (undergraduate teaching quality and teaching reform project of Guangdong education); Guangdong University of Education Network Engineering Key Subject (No. ZD2017004); The undergraduate teaching quality and teaching reform project of Guangdong University of Education (Experimental Teaching Demonstration Center of Computer Application) (No. 2018sfzx01).

References

[1] Dhundhara S, Verma Y P. (2018). Capacitive energy storage with optimized controller for frequency regulation in realistic multisource deregulated power system. Energy, 147: 1108-1128.

[2] Fernández-Porras P, Panteli M, Quirós-Tortós J. (2018). Intentional controlled islanding: When to island for power system blackout prevention. IET Generation Transmission & Distribution, 12(14): 3542-3549.

[3] Fang Y L, Shi Z K. (2019). Feedback linearization control of highway macroscopic discrete model. Science Technology and Engineering, 49(3): 59-65.

[4] So G B, Jin G G. (2018). Fuzzy-based nonlinear PID controller and its application to CSTR. Korean Journal of Chemical Engineering, 35: 819-825.

[5] Li W W, Hu Y M, You W X. (2019). Research on cascade robust control of hydro turbine speed governor system. Water Power, 45(7): 90-93.

[6] Wang F, He L. (2021). FPGA based predictive speed control for PMSM system using integral sliding mode disturbance observer. IEEE Transactions on Industrial Electronics, 68(2): 972-981.

[7] Tang Y, He Y J, Wang F X, Lee D H, Ahn J W, Kennel R. (2018). Back-emf-based sensorless control system of hybrid SRM for high-speed operation. IET Electric Power Applications, 12(6): 867-873.

[8] Lee J H, Song J Y, Kim D W, Kim J W, Jung S Y. (2017). Particle swarm optimization algorithm with intelligent particle number control for optimal design of electric machines. IEEE Transactions on Industrial Electronics, 65(2): 1791-1798.

[9] Han M, Ren W, Xu M, Qiu T. (2018). Nonuniform state space reconstruction for multivariate chaotic time series. IEEE Transactions on Cybernetics, 49(99): 1885-1895.

[10] Tang H, Gao J, Chen X, Yu K M, To S, He Y, Chen X, Zeng Z H, He S F, Chen C B, Li Y M. (2018). Development and repetitive-compensated pid control of a nanopositioning stage with large-stroke and decoupling property. IEEE Transactions on Industrial Electronics, 65(5): 3995-4005.

[11] Magdy G, Mohamed E A, Shabib G, Elbaset A A, Mitani Y. (2018). Smes based a new pid controller for frequency stability of a real hybrid power system considering high wind power penetration. IET Renewable Power Generation, 12(11): 1304-1313.

[12] Jia Z. Design of mechanical and electrical control system of mixed liquid gas pressure energy storage based on maximum power point tracking. Jordan Journal of Mechanical and Industrial Engineering, 2021, 15(1), 143-152.

[13] Erturk F, Akin B. (2019). Spatial inductance estimation for current loop auto-tuning in IPMSM self-commissioning. IEEE Transactions on Industrial Electronics, 67(5): 3911-3920.

[14] Aggarwal A. (2018). Current fluctuations of the stationary ASEP and six-vertex model. Duke Mathematical Journal, 167(2): 269-384.

[15] Merino-Caviedes S, Cordero-Grande L, Perez M T, Casaseca-de-la-Higuera P, Martín-Fernández M, Deriche R, Alberola-López C. (2018). A second order multi-stencil fast marching method with a non-constant local cost model. IEEE Transactions on Image Processing A Publication of the IEEE Signal Processing Society, 28(4): 1967-1979.

[16] Abdesselem C. Direct torque control of induction motor based on space vector modulation using a fuzzy logic speed controller. Jordan Journal of Mechanical and Industrial Engineering, 2014, 8(3), 169-176.

[17] Bouchut F, Chalons C, Sébastien G. (2020). An entropy satisfying two-speed relaxation system for the barotropic Euler equations: application to the numerical approximation of low Mach number flows. Numerische Mathematik, 145(1): 35-76.

JJMIE

Volume 16, Number 1, January. 2022
ISSN 1995-6665
Pages 31 - 40

Jordan Journal of Mechanical and Industrial Engineering

Gait Control System of Autonomous Mobile Robot Based on PMAC

Guobin Si*, Xiaofeng Jin, Chunxia Wang

College of Mechanical and Electronic Engineering, Jiaozuo University, Jiaozuo 454000, China

Received 14 July 2021 *Accepted 27 December 2021*

Abstract

In the current gait control system of autonomous mobile robot, the stability of robot motion control and the result of gait planning are poor, and the walking compliance and walking efficiency are low, a gait control system of autonomous mobile robot based on PMAC (Programmable Multi-Axis Controller) is designed. Through linear analysis of the control system of the autonomous mobile robot, the dynamic model of the motion control of the autonomous mobile robot is constructed, the walking cycle and key postures of the robot are analyzed, the stable walking gait is planned, and the dynamic model of the robot motion control is combined to reverse the robot correspondence. For the joint rotation angle, the motor rotation angle under the key gait is obtained by using the theory of series and parallel mechanisms, and the cubic spline interpolation method is used to generate a complete gait motion trajectory. According to the architecture, the servo system of the robot and the hardware structure with IMAC (Integrated Multi-Axis Controller) flex motion controller as the core of PMAC motion controller are designed. The software design of modular structure is used to realize the gait control of autonomous mobile robot. The experimental results show that the motion control stability and gait planning results of the proposed method are better, the gait trajectory is smooth and the walking compliance is high, which can effectively improve the walking efficiency of the robot.

Keywords: : PMAC; IMAC flex motion controller; Autonomous mobile robot; Gait control; Cubic spline interpolation method;

1. Introduction

Autonomous mobile robot is an integrated system which integrates environment perception, dynamic decision-making and planning, behavior control and execution. It has a high degree of self-planning, self-organization and self-adaptive ability, which is suitable for working in complex unstructured environment, and can realize object identification, autonomous reasoning, path planning and control functions in complex environment [1]. It brings together the research results of sensor technology, computer technology, mechanical engineering, electronic engineering, automation control engineering, artificial intelligence and other multidisciplinary fields. It is one of the most active areas of scientific and technological development [2]. With the rapid development of computer, network, mechanical and electronic, information, automation and artificial intelligence technology, the research of autonomous mobile robot has entered a new stage, and its application scope has also expanded to various fields of society. It is not only widely used in industry, agriculture, national defense, medical, service and other industries, but also in harmful and dangerous situations such as mine clearance, search and rescue, radiation and space fields [3]. However, the working environment faced by autonomous mobile robots is becoming more and more complex, and higher requirements are put forward for the controller of autonomous mobile robots. Different application fields require the controller to integrate different peripheral devices and application software, and even need to be transplanted between different software and hardware platforms. Therefore, the development of highly open autonomous mobile robot controller has become a research hotspot in this field.

Robot control system is a typical multi axis real-time motion control system, which mainly realizes the coordinated control of various walking robots, tracked robots, bionic robots and robot groups. At present, the research on the control system of robots has also made great progress. Reference [4] uses the natural stimulus algorithm Eagle strategy and particle swarm optimization (ESPSO) technology to design an adaptive control system for a two-wheeled inverted pendulum mobile robot. According to the multi input and multi output characteristics of two wheel inverted pendulum mobile robot, considering the instability of the inverted pendulum system, two loops are proposed in the design. One loop is used to balance the linear displacement, the other loop maintains the required angular motion, so as to realize the function of keeping the balance when the robot moves to the required position. The system has

* Corresponding author e-mail: haoxinqing1688@126.com.

the characteristics of nonlinear open-loop instability. Reference [5] designed a three-wheeled omnidirectional mobile robot sliding mode control system based on reduced-order extended state observer (ESO), constructed a dynamic model with unknown friction, and designed a controller. The reduced order ESO is used to estimate the friction compensation effect. According to the second-order sliding mode technology with parameter uncertainty, the other part of the work is controlled. The effectiveness and robustness of the control system in compensating different friction effects are good. However, there are some problems in the system, such as poor stability of robot motion control and gait planning, low walking compliance and walking efficiency.

Aiming at the above problems, an autonomous mobile robot gait control system based on PMAC is designed. Through the dynamic analysis of the motion control of the autonomous mobile robot, the dynamic model of the motion control of the autonomous mobile robot is constructed. The walking cycle and key posture of the robot are analyzed. The stable walking gait is planned, and the corresponding joint angle of the robot is inversely solved. According to the architecture design of the robot's servo system and the hardware structure with the IMAC Flex motion controller in the PMAC motion controller as the core, the software design of the modular structure is adopted to realize the gait planning and motion control of the autonomous mobile robot. The whole control system has good motion control stability, walking flexibility and smooth gait trajectory, which can effectively improve the walking efficiency of the robot.

2. Dynamic Analysis of Autonomous Mobile Robot Motion Control

In the process of autonomous mobile robot motion, its dynamics directly affect the speed, accuracy and efficiency of autonomous mobile robot. In this paper, through the linear analysis of autonomous mobile robot control system, the dynamic model of autonomous mobile robot motion control is constructed, and the analysis of autonomous mobile robot motion control dynamics is realized.

2.1. Linearization analysis of autonomous mobile robot control system

Because of the complex structure and multiple degrees of freedom of autonomous mobile robot, it is necessary to analyze and solve the dynamic equation of the autonomous mobile robot in motion control, and establish the dynamic model of the autonomous mobile robot motion control, so as to provide the basic basis for the control of its motion path and attitude.

The dynamic equation of autonomous mobile robot [6] is:

$$\boldsymbol{E}(\boldsymbol{q})\boldsymbol{R}+\boldsymbol{V}(\boldsymbol{q})+\boldsymbol{G}(\boldsymbol{q})+\boldsymbol{F}(\boldsymbol{q})\delta_s=\delta \quad (1)$$

In Equation (1), $\boldsymbol{E}(\boldsymbol{q})$ represents the $\alpha\times\beta$ dimensional inertia matrix, $\boldsymbol{R}$ represents the reaction force of the ground against the wheel of the autonomous mobile robot, $\boldsymbol{V}(\boldsymbol{q})$ represents the centripetal force vector, $\boldsymbol{F}(\boldsymbol{q})$ represents the gravity vector, δ_s represents the friction vector, δ represents the bounded unknown interference, and O represents the control force.

In order to prevent the uncertainty from interfering with the motion of the autonomous mobile robot, by adding a suitable state space Equation, the dynamic equation of the autonomous mobile robot is obtained as:

$$Y=\begin{bmatrix}[0_{n\times n}1_{n\times n}]\\ -\boldsymbol{U}^{-1}(\boldsymbol{x})\left[o(x)+g(x)+f(x)\right]\end{bmatrix}+\begin{bmatrix}0_{n\times n}\\ \boldsymbol{U}^{-1}(\boldsymbol{x})\end{bmatrix}(\delta-\delta_s) \quad (2)$$

In Equation (2), $Y=[\boldsymbol{q}\bullet\boldsymbol{R}];1_{n\times n}$ and $0_{n\times n}$ represent the $\alpha\times\beta$ dimensional unit matrix and the zero matrix, respectively, $\boldsymbol{U}(\boldsymbol{x})$ represents the joint vector of the autonomous mobile robot, $o(x)$ represents the $(\alpha-1)$ dimensional gravity term, $g(x)$ represents the $\alpha\times1$ dimensional joint torque, and $f(x)$ represents the reaction force of the wheel axle. Because the centripetal force vector and friction vector mode of the autonomous mobile robot during operation are complex and difficult to calculate, the dynamic equation needs to be simplified as:

$$Y=\boldsymbol{A}_s o(x)+\boldsymbol{P}f(x)+\boldsymbol{U}^{-1}(\boldsymbol{x})\delta-\boldsymbol{P}\boldsymbol{U}^{-1}(\boldsymbol{x})\delta_s \quad (3)$$

In Equation (3), the choice of $\boldsymbol{P}=\begin{bmatrix}0_{n\times n}\\ 1_{n\times n}\end{bmatrix}$,

$$f(x)=-\boldsymbol{U}^{-1}(\boldsymbol{x})\left[o(x)+g(x)+f(x)\right]-\left[A_{21}A_{22}\right]$$

, $\boldsymbol{A}_s=\begin{bmatrix}0_{n\times n}1_{n\times n}\\ A_{21}A_{22}\end{bmatrix}$, A_{21} and A_{22} directly affects the stability of $\boldsymbol{A}_s$.

According to Equation (2) and Equation (3), the motion defined control torque of autonomous mobile robot is as follows:

$$\delta=-\boldsymbol{U}(\boldsymbol{x})\hat{f}(x)+\boldsymbol{U}(\boldsymbol{x})\sigma \quad (4)$$

In Equation (4), $\hat{f}(x)$ represents the estimated value of $f(x)$, and σ represents a new control variable. Through stochastic linear quadratic optimal analysis, the dynamic equation of autonomous mobile robot is transformed into quadratic polynomial dynamic equation, and the linear analysis of autonomous mobile robot dynamic system is realized. The dynamic equation of quadratic polynomial is as follows:

$$Y=\boldsymbol{A}_s o(x)+\boldsymbol{P}\sigma+\overline{f}(x)-\boldsymbol{P}\boldsymbol{U}^{-1}(\boldsymbol{x})\delta_s \quad (5)$$

In Equation (5), $\overline{f}(x)=f-\hat{f}$ represents estimation error. The linear normalization of the

control system of the autonomous mobile robot can effectively optimize the motion performance of the autonomous mobile robot, reduce the interference error and improve the motion stability of the autonomous mobile robot.

2.2. Dynamic model of autonomous mobile robot motion control

When studying the motion control of autonomous mobile robot, its dynamic model is the key point of motion control, but the dynamic model is easily affected by nonholonomic constraints, thus affecting the control parameters [7]. In this paper, the dynamic model of autonomous mobile robot is adopted, and the input value in the control process is set as generalized force rather than velocity. Therefore, the kinematic model of autonomous mobile robot can not be used to study the relationship between motion with nonholonomic constraints and force and torque.

The dynamic model of a general autonomous mobile robot can be described by the following Euler-Lagrange equation:

$$\frac{\mathrm{d}}{\mathrm{d}t}\left[\frac{\partial L}{\partial Y}\right]^{T}-\left[\frac{\partial L}{\partial \boldsymbol{\lambda}}\right]^{T}=\boldsymbol{D}(\boldsymbol{q})\delta-\boldsymbol{B}(\boldsymbol{q})\gamma \tag{6}$$

In Equation (6), $\boldsymbol{\lambda}=\left[\boldsymbol{\lambda}_1,\boldsymbol{\lambda}_2,\cdots,\boldsymbol{\lambda}_{\alpha}\right]^{T}$ represents the α dimensional generalized coordinates of the autonomous mobile robot control system, L represents the Lagrange function, $\boldsymbol{D}(\boldsymbol{q})\delta$ represents the difference between kinetic energy and potential energy, $\boldsymbol{D}(\boldsymbol{q})$ represents the $\alpha\times\beta$ dimensional input transformation matrix, γ represents the Lagrange multiplier, $\boldsymbol{B}(\boldsymbol{q})$ represents the constraint matrix, and the product $\boldsymbol{B}(\boldsymbol{q})\gamma$ represents the constraint vector. Through the analysis of Euler Lagrange equation, the dynamic model of autonomous mobile robot is constructed as follows:

$$\boldsymbol{E}(\boldsymbol{q})\boldsymbol{R}+\boldsymbol{V}(\boldsymbol{q})\boldsymbol{R}=\boldsymbol{D}(\boldsymbol{q})\delta-\boldsymbol{B}(\boldsymbol{q})\gamma \tag{7}$$

Differentiate both sides of the kinematic model to reduce the interference to the motion control of the autonomous mobile robot, and obtain the dynamic model:

$$\begin{aligned}&\boldsymbol{E}(\boldsymbol{q})\left[\boldsymbol{W}(\boldsymbol{q})U(t)+\boldsymbol{w}(\boldsymbol{q})u(t)\right]+\\&\boldsymbol{V}(\boldsymbol{q})\boldsymbol{R}=\boldsymbol{D}(\boldsymbol{q})\delta-\boldsymbol{B}(\boldsymbol{q})\gamma\end{aligned} \tag{8}$$

In Equation (8), $\boldsymbol{W}(\boldsymbol{q})$ represents the friction force of the ground against the wheel, $\boldsymbol{w}(\boldsymbol{q})$ represents the external force received by the autonomous mobile robot, $U(t)$ represents the weight coefficient of the behavior toward the target, and $u(t)$ represents the weight coefficient of the behavior toward obstacle avoidance.

Then both sides are multiplied by $\boldsymbol{A}(\boldsymbol{q})$ at the same time, $\boldsymbol{A}(\boldsymbol{q})\boldsymbol{B}(\boldsymbol{q})\gamma=0$ is set to reduce the control energy consumption, and the Lagrange multiplier γ is eliminated, and the final autonomous mobile robot motion control dynamics model is:

$$\boldsymbol{A}(\boldsymbol{q})\chi\boldsymbol{W}(\boldsymbol{q})+\boldsymbol{A}(\boldsymbol{q})(\chi+\upsilon)u(t)=\boldsymbol{A}(\boldsymbol{q})\rho\delta \tag{9}$$

In Equation (9), $\boldsymbol{A}(\boldsymbol{q})$ represents the total control amount at the time of interpolation, χ represents rolling resistance, υ represents driving force, and ρ represents wheel rolling resistance coefficient.

In conclusion, through the linearization analysis of the control system of the autonomous mobile robot, the dynamic model of the motion control of the autonomous mobile robot is constructed, which provides the basis for the gait planning of the autonomous mobile robot.

3. Gait planning of Autonomous Mobile Robot

Firstly, the walking cycle and key posture of the robot are analyzed, and then the stable walking gait is planned. Combined with the dynamic model of the robot motion control, the corresponding joint angle of the robot is inversely solved. Then, the motor rotation angle under the key gait is obtained by using the theory of series parallel mechanism. Finally, the motor continuous motion trajectory of the complete gait is generated by using cubic spline interpolation method.

3.1. Walking cycle of autonomous mobile robot

A complete cycle movement of an autonomous mobile robot can be divided into two stages, one is the period of double-leg support and the other is the period of single-leg support. During the leg support period, both the front and rear legs are in contact with the ground. This cycle starts from the forefoot foot on the ground to the end of the hind leg toe off the ground [8]. During the single-leg support period, the support leg is stable on the support surface, and the swing leg moves from the back to the front. In the gait planning, it is assumed that the leg support period is instantaneous. In this case, the waist must move forward rapidly. Meanwhile, in order to maintain the dynamic and static stability, the center of gravity of the robot must complete the movement from backward to front leg during the instant leg support period. On the other hand, if the support period of the legs is too long, it will limit the speed of the robot's walking. According to the length of human legs supporting time, when planning gait, it takes about 20% of the whole gait. Analyze the whole biped robot walking cycle composed of the two-leg support period and the single-leg support period from the forward plane.

Assuming that the gait cycle of each step is t, the duration of the leg support period is t_s, r represents the r step, which defines that the right foot is about to leave the ground, and the left heel just touches the ground as the beginning of a complete gait, and the left heel is about to leave the ground, and the cycle ends when the right heel just hits the ground. The gait of the complete cycle is as Figure 1.

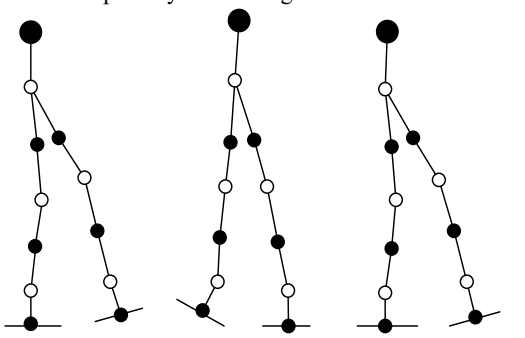

(a) *tr* moment (b) *tr*+*Ts* moment (c) (*r*+1) *t* moment

Figure 1. Gait cycle

3.2. Gait planning of autonomous mobile robots

In the gait planning process of autonomous mobile robot, in order to maintain the stability of the robot in the process of motion, the plantar trajectory is used to ensure the gait planning, that is, the plantar corresponding to the planned gait is located on the stable area. Considering the possible deviation of theoretical gait when applied to the actual physical model, such as the assumption that the robot is an ideal rigid body in theoretical planning, the influence of machining errors of mechanical transmission chain is ignored, and whether these errors are in the control loop, etc. [9]. When drawing gait, we should give full play to the role of the completed physical prototype of the autonomous mobile robot, and combine the theoretical gait with the physical prototype. That is to say, the initial posture of the prototype should be obtained according to the theoretical gait, and then according to the specific influence of the error and other factors on the actual physical prototype, the preliminary posture is adjusted, and then the final gait is determined.

In time, the complete motion of the autonomous mobile robot is divided into three stages. The first stage of gait planning is when the robot starts to walk until one leg is opened and its heel lands on the ground. The second stage is to take a complete gait cycle as the second stage, and the last stage is to take back the hind legs and stand together.

3.3. Inverse solution of forward kinematics of autonomous mobile robot

For the theoretical key gait, it is mainly the planning of the forward plane, therefore, only the inverse kinematics solution is made in this plane. Assuming that the given joint position of the theoretical key gait is known, the position of each joint point corresponding to the reference coordinate system is as follows, right plantar centroid (x_1, z_1), right ankle joint (x_2, z_2), right knee joint (x_3, z_3), left and right hip joints (x_g, z_g), left knee joint (x_4, z_4), left ankle joint (x_5, z_5), left plantar centroid (x_6, z_6) the relationship between the corresponding joint angle and the position of each joint point is as follows:

$$\begin{aligned}
\theta_1 &= \arctan\frac{x_2 - x_1}{z_2 - z_1} \\
\theta_2 &= \arctan\frac{x_3 - x_2}{z_3 - z_2} \\
\theta_3 &= \arctan\frac{x_g - x_3}{z_g - z_3} \\
\theta_4 &= \arctan\frac{x_4 - x_g}{z_4 - z_g} \\
\theta_5 &= \arctan\frac{x_5 - x_4}{z_5 - z_4} \\
\theta_6 &= \arctan\frac{x_6 - x_5}{z_6 - z_5}
\end{aligned} \tag{10}$$

According to the above conversion relationship, the rotation angle of the corresponding joint around the y axis along the positive direction of the x axis can be obtained, and the joint rotation angle combined with the characteristics of the autonomous mobile robot transmission chain is converted into the guide rod displacement, and the guide rod displacement is related to the rotation angle on the parallel mechanism fixed platform the changes are related as follows:

$$\begin{aligned}
Q_1 &= A_1 + \sqrt{A_1^2 - S_1} \\
Q_2 &= A_2 + \sqrt{A_2^2 - S_2}
\end{aligned} \tag{11}$$

In Equation (11), Q_1 and Q_2 respectively represent the coordinate values of the two ball joint connection points on the moving platform in the z direction of the reference coordinate system, which can reflect the movement of the two guide rods. For the inverse solution of the displacement of the guide rod to the angle of the joint motor, it can be obtained by converting the lead of the lead screw and the speed ratio of the planetary reducer.

According to the above steps, the feasible key gait has been inversely resolved into the theoretical rotation angle corresponding to the motor output

shaft. These theoretical rotation angles are controlled to act on the motor to judge whether the actual gait matches the planned theoretical gait. If not, adjust the actual gait accordingly. During the adjustment process, judge whether the adjustment is reasonable or not according to the feedback from the plantar until the actual motor output position corresponding to the key posture is finally determined.

3.4. Gait generation of autonomous mobile robot

According to the interpolation method of cubic spline, the discrete displacements of the above joints are fitted out according to the interpolation points to ensure the continuous change of the speed and acceleration of the turning point to produce a group of continuous displacements, and then coordinate together until a complete gait is generated [10].

Cubic spline interpolation is used to fit the joint motor position points corresponding to the above key posture. Suppose the interpolation function is $H(t)=f_i$, the corresponding first-order and second-order derivatives in this interval (t,t_m) are continuous, m represents the key time point, $W_i=(t_m,t_{m+1})$ represents the number of corresponding poses, $h_i=t_{m+1}-t_m$ represents the time interval, then $H(t)$ is expressed as:

$$H(t)=\frac{W_i}{6h_i}(t_{m+1}-t_m)^3+\left(f_i-\frac{Wh_i^2}{6}\right) \tag{12}$$

W_i is determined by the following equation:

$$W_i=\frac{f_{i+1}-f_i}{6h_i}-\frac{f_i-f_{i-1}}{3h_{i-1}} \tag{13}$$

From the initial condition $H'(t)=0$ and the termination condition $H'(t_m)=0$, it can be obtained that:

$$\begin{aligned} c_i&=\frac{f_{i+1}-tf_i}{t_m h_i}\\ b_i&=\frac{6(c_i-tf_i)}{t_m h_i}\end{aligned} \tag{14}$$

In Equation (14), c_i and b_i respectively represent the absolute distance of the two end points in the reference coordinate system.

In the specific fitting, the interpolation function of the first three time points is obtained, and then the cubic spline curve of the corresponding joint in the complete gait from t to t_m can be obtained step by step. Finally, the complete posture of the robot can be obtained through the coupling relationship between the joints.

4. Control System Hardware Design

The control system of autonomous mobile robot is a general designation of the software and hardware parts that control the autonomous mobile robot to complete the expected trajectory [11]. The control system of autonomous mobile robot is an important part to guarantee the performance of autonomous mobile robot, and is the command center of autonomous mobile robot system. Therefore, the control system of autonomous mobile robot must have high reliability, comprehensive function and fast response speed. The hardware part of the control system is the working platform of the autonomous mobile robot control system, which determines the performance of the control system and the scalability of the system.

4.1. Control system hardware composition

As the autonomous mobile robot needs to complete the work such as receiving instructions, adjusting the movement gait and positioning calculation in the work, with a large amount of calculation, therefore, the industrial computer is selected as the upper computer, and the touch screen is equipped to provide a convenient and practical human-computer interaction interface [12, 13]. When the autonomous mobile robot is moving, the positioning accuracy of the control system of the autonomous mobile robot is required to be higher, and the four axis linkage is needed in the moving process. The core of the control system is IMAC Flex motion controller of PMAC motion controller series. The hardware structure of the control system is as Figure 2.

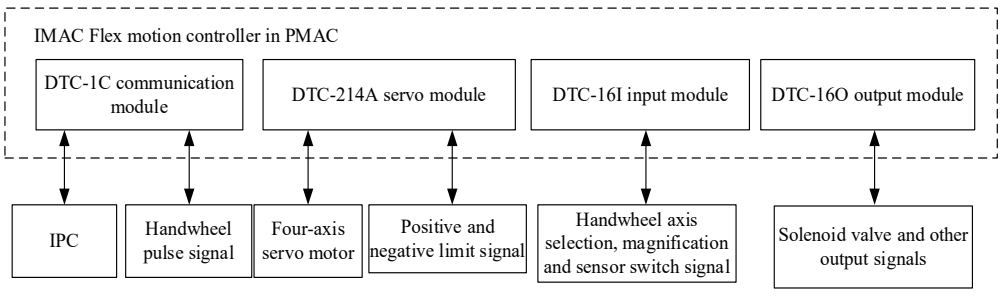

Figure 2. Control system hardware structure

IMAC Flex motion controller includes DTC-1C communication module, DTC-214A servo module, DTC-16I input module and DTC-16O output module. The controller can communicate with IPC through DTC-1C communication module and receive handwheel pulse signal. Four servo motors can be controlled by DTC-214A servo module, and 16 output points and 16 input points can be provided by input and output modules. In addition, PMAC can execute three kinds of commands: Online command, motion program command and PLC program command [14]. PMAC will execute the command immediately after receiving the online command, and will not store it. Motion program command is a group of buffer instructions stored in the buffer and executed by "R" command. Its function is to specify the motion position, motion mode and attribute, program logic control and variable assignment. PLC program command is also a group of buffer instructions, which can be repeated, including operations, logic control and information transmission commands.

The industrial computer has dual network cards, one network card is used to receive commands from the master control system, and the other network card is used to connect with the DTC-1C communication module [15]. After running the upper computer software on the windows platform, it can manually control the operation of the autonomous mobile robot, plan and store the path information of the autonomous mobile robot, and use the information to automatically write the motion program that PMAC can execute, and download it to PMAC to run [16].

The handwheel pulse signal is set to facilitate the staff to manually control the autonomous mobile robot to execute commands and collect key coordinate points in the path. The pulse signal from the handwheel is input to the DTC-1C communication module, and the handwheel axis selection signal and the handwheel override signal are input to the DTC-16I input module. The DTC-16I input module not only receives the axis selection and magnification switch signals of the handwheel, but also receives signals such as emergency stop switch buttons and sensors.

The output signals mainly include: gripping and releasing of fixture, servo power on control and servo alarm clearing.

4.2. Servo system construction

It can be seen from the above system hardware structure that to complete a given motion form, PMAC must output the control information in a certain form to the servo amplifier of the servo system. In this paper, P series AC servo motors and PY2 series servo amplifiers from Japan's SANYO DENKI Company are selected to construct a servo system for autonomous mobile robots. Since the inertial force, coupling reaction force and gravity load of the autonomous mobile robot change with the change of the motion space, the dynamic control is applied to each joint of the autonomous mobile robot as a separate linear uncoupled servo for closed-loop control [17]. According to the operating characteristics of autonomous mobile robots, both stable motion speed and accurate positioning are required. For autonomous mobile robots, the torque and speed are in the inner loop and the position is in the outer loop. The principle is as Figure 3.

The current closed loop is realized by servo amplifier, which can avoid circuit damage caused by current mutation; The speed closed loop is also realized by the servo amplifier and adopts proportional integral control. The user can adjust the proportional constant and integral constant according to the control requirements of different systems to obtain satisfactory speed closed loop characteristics; The position closed loop is completed by the PMAC motion control card. PMAC adopts the PID control method for the position closed loop. The parameters of the position loop can be adjusted by variables and can be set by the user within a certain range according to the different servo requirements of the system. At the same time, it is also possible to use PMAC to automatically detect the system load for automatic adjustment of PID parameters to complete the parameter tuning.

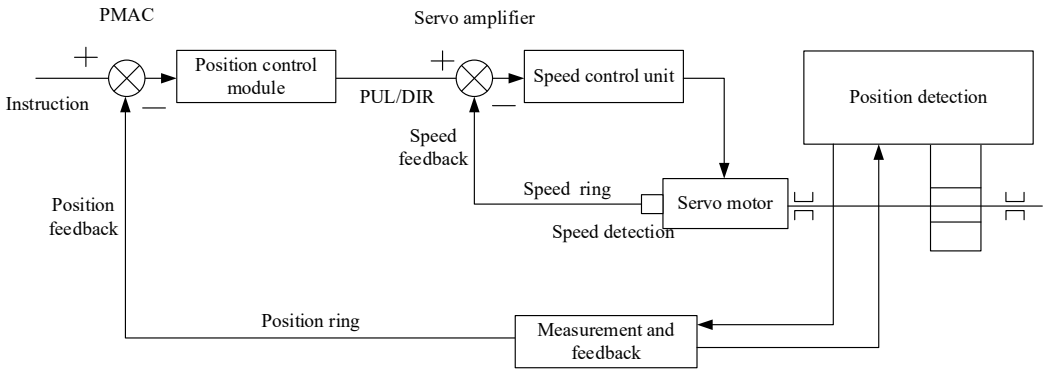

Figure 3. Servo control principle

5. Control System Software Design

This article uses the Windows 2 000 system as the operating system and supports graphical user interfaces. The currently widely used and powerful Visual C++ is selected as the software development tool. The control system software adopts modular structure design and is divided into upper computer human-computer interaction module and lower computer motion control module. The host computer adopts Visual C++6.0 high-level language for development, and communicates through PMAC's PTALK control. It is mainly used for motion trajectory planning, robot dynamic analysis, parameter setting, modification, motion simulation, operating command issuing, intelligent algorithm processing and other management modules. The software of the lower computer adopts PMAC's own language development, and uses its high-speed calculation function to realize autonomous mobile robot kinematics calculation, motion trajectory interpolation calculation, motion servo control, etc. The software structure of the control system is as Figure 4.

The communication function between PC and PMAC belongs to the system software, which is responsible for the communication between hardware. Its realization first loads the dynamic link library PComm32 to obtain its handle, and then calls the function through the entry pointer of the called function to realize the communication between the computer and PMAC. PMAC communication drive function library Pcomm32, as a communication bridge between Windows and PMAC, uses an interrupt mechanism to complete high-real-time tasks such as servo control, trajectory interpolation, and speed processing. When the buffer is cleared, PMAC will send an interrupt request signal. After receiving the signal, the host computer will carry out path planning control for the following trajectory segments, and write the calculated new control data into DPRAM. PMAC will read the data from DPRAM and send it to the servo drive device to complete the gait control of each joint of the autonomous mobile robot.

1. Human-computer interaction module: The main functions completed include initialization system, manual operation, compilation and connection module, teaching module, instruction download and information feedback, etc.
2. Motion control module: It is the core of the autonomous mobile robot control software. Its main functions include kinematics calculation, robot gait path planning, online quick adjustment of position, configuration of system parameters, and PLC program editing, management, system monitoring, etc. Based on the analysis of the linearization of the control system of the autonomous mobile robot, the dynamic model of the motion control of the autonomous mobile robot is established. On this basis, based on the interpolation method of cubic spline, the gait planning of the autonomous mobile robot is generated, and the motion control of the autonomous mobile robot is realized. Obtain information such as the position and pose coordinate sequence of the moving target of the autonomous mobile robot system and the motion trajectory control method, and calculate the angle that each joint needs to rotate through the inverse motion calculation according to the pose matrix of the initial position and the target position. It is transmitted to the PMAC servo control system, and PMAC is set according to some parameters of the user to realize the gait control of the autonomous mobile robot.

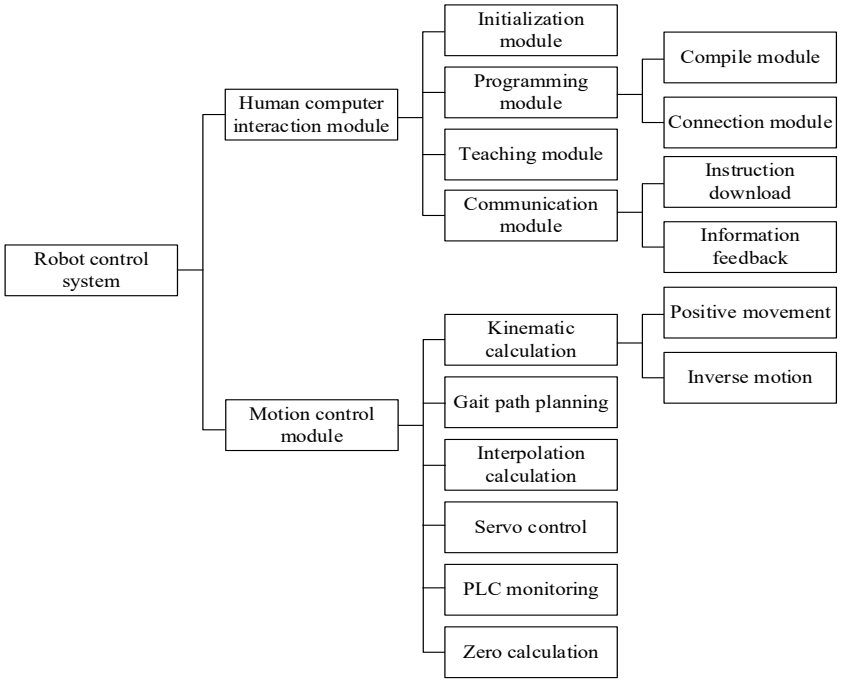

Figure 4. Control system software structure

6. Experimental Simulation and Analysis

6.1. Setting up the experimental environment

In order to verify the effectiveness of the gait control system of autonomous mobile robot based on PMAC, a computer with Inter Core i5-3470 processor, 8.00 G memory, 600 G hard disk and 64 bit Windows 7 operating system was used in the experiment. In the Visual C++ integrated environment, the C++ language is used to develop an autonomous mobile robot gait control system based on PMAC to realize and verify its performance. The hardware selection and parameter index are as Table 1.

6.2. Stability analysis of robot motion control

In this system, the dynamic model of the motion control of the autonomous mobile robot is established, the kinematics algorithm is imported into the simulation software, and the reference [4] method, the reference [5] method and the proposed method are used to compare the motion in different directions. Stability is an indicator, and the results of experimental analysis are shown in Figure 5.

Table 1. Hardware selection and parameter list

Hardware name	Model
Upper computer	Surface Pro2
Lower computer	STM32F103
CO sensor	MICROceLTM
CH_4 sensor	MICROpel
H_2S sensor	MICROceLTM
Temperature and humidity sensor	SHT15
Inertial navigation module	miniIMU AHRS
Camera	600 lines micro
Human body detection	HC-SR501
Infrared ranging	GP2Y0A02

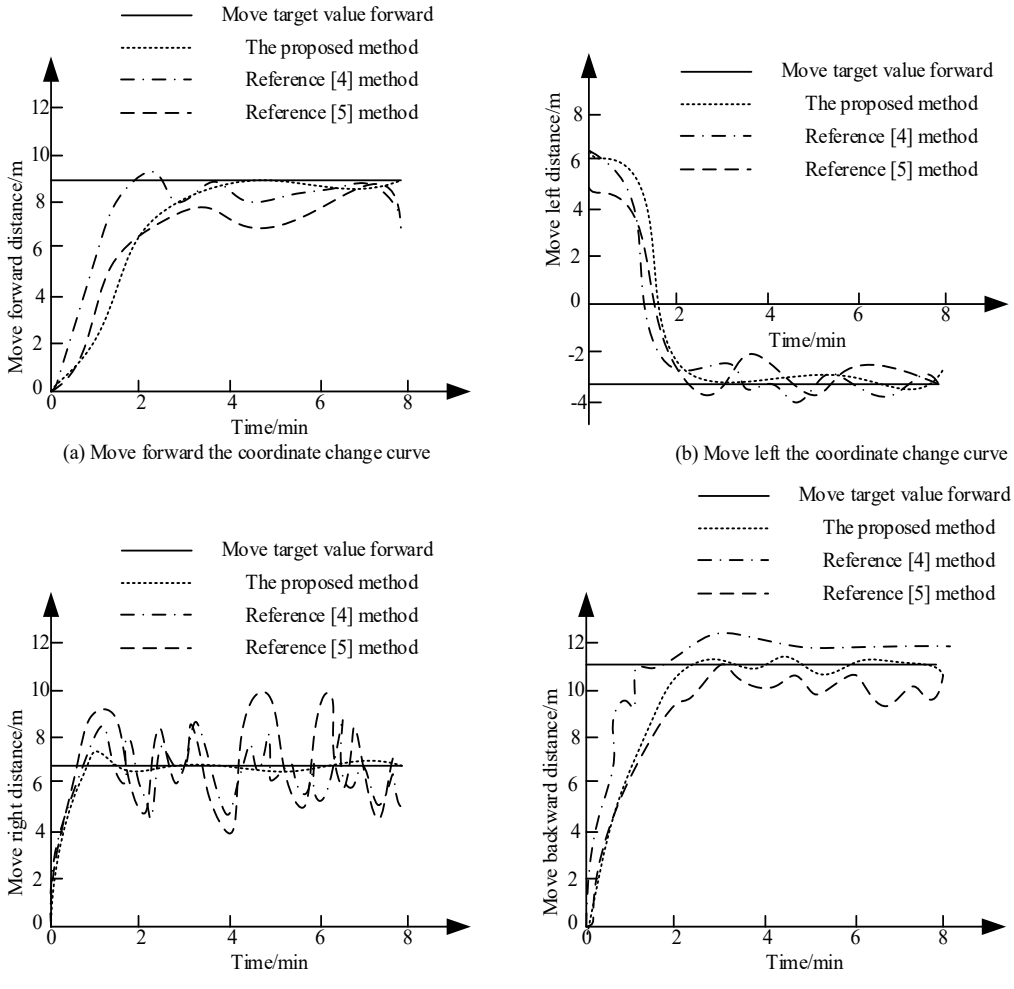

(a) Move forward the coordinate change curve

(b) Move left the coordinate change curve

(c) Move right the coordinate change curve

(d) Move backward the coordinate change curve

Figure 5. Comparison of robot motion control stability of different methods

It can be seen from Figure 5 that the position of the autonomous mobile robot controlled by the reference [4] method and the reference [5] method oscillates when it moves forward, and when it moves to the left, there is a steady-state error in the position. When moving, the position oscillates and the average value deviates from the target value. The proposed method can effectively avoid the oscillation caused by signal lag and increase the response to small deviations. The reason why the deviation of the leftward movement is slightly larger than the forward deviation is that when the control signal of the leftward movement is small, the inertial device cannot provide sufficient thrust. When the control signal is moved to the right, it is easily affected by the ground, and there are certain fluctuations in the backward movement. However, it is maintained near the target value as a whole. It can be seen that the motion control stability of the autonomous mobile robot using the proposed method is better.

6.3. Gait displacement and walking efficiency analysis of robot

In order to verify the walking compliance of the autonomous mobile robot gait control system based on PMAC, the reference [4] method, the reference [5] method and the proposed method were used to compare the robot gait displacement curves of different methods. The comparison results are as Figure 6.

According to Figure 6, it can be seen that the robot gait trajectory of the proposed method is smoother than that of the reference [4] method and the reference [5] method, and the robot walking compliance of the proposed method is higher than that of the reference [4] method and the reference [5] method. The average speed is used to measure the walking efficiency of autonomous mobile robots, namely:

$$\eta = \frac{\mu}{t} \tag{15}$$

In Equation (15), μ represents the step distance, and t represents the gait cycle. Since the step distance μ is 500 mm, the gait period t of the method in reference [4], the method in reference [5] and the proposed method are 7 s, 6 s and 5 s, respectively. According to Equation (15), the average speed of the reference [4] method, the reference [5] method and the proposed method are 71.4 mm/s, 83.8 mm/s and 100 mm/s, respectively. It can be seen that the average gait speed of the proposed method is larger and the walking efficiency is higher.

Based on the above comparative analysis, it can be seen that, compared with the robot gait displacement curve and the average gait speed of the reference [4] method and the reference [5] method, the robot gait motion trajectory of the proposed method is smooth and the walking flexibility is better. The average gait speed of the robot is relatively high, and the walking efficiency is relatively high.

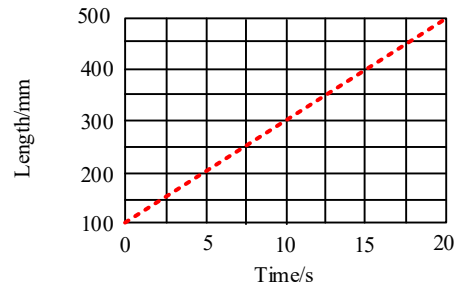

(a) Gait displacement of robot in the proposed method

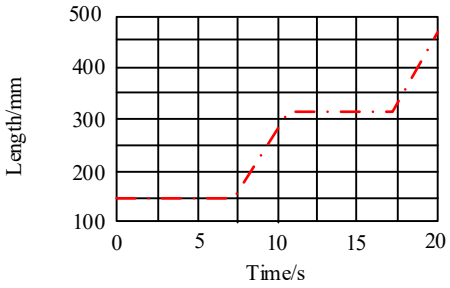

(b) Gait displacement of robot in the reference [4] method

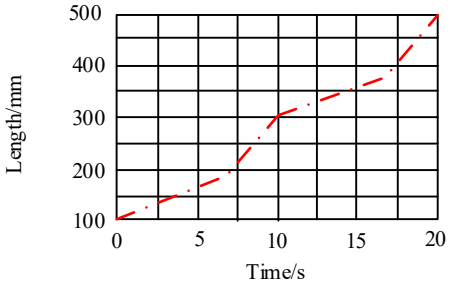

(c) Gait displacement of robot in the reference [5] method

Figure 6. Comparison of robot gait displacement curves of different methods

6.4. Robot gait path planning

In order to further verify the gait path planning effect of the autonomous mobile robot gait control system based on PMAC, the reference [4] method, the reference [5] method and the proposed method are used to compare the planning path of robot gait control system of different methods. The comparison result is as Figure 7.

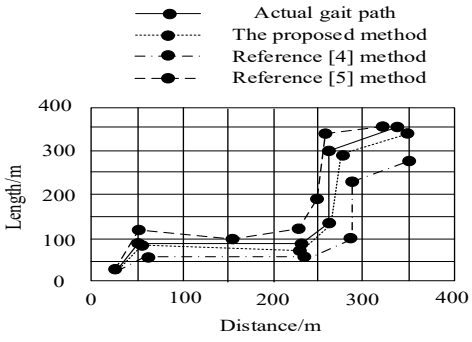

Figure 7. Comparison of robot gait path planning effects of different methods

According to Figure 6, it can be seen that there is a certain deviation between the robot gait path planning of the reference [4] method and the actual gait path, and the robot gait path planning of the reference [5] method has a large deviation from the actual gait path. The robot gait path planning of the proposed method is basically consistent with the actual gait path, and can successfully realize the movement from the starting point to the target point. Therefore, the robot gait path planning effect of the proposed method is better.

7. Conclusions

In this paper, the gait control system of autonomous mobile robot based on PMAC is proposed. The dynamic model of walking gait of autonomous mobile robot is constructed, and the walking period and key posture are calculated, thus the walking gait model of robot is designed. The series mechanism and parallel mechanism are used to control the rotation angle of the motor, and the gait trajectory is planned. Experiments show that this method can improve the walking compliance and walking efficiency of the robot.

However, in the process of gait control of autonomous mobile robot, information feedback such as robot attitude should be added to reduce the influence of machining and installation errors on the performance of control system. Therefore, a complete upper control system will be established in the next research to realize fast offline attitude planning and online real-time gait adjustment.

Acknowledgement

The research is supported by: The 2018 Henan provincial key teacher training program for colleges and universities (No. 2018GGJS268).

Reference

[1] Hutchinson, M.; Liu, C.; Chen, W.H. Information-based search for an atmospheric release using a mobile robot: Algorithm and experiments. IEEE Transactions on Control Systems Technology, 2019, 27(6): 2388-2402.

[2] Vassallo, C.; Olivier, A.; Souères, P.; Crétual, A.; Stasse, O.; Pettre, J. How do walkers behave when crossing the way of a mobile robot that replicates human interaction rules. Gait & Posture, 2018, 60: 188-193.

[3] Kantaros, Y.; Zavlanos, M.M. Distributed intermittent connectivity control of mobile robot networks. IEEE Transactions on Automatic Control, 2018, 62(7): 3109-3121.

[4] Venkatesh, A.; Rao, G.R. An improved adaptive control system for a two wheel inverted pendulum-mobile robot using eagle strategy with a particle swarm optimization. Multimedia Systems, 2018, 5(7): 137-145.

[5] Ren, C.; Li, X.; Yang, X.; Ma, S. Extended state observer based sliding mode control of an omnidirectional mobile robot with friction compensation. IEEE Transactions on Industrial Electronics, 2019, 66(12): 9480-9489.

[6] Lu, Q.; Han, Q.L. Mobile robot networks for environmental monitoring: a cooperative receding horizon temporal logic control approach. IEEE Transactions on Cybernetics, 2018, 49(2): 698-711.

[7] Paull, L.; Seto, M.; Leonard, J.J.; Li, H. Probabilistic cooperative mobile robot area coverage and its application to autonomous seabed mapping. International Journal of Robotics Research, 2018, 37(1): 278-295.

[8] Garrocho, C.T.B.; Da Silva, M.J.; Oliveira, R.A.R. D2D pervasive communication system with out-of-band control autonomous to 5G networks. Wireless Networks, 2020, 26(1): 373-386.

[9] Guo, Q.Y.; Shi, G.L.; Wang, D.M.; He, C.Y.; Hu, J.; Wang, W. Iterative learning based output feedback control for electro-hydraulic loading system of a gait simulator. Mechatronics, 2018, 54: 110-120.

[10] Kuwada, S.; Aota, T.; Uehara, K.; Nara, S. Application of chaos in a recurrent neural network to control in ill-posed problems: a novel autonomous robot arm. Biological Cybernetics, 2018, 112(5): 495-508.

[11] Ye, W.; Liao, C. Method for planning natural gait joint trajectory of embedded intelligent robot. Computer Simulation, 2020, 37(5): 301-305.

[12] Kuang, C.; Zheng, X.Y. Space trajectory planning of electric robot based on unscented kalman filter. Jordan Journal of Mechanical and Industrial Engineering, 2021, 15(1): 29-38.

[13] Ali, M.A.H.; Mailah, M. Path planning and control of mobile robot in road environments using sensor fusion and active force control. IEEE Transactions on Vehicular Technology, 2019, 68(3): 2176-2195.

[14] Kantaros, Y.; Guo, M.; Zavlanos, M.M. Temporal logic task planning and intermittent connectivity control of mobile robot networks. IEEE Transactions on Automatic Control, 2019, 64(10): 4105-4120.

[15] Tonin, L.; Bauer, F.C.; Millán, J.R. The role of the control framework for continuous teleoperation of a brain–machine interface-driven mobile robot. IEEE Transactions on Robotics, 2020, 36(1): 78-91.

[16] Mutawe, S.; Hayajneh, M.; BaniHani, S.; Qaderi, M.A. Simulation of trajectory tracking and motion coordination for heterogeneous multi-robots system. Jordan Journal of Mechanical and Industrial Engineering, 15(4): 337-345.

[17] Zheng, Z.; Zhao, H.; Swanson, A.R.; Weitlauf, A.S.; Warren, Z.E.; Sarkar, N. Design, development, and evaluation of a noninvasive autonomous robot-mediated joint attention intervention system for young children with ASD. IEEE Transactions on Human-Machine Systems, 2018, 48(2): 125-135.

JJMIE

Volume 16, Number 1, January. 2022
ISSN 1995-6665
Pages 41 - 51

Jordan Journal of Mechanical and Industrial Engineering

Optimal Control Method for Side Impact Safety of Vehicle Frame Structure

Mingming Wu*, Xueping Zhang

School of Mechanical Engineering, Anhui Sanlian University, Hefei 230601, China

Received 14 July 2021 *Accepted 22 December 2021*

Abstract

In order to verify the safety of side impact of vehicle frame structure and reduce the number of accidents of members injured due to side impact. On the basis of the basic theory of collision simulation and the theory of anti-side collision optimization design, the finite element model of side impact of the whole vehicle is established with the aid of the CAD model of a foreign mass production vehicle. With the finite element analysis software hyper mesh, the boundary and constraint conditions are set according to the requirements of GB20071-2006, so that the deformation speed and invasion amount of B-pillar in the important parts of side wall are normal. Through increasing the thickness of sheet metal, using ultra-high strength steel, adding structural strengthening parts, adopting different cross-section shape of anti-collision beam and optimizing the position of anti-collision beam, the safety of the original vehicle is verified by simulation test. The results show that different improvement methods can optimize the side impact performance of the vehicle, but the safety of the vehicle can be improved. The most effective way is to increase the reinforced parts reasonably without affecting the function of the original parts in the relevant position. The optimization method, the conclusion and the measures to improve the side impact performance provide a certain reference for the design and research of vehicle side impact safety performance optimization control.

*Keywords:*Automobile frame structure; Side impact; Safety optimization control;

1. Introduction

With the rapid development of economy, cars play an increasingly important role in people's daily life. However, with the rapid increase of car ownership, the number of various traffic accidents related to automobiles has risen sharply, which not only causes huge property losses, but also seriously threatens people's life safety. In all kinds of traffic accidents, the frequency of frontal and side impact is the highest. When the side impact occurs, the deformation speed and intrusion volume of the door are too large, which may cause serious injury to the passengers. Therefore, side impact is the highest form of accidents, with side impact accounting for 30% of all accidents. In automobile accidents, head and neck injuries account for 58% and trunk injuries at most injuries accounted for 32% and abdominal injuries accounted for 21% [1]. Therefore, the research on side impact safety has become an important research content in the field of vehicle passive safety, and has attracted the attention of automobile manufacturers and automobile research institutions all over the world.

In the research of automobile side impact, door and B-pillar are the key objects and important indexes to evaluate the side impact resistance of automobile. For the door and B-pillar, the displacement and speed changes of various components under the action of external force are mainly investigated, because these two indicators are directly related to the injury degree of passengers. In order to effectively reduce the injury of passengers in side impact, it is necessary to make the impact force evenly transmitted to all parts of the body, so as to ensure that the displacement and speed of the vehicle are reduced to the minimum. Automobile body is a large and complex system, and there are mutual constraints between the performance of the body. In the process of research and development of automobile body, we must comprehensively consider the interaction of multi-function and multi-disciplinary. Therefore, the impact of lightweight, NVH, dynamic performance and other disciplines should be considered in the study of vehicle side impact safety. To solve the problem that single discipline or single objective optimization method is difficult to achieve the comprehensive design of vehicle performance, multidisciplinary optimization technology was born. Multidisciplinary design optimization (MDO) technology fully considers the influence of performance, realizes multidisciplinary integration and optimization, and obtains the overall optimal design of the system.

* Corresponding author e-mail: wmm19842002@163.com.

Based on this, this paper uses different methods to optimize and improve the crashworthiness of the side structure in side impact from different aspects, and verifies the effectiveness of these optimization methods in theory. Aiming at the problem of mutual restriction between body side impact safety and body lightweight, uniform test design is used to construct the test, and the stepwise regression surrogate model is constructed according to the test data. Finally, the multi-disciplinary collaborative optimization research is carried out by using the sequential quadratic programming method and the adaptive weighting method. Finally, the optimization results meeting the design objectives are obtained. The security is verified by computer simulation.

2. Establishment and Experiment of Side Impact Finite Element Model

It is difficult to understand the dynamic response of human body in the real accident process because of the short time and great deformation of vehicle collision. However, in order to study the safety of vehicle side impact, the major automobile companies and research institutions must present the real accident process. In the early stage, they obtained the relevant data through the real vehicle experiment, while the research on human injury was obtained by placing the corpse or dummy on the test vehicle. With the rapid development of computer technology and the gradual improvement of mathematical model, computer simulation method has been widely used in the field of vehicle collision safety, and its analysis accuracy and feasibility are higher and higher. It can not only help researchers to obtain accurate information, improve the crash safety of the vehicle, but also reduce the development cost, so that the market competitiveness of the car is stronger. It has an important guiding significance for the research of automobile passive safety.

2.1. Key technologies of finite element analysis

The method of computer simulation is to replace the real vehicle collision with computer simulation through the establishment of vehicle collision model [2]. At the cost of accurate calculation efficiency, in order to ensure the calculation accuracy and reduce the calculation scale, reasonable finite element model simplification and mesh generation become the key of finite element analysis [3]. Relevant research shows that: The accuracy and calculation efficiency of simulation analysis results are related to the element type and contact algorithm, to a large extent, it also depends on the simplification degree of finite element model, the accuracy of mesh generation and the setting of material parameters. The following focuses on the simplification of finite element model and mesh generation.

2.1.1. Simplification of finite element model

In order to describe the vehicle structure and the connection between its components, the key of computer aided design (CAD) modeling is to ensure the accuracy of the model. However, the purpose of computer aided engineering (CAE) analysis is different from that of CAD. Many processing and assembly details (such as holes, steps, stiffeners, small chamfering, etc.) in CAD often lead to unit quality degradation when meshing in CAE. The reduction or even disqualification will affect the accuracy of simulation calculation, as well as the calculation time and efficiency. Therefore, when establishing the finite element model, the details of the model built by CAD should be reasonably simplified according to the actual calculation scale and accuracy requirements.

For side impact, the thin-walled metal parts at the impact part are the main deformation energy absorbing parts, such as B-pillar, threshold beam, roof beam and door, etc. When the geometric model of the above parts is established, its geometric characteristics must be accurately reflected and not too simplified. The structural stiffness of the parts, such as engine and gearbox, which are not deformed or not deformed in the process of collision, is much larger than that of thin-walled metal parts, so they can be treated as rigid bodies. For some non main body load-bearing parts, although the absorption of collision energy is very small, it has a great impact on the efficiency and accuracy of simulation calculation. Reasonable structure simplification can be carried out to reduce the workload of modeling and improve the work efficiency. So in this paper, according to the structural characteristics of the sample car and the actual calculation needs, the following simplification work is carried out in the finite element modeling.

1. Remove the hole, shoulder, concave and flanging on the surface of the component, and round and smooth it.
2. Omit some parts with small mass and less energy absorption, such as armrest, brake pedal bracket, instrument panel support, etc.
3. For those parts that conflict with the installation and use requirements of other components, the section shape of the components should be reasonably simplified.
4. Some parts (such as batteries) which have little influence on the simulation results are omitted, but the mass of these parts is large, which directly affects the position of vehicle centroid, so they can be reasonably distributed in the corresponding positions in the form of mass points.

2.1.2. Finite element mesh generation

The core idea of finite element analysis is block approximation. The mesh density or the degree of structural discretization have great influence on the calculation error. The increase of grid density will lead to the increase of calculation scale, which will increase the simulation cost and reduce the computational efficiency. When the element length is reduced by K times uniformly, the element density and calculation time will increase by K2 times and

K3 times respectively, which means that the calculation time increases nonlinearly with the element density of 1.5 power. Therefore, the selection of grid density has an important impact on the computational efficiency and accuracy. For the parts with large deformation, the grid density should be increased to better simulate the structural deformation, while for the parts with small deformation, the grid density should be reduced, the calculation time should be shortened and the calculation efficiency should be improved.

On the basis of balancing the calculation accuracy and efficiency and setting the grid density reasonably, we should ensure the grid quality. The better the mesh quality, the faster the calculation speed and the higher the calculation accuracy. Therefore, the following problems should be paid attention to in the process of meshing.

1. The degenerate shell element and body element should be avoided as far as possible. Compared with other common element types, they are too rigid and have poor calculation accuracy.
2. Due to the shell element type, attention should be paid to the minimum element size when meshing, that is, the minimum side length of shell element should be more than five times of its element thickness.
3. The side length of the element directly affects the calculation speed and accuracy. On the basis of ensuring the calculation accuracy, the calculation efficiency should be considered. In the case of certain material properties, the side length and area of the element should be increased as much as possible to avoid the occurrence of too large internal angle of the element.
4. The selection of element size follows the basic principle of gradual change in order to avoid the phenomenon that the size difference between adjacent elements is too large, and prevent the element from distortion, which will affect the calculation accuracy and simulation results.
5. On the premise of the same element type, the stiffness of small-size element is smaller than that of large-size element, and it is more prone to deformation. According to the deformation of car body in real vehicle crash test, the corresponding size element should be selected for different parts of car body to ensure the accuracy of simulation of actual car body deformation.
6. Check the quality of the unit, delete the repeated and cross elements, modify the warpage and deformation elements.

2.2. Establishment and verification of finite element model of moving deformable barrier

Vehicle frontal collision is a collision between the test vehicle and the rigid wall, while the side impact is to impact the stationary vehicle with the variable moving barrier. Therefore, the movable deformable barrier model must be established in the study of side impact simulation, which is the biggest difference between the simulation research of vehicle side impact and frontal collision. In the current side impact regulations, whether it is fmvss214 or ECER95 in Europe and America, or occupant protection in vehicle side impact (GB20071-2006) in China, the movable deformable barrier is the basic tool for side impact test research.

2.2.1. Establishment of finite element model of moving deformable barrier

According to GB20071-2006, the process of finite element modeling of MDB is: Firstly, the CAD model is transformed into the preprocessing software hyper through IGES graphics data exchange format. In mesh, mesh is used to mesh and define the materials and properties of each component, and the connection relationship between the components. Finally, the load, constraint or boundary conditions are applied to the model. According to the side impact standard of our country, the moving deformable barrier needs to impact the test vehicle at the speed of 50 km/h. The movable deformable barrier model is mainly composed of the mobile vehicle and the deformable impactor, and its overall dimensions are shown in Figure 1.

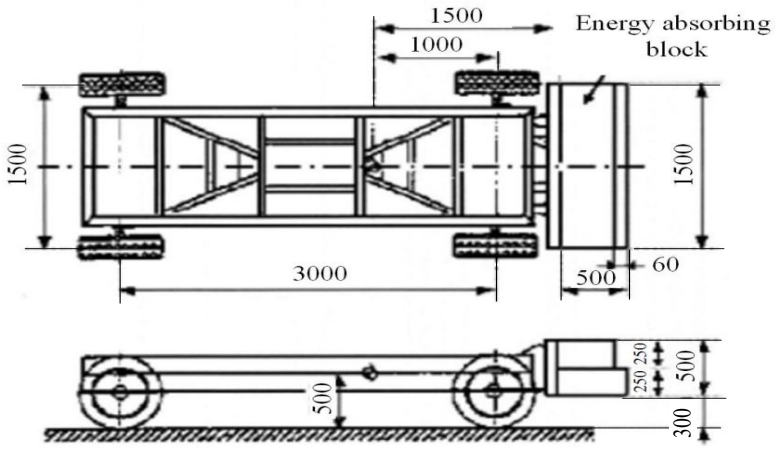

Figure 1. Overall structural dimensions of moving deformable barrier (unit: mm)

As shown in Figure 1, the standard requirements for the finite element model of movable variable barrier are shown in Figure 1, and the structural dimensions of the front end of the model are shown in Figure 2. The total mass of MDB was 950±20 kg, and the center of mass was within ±10 mm of the longitudinal symmetry plane. The finite element model of the movable deformable barrier is mainly composed of the moving frame model, the front energy absorbing block model, the middle glue and the front and rear connecting panels. The moving frame is simulated by shell element, because it will not deform in the whole collision process, so the rigid material (MAT) is adopted _ Rigid); The energy absorbing block in front of the frame is simulated by solid element, and the most commonly used honeycomb aluminum material (MAT) is used _ The glues in the middle are simulated by beam element, and the nonlinear plastic spring discrete material (MAT) is used _ NONLINEAR _ PLASTIC _ DISCRETE _ BEAM).

The trolley model is based on the frame, and some parts (such as wheels, rear connecting plate, key mass, etc.) pass through the CONSTRAINED _ RIGID _ BODIES. The definition of bodies establishes its connection with the frame. The energy absorbing block in the last part is connected with the rear connecting plate through tie contact. Based on the above modeling ideas, the final finite element model is shown in Figure 3 and the finite element model parameters are shown in Table 1.

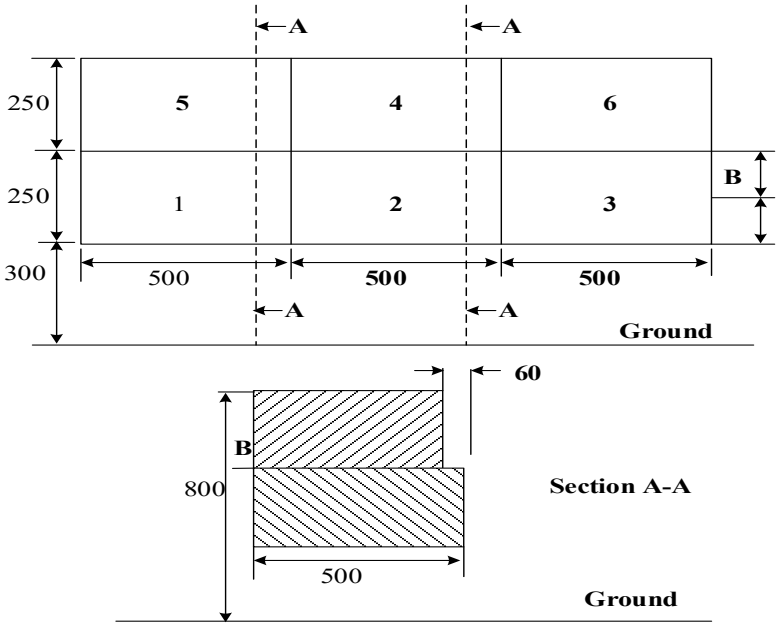

Figure 2. Structure size of energy absorbing block for moving deformable barrier (unit: mm)

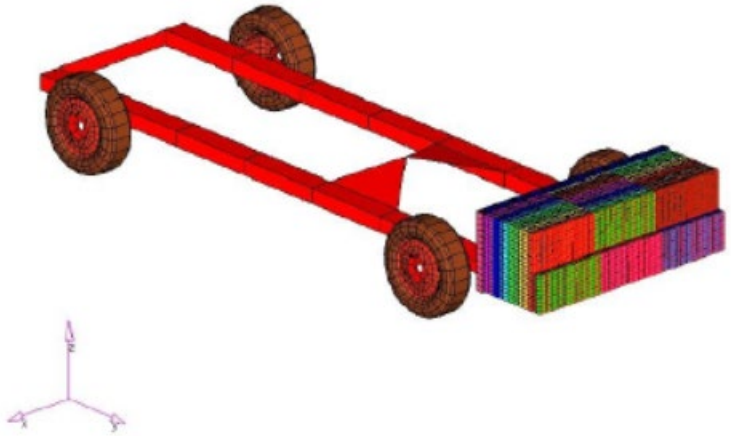

Figure 3. Finite element model of moving deformable barrier

Table 1. Model parameters

Mass of MDB (kg)	952.16
Location of MDB centroid (mm)	X = 0.45, y = -1859, 77 z = 511.43
Geometric parameters of mobile vehicle (mm)	Wheelbase 3000, wheelbase 1500, ground clearance 300
Initial speed of MDB (m/s)	9.722
Total number of units	239765
Number of deformable elements	18039
Number of rigid body elements	181375
Time step (ms)	0.76

2.2.2. Verification of finite element model of moving deformable barrier

Because the stiffness of the front part of the impact vehicle is mainly simulated by the energy absorbing block, the performance of the energy absorbing block needs to be tested dynamically. The verification of moving deformable barrier in ECE R95 regulations and China's side impact regulations is to examine the overall force displacement characteristics of the energy absorption block structure, the force displacement characteristics of each energy absorption block, and the energy absorption characteristics of each energy absorption block. The force displacement characteristics are required to be within the band range specified by the corresponding upper and lower limits, and the energy absorbed by each energy absorbing block meets a certain range [4-6].

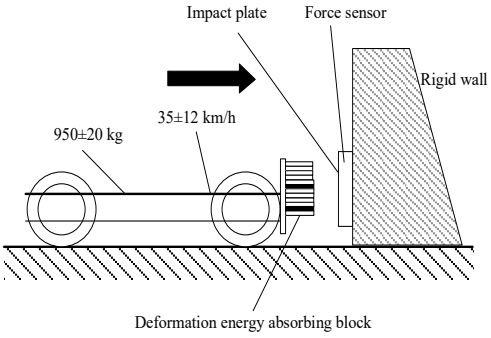

Figure 4. Schematic diagram of mobile barrier verification test

As shown in Figure 4, the schematic diagram of mobile obstacle avoidance verification test is shown. When the rigid wall is vertically impacted at the speed of 35 km/h, the force displacement curve and energy absorption situation of the energy absorption block installed at the front end of the moving barrier are investigated. Among them, the rigid wall is a rigid reinforced concrete structure, the width of one side contacting with the MDB is not less than 3 m, the height is not less than 1.5 m, and the total weight is not less than 70 t. The collision contact plane should be perpendicular to the runway axis, and the surface should be covered with load sensors to measure the total load of each part of the moving deformable barrier at the moment of collision. In the last part of the runway, in front of the rigid barrier, there should be at least 5 m horizontal and smooth pavement [7-9].

There is a force measuring wall in front of the rigid wall to measure the impact force during impact. Through the simulation test of the barrier module, the contact between the rigid wall, the ground and the barrier are defined in the inertial space [10-13]. The displacement curve and velocity curve of the barrier in the process of collision are output from the position of the mass center of the barrier, so as to obtain the motion characteristics of the moving barrier in the process of full-frontal impact [14, 15]. The force time history curves of six impact energy absorbing blocks are output from the model, which is converted into the curve of force variation with displacement, so as to test the stiffness characteristics of the front deformation energy absorption block.

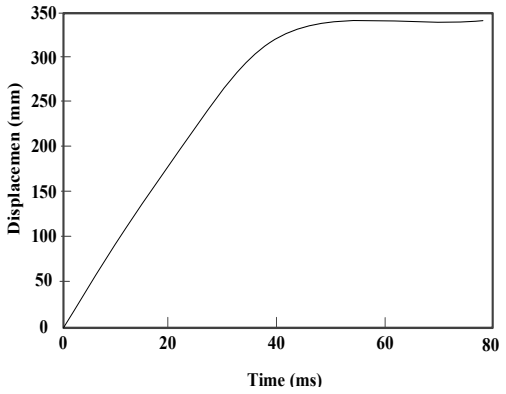

Figure 5. Displacement curve of MDB centroid

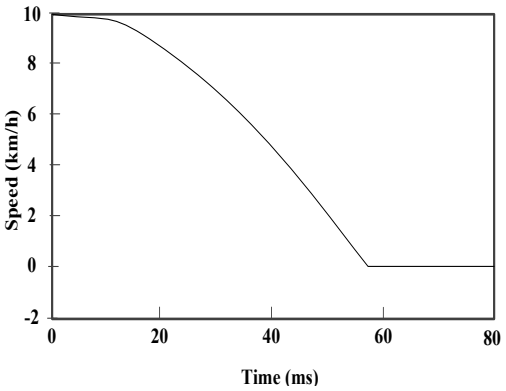

Figure 6. Speed time curve of MDB

As shown in the figure, Figure 5 shows the displacement diagram of the moving deformable barrier mass center with time, and Figure 6 shows the change diagram of the moving deformation barrier speed with time. From the displacement curve of the mass center of the moving deformation barrier (Figure 5), it can be seen that the maximum deformation of the moving barrier energy absorbing block is 341 mm, which meets the requirements of GB20071-2006 regulations of 330±20 mm. Figure 6 shows that the time for the moving barrier to

decelerate from the initial speed of 35 km/h to 0 is 56.5 ms, and then rebound, and the speed reaches -1.2 km/h.

See Figures 7-10, in which the dotted line is the upper and lower limit values of the force displacement curve, and the part surrounded by it is the stiffness characteristic range of the impactor meeting the requirements of regulations. It can be seen that the stiffness characteristics of the six deformation blocks are within the limits specified by the regulations, among which the stiffness characteristics of the first and third blocks are the same, the fifth and sixth blocks are the same, and the barrier model is symmetrical left and right. In addition, Table 2 shows that the energy absorbed by each energy absorption block meets the requirements of regulations. Through the verification test, it can be concluded that the moving deformable barrier finite element model meets the test requirements and can be used as the impactor of the side impact simulation model.

2.3. Establishment and verification of vehicle finite element model

2.3.1. Establishment of vehicle finite element model

In this paper, a mass production car abroad is taken as the research object. The whole vehicle model is built on the basis of CAD three-dimensional model, and the finite element pre-processing software hyper is used Mesh is divided in mesh [16-19]. In order to control the size of the model under the premise of ensuring the accuracy of the model and saving the calculation time, the smaller mesh is used in the main deformation parts of side impact, and the larger mesh is used in the secondary parts. The BIW, body panel and seat frame of the finite element model of the whole vehicle are simulated by shell element mesh, and the piecewise linear plastic material is used; The interior panel material is also defined as piecewise linear plastic material when the front door of the driver's side is added with the interior trim panel; The suspension system, door hinge and tire are defined according to their motion relations, mainly including: Ball Joint _ Spherical, joint _ Revolve), column hinge (joint) _ Cylindrical) and spring damping unit; The connection relationship between components is also referred to the real body manufacturing process, and the welding position is controlled _ Spotweld spot welding unit, bolt connection means constrained _ NODAL _ RIGID _ Body rigid connection; Powertrain part is simplified as rigid body, and other parts of vehicle harness, pipeline and sealing strip which have little impact on side impact are replaced or omitted by mass unit.

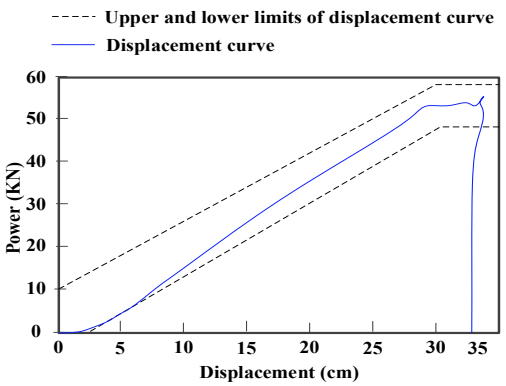

Figure 7. Force displacement curves of the first and third blocks

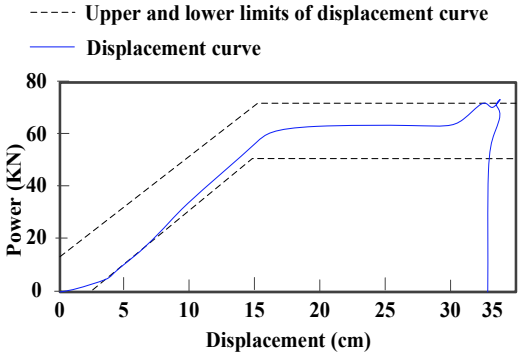

Figure 8. Force displacement curve of the second block

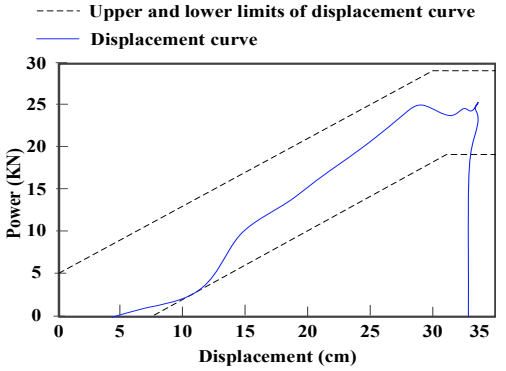

Figure 9. Force displacement curve of the fourth block

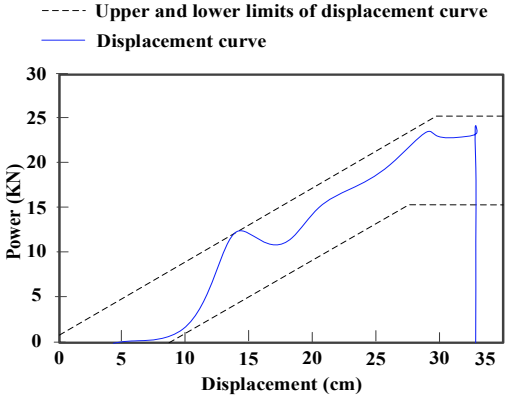

Figure 10. Force displacement curves of the 5th and 6th blocks

2.3.2. Validation of finite element model for vehicle side impact

Qualitative and quantitative evaluation methods are usually used to evaluate the authenticity and accuracy of simulation results [20-22]. The qualitative evaluation method is mainly to check and compare the deformation shape of the impact area in the test and simulation, the impact characteristics of the main components, and the movement of the vehicle and moving deformable barrier after the collision. Quantitative evaluation focuses on the comparison of deformation, acceleration and impact load of different parts of vehicle and moving deformable barrier.

In this paper, according to the requirements of GB20071-2006, the side impact simulation model is established, as shown in Figure 12. The moving deformable barrier (MDB) vertically impacts the side of the stationary vehicle at the speed of 50 km/h. Its vertical line passes through the R point of the front seat on the impact side of the vehicle. The simulation time is set at 140 Ms. According to the energy change of the side impact simulation process, confirm whether the parameters of the side impact simulation model are reasonable. The overall energy change of the system is shown in Figure 13.

It can be seen from Figure 13 that the energy composition of the model system is relatively reasonable, the total energy is conserved, the slip interface energy and hourglass energy keep very small positive values, and do not exceed 5% of the total energy. Therefore, it can be explained that in the modeling process, the standard of finite element mesh, the connection of models and the setting of various solution cards are reasonable. Figure 14 shows the simulation and experimental comparison of the acceleration time curve at the lower end of the B-pillar on the impacted side. It can be seen from the figure that the change trend of the acceleration curve is basically consistent, and the peak value is in good agreement with the occurrence time. The error may be caused by the omission of some body accessories, material parameters and solder joint model, which are different from the actual situation, but the overall error, especially at the first and second peak, is less than 5%. It can be seen that the side wall stiffness of the finite element model is basically consistent with that of the real vehicle, and this model can be used in the following side impact simulation analysis instead of the real vehicle.

Table 2. Energy absorbed by each energy absorption block (kJ)

Project	The first piece	The second piece	The third piece	The fourth piece	The fifth piece	The sixth piece	Population
Simulation	9.55	14.26	9.55	4.27	3.93	3.93	45.49
Regulatory requirements	9.5±2	15±2	9.5±2	4±1	3.5±1	3.5±1	45±3
Result	Qualified	Qualified	Qualified	Qualified	Qualified	Qualified	Qualified

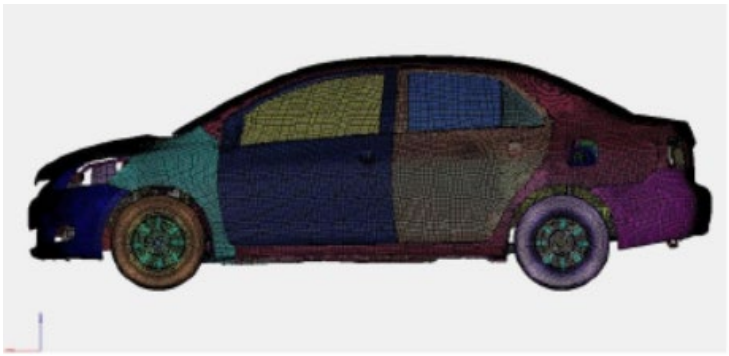

Figure 11. Finite element model of vehicle

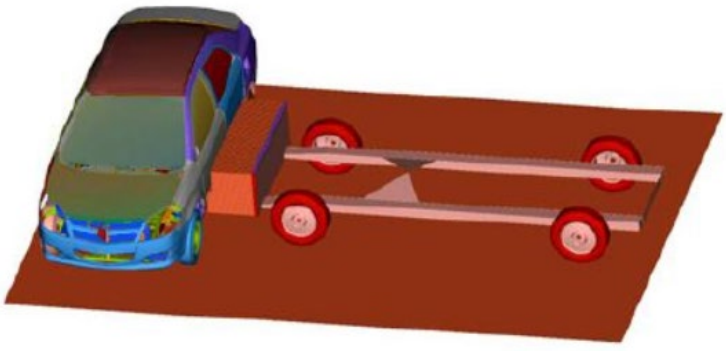

Figure 12. Vehicle side impact model

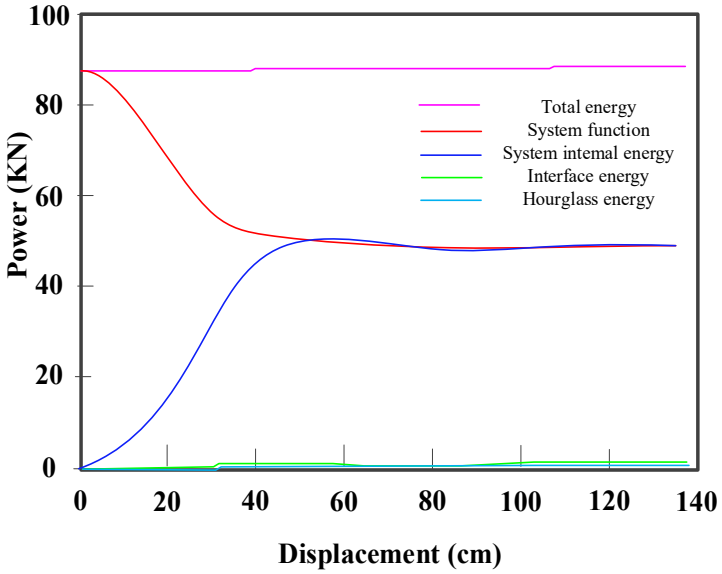

Figure 13. Overall energy curve of the system

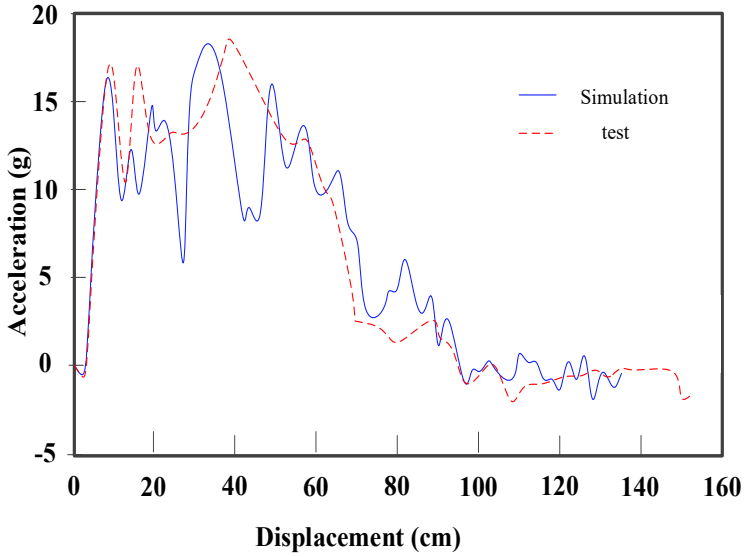

Figure 14. Acceleration at the lower end of B-pillar on the impacted side

3. Safety Optimization Design of Vehicle Side Impact

The optimization design of side impact safety performance can not completely rely on the real vehicle test method, the main means is to use CAE analysis and multidisciplinary optimization theory to optimize the body design. The main content of body multidisciplinary optimization research is to explore effective multidisciplinary collaborative optimization design strategy, realize the concurrent design of multi-disciplinary subsystems of the body, and finally obtain the global optimal solution of the body system.

3.1. Design objectives

Before multidisciplinary optimization design, it is necessary to define the safety design objectives of the vehicle. Through the test method of competitive product analysis, the safety analysis of competitive vehicles with high side impact safety in the market is carried out to obtain the design objectives. Refer to Table 3 for the safety performance of side impact and the design objectives of this model.

The B-pillar inner plate intrusion and B-pillar impact acceleration are selected as the optimization objectives and constraints, while other performance objectives are used as the verification conditions for the feasibility of the optimal design scheme.

Table 3. Side impact performance and design target of reference vehicle

Key position	Reference car	Target value
Front door inner panel (chest) invasion (mm)	147	≤ 140
B-pillar inner plate (chest) invasion (mm)	156	≤ 140
Invasion velocity of lower part of B-pillar (m·s-1)	7.4	≤ 7
B-pillar (head) acceleration (g)	142	≤ 135

3.2. Multidisciplinary collaborative optimization based on adaptive weighting

The essence of body multidisciplinary collaborative optimization problem is to find a set of vectors composed of design variables in the feasible region, so that the surrogate objective function values of various performance of the body system can be optimized as much as possible. In the past, the research on multi-disciplinary problems is often carried out with single objective optimization. However, it is difficult to find the overall optimal solution of the system by using the single objective optimization method because of the conflicts among the objectives. Aiming at the optimal solution problem of multi-objective collaborative optimization, a multidisciplinary collaborative optimization method based on adaptive weighting is proposed. The mathematical model is described as follows:

$$\min ...\mathrm{F}\left(\mathrm{t}\right)= \quad 0<$$

$$\begin{aligned} \min \quad & F(t)=\sum_{i=1}^{n} w_i F_i(t) \qquad 0 \le w_i \le 1 \cup \sum_{i=1}^{n} w_i \\ s.t. \quad & g_i(t)<0 \qquad i=1,2,\cdots,p \\ & g_j(t)=0 \qquad j=1,2,\cdots,q \end{aligned} \tag{1}$$

Among them, $F(t)$, $F_i(t)$, $g_i(t)$ and $g_j(t)$ are the weighted total objective function, the objective function of each performance, the inequality constraint function and the equality constraint function respectively; w_i is the weighting coefficient; n, p, q are the number of corresponding functions; t is a vector composed of design variables. In the process of optimization design, the weighting coefficient w_i is selected by adaptive adjustment, and the total objective function $F(t)$ is constructed. After the multi-objective is transformed into a single objective, multidisciplinary collaborative optimization is carried out according to the design requirements of the designer as constraints.

After the optimization, the design objective is taken as the judgment condition to judge whether the $F_i(t)$ value obtained by optimization meets the requirements of the design objective (fihop T). If it is, the optimization result will be output. Otherwise, the weighted coefficient w_i will be adaptively transformed according to the design requirements, and multidisciplinary optimization design will be carried out again. Finally, the optimal scheme of multi-objective optimization satisfying the design objectives is obtained, and the weighting coefficient w_i obtained from this is called adaptive weighting coefficient. The adaptive weighting method can adaptively increase or decrease the weight ratio of the response function according to the optimization results and optimization objectives. Finally, it can automatically obtain the global optimum and significantly reduce the optimization times. In the optimization design of the body structure, the side impact safety of the body and the lightweight performance of the body are optimized together. Under the condition that the body mass is not increased, the B-pillar intrusion and B-pillar acceleration are the minimum, so as to improve the safety of the side impact. According to the adaptive weighting method, the mathematical expression of multidisciplinary optimization is as follows:

$$\begin{aligned} \min \quad & F(t)=w_1 d_b + w_2 a_b \\ s.t. \quad & m < m_0 \\ & d_b \le 120mm \qquad a_b \le 120mm \\ & 0.8mm \le t \le 2.5mm \end{aligned} \tag{2}$$

Among them, w_1 and w_2 are adaptive weighting coefficients; m_0 is the total vehicle mass before optimization (1674.3 kg).

According to the design variables and optimization objectives, the sequential quadratic programming (SQP) method based on Lagrange Hessian matrix is used to solve the multi-objective optimization problem by using MATLAB software. The Hessian matrix is calculated by quasi Newton method. After several iterations, the optimization results are shown in Table 4.

Table 4. Optimization results

Name	w_1	w_2	F	d_b/mm	a_b/g	m/kg	t1	t2	t3	t4	t5	t6
Initial value	0.6	0.4	147.93	146.40	150.22	1674.3	1.6	2．0	2.8	1.8	1.8	1.6000
Optimization value	0.6	0.4	120.57	113.48	131.20	1673.9	2．0	1.5	1.6	2．0	2．0	0.8873

Considering the actual production and manufacturing process, the optimal values of each design variable are determined as follows: t1 = 2.0 mm, t2 = 1.5 mm, T3 = 1.6 mm, t4 = 2.0 mm, T5 = 2.0 mm, t6 = 0.8 mm. Evaluation of optimization results in order to verify whether the optimization results have practical significance, according to the optimization value of design variables, the optimized simulation model is established for simulation test. The simulation results are compared with those before optimization.

It can be seen from Table 5 that the performance of the optimized structure exceeds the design target, and the side impact safety is significantly improved without increasing the vehicle mass.

Table 5. Comparison of performance indexes before and after optimization

Name	Before improvement	After improvement
Front door (chest) intrusion (mm)	146.98	122.46
B-pillar (chest) invasion (mm)	142.00	122.05
B-pillar (head) acceleration (g)	150.20	132.8
B-pillar (bottom) invasion velocity (m·s-1)	10.70	6.3
Vehicle mass (kg)	1674.30	1673.8

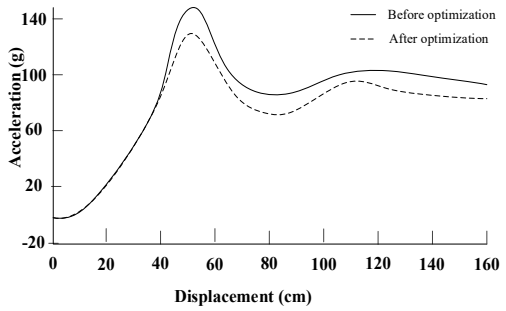

Figure 15. Acceleration comparison of B-pillar (head position) before and after optimization

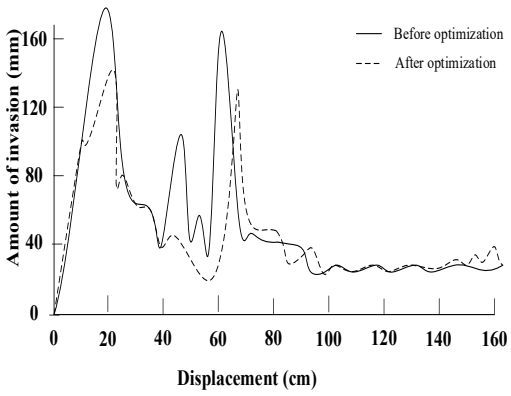

Figure 16. Comparison of B-pillar (chest position) invasion before and after optimization

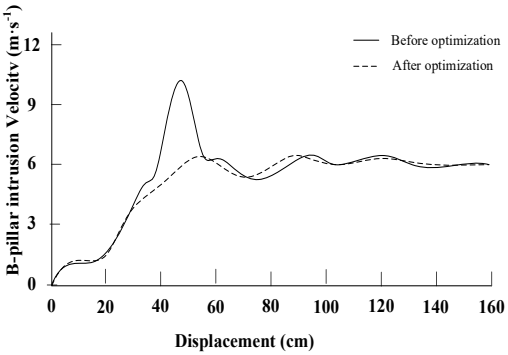

Figure 17. Comparison of invasion velocity of B pillar before and after optimization

At the same time, from the comparison diagram of acceleration, intrusion volume and intrusion speed before and after optimization in Figures 15-17, it can be seen that the acceleration value, intrusion volume and intrusion speed of the optimized structure are reduced by 20 g, 130 mm and 5.5 $m.s^{-1}$ respectively, which is significantly lower than that of the original model. Through the above analysis, it can be seen that the optimized structure is significantly better than the original vehicle in terms of side impact safety, which also shows that the optimization scheme proposed in this paper is feasible. The reason for this phenomenon is that the design method in this paper optimizes the position of the anti-collision beam by increasing the plate thickness, using ultra-high strength steel, increasing structural stiffeners, and using anti-collision beams with different section shapes. The safety of the original vehicle is verified by simulation test.

4. Conclusions

Because the defect of simulation analysis is that it can produce error, even result in error, so the correct result depends on the correct simulation model. The model is reliable after strict verification, and the analysis and optimization design on this model are effective. According to China's side impact regulations and standards, combined with the verification method of simulation models, the moving deformable barrier and vehicle models are verified respectively. The verification results show that the finite element model is reliable and effective. On this basis, the vehicle side impact simulation model is established and verified. The verified vehicle side impact simulation model can be used for further analysis and research. For front impact or rear end collision, the car body has larger buffer space design, but the side only provides a small collision buffer space. Therefore, it is very difficult to enhance the impact resistance of the side of the car and improve the anti-collision technology. In order to improve the side impact resistance of the vehicle body, the key point is to transfer the collision energy

to other protective beams, columns, floors, roofs and other parts of the car body. These parts disperse and absorb the impact force, which greatly limits the degree of possible injury, even to the minimum. Through the research on the impact characteristics of vehicle side impact, several improvement schemes are proposed to improve the crashworthiness of vehicle side impact structure. On this basis, the effectiveness of the scheme is analyzed and evaluated. The results show that the acceleration, intrusion volume and intrusion velocity of the optimized structure are reduced by 20 g, 130 mm and 5.5 $m.s^{-1}$ respectively, which is significantly lower than that of the original model. Through the evaluation of the optimization results, the feasibility of the optimization scheme is verified, and the side impact safety is significantly improved.

Acknowledgements

The research is supported by: The Key Project of Natural Science Research of Anhui Sanlian University: energy consumption prediction modeling and parameter optimization design of NC machine tools for low-carbon manufacturing (No.PTZD2021020); The Quality Engineering Project of Anhui Department of Education: Teaching Team of Engineering Graphics Course (No.2019jxtd123); The Quality Engineering Project of Anhui Sanlian University: first-class specialty of mechanical design, manufacturing and automation (No.20zlgc002).

References

[1] Kim, S.M.; Yang, I.C.; Park, S.Y.; Lee, M.P. Evaluation of wheelchair occupant safety in frontal & side impact of wheelchair loaded vehicle by computer simulation analysis method (Adams + Lifemod). Journal of Biomechanics, 2006, 39: S536-S536.

[2] Wang, J.Y. Strength optimization design and simulation of automobile shape shell structure. Computer Simulation, 2017, 34(3): 138-141.

[3] Matsui, Y.; Hitosugi, M.; Mizuno, K. Severity of vehicle bumper location in vehicle-to-pedestrian impact accidents. Forensic Ence International, 2011, 212(1-3): 205-209.

[4] Jost, G.; Allsop, R.; Ceci, A. Ranking EU progress on car occupant safety. Statistics, 2014.

[5] Youn, Y.; Koo, J.S. The effectiveness of the component impact test method for the side impact injury assessment of the door trim. International Journal of Modern Physics B, 2008, 22(9-11): 1766-1773.

[6] King, A.I. Biomechanics of automotive side impact protection. Fems Microbiology Letters, 1993, 112(1): 55-60.

[7] Chen, Y.K.; Wang, K.; King, M.; He, J.; Ding, J.X.; Shi, Q.; Wang, C.J.; Li, P.F. Differences in factors affecting various crash types with high numbers of fatalities and injuries in China. PloS One, 2016,11(7): e0158559.

[8] Segui-Gomez, M.; Arregui-Dalmases, C.; Dios, E.D.P.D; Lopez-Valdes, F. Risk factors for severe injuries among front seat occupants in side impact crashes. Communications of the Acm, 2009.

[9] Johnson, N.S.; Gabler, H. Injury risk posed by side impact of nontracking vehicles into guardrails. Transportation Research Record, 2013, 2377(1): 21-28.

[10] Yuan, Q.; Xu, X.C.; Xu, M.C.; Zhao, J.W.; Li, Y.B. The role of striking and struck vehicles in side crashes between vehicles: Bayesian bivariate probit analysis in China. Accident Analysis and Prevention, 2020, 134: 105324.

[11] Fein, S.M.; Jermakian, J.S.; Arbogast, K.B.; Maltese, M.R. Fatal side impact crash scenarios for rear seat and seat belt–restrained occupants from vulnerable populations. Traffic Injury Prevention, 2019, 20: S50-S56.

[12] Kelley, M.E.; Talton, J.W.; Weaver, A.A.; Usoro, A.O.; Barnard, E.R. Miller, A.N. Associations between upper extremity injury patterns in side impact motor vehicle collisions with occupant and crash characteristics. Accident Analysis & prevention, 2019, 122: 1-7.

[13] Viano, D.C.; Parenteau, C.S. Severe injury in multiple impacts: Analysis of 1997-2015 NASS-CDS. Traffic Injury Prevention, 2018, 19(5): 501-505.

[14] Hauschild, H.W.; Humm, J.R.; Pintar, F.A.; Yoganandan, N.; Kaufman, B.; Maltese, M.R.; Arbogast, K.B. The influence of enhanced side impact protection on kinematics and injury measures of far-or center-seated children in forward-facing child restraints. Traffic Injury Prevention, 2015, 16(sup2): S9-S15.

[15] Girasek, D.C; Taylor, B. An exploratory study of the relationship between socioeconomic status and motor vehicle safety features. Traffic Injury Prevention, 2010, 11(2): 151-155.

[16] Peng, Y.; Guo, X. Optimization design of B-pillar structure based on vehicle side impact safety. Mechanical Design and Manufacturing, 2020, (4): 150-155.

[17] Ning, P.F. An adaptive scheduling method for resources in used automobile parts recycling. Jordan Journal of Mechanical and Industrial Engineering, 2020, 14(1): 53-60.

[18] Yu, Y.; Li, W.; Li, L. Research on lightweight design of micro electric vehicle frame structure. Modern Manufacturing Engineering, 2019, (1): 75-81.

[19] Wu, K.; Su, X.; Wang, Q. Structural analysis and optimization design of construction machinery frame. Mechanical Design and Manufacturing, 2020 (7): 51-55.

[20] Zhang, Q.Y.; Wang, Y.R.; Lin, W.P.; Luo, Y.J.; Wu, X.J. Contact mechanics analysis and optimization of shape modification of electric vehicle gearbox. Jordan Journal of Mechanical and Industrial Engineering, 2020, 14(1): 15-24.

[21] Memar, A.H.; Esfahani, E.T. A robot gripper with variable stiffness actuation for enhancing collision safety. IEEE Transactions on Industrial Electronics, 2020, 67(8): 6607-6616.

[22] Zhang, F.; Zhou, M.; Qi, L.; Du, Y.; Sun, H. a game theoretic approach for distributed and coordinated channel access control in cooperative vehicle safety systems. IEEE Transactions on Intelligent Transportation Systems, 2020, 21(6): 2297-2309.

JJMIE

Volume 16, Number 1, January. 2022
ISSN 1995-6665
Pages 53 - 62

Jordan Journal of Mechanical and Industrial Engineering

Dynamic Response Analysis of the Impact Force of Steel Wheel on the Elastic Half-Space

Zhipo Cao[1,2], Naixing Liang[1*], Sheng Zeng[1], Xianshui Gang[3]

[1]School of Civil Engineering, Chongqing Jiaotong University, Chongqing 400074, China
[2]Department of Automobile Engineering, Dezhou Vocational and Technical College, Dezhou 253000, China
[3]Department of Architectural Engineering, Dezhou Vocational and Technical College, Dezhou 253000, China

Received 14 July 2021 Accepted 24 December 2021

Abstract

In order to discover the dynamic response of the impact force of steel wheel on elastic half-space, and to quantify the peak impact force and detect the elastic modulus of elastic half-space, a finite element model of the steel wheel impacting the elastic half-space is established. According to Palmgren empirical formula, take the impact height (h), elastic modulus (E) and Poisson's ratio (σ) of elastic half-space as the main influencing factors, and take the peak acceleration of steel wheel during the impact process as the research object. The process of impacting the elastic half-space with different elastic modulus and Poisson's ratio by the same steel wheel falling at different heights is simulated by finite element method. Then, the MAP diagram and fitting formula of the relationship between peak acceleration and main influencing factors are obtained. The results show that when the steel wheel impacts the elastic half-space, there is a quadratic nonlinear relationship between the peak acceleration and impact height of steel wheel and elastic modulus of elastic half-space, and the Poisson's ratio of elastic half-space has little effect on the peak acceleration of steel wheel. The error between the theoretical values and the interpolation as well as the simulation values are around 25%, meeting the engineering requirements. So it can be used in the calculation of dynamic process of impact force that steel wheel imposes on the elastic half-space. It can be seen that the peak acceleration of steel wheel is correlated with the main influencing factors during the impact process. The impact force and the elastic modulus of elastic half-space can also be predicted according to the fitting relationship.

Keywords: Steel wheel; elastic half-space; impact height; elastic modulus; peak acceleration;

1. Introduction

Collisional impact between moving objects is a common problem in engineering, and the study of impact process has always been an often discussed and difficult issue in the field of dynamics [1]. Steel wheel is a cylindrical component commonly seen in engineering. The impact between steel wheel and plane is a typical reflection of the impact between cylinder and plane in reality. Normally, in reality the plane is multi-layer structures, which can be considered as an equivalence to the elastic half-space structure [2]. Acceleration signal is an important parameter for it is easy to measure in the dynamic response, and can fully reflect the dynamic parameters such as impact force and impact duration in the impact process [3]. Therefore, the analysis on the changes of acceleration signal when steel wheel imposes impact force on the elastic half-space is of great significance in analyzing the dynamic response of moving objects during impacting process and quantifying the impacting force and dynamic modulus of elastic half-space [4].

The impact process has a strong nonlinear characteristic, and it is influenced by many factors including initial conditions, material characteristics, and structure shape [5]. So a complete theoretical system of impact dynamics has not yet been formed [6]. To study the impact process, Newton first proposed the kinematic recovery coefficient to describe the change in the velocity before and after the collision of two objects. Poisson also proposed the dynamic collision recovery coefficient from the perspective of the momentum. Several scholars studied the collision recovery coefficient from the view of energy [7-9]. Several Chinese scholars conducted studies on the collision dynamics, and compared the applicable conditions of three collision coefficients with the accuracy of collision impact process [10-12]. Several scholars used kinematic recovery coefficient to evaluate the dynamic response of rockfall impacting the ground [13, 14]. Research has shown that the collision recovery coefficient can well describe the change of object motion before and after the collision, but it cannot describe the change of dynamic parameters such as force and acceleration during the collision.

* Corresponding author e-mail: liangnx@cqjtu.edu.cn.

The research on dynamic response in the impact process focuses on the field of contact mechanics. The basic theory for collision impact between elastomers was proposed by Hertz [15]. Based on Hertz's contact mechanics, domestic and foreign scholars conducted a lot of studies on impact dynamics between sphere and sphere or between sphere and plane or cylinder to cylinder, and obtained an accurate theoretical explanation [16-18, 5]. However, it is difficult in the study of line contact between cylinder and plane, and there is not yet an accurate and convenient solution available [6]. Several scholars proposed a nonlinear model of the relationship between impact and strain based on Hertz contact theory, which can be used to analyze the dynamic response of impact between cylinder and plane [15, 19, 20]. However, the implicit equation adopted in the theory makes it difficult to be applied in engineering. To make it accessible, many scholars proposed empirical formulas that adopt display equations, and the Palmgren formula is the most widely used one [21].

Although the Palmgren empirical formula has a high computational accuracy, it is mainly used for the dynamics process of impact between solid cylinder and plane. The steel wheel is a common cylindrical shell structure in engineering [22]. There is no evidence to prove that the impact between steel wheel and elastic half-space can be solved by using this formula. In this paper, a simulation model of steel wheel impacting the elastic half-space is established by adopting finite element method. Based on Palmgren formula, main influencing factors affecting dynamic process of steel wheel impacting the elastic half-space are determined and the acceleration of steel wheel is taken as the dependent variable, establishing the relationship between various influencing factors and the acceleration of steel wheel.

2. Methods and Materials

2.1. Method to determine main influencing factors of impact process

To determine the influencing factors of dynamic response, simplify the model and determine the main influencing factors, the following assumptions to the model are made: (1) The elastic modulus of steel wheel differs greatly from that of elastic half-space, so the steel wheel is regarded as the rigid body; (2) In the impact process, the elastic half-space conforms to the condition of small strain; (3) In the impact process, there is only vertical force distributed on the contact surface while no horizontal force distributed; (4) The contact surface is smooth without frictional force. The impact dynamics model is established as shown in Figure 1.

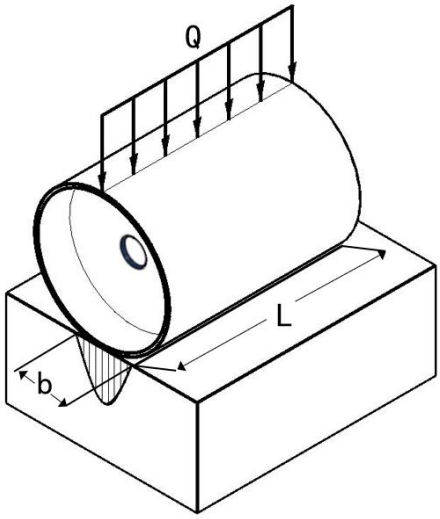

Figure 1. Schematic diagram of the steel wheel impacting the elastic half-space

According to the above assumptions, the maximum contact force is evenly distributed along the contact tessellation line, and its value can be solved by Hertz contact theory and Palmgreng empirical formula. When the cylinder imposes impact on the plane, the relationship between the impact force and the deformation of elastic half-space is shown in Formula (1).

$$F = K\varepsilon^n \tag{1}$$

where F *is* the impact force, N; ε is the deformation of elastic half-space, m; n *is* the nonlinear index of cylinder contact, n = 10/9 in the Palmgren elastic line contact model; K *i*s the equivalent stiffness of elastic contact, which is depended on the material and shape of contact body. According to Hertz contact theory and Palmgren elastic line contact model, the value of K is shown in Formula (2).

$$K = \frac{\pi}{\left(2\times 3.81\right)^n}\frac{E\times 10^{-6}}{1-\sigma^2}\left(1000L\right)^{\left(\frac{8}{9}\right)} \tag{2}$$

where E *is* the elastic modulus of elastic half-space material, MPa; σ is the Poisson's ratio of elastic half-space material; L is the contact length of elastic line, mm.

The maximum impact (F_m) when cylinder impacts the elastic half-space is shown in Formula (3).

$$F_m = K\left[1000\left(n+1\right)\frac{m_l}{K}gh\right]^{\left(\frac{n}{n+1}\right)} \tag{3}$$

where h is the impact height of steel wheel, mm; m_l is the mass of cylinder, kg.

According to Newton's Second Law, the maximum impact acceleration (a_m) when cylinder impacts the elastic half-space is shown in Formula (4).

$$a_m = \frac{F_m}{m_l} = \frac{K}{m_l}\left[(n+1)\frac{m_l}{K}gh\right]^{\left(\frac{n}{n+1}\right)} \quad (4)$$

As can be seen from Formula (4), in the process that cylinder impacts the elastic half-space, the dynamic response is correlated with the length (L), mass (m), impact height (h) of cylinder as well as the elastic modulus (E) and Poisson's ratio (σ) of the material of elastic half-space.

This paper focuses on the relationship between the change of the material of elastic half-space and the change of dynamic response of steel wheel as well as relationship among the change of impact height, elastic modulus and the dynamic response of steel wheel. So the length (L) and mass (m) of the steel wheel are set to constant values.

2.2. FEA model and materials

According to the assumptions, a finite element model is established in the finite element analysis software ABAQUS, see Figure 2(a). In this model, the length of the steel wheel is 600 mm while the density is 7.8 × 10^{-6} kg/mm^3. Calculation shows that the mass is 81.1 kg, the elastic modulus is 310 000 MPa, and the Poisson's ratio is 0.3.

The size of the elastic half-space is 6 000 × 3 000 × 3 000 mm and it adopts symmetry constraint to symmetric surfaces and fixed constraints to bottom surface and four sides. The density of elastic half-space is 2.4 × 10^{-6} kg/mm^3, and the elastic modulus and Poisson's ratio are set as independent variables. The value range of elastic modulus is 500-8500 MPa, and Poisson's ratio is 0.2-0.4 [2, 23].

The 8-node hexahedron linear reduction integral element (C3D8R) and the modified quadratic tetrahedron element (C3D10M) can be chosen to simulate the impact process in ABAQUS software. According to the assumptions, the impact force in the finite element model is vertically downward and there is no large deformation. Therefore, in order to give consideration to calculation accuracy and simulation efficiency, the C3D8R element is selected as the grid element, and its total energy is basically 0 in the calculation process, thus there is no hourglass problem, so the calculation result is reliable. If the element C3D10M is selected, although certain accuracy can be improved, the calculation time will be increased by more than 6 times.

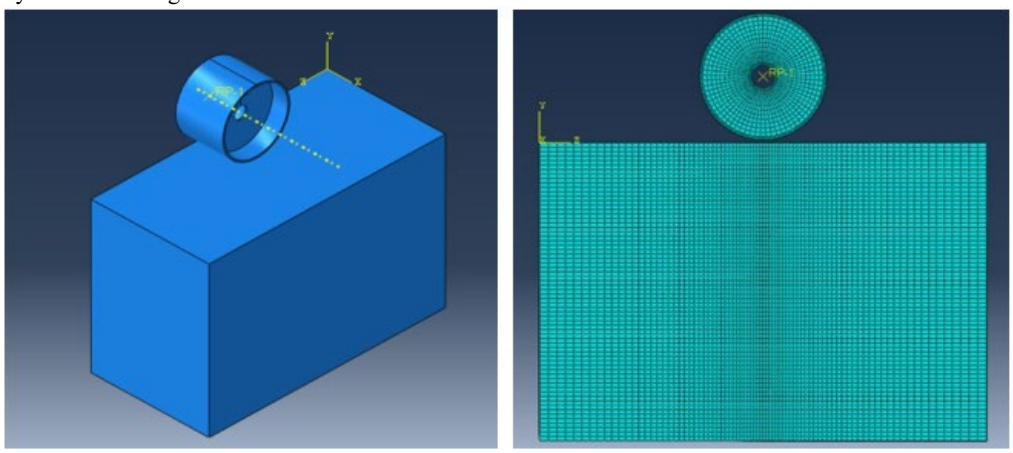

(a) The finite element model (b) The meshing method

Figure 2. The finite element model and meshing method

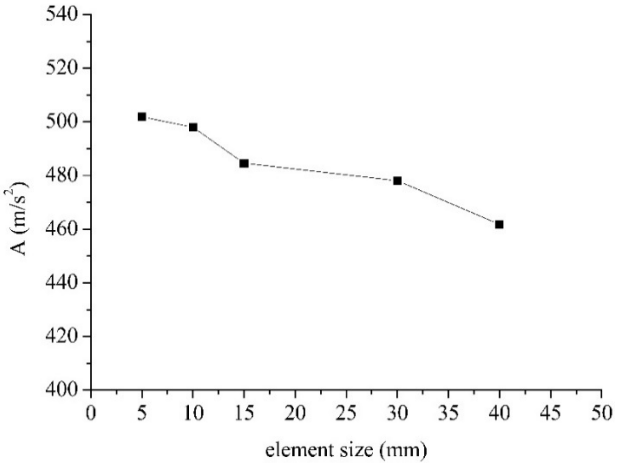

Figure 3. The sensitivity analysis results

In order to determine the mesh size, sensitivity analysis is carried out on the model. The elastic modulus of the elastic half-space is set as 6500 MPa and the Poisson's ratio is 0.3. The grid size is set to 40 mm, 30 mm, 15 mm, 10 mm and 5 mm respectively for simulation, and the results are shown in Figure 3. As can be seen from Figure 3, when the grid size is less than 10 mm, the change trend of acceleration response value slows down. Therefore, when the grid size is 5 mm, the calculation results tend to converge, but it takes a long time to calculate.

Then, set the grid along the Z direction, from 30 mm in the outermost part of the elastic half-space to 5 mm in the middle, and the other directions are set to 15 mm. The simulation result is basically the same as that when the grid is set to 5 mm, but the calculation time is reduced by about 28%. Therefore, the model is divided into grids as shown in Figure 2(b) in order to give consideration to both calculation accuracy and calculation speed.

3. Results and Discussion

3.1. Validation of the FEA model

To verify the rationality of finite element model, the elastic modulus of elastic half-space is set to 6 500 MPa and the Poisson's ratio is set to 0.3. The impacting process is simulated as the impact height (h) is at 10 mm, 20 mm and 30 mm. Figure 4 shows the stress nephogram when steel wheel falls at height of 30 mm. As can be seen in Figure 4, when the steel wheel impacts the plane, the contact force is evenly distributed along the contact tessellation line, and only slightly increased at the steel wheel rim. Moreover, the contact stress shows elliptic distribution within the contact width (b), which is in line with Hertz contact theory.

The steel wheel is rigid body, so the dynamic response of all points on the steel wheel are the same when steel wheel impacts the elastic half-space. Take the top center of steel wheel as the test point, set the drop height to 10 mm, 20 mm and 30 mm, the elastic modulus to 2 500 MPa and 6 500 MPa, Poisson's ratio to 0.3, the velocity, stress and acceleration response of steel wheel are shown in Figures 5-7.

Figure 5 shows the velocity response during the impact process. As can be seen from Figure 5, when steel wheel falls at different height and impacts elastic half-space with different elastic modulus and Poisson's ratio, the velocity is only affected by falling height and hardly affected by elastic modulus and Poisson's ratio. According to the definition of kinematic recovery coefficient e, as shown in Formula 5, and the results have been showed in Table 1.

$$e = \frac{v_t}{v_0} \tag{5}$$

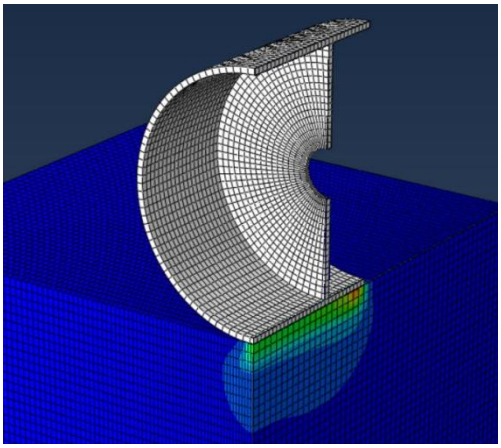

Figure 4. Stress nephogram in the impact process

Figure 6 shows the impact response curve when steel wheel impacts the half-space. As can be seen from Figure 6, during the impact process, the elastic modulus has a huge influence on impact force, which shows that greater the elastic modulus, greater the impact force. The elastic modulus also had an effect on impact duration, that is, the greater the elastic modulus, the shorter the impact duration; The Poisson's ratio of elastic half-space has little effect on impact force and impact time.

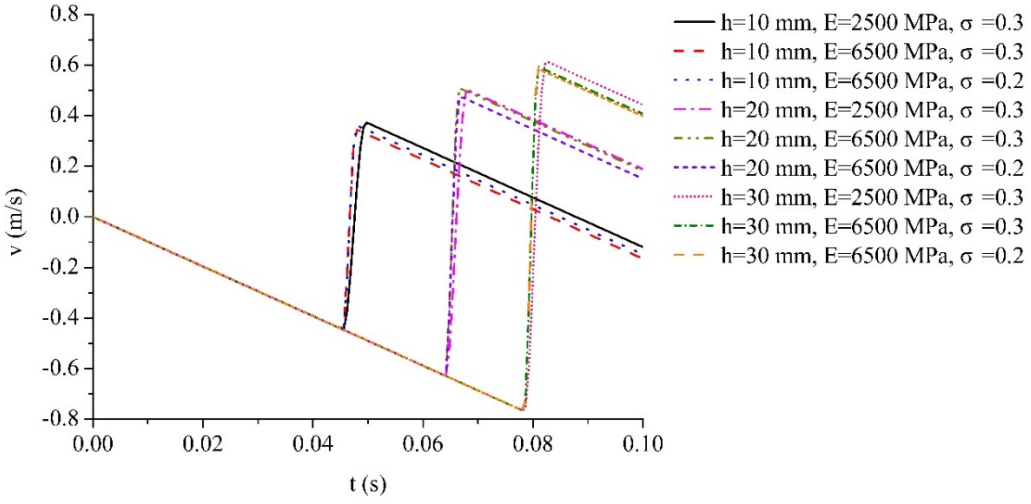

Figure 5. Curve of velocity response of steel wheel in the impact process

Figure 7 shows the curve of peak acceleration response of steel wheel in the impact process. As can be seen from Figure 7, the elastic modulus of elastic half-space has a great effect on acceleration response, that is, the greater the elastic modulus, the greater the peak acceleration; The Poisson's ratio of elastic half-space has little effect on peak acceleration response.

Compared between simulated velocity, impact and peak acceleration and the calculation result of acceleration and peak impact force according to Formula 3 and Formula 4 is as shown in Table 1.

As can be seen from Table 1, in the process that the elastic half-space with different elastic modulus and Poisson's ratio is impacted by the same steel wheel falling at different heights, the kinematic recovery coefficient before and after the impact is around 0.66. Therefore, the impact height of steel wheel and the material of elastic half-space does not affect the kinematic recovery coefficient of the impact system. The error between the simulation results of peak impact force and the calculation results of peak impact force by Formula (3) is less than 10%, and the error between the simulation results of peak acceleration and the calculation results of peak acceleration by Formula (4) is less than 20%, meeting the requirement of engineering use. Therefore, the finite element model is reasonable, and its simulation results can be used in the analysis of dynamic process of the steel wheel impacting the elastic half-space.

3.2. Effect law of the change of Poisson's ratio on acceleration response

To find out how the change of Poisson's ratio affects the dynamic response of steel wheel, the impact process is simulated when elastic modulus is set to 500 MPa, 2 500 MPa, 4 500 MPa, 6 500 MPa, 8 500 MPa, Poisson's ratio is set to 0.2, 0.25, 0.3, 0.35, 0.4 and the falling height is set to 10 mm, 30 mm respectively. The Figure 8 shows the simulation result of peak acceleration change when the impact height is at 10 mm and 30 mm and the Poisson's rate changes from 0.2 to 0.4 with different elastic modulus.

As can be seen from Figure 8, when the elastic half-space with the same elastic modulus and Poisson's ratio of 0.2-0.4 is impacted by the same steel wheel falling at the same height, the peak acceleration of steel wheel has little change. Thus, the change of Poisson's ratio of elastic half-space has little effect on the peak acceleration of steel wheel.

Figure 9 shows the simulated result of impact duration when the impact height is at 10 mm and 30 mm and the Poisson's rate changes from 0.2 to 0.4 with different elastic modulus.

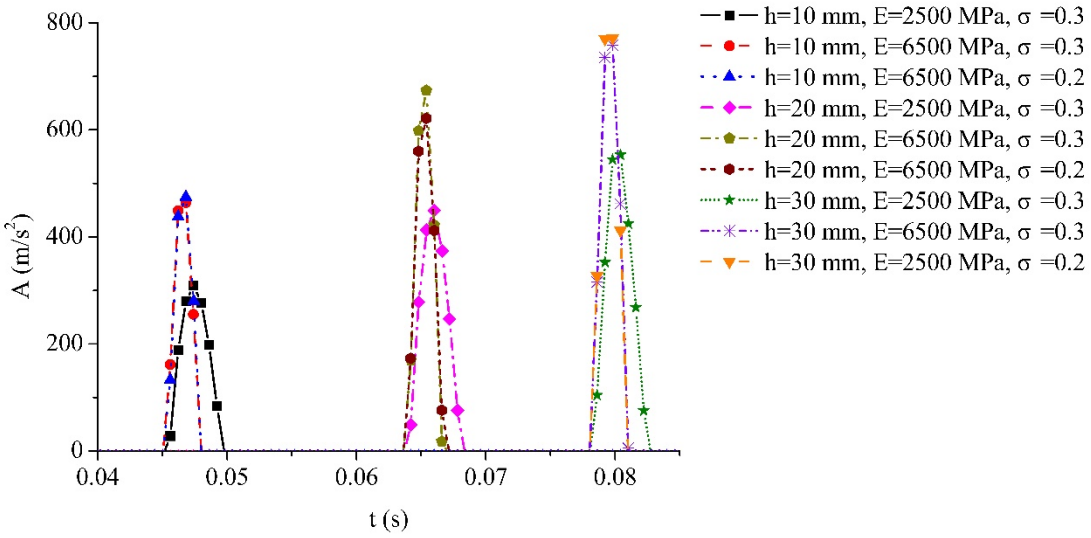

Figure 7. Curve of peak acceleration response of steel wheel in the impact process

Table 1. Comparison between the simulation results and the calculation results

Impact height *h* /mm	Elastic modulus E/MPa	Steel wheel velocity v/(m·s^{-1})		Recovery coefficient *e*	Impact force F/KN		Error	Acceleration A/(m·s^{-2})		Error
		Before the impact v_0	After the impact v_t		Theoretical value	Simulation value		Theoretical value	Simulation value	
10	2500	0.44	0.30	0.68	31.07	33.28	7.11%	383.22	308.72	19.44%
	6500		0.29	0.66	48.85	52.73	7.94%	602.59	501.702	16.74%
20	2500	0.63	0.43	0.68	44.75	49.15	9.83%	551.96	449.01	18.65%
	6500		0.41	0.65	70.36	64.05	8.97%	867.91	766.78	11.65%
30	2500	0.77	0.50	0.65	55.39	55.26	0.23%	683.26	592.610	13.27%
	6500		0.49	0.64	87.10	91.27	4.79%	1074.36	895.20	16.68%

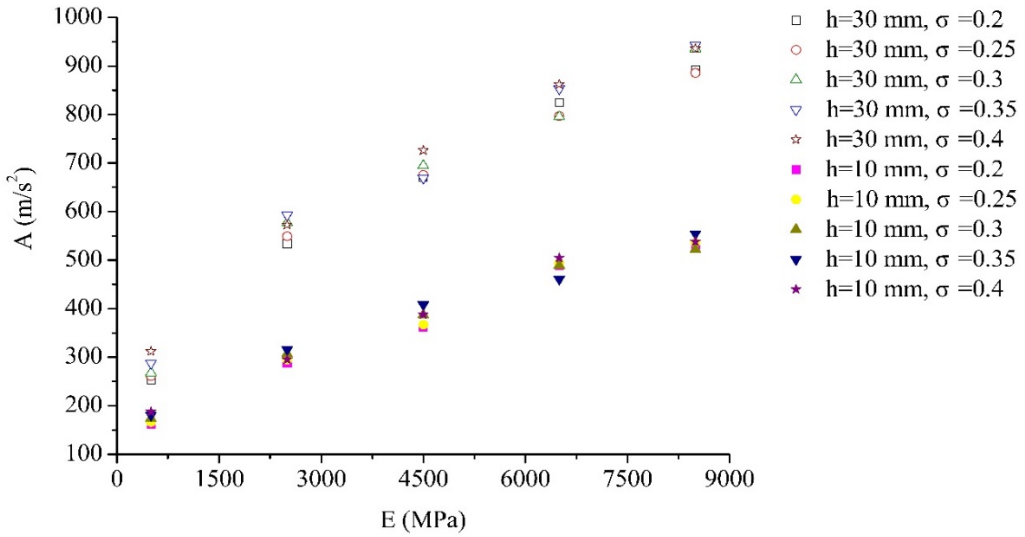

Figure 8. The relationship between peak acceleration and elastic modulus at different Poisson's ratio

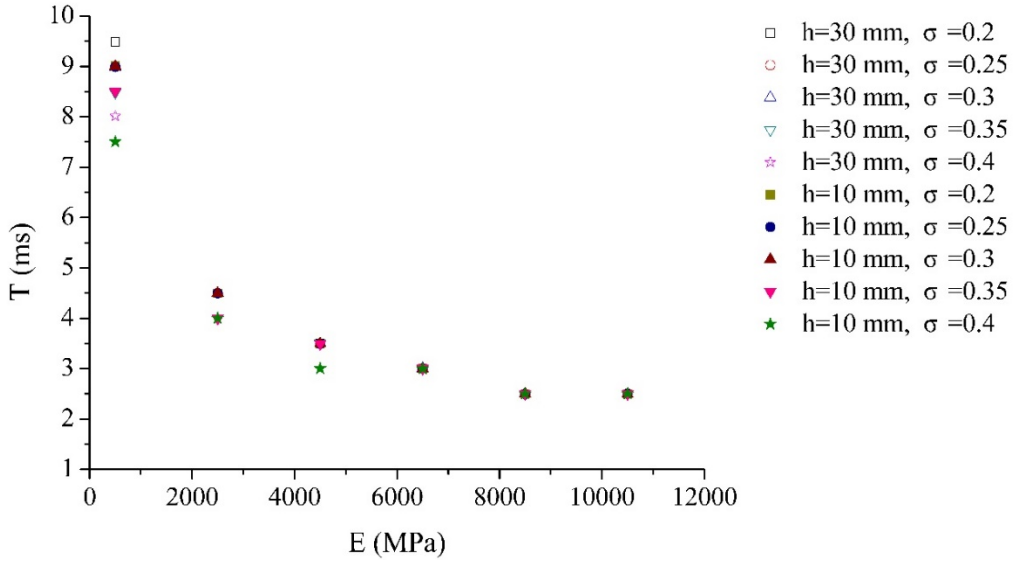

Figure 9. The relationship between impact duration and elastic modulus at different Poisson's ratios

As can be seen from Figure 9, when the elastic modulus is smaller than 2 500 MPa, Poisson's ratio change has a great effect on impact duration. However, when the elastic modulus is greater than 2 500 MPa, Poisson's ratio change has no effect on impact duration. Thus, the Poisson's ratio change of elastic half-space has little effect on the impact duration of steel wheel.

3.3. Effect law of elastic modulus change on acceleration response

To find out how the change of elastic modulus of the material of elastic half-space affects the dynamic response of steel wheel, the elastic half-space with Poisson's rate is 0.3 and the elastic modulus is between 500 to 14 500 MPa impacted by the steel wheel at height of 10 mm to 40 mm is simulated. Figure 10 shows the relationship between peak acceleration and elastic modulus.

As can be seen from Figure 8, when the steel wheel impacts the elastic half-space at the same height, the peak acceleration increases with the increase of elastic modulus, and presents a quadratic nonlinear relationship. The fitting relationship between peak acceleration and elastic modulus at different heights is shown in Fit Curve10-Fit Curve40. From the curves it can be seen that the R^2 of the fitting curve is above 0.95, so the fitting curve has a high fitting accuracy.

3.4. Effect law of impact height change on acceleration response

To find out how the change of impact height affects the dynamic response of steel wheel, the elastic half-space with the Poisson's rate is 0.3 and the elastic modulus is 500 MPa to 14 500 MPa is impacted by the steel wheel at height of 10 to 40 mm is simulated. Figure 9 shows the relationship between peak acceleration and impact height.

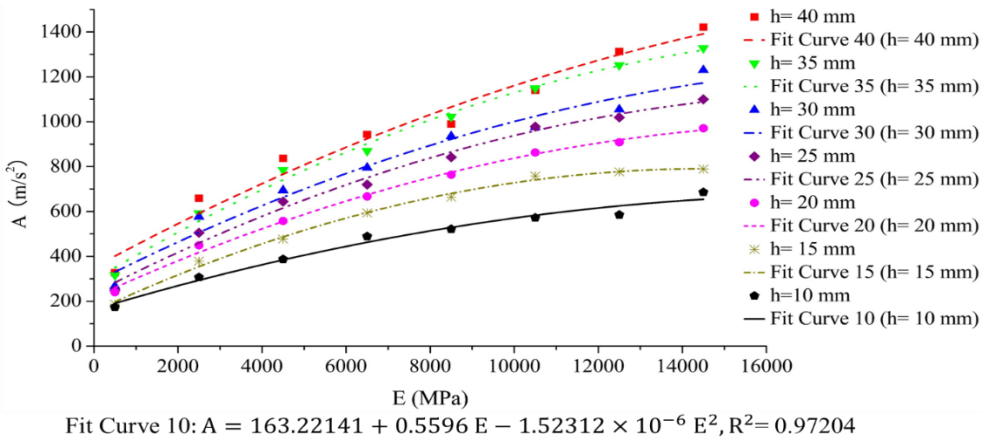

Fit Curve 10: $A = 163.22141 + 0.5596\,E - 1.52312 \times 10^{-6}\,E^2, R^2 = 0.97204$

Fit Curve 15: $A = 154.7949 + 0.08719\,E - 2.98888 \times 10^{-6}\,E^2, R^2 = 0.9941$

Fit Curve 20: $A = 218.4849 + 0.8539\,E - 2.34962 \times 10^{-6}\,E^2, R^2 = 0.99423$

Fit Curve 25: $A = 236.21379 + 0.09567\,E - 2.54728 \times 10^{-6}\,E^2, R^2 = 0.98453$

Fit Curve 30: $A = 283.50127 + 0.09476\,E - 2.30404 \times 10^{-6}\,E^2, R^2 = 0.95937$

Fit Curve 35: $A = 294.8684 + 0.11184\,E - 2.83986 \times 10^{-6}\,E^2, R^2 = 0.99013$

Fit Curve 40: $A = 350.88007 + 0.10147\,E - 2.04941 \times 10^{-6}\,E^2, R^2 = 0.96056$

Figure 10. The relationship between peak acceleration and elastic modulus

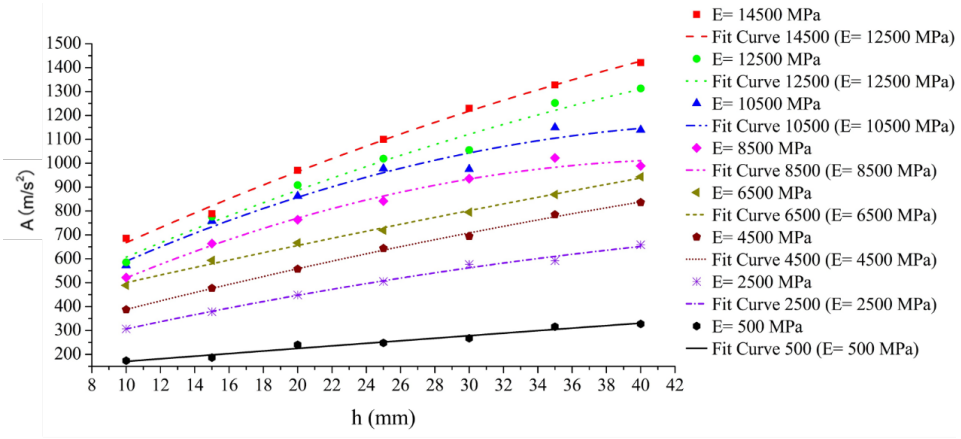

Fit Curve 500: $A = 115.85871 + 5.54435\,h - 0.00421\,h^2, R^2 = 0.95335$

Fit Curve 2500: $A = 140.17557 + 17.94033\,h - 0.12879\,h^2, R^2 = 0.99038$

Fit Curve 4500: $A = 197.43964 + 20.09649\,h - 0.102\,h^2, R^2 = 0.99671$

Fit Curve 6500: $A = 334.9895 + 17.01792\,h - 0.04847\,h^2, R^2 = 0.99364$

Fit Curve 8500: $A = 182.92507 + 38.0396\,h - 0.43356\,h^2, R^2 = 0.9806$

Fit Curve 10500: $A = 239.49214 + 39.13628\,h - 0.41175\,h^2, R^2 = 0.95443$

Fit Curve 12500: $A = 281.81214 + 34.8003\,h - 0.22721\,h^2, R^2 = 0.97367$

Fit Curve 14500: $A = 325.44071 + 36.41516\,h - 0.22199\,h^2, R^2 = 0.99457$

Figure 11. The relationship between peak acceleration and impact height

As can be seen from Figure 11, when the elastic modulus remains same, the peak acceleration increases with the increase of impact height, and presents a quadratic nonlinear relationship. The fitting relationship between peak acceleration and impact height at different heights is shown in Fit Curve500-Fit Curve14500 in Figure 11. From the curves, it can be seen that the R^2 of the fitting curve is above 0.95, so the fitting curve has a high fitting accuracy.

3.5. The effect law of the change of different influencing factors on acceleration response

To analyze the effect of different influencing factors on the acceleration response of steel wheel, the elastic modulus of elastic half-space and the impact height of steel wheel are taken as the independent variables, while the peak acceleration of steel wheel as the dependent variable, the MAP diagram of the relationship between peak acceleration and different influencing factors is as shown in Figure 12.

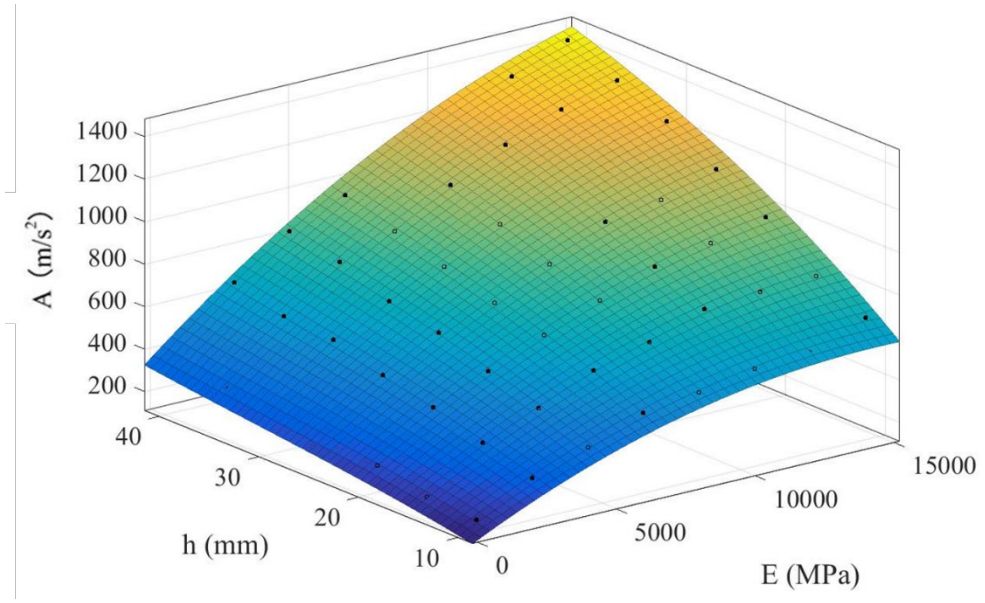

(a) MAP diagram

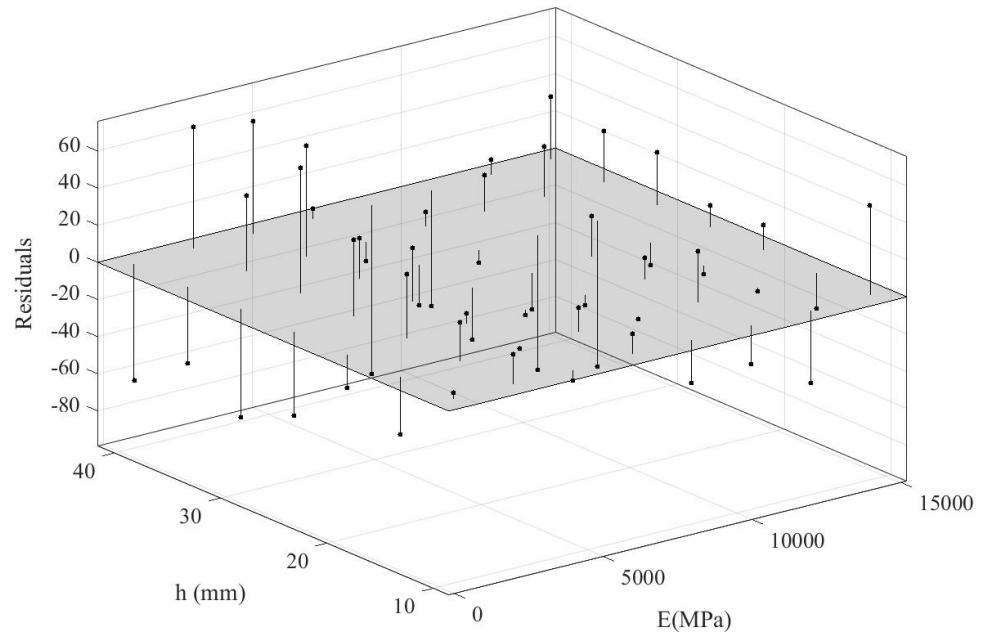

(b) Residual plot

Figure 12. The relationship between peak acceleration and different influence factors

Figure 12(a) shows the MAP diagram of the relationship between peak acceleration and different influence factors, and Figure 10(b) shows the residual plot of the fitting curves. As can be seen from Figure 12(b), the points depicted based on the elastic modulus and impact height of elastic half-space as the horizontal axis and the residual value as the vertical axis has no outliers. The points are randomly scattered up and down around a plane with a residual equal to 0, which shows that the fitting of the simulation values is well fitted with the regression surface. The fitting relationship is shown in Formula 6.

$$A = -30.36 + 0.05878E + 16.66h - 2.372\times10^{-6}E^2 + 0.001262Eh - 0.1972h^2 \quad (6)$$

To verify the correctness of the fitting results, 4 different impact height and 4 different elastic modulus are randomly selected to be calculated and simulated. The comparison result is as shown in the Table 2.

Table 2. Comparison between the simulation results and the calculation results

Impact height h (mm)	Elastic modulus E (MPa)	Theoretical value (m/s^2)	Interpolation (m/s^2)	Simulation value (m/s^2)	Error (%)	
					Interpolation	Simulation value
16	3500	597.1	433.1	464.9	27.1	22.1
24	7500	1060.4	790.5	903.9	25.5	14.8
32	10500	1446.9	1080.5	1132.4	25.3	21.7
40	15500	1956.9	1444.2	1587.7	26.2	18.9

As can be seen from Table 2, in the impact process combined with four randomly selected impact height and elastic modulus, all the theoretical values obtained from Formulas (1)-(4) are higher than the interpolation and simulation values and the error is around 25%, meeting the engineering requirements. So it can be used in the calculation of dynamic process of a particular steel wheel, which 600 mm long and 81.1 kg, impacting the elastic half-space.

4. Conclusion

1. A finite element model of elastic half-space impacted by steel wheel is established. According to Hertz contact theory and Palmgren empirical formula, it is confirmed that the main influencing factors of the dynamic response of impact process include the length and mass of steel wheel, the impact height, elastic modulus and Poisson's ratio of elastic half-space. The process of impacting the elastic half-space with elastic modulus of 2 500 MPa, 6 500 MPa and Poisson's ratio of 0.3 by the same steel wheel falling at heights of 10 mm, 20 mm and 30 mm is simulated respectively. The results show that the kinematic recovery coefficient of each impact process is consistent. The error between the simulation results of peak impact force and the calculation results of peak impact force by Formula (3) is less than 10%, and the error between the simulation results of peak acceleration and the calculation results of peak acceleration by Formula (4) is less than 20%, meeting the engineering requirements. So the finite element model is proved to be reasonable, and its simulation results can be used in the analysis of dynamic process of steel wheel impacting the elastic half-space;
2. The process of elastic half-space that the elastic modulus changes from 500 MPa to 8 500 MPa and the Poisson's rate changes from 0.2 to 0.4 impacted by steel wheel from the height of 10 mm and 30 mm is simulated. The simulation result shows that when the elastic modulus is smaller than 2 500 MPa, Poisson's ratio change has a great effect on impact duration and little effect on peak acceleration. However, when the elastic modulus is greater than 2 500 MPa, Poisson's ratio change has no effect on impact duration and no significant effect on peak acceleration;
3. The process of elastic half-space that the elastic modulus changes from 500 MPa to 14 500 MPa and the Poisson's rate is 0.3 impacted by steel wheel from the height from 10-40 mm is simulated. The results show that when the steel wheel impacted the elastic half-space at the same height, the peak acceleration increases with the increase of elastic modulus, and presents a quadratic nonlinear relationship;
4. Based on the simulation results, the elastic modulus of elastic half-space and the impact height of steel wheel is taken as the independent variables and the peak acceleration of steel wheel as the dependent variable, the MAP diagram and fitting formula of the relationship between peak acceleration and different influencing factors is made. Four different impact height and four different elastic modulus are randomly selected to be calculated and simulated, which shows that all the theoretical values are higher than the interpolation and simulation values and the error is around 25%, meeting the engineering requirements. So it can be used in the calculation of dynamic process of a particular steel wheel, which 600 mm long and 81.1 kg, impacting the elastic half-space.

References

[1] Li, H. Impact and rebound of thin-walled structures on a rigid target. Hangzhou: Zhejiang University, 2018.

[2] Cao, Z.P., Liang, N.X., Cao, Y.W. Method for continuously testing pavement structural composite modulus. Journal of Harbin Institute of Technology, 2020, 52(3): 90-98.

[3] Chen, W.Z., Wang, B.W., Hu, X.Y. Acceleration signal processing by time domain integration. Journal of Huazhong University of Science and Technology (Natural Science Edition), 2010, 38(1): 1-4.

[4] Ismail, A., Zenasni, R., Amine, K.S.M., Ahmed, S. Effect of tempering temperature on the mechanical properties and microstructure of low alloy Steel DIN 41Cr4. Jordan Journal of Mechanical and Industrial Engineering, 2019, 13(1): 9-14.

[5] Wang, X.P., Lin, W.Z., Liu, G., Ma, S.J., Tong, R.T. Advance in impact force model research with evolution of newton restitution coefficient. Mechanical

Science and Technology for Aerospace Engineering, 2020, 39(10): 1526-1533.

[6] Machado, M., Moreira, P., Flores, P., Lankarani, H.M. Compliant contact force models in multibody dynamics: Evolution of the Hertz contact theory. Mechanism and Machine Theory, 2012, 53: 99-121.

[7] Stronge, W.J. Impact mechanics. Cambridge: Cambridge University Press, 2000.

[8] Wagg, D.J. A note on coefficient of restitution models including the effects of impact induced vibration. Journal of Sound and Vibration, 2007, 300: 1071-1078.

[9] Ivanov, A.P. Energetics of a collision with friction. Journal of Applied Mathematics and Mechanics, 1992, 564: 527-534.

[10] Yao, W.L., Yue, R. Advance in controversial restitution coefficient study for impact problems. Journal of Vibration and Shock, 2015, 34(19): 43-48.

[11] Dong, F.X., Hong, J.Z. Review of impact problem for dynamics of multibody system. Advances in Mechanics, 2009, 39(3): 352-359.

[12] Zhang, J.Z. The suitable situation of formula of coefficient of restitution for general rigid body of motion. Mechanics in Engineering, 2010, 32(3): 116-117.

[13] Ye, Y., Zeng, Y.W., Peng, Z.X., Sun, H.W., Ren, S.L., Wang, K. Experimental study on normal coefficient of restitution and fragmenting of marble spheres. Chinese Journal of Rock Mechanics and Engineering, 2018, 37(7): 1680-1690.

[14] Bi, R., Li, S.Y., Liu, G., Ren, J.X., Song, Y.J., Tsai, S.B. Investigating the effect of preimpact energy dissipation on coefficient of restitution regarding the slope-boulder interaction. Advances in Civil Engineering, 2021, 2021: 1-23.

[15] Johnson, K.L. Contact Mechanics. Cambridge: Cambridge University Press, 1985.

[16] Xu, G.H., Shen, W.C., Liu, Y.J. Measurement and calculation of impact stress in ball mills. Journal of Tsinghua University (Science and Technology), 1996, 36(4): 87-92.

[17] Li, L.Y., Thornton, C., Wu, C.Y. Impact behaviour of elastoplastic spheres with a rigid wall. Journal of Mechanical Engineering Science, 2000, 214(8), 1107-1114.

[18] Yin, M.G., Thibaut, C., Wang, L.W., Nelias, D., Zhu, M.H., Cai, Z.B. Impact-sliding wear response of 2.25Cr1Mo steel tubes: Experimental and semi-analytical method. Friction, 2021, 2021:1-19.

[19] Cândida, M.P., Amílcar, L.R., Jorge, A.A. A critical overview of internal and external cylinder contact force models. Nonlinear Dynamics, 2011, 63(4): 681-697.

[20] Lankarani, H.M., Nikravesh, P.E. Continuous contact force models for impact analysis in multibody systems. Nonlinear Dynamics, 1994,5(2): 193-207.

[21] Li, Y.G., Chen, T.N., Wang, X.P., Yu, K.P. Theoretical analysis and numerical simulation for impact noise due to collision of two cylinders. Journal of Vibration and Shock, 2014, 33(15): 162-173.

[22] Kachapi, S.H.H. Nonlinear vibration and frequency analysis of functionally graded- piezoelectric cylindrical nano-shell with surface elasticity. Jordan Journal of Mechanical and Industrial Engineering, 2018, 12(4): 293-312.

[23] Liu, B.Y. Specifications for design of highway asphalt pavement. Beijing: China Communications Press, 2017.

JJMIE

Volume 16, Number 1, January. 2022
ISSN 1995-6665
Pages 63 - 72

Jordan Journal of Mechanical and Industrial Engineering

Application of Direction Vector Model of Multibody System Dynamics in Sports Posture Positioning

Feng Liu*

College of physical Education, Henan University, Kaifeng 475000, China

Received 14 July 2021 *Accepted 22 December 2021*

Abstract

Conventional sports posture positioning method, using convolution neural network, only uses Fast RCNN algorithm to locate sports posture, which leads to low accuracy of sports posture positioning. This paper proposes the application of multi-body system dynamic direction vector model in sports posture positioning. In this paper, the direction vector model of multi-body system dynamics is used to design the constraint of direction vector property and hinge between objects, calculate the activity of objects, and establish the motion posture model; The four coordinate systems of image, pixel, camera and world are established, and the spatial relationship of the four coordinate systems is calculated to complete the spatial transformation of each coordinate system; The gray transformation is carried out for the image to obtain an image. Gray human body image is used to obtain the target image and extract the contour of human body region; Similar to Fast RCNN algorithm and multi-scale context information are used to form a multi scale convolution neural network to locate the sports posture. The experimental results show that positioning sports posture has better positioning effect, higher positioning accuracy and faster positioning efficiency.

Keywords: Multi Body System Dynamics; Direction Vector Model; Athletic Sports; Attitude Positioning;

1. Introduction

In the process of training, athletes need to achieve the correct posture standard and the correct position of force. In addition, in the process of sports, the winning and losing of sports also need to be judged according to the posture of the athletes. It is difficult to accurately judge the sports posture of the athletes, especially football and basketball, etc. at the speed of speed the sports events with speed endurance and endurance are the most important. With the development of the times, the competition of these kinds of events is becoming more and more intense, the conversion of attack and defense becomes faster and faster. It is difficult to judge the athletes' movement posture and correct the athletes' movements by the coach naked eye. In the course of the competition, it is difficult for the referee to judge whether the athletes violate the rules of the competition according to the competition process the image, affect the result of sports match judgment. Therefore, some experts put forward the word "posture orientation" to improve the training efficiency, reduce the physical injury of athletes, ensure the fair competition, and have far-reaching significance for improving the teaching and competitive level of sports. Therefore, the orientation of sports posture has become a hot topic in the relevant departments.

With the development of sports posture positioning method, the camera and computer technology are combined. In the training and competition field, more than two cameras are used to locate the whole game image. According to the whole game image, the players' moving position, time and other data are accurately determined, and these data are automatically converted into moving speed and distance, so as to locate the athletes' Sports posture [1, 2]. Sup (Sport universal) is used, the software includes two parts: analysis software and advanced camera [3]. The advanced camera has the function of thermal imaging. It only needs to install the advanced camera in the training and competition field to record the whole process of the competition. Through the analysis software decomposition in sup, we can get the athletes' movement data and estimate the athletes' position, each set of sup at least reaches several million, and needs special personnel to debug and install, which leads to the problem of large-scale promotion of the software. The emitter and upper computer are located safely on the athletes [4]. According to the athletes' sports video captured by the camera, the sports field is gridded, the first rectangular coordinate system is established, and the reference node is designed. The transmitter and upper computer on the athletes are determined, and the

* Corresponding author e-mail: liufeng810107@163.com.

constant values of RF parameters and signal transmission are determined. The distance and seat distance between the athletes' position and each reference node are calculated. However, this method needs to constantly determine the position of the athletes, needs a lot of time to calculate the position of the athletes, and affects the positioning accuracy of the athletes' Sports posture. Taking volleyball players as an example, we collected volleyball players' sports videos, used the background difference theory to obtain the regional position of the players' Sports posture, and divided the volleyball players' sports videos into the color histogram and the gradient direction histogram according to the color and video gradient, and fused the two histograms to determine the regional position of the players and calculate the posture [5]. The weight of the target region feature is used to get the athletes' Sports posture and background feature components, so as to locate the athletes' Sports posture. This method needs less calculation, but it has the problem of low reliability of posture target. Literature uses the average frame difference technology to locate the athletes' Sports posture. It also uses the average frame difference technology to detect the athletes' region in the video based on the athletes' sports video. According to the characteristics of the distribution of the mark points, it uses the horizontal projection theory to separate the mark points and non mark points in the athletes' region. Combined with the distribution law of the mark points, it uses the K-means clustering algorithm. This method is relatively simple, but it has the problem of low positioning accuracy.

In view of the problems in the above research, multi-body system dynamics is introduced to locate the coordinates of athletes in the process of sports, study the rules of athletes' sports, and then combine with the direction vector. By using the compatibility of proper direction and the characteristics of easy programming, the direction vector model of multi-body system dynamics is established to locate the athletes' Sports posture, and the multi-body system dynamics is proposed the application of mechanical direction vector model in sports posture positioning.

2. Sports Posture Positioning Method Based on Direction Vector Model of Multi Body System Dynamics

2.1. Motion attitude model based on direction vector model of multibody system dynamics

Suppose that the dynamics of multi-body system is a multi-body system composed of n_i objects and n_j hinges connected with each other, so the set of objects $B=\{b_1,b_2,\cdots,b_i,\cdots,b_n\}$ is established, where $i=1,2,\cdots,n$, and $j=1,2,\cdots,n$ denote the number of hinges. At this time, select the center of mass b_i in the object set B, take the inertia of the rigid body as the main axis, establish the connected base coordinate system $b_i e_1^{(i)} e_2^{(i)} e_3^{(i)}$, the position vector $r^{(i)}=\left[r_1^{(i)} r_2^{(i)} r_3^{(i)}\right]$ of the origin b_i relative to the inertia base oe1, then the kinetic energy E_i of the object set B is:

$$E_i=\frac{1}{2}\int_E p\dot{r}_p^{(i)T}\dot{r}_p^{(i)}dE=\frac{1}{2}\dot{r}^{(i)T}m_i\dot{r}^{(i)}+\frac{1}{2}\sum_{j=1}^{3}\dot{e}_j^{(i)T}\Pi_j\dot{e}_j^{(i)}=\frac{1}{2}\dot{q}^{(i)T}M_i\dot{q}^{(i)} \tag{1}$$

In Formula (1), E is the potential energy matrix of object set B, and $E=V\left(q^{(i)}\right)$; dE is the integral of potential energy matrix E; $\dot{r}_p^{(i)}=\dot{r}^{(i)}+\sum_{j=1}^{3}\dot{e}_j^{(i)}$ is the absolute velocity of any point p on object set B; $\dot{q}^{(i)}=\left[\dot{r}^{(i)T},\dot{e}^{(i)T}\right]^T$, $e^{(i)}=\left[e_1^{(i)T}e_2^{(i)T}e_3^{(i)T}\right]$, $e_j^{(i)}=\left[e_{1j}^{(i)}e_{2j}^{(i)}e_{3j}^{(i)}\right]$, $j=1,2,3$, $M_i=diag\left(m_iE,\Pi_1^{(i)}E,\Pi_2^{(i)}E,\Pi_3^{(i)}E\right)$, $m_i=\int_E pdE,\Pi_j^{(i)}=\int_E pdE$ [6]. In this case, the constraints on the multi rigid body system composed of n_i objects and n_j joints can be divided into two parts: the constraints on the properties of direction vector and the constraints on the joints between objects, in the formula, the direction vector property constraint ψ is:

$$\psi^{(i)}=\begin{bmatrix}\frac{1}{2}\left(e_1^{(i)T}e_1^{(i)}-1\right)\\ \frac{1}{2}\left(e_2^{(i)T}e_2^{(i)}-1\right)\\ \frac{1}{2}\left(e_3^{(i)T}e_3^{(i)}-1\right)\\ e_1^{(i)T}e_2^{(i)}\\ e_1^{(i)T}e_3^{(i)}\\ e_2^{(i)T}e_3^{(i)}\end{bmatrix} \tag{2}$$

The constraints of joints between objects are more than the constraints of directional vector properties, which can be roughly divided into the following: (1) Suppose that any vector a_i and a_j on the joints between objects are perpendicular, $\psi\left(a_i,a_j\right)=a_i^Ta_j=0$; (2) Assuming that the

relative vector of any two points on the hinge between objects is φ_{ij}, $\psi\left(a_i,\varphi_{ij}\right)=a_i^T\varphi_{ij}=0$ when the vector a_i is perpendicular to φ_{ij}; (3) Suppose that the hinge points between objects are d_i and d_j, when two hinge points d_i and d_j coincide, $\psi\left(d_i,d_j\right)=r_p^{(j)}-r_p^{(i)}=0$; When the distance between two hinge points d_i and d_j remains unchanged, $\psi\left(d_i,d_j\right)=\varphi_{ij}^T\varphi_{ij}-b^2=0$; (4) It is assumed that there is a consolidated coordinate system $\left(d_if_ig_ih_i,d_jf_jg_jh_j\right)$ between the two hinge points d_i and d_j, where $f_ig_ih_i$ and $f_jg_jh_j$ both represent parallel vectors, $\psi\left(h_i,h_j\right)=\begin{bmatrix}\psi\left[f_i,h_j\right]\\ \psi\left[g_i,h_j\right]\end{bmatrix}=0$ when h_i and h_j are parallel to each other; $\psi\left(h_i,\varphi_{ij}\right)=\begin{bmatrix}\psi\left[f_i,\varphi_{ij}\right]\\ \psi\left[g_i,\varphi_{ij}\right]\end{bmatrix}=0$ when h_i and φ_{ij} are parallel.

By substituting the above constraints into Formula (1), Formula (1) can be regarded as the direction vector model of multibody system dynamics. At this time, the object and the hinge between the objects in the above calculation process represent the athlete's limbs and trunk respectively. At this time, the direction vector model of multi-body system dynamics shown in Formula (1) is the athlete's motion posture model.

2.2. Determine camera coordinate system

Before camera calibration, the camera model must be established. According to the simplest pinhole imaging principle, the light in the scene passes through the camera aperture, and then hits the CCD sensor on the back of the camera to get the corresponding image [7]. Therefore, four coordinate systems are established as follows: (1) Image coordinate system $\left(x,y\right)$; (2) Pixel coordinate system $\left(o,v\right)$; (3) Camera coordinate system $\left(X_1,Y_1,Z_1\right)$; (4) World coordinate system $\left(X_2,Y_2,Z_2\right)$. Calculate the spatial relationship of the four coordinate systems, and complete the spatial transformation of each coordinate system.

The spatial relationship between image coordinate system $\left(x,y\right)$ and pixel coordinate system $\left(o,v\right)$. The position relationship between image coordinate system and pixel coordinate system can be divided into vertical and non-vertical. When the two coordinate axes are perpendicular to each other, there is a relationship between coordinate systems as shown in the following formula:

$$\begin{cases}o=\dfrac{x}{d_x}+o_0\\ v=\dfrac{y}{d_y}+v_0\end{cases}\tag{3}$$

In Formula (3), d_x represents the actual size of the pixel in the x-axis direction; d_y represents the actual size of the pixel in the y-axis direction; $\left(o_0,v_0\right)$ represents a coordinate position in the pixel coordinate system $\left(o,v\right)$ [8]. In general, the two axes of the position relationship between the image coordinate system and the pixel coordinate system are not perpendicular to each other, and there is a certain angle θ, then:

$$\begin{aligned}o&=o_0+\frac{x_d}{d_x}-\frac{y_d cot\theta}{d_x}\\ v&=v_0+\frac{y_d}{d_y sin\theta}\end{aligned}\tag{4}$$

The spatial relationship between camera coordinate system $\left(X_1,Y_1,Z_1\right)$ and image coordinate system $\left(x,y\right)$. The X_1 and Y_1 axes of the camera coordinate system should be parallel to the x and y axes of the image coordinate system, while the Z_1 axis of the camera coordinate system is the optical axis. According to the similarity principle of triangles, it can be concluded that:

$$Z_1 \cdot \begin{bmatrix} x \\ y \\ 1 \end{bmatrix} = \begin{bmatrix} f & 0 & 0 & 0 \\ 0 & f & 0 & 0 \\ 0 & 0 & 1 & 0 \end{bmatrix} \cdot \begin{bmatrix} X_1 \\ Y_1 \\ Z_1 \\ 1 \end{bmatrix} \quad (5)$$

The spatial relationship between camera coordinate system (X_1, Y_1, Z_1) and world coordinate system (X_2, Y_2, Z_2). The world coordinate system will associate the image coordinate system, pixel coordinate system, camera coordinate system with the space object. According to the transformation principle of the space coordinate system, the following relationship can be obtained:

$$\begin{bmatrix} X_1 \\ Y_1 \\ Z_1 \end{bmatrix} = \begin{bmatrix} T & \varepsilon \\ 0 & 1 \end{bmatrix} \cdot \begin{bmatrix} X_2 \\ Y_2 \\ Z_2 \\ 1 \end{bmatrix} \quad (6)$$

In Formula (6), T represents the rotation matrix, which belongs to the orthogonal unit matrix with the size of 3 * 3; ε represents the three-dimensional vector [9]. By synthesizing the above four calculation formulas, the relationship between the four coordinate systems is obtained, so as to obtain the coordinate system of the equipment in the process of athletes' sports, determine the coordinates of the camera position of the athletes, obtain the target image, and extract the contour of the human body region.

2.3. Extracting the contour of human body region from the target image

According to the collected sports video sequence, we need to select the image of the motion posture to be located as the target image of the motion posture positioning. Therefore, on the basis of the determined position of the camera to capture the athletes' Sports posture image, the gray-scale transformation of the image is carried out, and a gray-scale human body image is obtained. Then m consecutive image sequences $f_t(t = 1, 2, \cdots, m)$ are selected from the video data. Suppose that the gray value of a pixel (x, y) on the j-th image is $G_j(x, y)$, then for the m-th image sequence, the average gray value of the pixel (x, y) is:

$$\bar{G}_j(x, y) = \frac{1}{m} \sum_{j=1}^{m} G_j(x, y) \quad (7)$$

Using Formula (7), the average gray values $\bar{G}_1(x, y)$, $\bar{G}_2(x, y)$, ⋯, $\bar{G}_m(x, y)$ of m image sequences on each pixel point are calculated in turn. Then the new image composed of pixels with average gray values is the calculated background image.

After obtaining the target image and the background image, we can use the background difference method to calculate the difference between the target image and the background image, so as to obtain the contour of the human body. Set a frame containing the human body selected from the video data to $H(x, y)$ after gray conversion, and the obtained background image is $G(x, y)$, and the threshold value is D, then:

$$\begin{cases} (x, y) \in \textit{target if } |H(x, y) - G(x, y)| > D \\ (x, y) \in \textit{background} \qquad \textit{others} \end{cases} \quad (8)$$

Usually, there are isolated noise points of different sizes in the human body region obtained by background difference method, which will interfere with the subsequent processing and affect the effect of human contour extraction. The commonly used solution is to use median filter to denoise the preliminary human body region image [10]. Median filtering uses the median value of the gray value of all pixels in the neighborhood window of a pixel to replace the gray value of the pixel, which has a good effect on eliminating the noise points in the extracted human body region image [11].

Some human body region images will appear cavity, fracture or loss of some parts of the human body during processing [12]. Therefore, it needs to be repaired. The usual method is to use the image morphology methods such as dilation operation and erosion operation to deal with the unsatisfactory human body region image. Firstly, the denoised human body image is expanded to fill the small holes, then:

$$X \oplus Y = \{u \in \gamma^2, u = x + g, x \in X\} \quad (9)$$

In Formula (9), γ^2 represents the two-dimensional space of the human body region image; u represents a point in the human body region image; x represents any point in the pixel (x, y), X represents the set of pixel (x, y), and g represents the hole position in the background image [13]. Next, the image of human body region is corroded to eliminate the noise of small area, then:

$$X \ominus Y = \{u \in \gamma^2, u + g \in X\} \quad (10)$$

After the human body region image is restored by morphological method, it is binarized:

$$g(x,y)=\begin{cases}0 & spot(x,y)\in Contour\ area\\ 1 & spot(x,y)\notin Contour\ area\end{cases} \quad (11)$$

By synthesizing the Formula (5), the contour extraction of the positioning target is completed, and the clarity of the extracted contour can be guaranteed. At this time, only according to the movement posture model, we can locate the posture of athletes in sports.

2.4. Positioning the posture of sports

In this study, the multi-scale convolution neural network will be used to locate the sports posture based on the movement posture model. The multi-scale convolutional neural network is composed of a candidate frame generation sub network and a positioning sub network [14]. The candidate frame can be generated at different levels in the sub network by using a small positioning network to generate candidate frames of different scales [15]. Therefore, in the positioning sub network, the candidate box output from the sub network is used as the input. In the multi-scale convolution neural network algorithm, the candidate frame is generated into a sub network. In four convolution layers with different depths, the candidate frame is generated for the target. Each small network only trains the training samples within a certain scale, ignoring the contribution of the target outside the scale to the small network. Assume that the whole training set is $S=\{S_1,S_2,\cdots,S_k\}$, and S_k is the sample set contained in scale k, which only contributes to the k-th small location network. The loss function of the network is defined as follows:

$$L(\eta)=\sum_{k=1}^{4}\sum_{i\in S_k} w_k\left(l\left(I(X),U\right)+\delta[U=1]l(q,\tilde{q})\right) \quad (12)$$

In Formula (12), $L(\eta)$ is the loss of multi-scale convolutional neural network; η is the learning parameter of the network; w_k is the weight of k range of each scale; l_1 is the classification loss; $I(X)$ is a function of predicting classification probability and the real label U; l_2 is the regression loss of rectangular box, which is a function of positive sample prediction box $\tilde{q}$ and real box q; δ is the weight parameter representing the regression loss of positive sample rectangle [16].

According to the multi-scale convolutional neural network structure selected above, the network loss function calculation formula is determined, and the Fast RCNN algorithm is used to locate the final sports posture. The convolution layer backbone is shared with the convolution layer of the candidate frame generation sub network, which only extracts the features used to locate the motion posture in the conv4-3 layer of the convolution backbone, and the definition of the loss function is the same as that of the Fast RCNN algorithm, which is divided into classification loss and rectangular frame regression loss [17]. Different from Fast RCNN algorithm, deconvolution operation and single scale context information extraction strategy are used in sports posture positioning sub network.

Due to the great difference of sports posture, the scale span of sports posture to be located is large. In the process of sports, many athletes are far away from the sports field monitoring, resulting in their scale in the image area is very small. Suppose a pedestrian target with a width of 32 pixels, its characteristic width in the fourth convolution layer is only eight times of the original 1. Only 4 pixels are occupied in the feature map [18]. At this time, ROI-pooling will introduce large feature error. Therefore, the feature graph is up sampled to avoid the introduction of additional parameters and computational complexity.

Based on the above analysis, according to the extracted sports posture positioning target and the analysis results of sports posture model, in the selected multi-scale convolution neural network, multi-scale extraction context information is used to help multi-scale convolution neural network locate sports posture [19]. Because the “multi-scale” in the multi-scale convolution neural network algorithm is mainly reflected in the candidate frame generation sub network, but in the target positioning sub network, it only extracts features in one convolution network layer, which ignores a very important concept of deep convolution network, that is, the features of different convolution layers express different levels of information in the image.

The convolution layer of deep convolution neural network uses the learned template to carry out linear transformation on the pixels in the input image in the form of sliding window. From the perspective of network structure, multiple convolution layers are connected in a cascade way, that is, the template is used to continuously carry out linear transformation on the transformed image [20]. After visualizing these different levels of features, we can get the conclusion that the shallow convolution layer output generally contains more local edge information, which is not robust to noise, while the deep convolution layer output contains semantic information about the whole image [21, 22]. Although many details are ignored, the semantic judgment of the target is relatively robust. These features of different levels are simply connected together. For the convoluted feature map of different levels, the corresponding feature map area of the sample is found in the feature map, and then the feature of the area is extracted by ROI-pooling method, and these features are stacked together by

the connection layer, so that the target is easy to understand A convolution layer is used to simplify the parameters of these features, and finally the full connection layer is used for classification and rectangular box regression. So far, the positioning of sports posture is completed.

Definitions of all the variables in the text are shown in Table 1.

Table 1. Variable definition

Symbol abbreviation	Meaning
n_i	objects
n_j	hinges
B	the set of objects
i, j	the number of hinges
b_i	the center of mass in the object set B
$b_i e_1^{(i)} e_2^{(i)} e_3^{(i)}$	the base coordinate system
$r^{(i)}$	the position vector relative to the inertial base
E	the potential energy matrix of the target set
dE	the integrals of the potential energy matrix
p	any point in the collection B
$\dot{r}_p^{(i)}$	the absolute speed of any point p
ψ	the property constraint for the direction vector
a_i , a_j	any arbitrary vector of the nodes between objects
φ_{ij}	relative vector of any two points on the hinge between objects
d_i , d_j	the hinge points between objects
$f_i g_i h_i$, $f_j g_j h_j$	the parallel vectors between the two hinge points d_i and d_j
(x, y)	the image coordinate system
(o, v)	the pixel coordinate system
(X_1, Y_1, Z_1)	the camera coordinate system
(X_2, Y_2, Z_2)	the world coordinate system
d_x	the actual size of the pixel in the x -axis direction
d_y	the actual size of the pixel in the y -axis direction
(o_0, v_0)	the coordinate position in the pixel coordinate system (o, v)
θ	the horizontal and vertical axis angle between image system and pixel system
T	the orthogonal rotation matrix of size 3 * 3
ε	three-dimensional vector
f_t	the serial sequence of continuous images selected from the video data
m	the number of image sequences
$G_j(x, y)$	the gray value of a pixel (x, y) on the j -th image
$\bar{G}_j(x, y)$	the average gray value of the pixel (x, y)
$H(x, y)$	all frame sets after image gray scale conversion selected from the video data
$G(x, y)$	the grayscale-transformed background images
D	the threshold value for the grayscale conversion
γ^2	the two-dimensional space of the human body region image
u	a point in the human body region image
X	the set of pixel (x, y)
g	the hole position in the background
k	ratio scale
S_k	the sample sets trained by proportion in convolutional neural networks
$L(\eta)$	the loss of multi-scale convolutional neural network
η	the learning parameter of the network
w_k	the weight of k range of each scale
l_1	the classification loss
U	the real label
$I(X)$	a function of predicting classification probability and the real label U
$\tilde{q}$	the positive sample prediction box
q	the real box
l_2	the regression loss of rectangular box, which is a function of positive sample prediction box $\tilde{q}$ and real box q
δ	the weight parameter representing the regression loss of positive sample rectangle

3. Experimental Results and Analysis

Three groups of conventional sports posture positioning methods were selected, and EOS C300 Mark 2 high-definition camera was used to collect the far mobilization video of volleyball. Taking the movement posture of volleyball players in sports as the experimental object, the sports posture positioning method based on multi-body system dynamics direction vector model was verified. Compare four groups of sports posture positioning methods, positioning sports posture performance.

3.1. Experimental preparation

According to this experiment, the experimental camera EOS C300 Mark 2 HD camera is shown in Figure 1.

Figure 1. EOS C300 Mark 2 HD camera

The parameters of EOS C300 Mark 2 HD camera are shown in Table 2.

Table 2. Parameters of EOS C300 Mark 2 HD camera

Product configuration		Specifications
Sensor	Type	Super 35mmcmos single chip sensor
	Total prime number	nine million eight hundred and forty thousand
	Effective pixel	eight million eight hundred and fifty thousand
Camera lens	Filter	RGB primary filter
	Bayonet type	EF bayonet
	Support lens	EF LENS, EF cinema lens
Exposure control	Exposure mode	Manual/single automatic aperture/automatic aperture control
	Shutter settings	Speed, angle, clear scan, slow or off
	Aperture setting	Manual setting (you can choose to set in 1/2 or 1/3 or fine display setting)
	ISO sensitivity setting	Iso100*-102400* (extended sensitivity)
	Gain setting	Normal setting (-6 db to 54 db*) Fine setting (can be set in 0.5 dB between -6 db and 54 db)
	ND filter	Built in, electric, 5 density settings (2, 4, 6, 8*, 10*)
Video storage format		CFAST card record video format

Under the condition of EOS C300 Mark 2 high-definition camera parameters as shown in Table 2, the collected volleyball player sports video sequence contains a total of 500 images. From these 500 images, 200 images are selected as training samples and 300 images are selected as test samples. The selected volleyball player sports video sequence image example is shown in Figure 2.

According to the experimental object shown in Figure 2, the four groups of sports posture positioning methods need to be run on the computer to locate the volleyball players' Sports posture. Therefore, the operation environment of the four groups of positioning methods is designed as shown in Table 3.

Figure 2. Example of video sequence image of Volleyball Players

Table 3. Operation environment of four groups of positioning methods

Environment	To configure	Specifications
Hardware environment	Hard disk	500 GB/5400 rpm
	Memory	DDR3 4G
	Processor	Intel Core i5 2.4 GHz processor
	Graphics card	Intel(R) HD Graphics 3000
Software environment	Operating environment	Windows 7, 64 bit operating system
	Development environment	MATLAB language, MATLAB R2012b software

Based on the experimental object selected in this experiment and the designed experimental environment, four groups of sports posture positioning methods are used to locate the volleyball players' Sports posture respectively. The four groups of sports posture positioning methods are compared to locate the volleyball players' Sports posture effect, efficiency and accuracy. The experimental results and experimental process are as follows.

3.2. Experimental result

3.2.1. The first group of experimental results

Four groups of positioning methods are used to locate the volleyball players' movement posture in the video sequence image example of volleyball players as shown in Figure 2, and the positioning results of volleyball players' movement posture are calibrated, so as to judge the four groups of sports posture positioning methods and locate the effect of volleyball players' movement posture. The experimental results are shown in Figure 3.

It can be seen from Figure 3 that the three groups of conventional methods can only locate the movement posture of volleyball players by a large margin, but the positioning range of conventional method 1 is wide, which objectively shows that the positioning accuracy of conventional method 1 is low, and the positioning range of conventional method 2 is wide. Conventional method 1 is small,

which objectively indicates that conventional method 2 has high accuracy in positioning volleyball players' motion posture; Conventional method 3 has deviation in positioning volleyball players' motion posture, when the distance between two players is relatively close, the two players' motion posture will be positioned together, which objectively indicates that conventional method 3 is extremely low in positioning volleyball players' motion posture; However, the research method is limited Positioning the movement posture of volleyball players, as long as the players have movement posture, they will be positioned to the movement posture of volleyball players, and the positioning range is small, so the movement posture of each part of the players can be positioned separately. It can be seen that the research of sports posture positioning method, positioning the athletes of all parts of the movement posture effect is better.

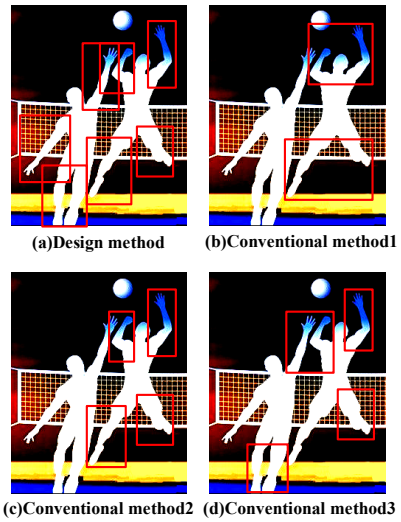

Figure 3. The effect of four groups of methods in positioning volleyball players' movement posture

3.2.2. The second group of experimental results

On the basis of the first group of experiments, the second group of experiments was carried out to calculate the accuracy of the four groups of positioning methods in positioning the movement posture of volleyball players, and to verify the accuracy of the four groups of positioning methods in positioning the movement posture of volleyball players. In this experiment, a total of 300 video sequence images of volleyball players as shown in Figure 2 are selected as the sample data of this group of experiments to test the accuracy of four groups of positioning methods to locate different numbers of volleyball players' movement posture samples. In order to ensure the preciseness of the experiment, the positioning accuracy is recorded every 25 volleyball players' movement posture images, including the first and last experimental values. The experimental results are shown in Table 4.

Table 4. The correct rate of positioning volleyball players' movement posture with four groups of positioning methods

Number of experimental samples	Design method (%)	Conventional method 1 (%)	Conventional method 2 (%)	Conventional method 3 (%)
1 sheet	97.8	94.6	93.6	92.5
25 sheet	97.6	95.1	93.0	92.6
50 sheet	97.0	94.3	93.3	93.0
75 sheet	97.9	94.5	93.5	94.7
100 sheet	97.4	95.0	93.7	92.9
125 sheet	97.5	93.9	93.0	94.0
150 sheet	98.0	94.2	92.9	92.8
175 sheet	97.6	94.9	93.2	94.1
200 sheet	97.7	93.8	93.3	92.7
225 sheet	97.5	94.1	93.5	92.5
250 sheet	98.0	94.5	94.0	93.3
275 sheet	97.3	94.3	94.1	92.8
300 sheet	97.7	94.2	93.2	92.7

It can be seen from Table 4 that the difference between the maximum and minimum values of the conventional method 1 is 1.3%, with an average of 94.4%; The difference between the maximum and minimum values of the conventional method 2 is 1.2%, with an average of 93.4%; The difference between the conventional method 3 and the conventional method 3 is 1.2%. The results show that the difference between the maximum and minimum value of the correct rate of the sample is 2.2%, with an average of 93.1%; The difference between the maximum and minimum value of the correct rate of the sample is 1%, with an average of 97.6%; It can be seen that the correct rate of the sample of the different number of volleyball players is the highest. The differences between the maximum and minimum values were 0.3%, 0.2% and 1.2% smaller than those of the three conventional methods, and the average values were 3.2%, 4.2% and 4.5% smaller than those of the three conventional methods. Therefore, the accuracy of the research method is significantly higher than that of the three conventional methods.

3.2.3. The third group of experimental results

On the basis of the first group and the second group of experiments, the third group of experiments is carried out to calculate the positioning time of the four groups of positioning methods to locate the volleyball players' movement posture and verify the efficiency of the four groups of positioning methods to locate the volleyball players' movement posture. In this experiment, 300 video sequence images of volleyball players as shown in Figure 2 are also selected as the sample data of this group of experiments to test the time for four groups of positioning methods to locate different numbers of samples of volleyball players' movement posture. In order to ensure the preciseness of the experiment, the positioning accuracy is recorded every 25 volleyball players' movement posture images, including the

first and last experimental values. The experimental results are shown in Table 5.

Table 5. Positioning time of volleyball players' movement posture by four groups of positioning methods

Number of experimental samples	Design method (s)	conventional method 1 (s)	conventional method 2 (s)	conventional method 3 (s)
1 sheet	0.62	1.57	1.10	1.05
25 sheet	1.31	2.56	1.75	1.81
50 sheet	1.62	3.40	2.51	2.58
75 sheet	2.35	4.34	2.99	3.28
100 sheet	2.65	5.06	3.35	3.98
125 sheet	3.23	5.99	3.81	4.11
150 sheet	3.75	7.53	4.58	4.92
175 sheet	4.30	8.14	5.35	5.57
200 sheet	4.98	8.96	5.98	6.02
225 sheet	5.57	9.70	6.72	6.97
250 sheet	6.34	10.03	7.12	7.85
275 sheet	6.91	10.94	7.95	8.95
300 sheet	7.89	11.42	8.70	9.87

It can be seen from Table 5 that with the increase of the number of volleyball players' movement posture samples, the positioning experiment increases. Among them, the difference between the maximum and minimum values of routine method 1 is 9.85 s, and the average value is 6.9 s; The difference between the maximum and minimum of the sample time of different number of volleyball players' movement posture is 7.6 s, with an average of 4.8 s; The difference between the maximum and minimum of the sample time of different number of volleyball players' movement posture is 8.82 s, with an average of 5.2 s; The difference between the sample time of different number of volleyball players' movement posture is 8.82 s, with an average of 5.2 s. The difference between the minimum value and the maximum value is 7.27 s, and the average value is 4.0 s. It can be seen that the difference between the maximum and minimum values of different number of volleyball players' movement posture sample time is 2.58 s, 0.33 s, 1.55 s less than the three groups of conventional methods, and the average value is 2.9 s, 0.8 s, 1.2 s less than the three groups of conventional methods. Therefore, the efficiency of the research method is significantly higher than that of the three conventional methods.

Based on the above three groups of experimental results, we can see that the sports posture positioning method has better positioning effect, higher positioning accuracy and faster positioning efficiency.

4. Conclusion

This paper applied a directional vector model for the dynamics of many-body systems. The combination of multi-body system dynamics model and direction vector, constitute a multi-body system dynamics direction vector model, determine the athletes in the process of sports, limbs, trunk and head and other parts, the existence of the movement law and direction. The experimental results show that this method improved the positioning effect of the motor posture, provided with a better positioning accuracy, shortened the positioning time, and provided with a theoretical reference for the coach to accurately judge the movement posture and correct the athlete movements. However, there are still some deficiencies in this research. In the future research, we need to further study the constraint information of joint points in the sports posture positioning method, solve some depth differences, and further improve the positioning accuracy.

References

[1] Zhu Y, Zhang T, Xu S, et al. A calibration method of USBL installation error based on attitude determination. IEEE Transactions on Vehicular Technology, 2020, 69(8): 8317-8328.

[2] Wang D, Liu A, Xia X. New method for airborne SAR image positioning. The Journal of Engineering, 2019, 2019(19): 6021-6023.

[3] Shi B, Zhang F, Yang F, et al. A positioning error compensation method for a mobile measurement system based on plane control. Sensors, 2020, 20(1): 294.

[4] Xu X, Liu X, Zhao B, et al. An extensible positioning system for locating mobile robots in unfamiliar environments. Sensors, 2019, 19(18): 4025.

[5] Zheng Y, Li Q, Wang C, et al. Magnetic-Based positioning system for moving target with feature vector. IEEE Access, 2020, 8: 105472-105483.

[6] Lee M, Szuttor K, Holm C. A computational model for bacterial run-and-tumble motion. The Journal of Chemical Physics, 2019, 150(17): 174111.

[7] Xu H, Yan R. Research on sports action recognition system based on cluster regression and improved ISA deep network. Journal of Intelligent and Fuzzy Systems, 2020, 39(4): 5871-5881.

[8] Amin S M. A new robust combined control system for improving manoeuvrability, lateral stability and rollover prevention of a vehicle. Proceedings of the Institution of Mechanical Engineers, Part K: Journal of Multi-body Dynamics, 2019, 234(1): 198-213.

[9] Sannikova T N, Kholshevnikov K V. The averaged equations of motion in the presence of an inverse-square perturbing acceleration. Astronomy Reports, 2019, 63(5): 420-432.

[10] Al-Solihat M K, Behdinan K. Nonlinear dynamic response and transmissibility of a flexible rotor system mounted on viscoelastic elements. Nonlinear Dynamics, 2019, 97(2): 1581-1600.

[11] Chebly A, Talj R, Charara A. Coupled longitudinal/lateral controllers for autonomous vehicles navigation, with experimental validation. Control Engineering Practice, 2019, 88: 79-96.

[12] Neves R, Sanchez J P. Multifidelity design of low-thrust resonant captures for near-earth asteroids. Journal of Guidance, Control, and Dynamics, 2019, 42(2): 335-346.

[13] Shvetsov I V, Zhelnov D V, Zubarev Y M. On dynamics and control when finishing body parts. IOP Conference Series Materials Science and Engineering, 2019, 65(12): 012048.

[14] Palikhe S, Kim S, Kim J J. Critical success factors and dynamic modeling of construction labour productivity. International Journal of Civil Engineering Transaction a Civil Engineering, 2019, 17(3): 427-442.
[15] Ramesh R S, Fredette L, Singh R. Identification of multi-dimensional elastic and dissipative properties of elastomeric vibration isolators. Mechanical Systems and Signal Processing, 2019, 118: 696-715.
[16] Takao Y, Mori O, Kawaguchi J. Analysis and design of a spacecraft docking system using a deployable boom. Acta Astronautica, 2021, 179: 172-185.
[17] Lin R, Molignini P, Papariello L, et al. MCTDH-X: The multiconfigurational time-dependent Hartree method for indistinguishable particles software. Quantum Science and Technology, 2020, 5(2): 024004 (16pp).
[18] Ghabraei S, Moradi H, Vossoughi G. Investigation of the effect of the added mass fluctuation and lateral vibration absorbers on the vertical nonlinear vibrations of the offshore wind turbine. Nonlinear Dynamics, 2021, 103: 1499-1515.
[19] Yazdankhoo B, Nikpour M, Beigzadeh B, et al. Improvement of operator position prediction in teleoperation systems with time delay: Simulation and experimental studies on Phantom Omni devices. Jordan Journal of Mechanical and Industrial Engineering, 2019, 13(3): 197-205.
[20] Sòria-Perpinyà X, Urrego P, Pereira-Sandoval M, et al. Monitoring the ecological state of a hypertrophic lake (Albufera of València, Spain) using multitemporal Sentinel-2 images. Limnetica, 2019, 38(1): 457-469.
[21] Rogge T, Jones D, Drossel B, et al. Interplay of spatial dynamics and local adaptation shapes species lifetime distributions and species-area relationships. Theoretical Ecology, 2019, 12(4): 437-451.
[22] Verjans M, Schleer P, Griesbach J, et al. Modelling patient dynamics and controller impact analysis for a novel self-stabilizing patient transport aid. IFAC-PapersOnLine, 2019, 51(34): 208-213.

JJMIE

Volume 16, Number 1, January. 2022
ISSN 1995-6665
Pages 73 - 78

Jordan Journal of Mechanical and Industrial Engineering

Theoretical Research of Corn Orientation Device

Liai Pan[1*], Yanli Wu[2]

[1]College of Mechanical and Vehicle Engineering, Changchun University, Jilin 130022, China
[2]Institute of Paddy Field Machinery Technology, Jilin Academy of Agricultural Machinery, Jilin 130021, China

Received 14 July 2021 Accepted 28 December 2021

Abstract

Orientation of corn is an essential step in the corn product processing. Corn processing mainly includes cutting root, tip, segment, and grain, and the whole ear packaging, etc., and at each step, the ear needs to be operated in a straight direction. In this paper, the physical parameters of three kinds of corn have been measured, and combined with the characteristics of corn shape geometry, the corn orientation solutions have been put forward. The corn orientation device has been designed, and its working principle has been introduced. When the primary belt speed was 1.426 m/s, all of corn can come off the belt. In order to ensure the requirements of corn processing technology, the orientation device can solve the following problems. When the corn was transmitted in the front of corn small diameter, corn orientation device could make the corn flip in the former of corn big diameter. The corn was transmitted in the front of corn big diameter; corn orientation device keeps its original direction remains the same.

Keywords: corn; orientation device; physical parameters; the primary belt speed;

Name

L_1	length of swinging rod, m	L	length of corn, m
L_3	the length between gravity of the swinging rod and point A, m	F_{AX}	the stress what swinging rod at point A was in horizontal, N
F_{AY}	the stress what swinging rod at point A was in vertical direction, N	F_{BX}	the stress what swinging rod at point B was in horizontal direction, N;
F_{BY}	the stress what swinging rod at point B was in vertical direction, N;	G_1	the gravity of the swinging rod, N
α	angle between swinging rod and the vertical direction, °	L_4	length between corn centroid and the big diameter end, m
F_{bX}	the stress what corn in point B was in horizontal direction, N	F_{bY}	the stress what corn in point B was in vertical direction, N
F_{cX}	the stress what point C was in horizontal directions, N;	F_{cY}	the stress what point C was in vertical directions, N;
β	angle between corn and horizontal plane, °	m_1	the mass of the swinging rod, kg
m_2	the mass of corn, kg	P_0	momentum of collision of corn and swinging rod, N·m
v_0	the primary belt speed, m/s	J	the rotational inertia of swinging rod
ω	angular velocity after collision of swinging rod	h_1	center height of gravity of swinging rod from natural state to graphic state, m
h_2	height of the focus from corn ever collide with the swinging rod to chart the critical state, m		

1. Introduction

Fruit and vegetable classification system is an important part of fruit and vegetable commercialization treatment after picking. It can reduce the production cost of fruit and vegetable storage, packaging, processing and so on. It plays an important role in increasing farmers' economic income and improving enterprises' economic benefits. In the corn grading system and production process, it is imperative to study corn ear orientation. Many institutions have carried out research on the directional mechanism of fruits and vegetables. Such as, in 2008, in Nanjing Forestry University, Huang et al. researched that in apple automatic grading production line, an automatic orientation system has been installed. It can make the apple stem in a vertical position, and implemented apple's direction [1]. It was composed of apple transportation system, automatic orientation trolley, computer visual control system and grading execution equipment. The grading of apple was judged according to the national standards and the location information of apples was confirmed. By computer recognition control system, the grading of apples was completed. In Xinjiang Agricultural University, a research study demonstrated that the automatic orientation device of apricot, it was through the two-conveyor belt of apricot to realize the direction [2, 3]. It was reported that in South China University of Technology, the orientation device of automatic pencil sharpener was studied, and the pencil sharpener automate assembly was made [4, 5]. And there's some literature that shows that in the analysis of the directional device, the theory of position degrees of freedom

* Corresponding author e-mail: 43511252@qq.com.

and gesture coefficient theory respectively were put forward [6].

To sum up, in the paper, the study of corn ear orientation device was proposed to better solve the problems of corn classification and processing.

2. Physical Parameters Experiment of Corn

Physical parameters of corn include appearance size, quality of corn. They are important parameters, which determine the scheme and structure of the corn orientation device.

2.1. Experimental instruments and materials

Experimental instruments: vernier caliper and ruler;

Experimental materials: three kinds of fresh corns including sweet 6, jin cui wang and Heji waxy 3 with widely planted area in Jilin province. (These are 3 kinds of corns.)

2.2. Experimental method

In this paper, 50 ears of each corn ear were taken for measurement. Their big diameter, small diameter, length and quality have been measured. Because the small diameter of the corn at the top end is too small, and the value changes very big, the section diameter was taken the top 10 mm distance from top end. Length of corn didn't include the length of corn handle. Each product was measured three times and took its average as the measured results [7].

2.3. Experimental results

In the paper, measurement results of three kinds of corn were analyzed. Extreme value range of length, big diameter, small diameter and quality of corn was as shown in Table 1. Distribution table of length, big diameter, small diameter and quality of corn was as shown in Table 2.

In Table 1, the variation range of corn appearance size and the mass were illustrated. In Table 2, the corn with big diameter between 46 and 58 mm was 85% of the total corn. The corn with small diameter in the range of 34-40 mm was 85% of the total corn. Corn with length in the 170-200 mm was 87% of the total corn. The corn in mass of 200-230 g was for 87% of the total corn. These four parameters are the basis for designing corn orientation device and building entity model of corn. Therefore, the establishment of mathematical model among diameter, diameter, mass and length has a certain guiding significance for the design and research of the corn orientation device.

Table 1. Extreme value table of appearance size and the mass of corn

Project	Big diameter (mm)	Small diameter (mm)	Length (mm)	The mass of corn (g)
Maximum value	61.7	41.5	218.7	238.7
Minimum value	39.1	31.2	161.4	181.4

3. Structure and Working Principle of Corn Orientation Device

Corn orientation is an important step in corn grading. According to the physical parameters of corn, the structure of corn orientation device was designed and its working principle was described in detail.

3.1. Structure of corn orientation device

Corn orientation device was mainly composed of two belts and a swinging rod mechanism. The swinging rod mechanism was the core. Three-dimensional modeling diagram is shown in Figure 1.

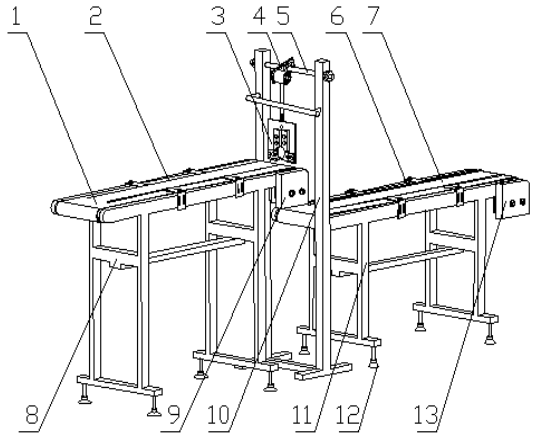

Figure 1. Three-dimensional modeling diagram of corn orientation device

1. primary belt; 2. guide bar of primary belt; 3. swinging rod; 4. swinging shaft; 5. beam; 6. guide bar of auxiliary belt; 7. auxiliary belt; 8. the primary belt frame; 9. primary belt motor; 10. swinging rod frame; 11. the auxiliary belt frame; 12. supporting foot of the belt frame;13. auxiliary belt motor

Table 2. Distribution table of appearance size and quality of corn

No	Big diameter		Small diameter		Length of corn		Quality	
	Value range (mm)	Proportion (%)	Value range (mm)	Proportion (%)	Value range (mm)	Proportion (%)	Value range (g)	Proportion (%)
1	38-42	1	30-32	1	160-170	6	180-190	1
2	42-46	5	32-34	6	170-180	12	190-200	6
3	46-50	12	34-36	13	180-190	38	200-210	13
4	50-54	39	36-38	42	190-200	37	210-220	36
5	54-58	34	38-40	30	200-210	5	220-230	38
6	58-62	9	40-42	8	210-220	2	230-240	6

Note: Proportion is the ratio of corn with different parameters to the total amount of corn. Such as corn diameter value in the 38-42 range of corn accounted for 1%.

(1) Guide bar

Figure 1 shows, the guide bar (2) (6) was fixed belt rack to make the corn motion on the belt adjusted for the axial and horizontal velocity in the same direction. Guide bar. It's the structure that is shown in Figure 2.

(2) Swinging rod

Figure 1 shows, the role of the Swinging rod (3) was to connect beam and support beam. It consisted of a terminal with a threaded shaft and with a notch plate welding, is shown in Figure 3.

(3) Primary belt

Figure 1 shows, the role of primary belt (1) was for swinging rod institutions conveying corn grain, and make corn grain out of the primary belt.

(4) Auxiliary belt

Figure 1 shows, the role of auxiliary belt (7) was to help the corn orientation and down a workstation.

(5) Swinging rod frame

Figure 1 shows, swing rod frame (10) has two roles, one was the fixed beam; The other was to use gear lever of the welding rod placed in the swing swinging frame consumption of energy, to make the swinging rod to rest as soon as possible, for the next downstream.

(6) Swing rod

Figure 1 shows, swinging rod (3) was the key to achieve corn orientation. It consists of a total of five plates, a rod body and a number of fasteners, its structure is shown in Figure 4.

3.2. Working principle of corn orientation device

Speed of corn on the primary belt was equal with speed of the primary belt tape, and through the role of the guide bar, direction of the axis of the corn was same with the speed of the horizontal motion [8]. At this time, big diameter of the corn may be in the front, or small diameter of the corn may also be in the front.

In Figure 5, when small diameter end of the corn was in the front, because the diameter of small diameter end of the corn was less than the diameter of the hole of the swinging rod, the corn would be inserted to the hole of the swinging rod, then as seen if Figure 5(a). Under the action of corn, the swing rod was swinging, and small diameter end of the corn was swinging with swinging rod movement, then as seen if Figure 5(b). When swing rod was a certain angle, corn would drop out the primary belt, then as seen if Figure 5(c). At same time, under the action of the swing rod and auxiliary belt, corn was flipped and the big diameter end of the corn was in the front to delivery, then as seen if Figure 5(d). When the swinging rod was swinging back, the swing rod would be collided with the pendulum rod rack of swing rod to consume mechanical energy of swinging rod and make it static fast. When small diameter end of the corn was in the front, the process diagrams of orientation device were shown in Figure 5(a-d). In the Figure 5, the direction of the arrow was the movement direction of the corn in horizontal direction.

In Figure 6, when the big diameter end of the corn was in the front, because the diameter of big diameter end of the corn was larger than the swinging rod, the big diameter end of the corn couldn't insert into the hole of the swinging rod, then as seen if Figure 6(a). Under the action of corn, the swinging rod was rotating then as seen if Figure 6(b), and then the corn was on auxiliary belt. At the time, the corn was delivered at big diameter end of the corn before as seen if Figure 6(c). When the swinging rod was swinging back, it would collide with the rod rack of the swinging rod frame to consume mechanical energy of the swinging rod and stop it quickly. The process diagrams of orientation device were shown below in Figure 6(a-c). In the Figure.6, the direction of the arrows was for the movement direction of the corn in horizontal direction.

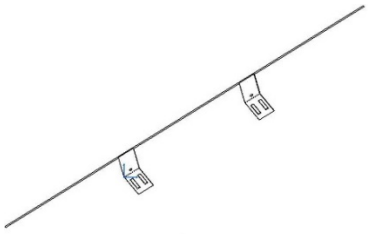

Figure 2. Guide bar

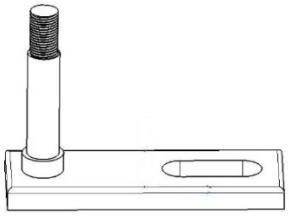

Figure 3. Swinging rod

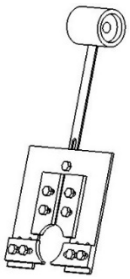

Figure 4. Structure of swinging rod

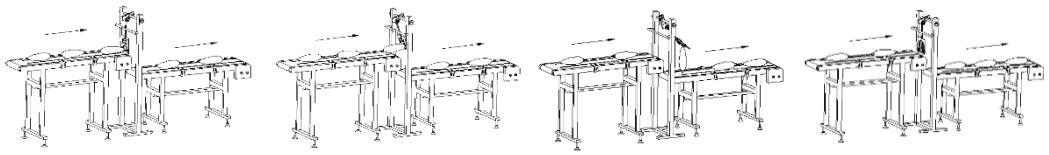

(a) (b) (c) (d)

Figure 5. The process diagrams of orientation device when small diameter of the corn was in the front

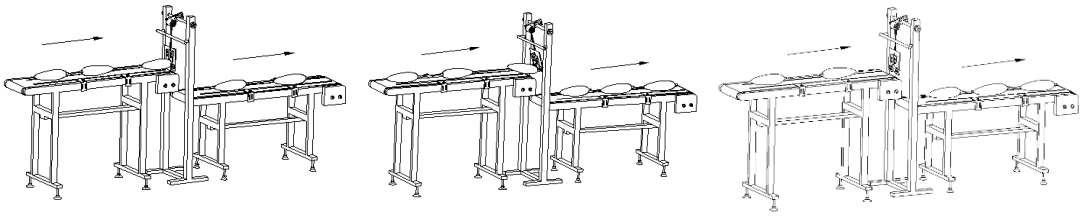

(a) (b) (c)

Figure 6. The process diagrams of orientation device when big diameter of the corn was in the front

4. Mechanism of Corn from the Primary Belt

During the separation of corn from the primary belt, there might be two things: Firstly, static friction force was large enough between corn and the belt, on which the corn could be out of the primary belt by the static friction force between corn and the primary belt; Secondly, the static friction force is not big enough between corn and the primary belt. The relative sliding would be produced between corn and the primary belt. Corn could be out of the belt mainly depending on its own momentum.

4.1. Analysis idea

In order to determine the mechanism of the corn from the primary belt, which belongs to the first kind of case or to the second case. In this paper, "friction" in critical state of the corn needed to be analyzed. The flow chart of analysis idea was shown in Figure 7.

4.2. Analysis process

When small diameter end of the corn was in the front, diameter of small diameter end of the corn was less than the diameter of swinging rod hole. Small diameter end of the corn would be inserted to hole of the swinging rod. Then it was swinging with the swinging rod movement, until corn was out of the primary belt. In this process, the contact between corn and swinging rod was simplified. The corn was simplified to connecting rod. When corn was in the critical state, the following result was shown in Figure.8, in which A was articulated point of the swinging rod and swinging shaft, B was hinged point of corn and swinging rod, C was application point of the primary belt and corn, α was angle between swinging rod and the vertical detection in the critical state, β was angle between corn in the critical state and horizontal plane, h_1 was gravity elevated height of swinging rod from the state of nature to graphic state, h_2 was gravity elevated height of corn from the state never in contact with the rocker to graphic state, direction of the arrows was the direction of rotation for the pulley in Figure 8.

When the corn would be out of the primary belt, length of the corn was ignored which plug into swinging rod hole. At the time, the length of the corn was its overall length in Figure.8. By the geometric relationship, the formula was taken.

$$\cos\alpha = \frac{L_1^2 + L_1^2 - L^2}{2L_1^2} \tag{1}$$

In the formula, L_1 was length of swinging rod, m; L was length of corn, m.

$$\beta = \frac{\pi}{2} - \frac{\pi - \alpha}{2} \tag{2}$$

After the linkage was decomposed to analyze in Figure 8. The stress of swinging rod and the corn were shown in Figure 9 and Figure 10 respectively.

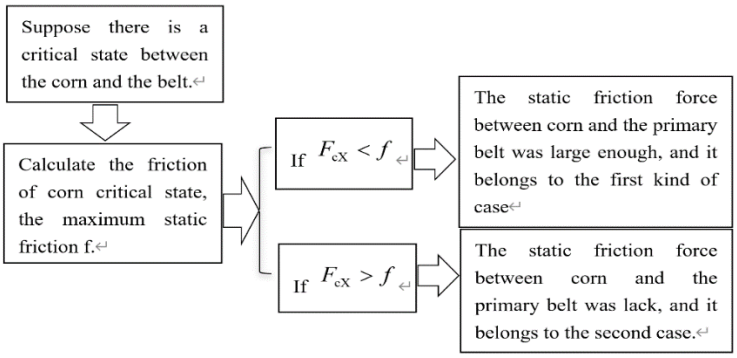

Figure 7. The flow chart of analysis idea
f: the maximum static friction, N. F_{cX}: the friction force between corn and the primary belt, N.

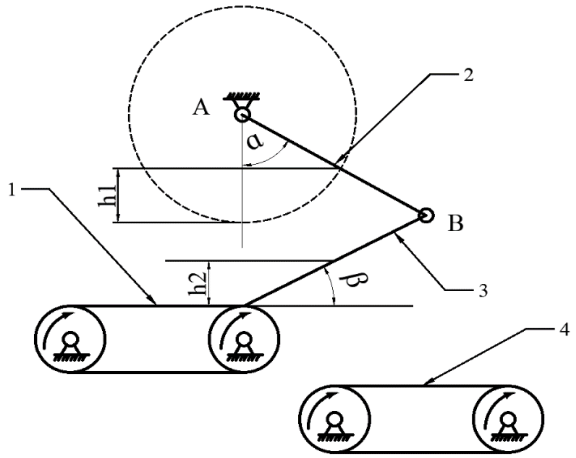

Figure 8. Model what corn would be out of the primary belt
1. The primary belt; 2. Swinging rod; 3. Corn; 4. The auxiliary belt

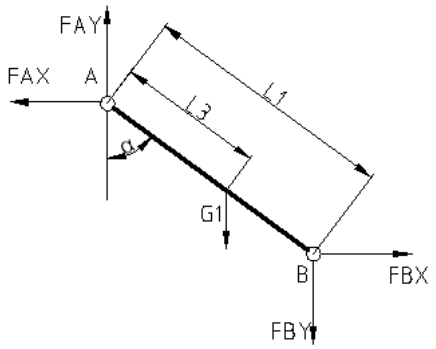

Figure 9. Stress analysis diagram of swinging rod

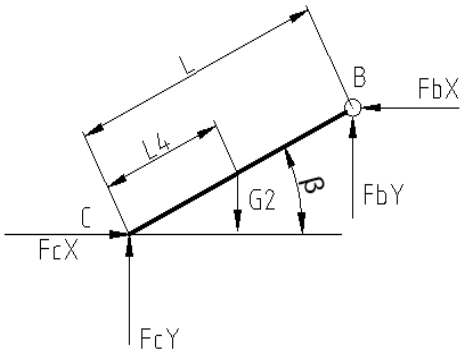

Figure 10. Stress analysis diagram of corn

According to Figure 9 and Figure 10, by mechanics knowledge, they were known:

$$F_{BX} \cdot L_1 \cdot \cos\alpha - F_{BY} \cdot L_1 \cdot \sin\alpha - G_1 \cdot L_3 \cdot \sin\alpha = 0 \quad (3)$$

$$F_{BX} - F_{bX} = 0 \quad (4)$$

$$F_{BY} - F_{bY} = 0 \quad (5)$$

$$F_{bX} - F_{cX} = 0 \quad (6)$$

$$F_{bY} \cdot L \cdot \cos\beta + F_{bX} \cdot L \cdot \sin\beta - G_2 \cdot L_4 \cdot \cos\beta = 0 \quad (7)$$

By type (3), (4), (5), (6) and (7), they could be obtained:

$$F_{CX} = \frac{G_1 \cdot L_3 \sin\alpha \cdot L \cdot \cos\alpha + G_2 \cdot L_4 \cos\beta \cdot L_1 \sin\alpha}{L \cdot \sin\beta \cdot L_1 \cdot \sin\alpha + L_1 \cdot \cos\alpha \cdot L \cdot \cos\beta} \quad (8)$$

Length of the swinging rod was L_1, $L_1 = 0.236$ m; By suspension line method, center of gravity of the swinging rod was measured, taking $L_3 = 0.19$ m; The mass of the swinging rod was m_1, $m_1 = 0.450$ kg; Assume that center of gravity of the corn was focus on its axis, so $L_4 = \frac{1}{2}L$. The values of m_1, L_1 and L_3, and limit length and quality of maize corn in Table 1 respectively have been plugged into type (8).

When length of corn was $L = 0.1614$ m, the mass of corn was $m_2 = 0.1814$ kg, $F_{cX} = 2.095$ N. When length of corn was $L = 0.2187$ m, quality was $m_2 = 0.2387$ kg, $F_{cX} = 2.350$ N. By experiments, maximum static friction coefficient between the corn and belt A was measured to be 0.42, then:

$$f = m_2 g\mu = 0.2387 \times 10 \times 0.42 = 1.00254 \text{ N} \quad (9)$$

Obviously $F_{cx} > f$, it belonged to the second case. When small diameter end of the corn was in the front, corn would depend mainly on its own momentum from the primary belt. At the same time, it was not necessary to analyze the case that big diameter end of the corn was in front.

4.3. Determination of the primary belt speed

Through the above analysis, there was a critical value V for the primary belt speed. When the primary belt speed was greater than V, corn could be separated from the primary belt; When the primary belt speed was less than V, it could not guarantee that all corn could be separated from the primary belt. In this paper, critical speed V of the primary belt has been estimated. From collisions between corn and swinging rod to the corn out of the primary belt, three stages have been divided into: the first stage was before the collision of corn ear and swinging rod; the second stage was collision moment between corn and swinging rod; in the third stage, corn was out of the primary belt after collision between corn and swinging rod.

The first stage was the corn grain and swinging rod before the collision. The corn with the belt on the primary belt was at synchronous movement, namely the size of the corn grain rate is equal to the size of the primary belt speed. In order to simplify the calculation, quality of maize grain is simplified to homogeneous cylinder, the swinging rod was simplified to the rod body (uneven quality), and the center axis of maize grain and the end of the rod body were in the same horizontal plane. Schematic diagram before collision of corn and swinging rod was shown in Figure 11. Directions of the arrows in figure were the direction of corn grain. At this time, maize grain has momentum for P_0, then:

$$P_0 = m_2 v_0 \quad (10)$$

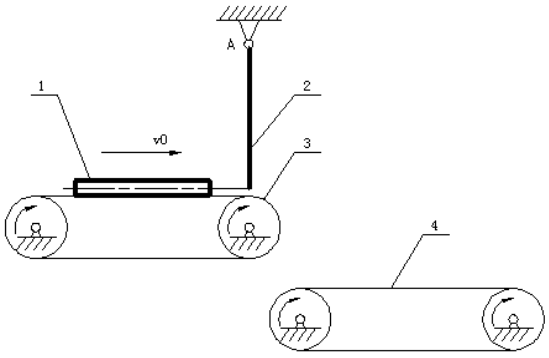

Figure 11. Schematic diagram before collision of corn and swinging rod
1. corn; 2. swinging rod; 3. the primary belt; 4. the auxiliary belt

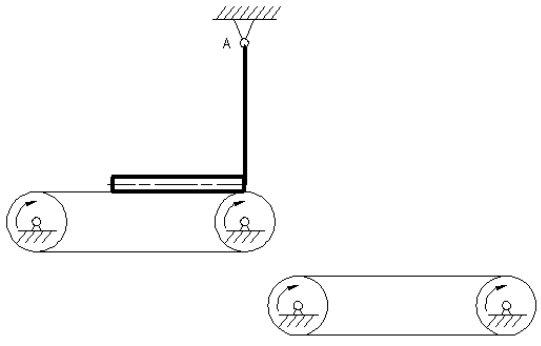

Figure 12. Moment of collision of corn and swinging rod

The second stage was the moment of collision corn and swinging rod. The system of corn and swinging rod was as the research object, at the moment of collision, the small diameter end of corn was interacted with swinging rod. Because at the moment of collision of corn and swinging rod, the displacement couldn't occur, external forces didn't affect the system, and momentum of the system was conservative, as shown in Figure 12. At this moment, the speed direction of the corn was horizontal. And because the small diameter end of corn was turned together as the swinging rod, the constraint between the small diameter end of corn and swinging rod was simplified to hinge. To sum up, at the moment of collision, the momentum of the system was conservative, and corn was hinged to swinging rod [9].

$$m_2 v_0 L_1 = m_2 \omega L_1^2 + J\omega \tag{11}$$

In the third stage, after collision of the corn and swinging rod, it would be coming off the primary belt. In the process, the system of corn and swinging rod still was the research object. Because the critical speed was solved, when the corn was separated from the primary belt, the kinetic energy of corn and swinging rod was converted into all their potential energy, and the internal energy between swinging shaft and swinging rod. At this stage, the external force of the system was friction F_1 between corn and the primary belt, friction F_2 was between swinging rod and swinging shaft. On the system, what F_1 did was positive work W_1, what F_2 did on system was negative work W_2. According to the law of conservation of energy, the formula was taken:

$$\frac{1}{2} m_2 \left(\omega L_1\right)^2 + \frac{1}{2} J\omega^2 + W_1 - W_2 = m_1 g h_1 + m_2 g h_2 \tag{12}$$

In order to simplify the calculation, the corn was simplified to rod. When it was in the critical state, it was as shown in Figure 4. By the geometric relationship, the formula was taken:

$$h_1 = L_3 \times \left(1 - \cos\alpha\right) \tag{13}$$

$$h_2 = L_4 \times \sin\beta \tag{14}$$

By type (1), (2), (13) and (14), the calculated results were $L = 0.2187$ m, $L_3 = 0.19$ m, $L_4 = 0.10935$ m, $h_1 = 0.0802$ m, $h_2 = 0.0231$ m.

Because W_1 could make corn from the primary belt, without considering the circumstances, the primary belt speed could guarantee corn from the primary belt. Because the friction force between the swinging rod and the swinging shaft was enough small, it was neglected. In the case of ignoring W_1 and W_2, the system of corn and swinging rod was as the ideal model. By vertical type (12) (11), the formula was taken:

$$v_0 = \sqrt{\frac{2\left(m_1 g h_1 + m_2 g h_2\right) \times \left(m_2 L_1^2 + J\right)}{m_2 L_1^2}} \tag{15}$$

In CATIA, the rotational inertia of the swinging rod were that $J = 0.0195$ kg·m^2, $h_1 = 0.0802$ m, $h_2 = 0.0231$ m, $L_1 = 0.238$ m, $m_1 = 0.45$ kg and $m_2 = 0.2387$ kg. They were plugged into type (15), taking $v_0 = 1.426$ m/s.

Under the influence of ignoring the frictions between the primary belt and corn and between swinging rod the swinging shaft, the primary belt speed was v_0, $v_0 = 1.426$ m/s. The corn could be separated from the primary belt. So, the primary belt speed should not be less than 1.426 m/s.

5. Conclusions

In this paper, the following conclusions are drawn through measurement test and analysis.

1. The big diameter, small diameter, length and the mass of corn were measured. The four parameters are the basis for designing corn orientation device and building entity model of corn.
2. Combined with the physical parameters of corn, A corn orientation device was designed and manufactured, and the function of the main components was explained.
3. In order to be able to ensure that all of corn from the primary belt during the transfer process, the belt speed is not lower than 1.426 m/s.

References

[1] Huang XL, Zheng JQ, Zhao MC. Study on the production line for the intelligent grading of apple quality based on automatic orientation. Journal of Anhui Agricultural Sciences, 2008, 36(7): 3037-3041.

[2] Cheng WL, Liang QA, Sun Y, Liu XD. Fruit automatic orientation principle and experimental analysis of influencing factors. Xinjiang Agricultural Mechanization, 2007, (4): 34-35.

[3] Chen WL. Simulation and test of belt directional system for apricots cutting and stoning. Xinjiang Agricultural University, Wulumuqi, 2007, pp. 26-35.

[4] Ouyang HF, Xie CX, Zheng JY. Design and experiment of guide rail automatic orientation device. Combination Machine Tools and Automatic Processing Technology, 1997, (10): 33-36.

[5] Ouyang HF, Xie CX. Design and experiment of pencil sharpener automatic orientation device. Combination Machine Tools and Automatic Processing Technology, 1996, (7): 18-21.

[6] Liu Y.S. Conveying position and their types study for block articles. Journal of Hunan University of Technology, 2008, 22(1): 9-12.

[7] Ren L.Q. Editor: Design and analysis of experimental optimization. Jilin Science & Technology Press, Changchun, 2001, pp. 120-128.

[8] Chang QL, Hou L. Parallel translating mechanism process-oriented mathematical model and 3-D model for cylindrical gears with curvilinear shaped teeth. Jordan Journal of Mechanical and Industrial Engineering, 2016, 10(3): 171-177.

[9] Hu XS, Liu XF, Zhao HY, Li DH, Hu ZQ. Multivariate analysis of variance in EXCLE table. Journal of Northwestern Polytechnical University, 2006, 15(2): 174-179.

JJMIE

Volume 16, Number 1, January. 2022
ISSN 1995-6665
Pages 79 - 86

Jordan Journal of Mechanical and Industrial Engineering

Parallel Computing-Based Dynamics Model for Tracking Moving Targets

Yugang Cui*

Department of Architectural Engineering, Zhengzhou Technical College, Zhengzhou 450121, China

Received 14 July 2021 *Accepted 25 December 2021*

Abstract

In order to solve the problem of low tracking accuracy of tennis ball trajectory caused by noise processing in the past methods based on mean shift algorithm and infrared spectrometer, a dynamic model of tennis ball moving target tracking based on parallel computing is proposed. Based on the analysis of tennis ball movement mechanics, a tennis ball movement image segmentation method based on image segmentation and distortion dynamic information is proposed. Based on image segmentation, the data is denoised. According to the tracking process of parallel computing, the gravity, visual and aerodynamic models are established to track the movement trend of tennis ball after hitting, and the strong tracking filter is used to compensate and correct the mutation points in different directions in the process of tennis ball movement. The experimental results show that the coordinates of the highest point of the tennis ball trajectory in the three-dimensional coordinate system are (-200, 150, 140), which is consistent with the coordinates of the highest point of the actual motion path, and has high robustness to external disturbances.

Keywords: corn; orientation device; physical parameters; the primary belt speed;

1. Introduction

With the rapid development of China's domestic tennis ball and the world's second-largest professional tennis ball players, it has achieved brilliant results in the world [1]. With the development of computer software and hardware technology, the use of computer technology to analyze tennis ball has attracted the active participation of many domestic scientific research workers [2, 3]. Among them, how to track and locate the moving tennis ball target is one of the difficulties to be solved. An improved BTV target tracking technology is proposed in Reference [4]. In order to track the ball, a logical operation is applied between the created background and the image difference, and then the candidate ball is detected by applying threshold and magnification, which can finally lead to the ball tracking. Player detection is performed by finding the largest spot and filling the entire detection object by removing small spots, and the player is tracked according to the contour. Experimental results show that this method achieves high accuracy in target recognition and tracking. Ball tracking has high hit rate and low failure rate, while player tracking hit rate is measured by multi-target tracking accuracy (motp). A tennis target tracking method based on infrared spectrometer is proposed in Reference [5]. The interferogram of moving target is collected by infrared spectrometer, the spectrum is restored, and its phase difference is compared with the actual spectrum. The moving target is marked by local background weighting to track the moving target. Due to the phase difference between the reconstructed spectrum and the actual spectrum and the influence of external dynamic background, the tennis moving target tracking effect is poor. Aiming at solving the problems and shortcomings in target tracking, a tennis target tracking dynamic model based on parallel computing is proposed in this paper. According to the excellent localization characteristics of parallel computing in both time and spatial domain, the adjacent video images are differentiated to extract the feature information reflecting the foreground moving target, so as to overcome the adverse factors of illumination change and the continuous change of moving target scale at any time. At the same time, based on the structural characteristics of the tennis ball court, the adverse interference factors outside the court are excluded.

2. Tennis Ball Moving Object Segmentation

Tennis ball is affected by gravity and air resistance in flight. After the ball is released, it will encounter certain air resistance in flight, which will increase the pressure resistance. The vibration caused by the impact of the ball will produce simple harmonic vibration to the air [6-8]. When the rotating sphere moves forward, the interaction between circulation and air flow changes the streamline distribution and forms a certain pressure difference [9].

The difference between topspin and flat shot is that there is upward and forward pulling action when hitting the ball, so the ball has upward rotation around itself in the first flight. Because the ball has upward rotation trend, the air pressure above the ball is greater than the pressure below.

* Corresponding author e-mail: cuiyugang@163.com.

Therefore, when the ball drifts in the first flight, the ball tends to fall, so the ball falls quickly after passing the net, and it is not easy to hit the bottom line [10-12]. Forehand topspin is faster than flat shot in rotation speed, so under the same conditions, the topspin is faster than flat shot in the second flight. The pressure difference between the upper and lower air flow of the tennis ball will also further expand, resulting in a synchronous increase in the falling trend of the ball [13, 14].

In the instant of hitting, a positive main hitting force $p1$ is applied to the ball to realize the charge of the ball, and a vertical and positive upward movement is added to the racket to make the racket grip the tennis ball and twist it from the back, so that the ball can obtain an additional upward rotation force T. Under the action of this T force, the ball rotates around its center axis OY according to the corresponding speed n (which is usually expressed as several revolutions per minute) [15]. The batter looks up in the direction of the ball. If the additional rotation force T is greater, the rotation speed n of the ball is greater.

At the moment of hitting, a rotating force T is added to the ball, that is to say, friction is applied to the ball to rub and rotate the ball. Therefore, the time for the ball to stay on the chord plane of the racket is much longer than the time for flat hitting, and its contact with the racket, that is, the impact point, is not a fixed point, but a moving line segment [16, 17].

According to the principle of mechanics, a rotating ball must have a moment (M). The moment is equal to the product of the force (F) acting on the sphere and the vertical distance (L) from the force to the center of the sphere. If $L = 0$, the force is passing through the center of the ball, the ball does not produce any rotation, but the ball flies the fastest forward; If F is constant, l increases, M also increases, and the ball rotates faster; If F is constant, the greater the forward force of $F1$ is, the smaller the upward force of $F2$ is, and the faster the ball flies; The greater the $F2$ is, the smaller the $F1$ is, and the faster the ball rotates [18, 19]. It is not difficult to see from the above, the topspin ball must be in the forward force at the same time, but also upward force to rub the ball. The forward force gives positive pressure to the ball and makes the ball fly forward through the center of the ball; The upward force comes from the friction between the racket and the ball, so that the force line on the ball does not pass through the center of the ball and has a vertical distance with the center of the ball, causing the ball to rotate. In this way, the ball can not only move forward, but also rotate to form a topspin ball [20, 21].

Combined with the motion mechanics of tennis ball, the image segmentation process is designed, as shown in Figure 1.

As can be seen from Figure 1, the normal mode of image segmentation is combined with the dynamic information of segmentation distortion, which is used to segment different sub images of tennis ball motion image. Color and texture features are combined, and the hidden layer is processed according to the feature fusion principle to extract color and texture features [22]. In order to realize the target segmentation, the image is segmented by thresholding combined with gray and gradient information.

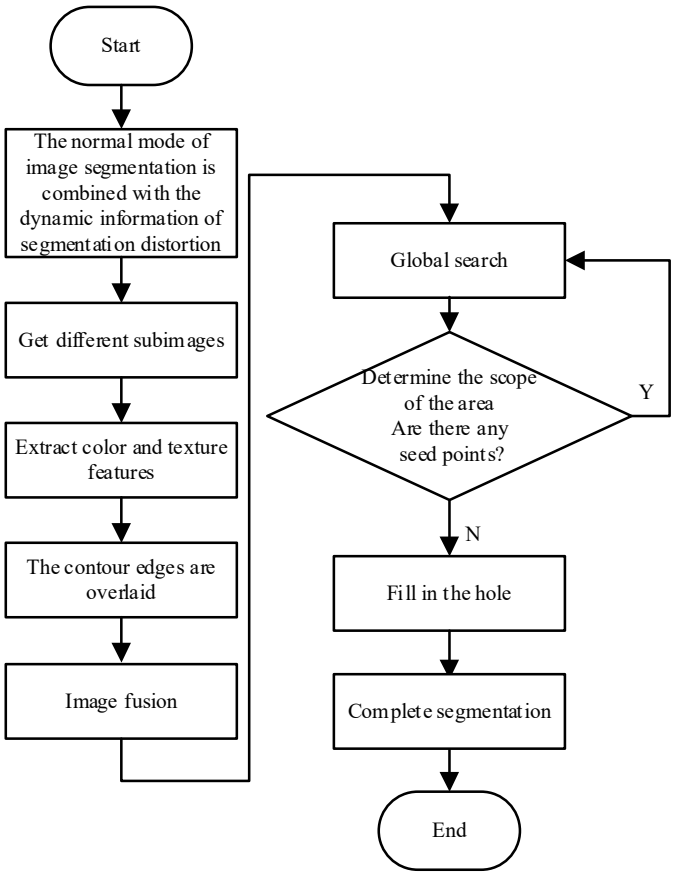

Figure 1. Image segmentation process

The details are as follows:

Step 1: Overlay the edge of the image contour to be segmented;

Step 2: The region growing method is used to superimpose the edge of the contour, and the maximum contour method is used for fusion;

Step 3: Take the upper left corner of the image as the starting point, and use it as the seed point of the search area to search globally, and get the first non-zero gray value pixel. The global search rule takes the seed point as the starting point, and starts the search from top to bottom. After setting the search compensation threshold, it finds the next non-zero pixel. When it finds the region that meets the condition, it determines whether there are seed points in the region [23]. If there are seed points in the area, continue to search until no more seed points appear;

Step 4: Fill in the empty target to make the target have a complete target control;

Step 5: The whole target contour is etched to process the edge redundant information, and the contour is inflated by combining with morphological filtering to get the complete segmentation image.

3. Noise Reduction Algorithm Based on Parallel Computing

In order to track and locate the tennis ball moving target, based on the above-mentioned segmentation method of tennis ball trajectory image, the position of tennis ball is obtained and used as the initial observation value to train and predict the tennis ball moving position based on the Haar like features of tennis ball.

Because the video scene is always affected by noise and tennis ball non-uniform motion, it is easy to lead to its movement often accompanied by multiple or even dozens of pixel size jumps between adjacent two frames, as well as the inevitable occlusion effect in the process of movement, resulting in tennis ball moving target loss [24-26]. In order to overcome the above adverse factors, the following optimization is done in the process of tennis ball target tracking.

If the current tennis ball moving target detection fails, it indicates that the position jump of the front and back of it is larger, or its moving target is temporarily separated from the video image area. In view of the above situation, expand the region of interest of tennis ball target detection, expand the length M and width N of the region of interest correspondingly (in the experiment, $M = N = 25$), and find the target in the expanded region of interest [27, 28]. If the tennis ball target can not be detected after the above processing, it indicates that the tennis ball has been occluded or separated from the video image area, then the lost target is marked accordingly, and the noise reduction algorithm based on parallel computing is used to detect the tennis ball target in the next image.

The data collected under the support of data synchronization protocol has large interference data, so it is necessary to denoise the data. Therefore, the scale transformation method based on parallel computing is designed to process the interference data.

The noise area is assumed to be the (x, y) direction of the ball, and the ball motion path is assumed to be the $x \in [0, W-1], y \in [0, H-1])$ direction of the ball, the background image and foreground image are denoised to get the noise distribution area. Where W is the horizontal displacement and H is the vertical displacement.

The dynamic error of the target image is corrected by using 3D viewpoint switching mode, the expression formula is:

$$\begin{aligned} x &= V\cos\theta\cos\vartheta_1 \\ y &= V\sin\theta \\ z &= -V\cos\theta\sin\vartheta_1 \end{aligned} \tag{1}$$

In Formula (1), x, y, z represents the local information feature points of tennis ball trajectory, and ϑ_1 represents the switching angle of tennis ball trajectory.

If the tennis ball target can not be detected in several consecutive frames, the tracking fails. If the tennis ball target is detected again after the short-term tennis ball target is lost, the tennis ball target tracking training and prediction will be carried out again as the measured value input [29].

4. Dynamic Model Construction of Tennis ball Moving Target Tracking

Parallel computing is one of the most practical algorithms for local optimal solution. It belongs to one of the tracking methods based on the direction information of motion, and can track the target of specific direction of motion. The tracking flow based on parallel computing is shown in Figure 2.

As can be seen from Figure 2, the target location is based on the fact that the real distance of the target is obtained by means of the inverse ratio of parallax and depth. After stereo matching, the parallax map can be calculated to perform 3D ranging operation. The internal and external parameters of the camera are obtained by MATLAB calibration toolbox, and then the reprojection matrix can be obtained by stereo calibration with parallel computing algorithm.

4.1. Dynamic model of target tracking

Assuming that the radar station coordinates are east north one day coordinate system, the aerodynamic model and thrust model are analyzed in half speed, and the gravity and apparent vision model and aerodynamic model are constructed in geocentric inertial coordinate system:

$$v(k) = a_G(k) + a_T(k) + a_A(k) + a_c(k) \tag{2}$$

In Formula (2), $a_T(k)$ and $a_A(k)$ represent thrust and aerodynamic acceleration respectively, $a_G(k)$ represents gravity acceleration vector, and $a_c(k)$ represents visual acceleration.

4.1.1. Gravity and expressive force model

Assuming that the position states of the target in the east north one day coordinate system and the geocentric inertial coordinate system are X_A and X_B respectively, and assuming that the longitude and latitude heights of the radar station are L, B, H, the conversion from the east north one day coordinate system to the geocentric inertial coordinate system is as follows:

$$\mathbf{X}_{\mathrm{B}} = \mathbf{T}_{\mathrm{A}}^{\mathrm{B}}\mathbf{X}_{\mathrm{A}} - \left[0, 0, R_e + H\right]^{\mathrm{T}} \tag{3}$$

In Formula (3), R_e is the equivalent radius of the earth.

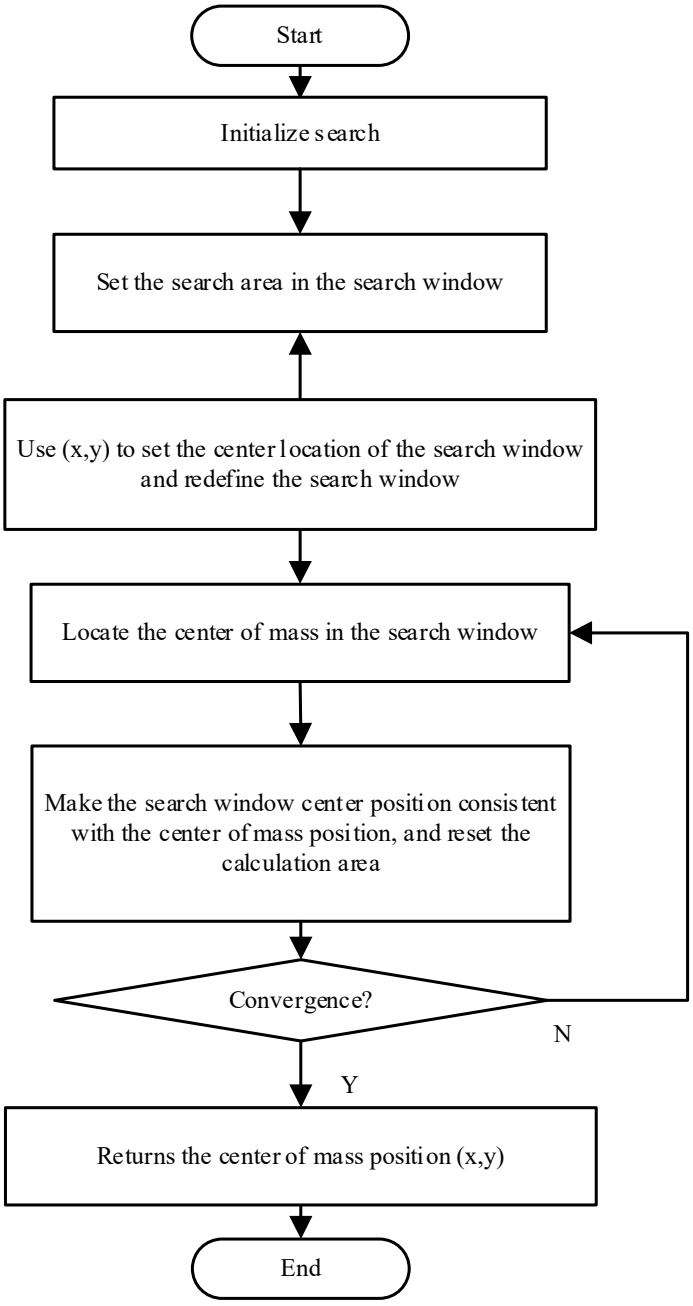

Figure 2. Tracking process based on Parallel Computing

In Formula (3), R_e is the equivalent radius of the earth. The transformation matrix in Formula (3) is as follows:

$$\mathbf{T}_{\mathrm{A}}^{\mathrm{B}}=\begin{bmatrix} -\sin\left(L+\theta_e t\right) & \cos\left(L+\theta_e t\right) & 0 \\ -\cos\left(L+\theta_e t\right)\sin(B) & -\sin\left(L+\theta_e t\right)\cos(B) & \cos(B) \\ \cos\left(L+\theta_e t\right)\cos(B) & \sin\left(L+\theta_e t\right)\cos(B) & \sin(B) \end{bmatrix} \quad (4)$$

In Formula (4), $\theta_e t$ represents the angle between the geocentric inertial coordinate system and the geocentric coordinate system from the reference time to the time t (it is generally assumed that the geocentric coordinate system and the geocentric inertial coordinate system coincide when the radar detects the target). Then the target acceleration in the east north one day coordinate system is:

$$\mathrm{a}_{\mathrm{A}}=\mathbf{T}_{\mathrm{A}}^{\mathrm{B}}\ddot{\mathbf{X}}_{\mathrm{A}}+2\dot{\mathbf{T}}_{\mathrm{ECI}}^{\mathrm{B}}\dot{\mathbf{X}}_{\mathrm{A}}+\ddot{\mathbf{T}}_{\mathrm{AI}}^{\mathrm{B}}\mathbf{X} \quad (5)$$

One term in Formula (5) is the specific expression of gravity acceleration in the east north one day coordinate system. The acceleration conversion from the geocentric inertial coordinate system to the east north one day coordinate system is based on the target position. The coordinate conversion of acceleration is obtained through the second derivative of time. In this process, the conversion matrix is obtained T_A^B is a function of time, resulting in the conversion of the final gravitational acceleration with two terms.

4.1.2. Aerodynamic model

The acceleration produced by thrust is realized by acting on the air, therefore, the thrust model can be regarded as a

special superposed aerodynamic force, it can be expressed as:

$$F(k)=\frac{1}{2}\rho(k)v^2(k)\left[\mathrm{a}_v,b_t,c_i\right]\left[-a_d(k),a_t(k),a_b(k)\right]^{\mathrm{T}} \quad (6)$$

In Formula (6): a_v,b_t,c_i represents unit vector of half speed coordinate axis, $\rho(k)$ represents air density, $a_d(k)$ is resistance acceleration, $a_t(k)$ is lateral turning acceleration, and $a_b(k)$ is climbing acceleration. The dynamic model in the half velocity coordinate system has obvious physical significance in expressing the horizontal and vertical plane motion of the target. When the lateral turning acceleration is greater than zero, the tennis ball will fly to the left. When the lateral turning acceleration is less than zero, the tennis ball will fly to the right; The climbing acceleration determines the movement mode of the target in the longitudinal plane; When the climbing acceleration is greater than zero, the tennis ball will fly upward. When the climbing acceleration is less than zero, it falls down.

4.2. Filtering correction of acceleration mutation point

When there is power phase conversion, the tennis ball will produce larger maneuvering acceleration, which will lead to the increase of tracking error. After the initial tracking model is adjusted to match the target motion pattern for a period of time, the tennis ball motion is described more stably, and the predictor is modified by gain. The model needs to ensure the robustness of the tracking algorithm as a whole, and its acceleration will not change abruptly. At the same time, some measurement samples are needed to correct the error of filtering algorithm, so the error of maneuver jump position will increase. To solve this problem, a strong tracking filter is introduced to compensate and correct the maneuvering mutation point. Considering that the power conversion is mainly used to push the tennis ball to pull up from the low point of trajectory, the lift acceleration $a_c(k)$ is selected as the detection parameter of maneuver mutation. Judgment volume:

$$\varepsilon(k)=\lg\frac{a_c(k)-a_c(k-1)}{a_c(k-1)-a_c(k-2)} \quad (7)$$

It can be seen from Formula (7) that when the difference between adjacent accelerations reaches more than two orders of magnitude, that is $\varepsilon(k)\geq 2$, the maneuver mutation is considered to occur, and the strong tracking filter is used to filter and correct the measurement at the current time. The physical picture of the strong tracking filter and the tennis ball track after filtering and correction are shown in Figure 3.

5. Experiment

In order to verify the rationality of the dynamic model of moving target tracking based on parallel computing, tennis ball is taken as the research object to carry out the experimental verification analysis.

5.1. Experimental preparation and segmentation result analysis

In an 80 m^2 laboratory, tennis ball is used as the experimental object to track its moving target. Set the maximum speed of the tennis ball as 20 m/s and the maximum angular speed as 10 °/s. install the camera above the tennis ball and collect the image every 3 s.

Table 1 shows the number record of tennis ball track images with 30700 filters after segmentation by using the method in this paper, average displacement algorithm and infrared spectrometer method under the conditions of frame 1, 200, 400 and 600.

Table 1. Record of three methods

Number of frames	Paper method	Average displacement algorithm	Infrared spectrometer method
1	194136	165660	153840
200	122856	111004	153803
400	136238	124189	154083
600	193572	173141	154872

Using the sample data segmented by the three methods shown in Table 1, the root mean square errors of the three methods under different segmentation ratios are counted. The results are shown in Figure 4.

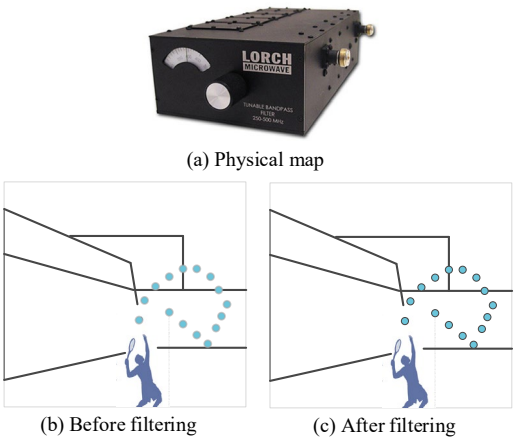

(a) Physical map

(b) Before filtering (c) After filtering

Figure 3. Variation of root mean square error of segmentation

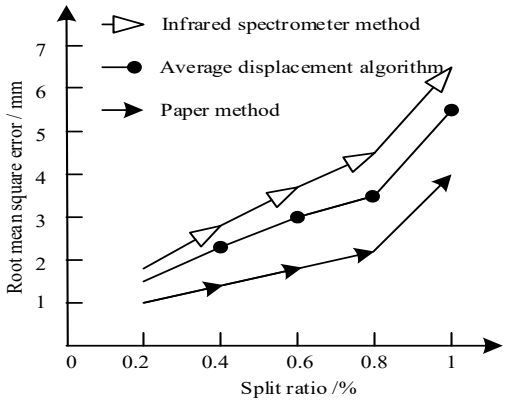

Figure 4. Variation diagram of root mean square error of segmentation

As can be seen from Figure 4, under the same segmentation ratio, the change curve of root means square error of segmentation using the method in this paper is always lower than that of average displacement algorithm and infrared spectrometer method, and the curve is relatively flat. It shows that under the same segmentation ratio, the segmentation error of this method is smaller and more suitable for the actual needs.

5.2. Target setting

Through the image video sequence to obtain 1000 images, the characteristics of the collected image and video are analyzed, and the acquisition process is interfered by external noise. According to the experimental environment, the simulation experiment of tennis ball movement path capture is carried out. First of all, the video sequence of a tennis ball image in the process of throwing is collected to obtain the original image, as shown in Figure 5.

It can be seen from Figure 5 that the camera of IO Industries company is used to take fixed-point pictures of the experimental objects. The camera is placed on the right side of the tennis ball court, 5 m away from the server. The number of the server is recorded through the camera. The characteristics of the best hitting point of the tennis ball server are analyzed by the trajectory of the marker points of the player's arm.

5.3. Experimental results and analysis

Combined with the tennis ball trajectory in Figure 5, the motion path coordinates are analyzed in detail, as shown in Figure 6.

It can be seen from Figure 6 that the coordinates of the highest point of the tennis ball trajectory in the three-dimensional coordinate system are (-200, 150, 140). Under the support of each coordinate point of the actual motion path, the tennis ball trajectory is tracked by using the Mean Shift algorithm, infrared spectrometer and parallel computing methods, as shown in Figure 7.

It can be seen from Figure 7 that the highest point coordinate of the tennis ball trajectory based on Mean Shift algorithm in the three-dimensional coordinate system is (-100, 80, 160), and the tracking points are less, so the tennis ball landing speed is faster; The highest point coordinate of the tennis ball trajectory based on infrared spectrometer in the three-dimensional coordinate system is (-200, 180, 110). Using the parallel computing method, the highest point coordinates of the tennis ball trajectory in the three-dimensional coordinate system are (-200, 150, 140), which are consistent with the highest point coordinates of the actual motion path. Through the above analysis, it can be seen that the tracking result based on the parallel computing method is more accurate.

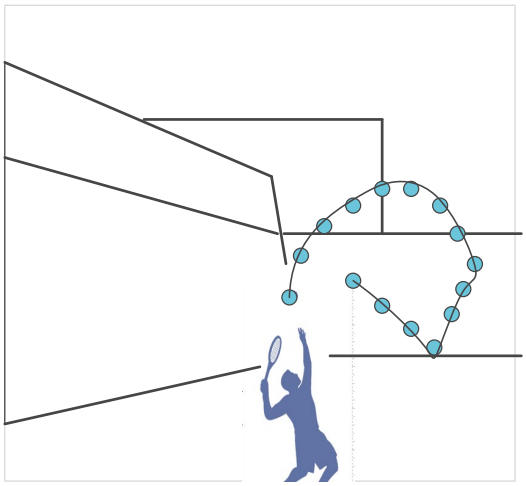

Figure 5. Tennis ball trajectory

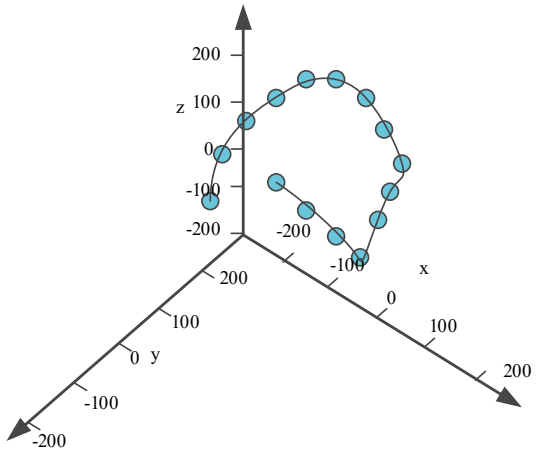

Figure 6. Tennis ball trajectory analysis in 3D coordinated system

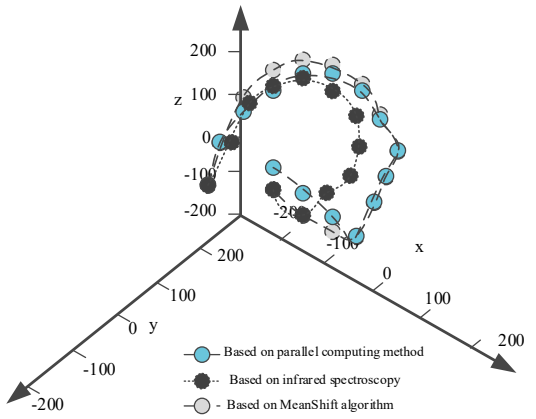

Figure 7. Tennis ball trajectory tracking with different methods

6. Conclusion

The tennis ball moving target tracking dynamic model based on parallel computing can effectively improve the problem of low accuracy of tracking results based on average shift algorithm and infrared spectrometer, which is verified by experiments. The following conclusions are drawn:

1. The accurate prediction of tennis ball moving target tracking trajectory needs high-precision prediction initial value points as the premise. Filtering the tennis ball moving target data can reduce the influence of random error and improve the data accuracy, but it is difficult to meet the requirements of high-precision trajectory prediction of tennis ball moving target. Therefore, starting from the motion characteristics of tennis ball moving target. The dynamic equation of tennis ball moving target is used to constrain the state equation in real time, and the dynamic model of tennis ball moving target tracking based on parallel computing is established. It is modified in real time to improve the target tracking accuracy.
2. The experimental results show that the model in this paper has a high accuracy when tracking the coordinates of the highest point of the trajectory of the tennis ball moving target.

Although this method has accurate capture effect, there are still many problems due to conditions and time constraints, which need to be further improved and studied:

1. During the experiment, when the camera device is used to capture the flight trajectory of the tennis ball flying object, the camera will obtain an image. The exposure time of the camera and the high-speed motion of flying objects blur the image. Therefore, how to eliminate fuzziness and improve the accuracy of positioning results remains to be further studied.
2. It is difficult to keep the background stable when grasping flying objects with the manipulator, so more anti-interference algorithms are needed to extract objects such as regional color segmentation, so as to avoid the interference problem caused by the experimental process.

References

[1] Oshita M, Inao T, Ineno S, et al. Development and evaluation of a self-training system for tennis shots with motion feature assessment and visualization. The Visual Computer, 2019, 35(3): 1-13.

[2] Zhang W, Yang F, Liang Y. A Bayesian framework for joint target tracking, classification and intent inference. IEEE Access, 2019, 7: 66148-66156.

[3] Na W C, Zhang W R, Yan S X, et al. Automated neural-based modeling of microwave devices using parallel computation and interpolation approaches. IEEE Access, 2019, 7: 73929-73937.

[4] Archana M, Kalaisevi Geetha M. Object detection and tracking based on trajectory in broadcast tennis video. Procedia Computer Science, 2015, 58: 225-232.

[5] Matsuoka M., Nakamura T., Osawa T., et al. An evaluation method of reflectance spectra to be obtained by Hayabusa2 Near-Infrared Spectrometer (NIRS3) based on laboratory measurements of carbonaceous chondrites. Earth, Planets and Space, 2017, 69: 120.

[6] Popescu R I, Raison M, Popescu G M, et al. Design and development of a novel type of table tennis aerial robot player with tilting propellers. Mechatronics, 2021, 74(4): 102483.

[7] Bańkosz Z, Winiarski S. Statistical parametric mapping in table tennis topspin backhand shot – Inter-individual differences in angular movement. Gait and Posture, 2020, 81(3): 26-27.

[8] Drees C, Knieb M, Fechner A, et al. Detection of illegal treatment of table tennis rackets using gas chromatography coupled to ion mobility spectrometry – A feasibility study. Analytica Chimica Acta, 2021, 1154(2): 338227.

[9] Bo R, Ming M, Guangguo L. et al. Action recognition model of athletes at the scene of the game based on SVM and multitarget tracking algorithm. Journal of Intelligent and Fuzzy Systems, 2020, 38(6SI): 7303-7314.

[10] Grüschow S, Sadler J C, Sharratt P J, et al. Phenylalanine meta-Hydroxylase: A single residue mediates mechanistic control of aromatic amino acid hydroxylation. Chembiochem, 2020, 21(3): 417-422.

[11] Hu Y, Huang P, Meng Z, et al. Optimal control of approaching target for tethered space robot based on non-singular terminal sliding mode method. Advances in Space Research, 2019, 63(12): 3848-3862.

[12] Zhao Z, Li M, Wang C, et al. Dynamic modeling of brake in power-split DHT and pressure tracking control with sliding mode variable structure method. International Journal of Automotive Technology, 2019, 20(3): 521-530.

[13] Tang F, Lu X, Zhang X, et al. Deep feature tracking based on interactive multiple model. Neurocomputing, 2019, 333: 29-40.

[14] Zhang C, Guan Y. Research on related technologies of vision target tracking based on discrete differential algorithm for deep learning. Journal of Intelligent and Fuzzy Systems, 2019, 37(3): 3267-3274.

[15] Liu S, Wang Y, Dai F, et al. Simultaneous 3D motion detection, long-term tracking and model reconstruction for multi-objects. International Journal of Humanoid Robotics, 2019, 16(4): 2255-2262.

[16] Liu J, Jiang X, Tian X, et al. Hybrid particle filter based dynamic compressed sensing for signal-level multitarget tracking. IEEE Access, 2020, 8: 17134-17148.

[17] Prakash R, Behera L, Mohan S, et al. Dynamic trajectory generation and a robust controller to intercept a moving ball in a game setting. IEEE Transactions on Control Systems Technology, 2020, 28(4): 1418-1432.

[18] Yao G, Saltus R, Dani A. Image moment-based extended object tracking for complex motions. IEEE Sensors Journal, 2020, 20(12): 6560-6572.

[19] Dao D, Guo L. New hybrid SPEA/R-deep learning to predict optimization parameters of cascade FOPID controller according engine speed in powertrain mount system control of half-car dynamic model. Journal of Intelligent and Fuzzy Systems, 2020, 39(1): 53-68.

[20] Lu Y, Yang T, Hatfield B D, et al. Influence of cognitive-motor expertise on brain dynamics of anticipatory-based outcome processing. Psychophysiology, 2020, 57(2): e13477.

[21] Liu W, Zhu L Y, Jin B B, et al. Dynamic modeling of parallel mechanism based on particle system. Journal of Mechanical Engineering Research and Developments, 2016, 39(2): 483-491.

[22] Tang X, Li M, Tharmarasa R, et al. Seamless tracking of apparent point and extended targets using gaussian process PMHT. IEEE Transactions on Signal Processing, 2019, 67(18): 4825-4838.

[23] Muynck G D, Soenens B, Delrue J, et al. Strengthening the assessment of self-talk in sports through a multi-method approach. Scandinavian Journal of Medicine and Science in Sports, 2020, 30(3): 602-614.

[24] Zhu Y Y, Guo N. Unmanned vehicle route tracking method based on video image processing. Jordan Journal of Mechanical and Industrial Engineering, 2020, 14(1): 139-147.
[25] Han B, Huang H, Lei L, et al. An improved IMM algorithm based on STSRCKF for maneuvering target tracking. IEEE Access, 2019, 7: 57795-57804.
[26] Zheng Y J, Feng Y, Joshi S. Construction and study of multi-DOF automobile dynamic model. Journal of Mechanical Engineering Research and Developments, 2016, 39(1): 187-196.
[27] Kachapi, Hashemi S H. Nonlinear vibration and frequency analysis of functionally graded- piezoelectric cylindrical nano-shell with surface elasticity. Jordan Journal of Mechanical and Industrial Engineering, 2018, 12(4): 293-312.
[28] Sidney M, Machar R, Anne-Marie M, et al. Do magnetic resonance imaging abnormalities of the non-dominant wrist correlate with ulnar-sided wrist pain in elite tennis players? Skeletal Radiology, 2020, 49(3): 407-415.
[29] Zhang X Y. Optimized design of adhesive formations for tennis ball. Journal of Mechanical Engineering Research and Developments, 2016, 39(1): 217-225.

JJMIE

Volume 16, Number 1, January. 2022
ISSN 1995-6665
Pages 87 - 95

Jordan Journal of Mechanical and Industrial Engineering

Coordinated Gait Control of Snake Like Robot Based on Electromechanical Tracking

Jianwei Guo*, Yongbo Lv*, Han Zhang

School of Traffic and Transportation, Beijing Jiaotong University, Beijing 100044, China

Received 14 July 2021 *Accepted 22 December 2021*

Abstract

In order to improve the stability of snake-like robot in unknown environment. The coordinated control method of snake like robot gait based on electromechanical tracking is proposed. The motion angles of each joint are designed according to the actual needs. The desired motion curve is designed based on the curve discretization. The coordinated control design of all kinds of gait is completed by discretization. The snake is realized by electromechanical tracking combined with the control system with TwinCAT soft PLC as the main control unit Gait coordination control of the robot. The experimental results show that the proposed method has good control effect on the snake like robot prototype's winding gait and plane rolling gait, and the overall performance and control stability are good. It has certain reference value for the improvement and perfection of snake like robot in the future.

Keywords: Snake Like Robot; Kinematics Analysis; Discretization; Gait Coordination Control.

1. Introduction

The small size and flexible movement of snake-like robot make it competent for search and rescue work, and search and rescue personnel can enter the place where it is easy to collapse to search [1, 2]. In toxic environment, pipeline detection, bridge detection, nuclear power station radiation inspection and other occasions, snake like robots carry cameras and detection equipment to replace people to enter these high-risk or difficult to reach occasions, and assist human beings to successfully complete the specified tasks [3]. The snake-like robot has the characteristics of high degree of freedom redundancy, unfixed base and forward power provided by friction force with the ground or contact force with the surrounding environment. It brings variety of motion forms, but also brings great difficulty to its dynamic modeling and motion control mode.

On the research of snake-like robot, some scholars have begun to study it gradually. Berthet-Rayne et al. focused on the real-time remote operation and control of redundant snake like robot for minimally invasive surgery under the master-slave structure [3]. Based on the mapping between DOF of master robot and redundant slave robot, six different control methods are proposed. Through simulation and user research, the proposed method performs better in terms of visualization, real-time performance and total consumption, but there is still room

for improvement in control stability; Kano et al. proposed a decentralized control scheme for snake like robot based on Tegotae [4], which is a Japanese concept describing the matching degree of perception response and expected value. In this study, a snake like robot is developed. The experimental results show that the proposed control scheme can generate multi-functional gait patterns without changing any parameters, such as scaffold based movement on irregular terrain and Concerto movement in narrow channels, but the robustness of the method still has room for improvement; Ryo et al. studied the trajectory tracking problem of planar snake like robot without lateral constraint [5]. The reference trajectory of the head position and the orientation of the connecting rod 1 are given, and the torque control is determined to reduce the tracking error. The performance of the controller is tested through a large number of simulations. The robustness of actuator failure is studied. It is assumed that one of the actuators is damaged and the corresponding joint becomes passive. As a more realistic situation, some states are not easy to obtain from the sensor readings and need to be estimated by the observer. The performance of the closed-loop system with observer is verified by simulation [5]. This method has good control performance, but it has higher requirements for the collection of external environment information.

On this basis, this paper proposes a coordinated control method of snake like robot gait based on electromechanical tracking. The method of curve discretization is used to design the gait of snake like robot. The coordinated control of snake like robot gait is realized by electromechanical tracking combined with software design. The effectiveness of the proposed method is verified by experiments.

* Corresponding author e-mail: 19114023@bjtu.edu.cn ; yblv@bjtu.edu.cn

1.1. Gait design of snake like robot

1.1.1. Serpenoid curve and its discretization

The symbols used in this paper are shown in Table 1.

Table 1. Corresponding interpretation of symbols

K_n	the number of propagation waves formed by the snake like robot
L	the overall length of the snake like robot
s_p	the length of the snake and the robot along the curve
s	the arc length
n	the number of joints
φ	the angle of positive direction turning anticlockwise to the connecting rod direction
α	the amplitude of joint angle
β	the phase difference between adjacent joints
γ	the control parameter of motion direction
ω	angular velocity
θ_{even}	the horizontal joint function of the snake like robot
θ_{odd}	the vertical motion joint function of the snake like robot
A	the amplitude of the joint motion
t	the joint motion frequency
κ	the curvature of the curve
τ	the torsion of the curve
e_1	the unit tangent vector
e_2	the principal normal vector
e_3	the secondary normal vector

Serpenoid curve is a curve that imitates the plane motion of snakes in nature [6]. When the snake moves, it is equivalent to serpenoid curve and propagates in the plane. Serpenoid curve is defined by curvature equation [7]:

$$\kappa(s)=\frac{2K_n\pi\alpha_0}{L}\sin(\frac{2K_n\pi}{L}s_p) \tag{1}$$

where K_n is the number of propagation waves formed by the snake like robot; L is the overall length of the snake like robot; s_p is the length of the snake and the robot along the curve. The curvature equation is decomposed in two directions, x and y, in rectangular coordinate system:

$$\begin{cases} x(s)=\int_0^s \cos(a\cos(\alpha)+c\alpha)d\alpha \\ y(s)=\int_0^s \sin(a\cos(\alpha)+c\alpha)d\alpha \end{cases} \tag{2}$$

The point (x (s), y (s)) is the coordinate point along the direction from the starting point to the arc length s. a determines the amplitude of the curve motion, b determines the number of periodic waveforms in the unit length, and c determines the direction of the curve.

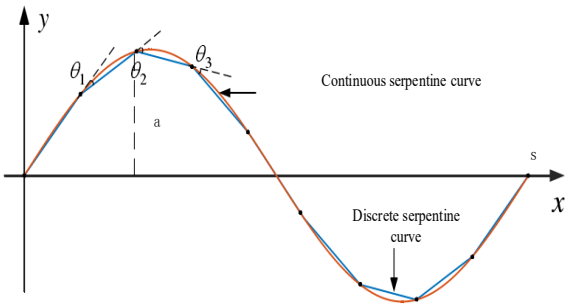

Figure 1. Discretization of serpentine curve

As shown in Figure 1, the discrete serpentine curve is approximately simulated as a continuous serpentine curve by discretization. Since the snake-like robot is a series of rigid joints with fixed length, it can not move continuously according to the serpenoid curve [8]. It is necessary to discretize the serpentine curve by segments, and the length of each segment is the length of a single joint of the robot. The overall length of the snake like robot is L. If the robot is divided into n segments according to the number of joints, the length of each segment is L/n, that is, the length of the joint module of the snake like robot. The length along the robot body from the initial point of the snake like robot to the i joint point is$s_i = iL/n$, $i = 0, 1, \ldots, n$. The discrete diagram of serpentine curve is shown in Figure 1. The discrete points (x (s), y (s)) on the serpentine curve after discretization. the position of joints, can be expressed as follows:

$$\begin{aligned} x_i &= \sum_{k=1}^{i}\frac{L}{n}\cos[a\cos(\frac{kb}{n})+\frac{kc}{n}] \\ y_i &= \sum_{k=1}^{i}\frac{L}{n}\sin[a\cos(\frac{kb}{n})+\frac{kc}{n}] \end{aligned} \tag{3}$$

Mark the connecting rod between each position point as i, and define the angle of x positive direction turning anticlockwise to the i-th connecting rod direction as $\varphi_i, i=1,2,...n$, then Equation (4) can be obtained:

$$\tan\varphi_i\frac{\sum_{k=1}^{i}\frac{L}{n}\cos[a\cos(\frac{kb}{n})+\frac{kc}{n}]}{\sum_{k=1}^{i}\frac{L}{n}\sin[a\cos(\frac{kb}{n})+\frac{kc}{n}]}=\tan[s\cos(\frac{ib}{n})+\frac{ic}{n}] \tag{4}$$

The angle between the connecting rod and the moving direction can be obtained as follows:

$$\varphi_i=[s\cos(\frac{ib}{n})+\frac{ic}{n}] \tag{5}$$

When analyzing the gait of the robot and making joint control, the angle between the extension lines of adjacent connecting rods is applied in practice θ_i :

$$\theta_i=\varphi_i-\varphi_{i+1}=\alpha\sin(i\beta+\frac{\beta}{2})+\gamma \tag{6}$$

where, $\alpha=2a\sin\frac{b}{2n}$ represents the amplitude of joint angle, $\beta=\frac{b}{2n}$ represents the phase difference between adjacent joints, and $\gamma=-\frac{c}{n}$ represents the control parameter of motion direction.

When the discrete serpentine curve propagates forward at angular velocity ω, it can be expressed as follows:

$$\varphi_i = \alpha \cos(\omega t + \frac{ib}{n}) + \frac{ic}{n} \tag{7}$$

From Equation (6) and Equation (7), it can be seen that the value of ω affects the change speed of φ_i, thus affecting the speed of the snake like robot. By changing the parameters *a, b, c* in the curve, the snake-like robot can move in different directions and at different speeds. For the snake like robot with orthogonal joints, only odd joints move in 2D planar meandering motion, and the initial angle of each joint can be any value. As long as the phase difference of adjacent odd joints is β, the winding motion can be guaranteed:

$$\begin{aligned} &\theta_{even} = A\cos(\omega t + (i-1)\beta), i = 1,3,5,.. \\ &\theta_{odd} = 0, i = 2,4,6,... \end{aligned} \tag{8}$$

where, θ_{even} is the horizontal joint function of the snake like robot; θ_{odd} is the vertical motion joint function of the snake like robot; *A* is the amplitude of the joint motion; *t* is the joint motion frequency; β is the adjacent joint phase.

1.1.2. Spine curve and discretization

When the snake-like robot is required to move in three dimensions according to the desired trajectory, a three-dimensional spine curve can be designed according to the motion constraints of the surrounding environment and the snake body [9, 10], and then the motion planning is carried out by discretizing the spine curve. According to the knowledge in differential geometry and based on FrenetSerret frame [11], a three-dimensional spine curve can be designed, as shown in Equation (9):

$$\begin{cases} \dfrac{dc}{ds} = e_1 \\ \dfrac{de_1}{ds} = \kappa(s)e_2 \\ \dfrac{de_2}{ds} = \kappa(s)e_1 + \tau(s)e_3 \\ \dfrac{de_3}{ds} = -\tau(s)e_2 \end{cases} \tag{9}$$

where κ is the curvature of the curve and τ is the torsion of the curve. The shape of the curve can be determined by the two. $c\{x(s), y(s), z(s)\}$ are the coordinates of point *s* on the curve, $\{e_1, e_2, e_3\}$ are orthogonal coordinate systems, e_1 represents the unit tangent vector at point *s*, e_2 represents the principal normal vector, e_3 represents the secondary normal vector at point *s*.

The joint configuration of the snake like robot is a single degree of freedom orthogonal joint, as shown in Figure 2.

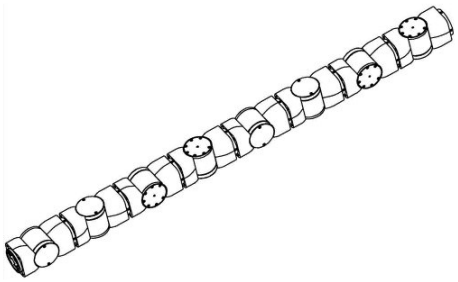

Figure 2. Orthogonal configuration of snake like robot

The Frenet-Serret frame of the spine curve of the snake like robot is shown in Figure 3.

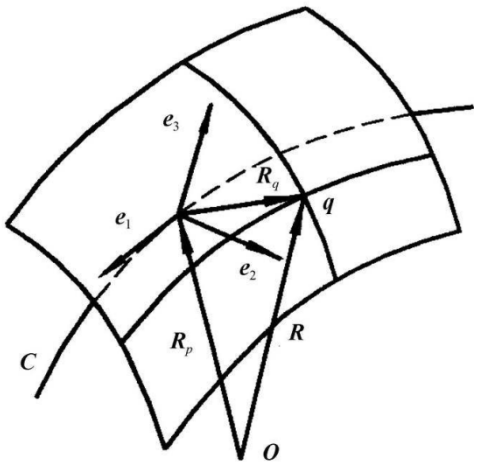

Figure 3. Frenet-Serret frame of spine curve

In order to plan the motion of climbing cylinder for snake-like like robot, it is necessary to design spiral rolling gait to complete the movement of climbing cylinder. Because of the constraint of the cylinder, the trajectory of the snake like robot is designed to be a cylindrical helix, and the spine curve is designed according to the cylindrical helix.

$$\begin{cases} x = r\cos\varphi \\ y = r\sin\varphi \\ z = p\varphi \end{cases} \tag{10}$$

After the design of the spine curve is completed, the spine curve needs to be discretized to calculate the corresponding joint angle. The discretization of planar arc and cylindrical helix is shown in Figure 4.

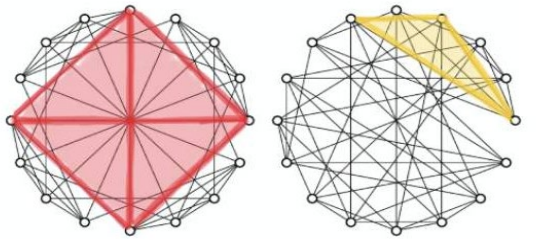

(a). Discretization of circular arc (b). Discretization of cylindrical helix

Figure 4. The discretization of planar arc and cylindrical helix

The equation of joint angle generated by discretization is as follows:

$$\theta_i = \begin{cases} \int_{s_1}^{s_2} \kappa(s)\sin\varphi, i = 1,3,5,... \\ \int_{s_1}^{s_2} \kappa(s)\cos\varphi, i = 2,4,6,... \end{cases} \quad (11)$$

The gait of planar rolling gait can be obtained as follows:

$$\theta_i = \begin{cases} \frac{2L}{r}\cos(\alpha t), i = 1,3,5,... \\ \frac{2L}{r}\sin(\alpha t), i = 2,4,6,... \end{cases} \quad (12)$$

The gait equation of spiral rolling is as follows:

$$\theta_i = \begin{cases} A\cos(\alpha t + \omega i), i = 1,3,5,... \\ A\sin(\alpha t + \omega i), i = 2,4,6,... \end{cases} \quad (13)$$

2. Design of Control System for Snake Like Robot

When the snake-like robot moves in the complex unknown space, the motion control system is required to have good real-time performance and openness, and can effectively avoid obstacles in the environment [12-14]. The snake like robot needs 15 motors to operate at the same time, and the control system needs strong processing ability. In this paper, the hybrid programming method of C++ and PCL, combined with CAN bus technology [15, 16], realizes the effective control process of gait coordination in the process of snake like robot movement.

2.1. Hardware design of control system

In view of the complexity of the snake-like robot's space attitude, a servo control system with TwinCAT software PCL as the center and can bus as the communication bus is constructed. The overall hardware structure of the snake robot control system is shown in Figure 5. It includes industrial PC, EtherCAT coupler, CAN master station, servo driver and servo motor.

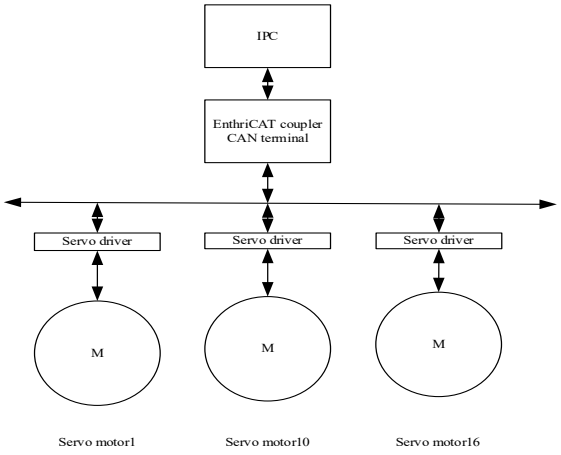

Figure 5 .Hardware structure of snake like robot control system

(1) EtherCAT coupler

EtherCAT coupler is mainly used to convert the transmission message from Ethernet to e-bus signal. A station can be composed of any number of EtherCAT terminal modules and a terminal module of a terminal station. The main parts should be illustrated in Figure 6.

In the control system, it is mainly used to connect the industrial PC and CAN master station, convert some instructions of the upper computer into e-bus signals and send them to the CAN master station, and then send them to the lower actuator, such as servo driver, through the CAN master station.

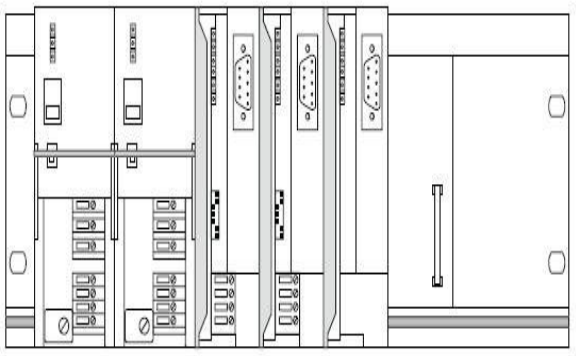

Figure 6. EtherCAT coupler

(2) CAN terminal

El6751 of bechoff company is selected as CAN master station. In EtherCAT network, any CANopen equipment can be integrated through El6751. The equipment itself CAN be used as master station or slave station. In the control system, it mainly realizes the communication function with CAN slave station equipment.

(3) Servo driver

The servo driver is the solowstldigital servo driver of Emlo. The driver is based on DSP and has CANopen interface. It can be used as a slave station in the control network to receive and send signals, so as to control the servo motor. At the same time, the position information on the code disk can be directly fed back to the upper computer. Solowestl servo driver integrates control circuit and drive circuit. It can be programmed by composer, the programming software of Emlo. It can also directly write the program in the upper computer to realize complex control algorithm [17, 18], which makes the motor control more intelligent and digital. In this project, only three servo drivers are used to control three servo motors synchronously to control the motion state of a single joint. In the motion control of snake like robot, position mode is used for parallel control.

2.1.1. Composition of servo system

Servo system is composed of servo driver and servo motor. The control system sends the control command to the servo driver through CAN bus. The servo driver receives the control command and drives the servo motor to move. At the same time, the position pulse received from the encoder is fed back to the control program through CAN bus. Elmo's digital servo driver is in the core position of the whole servo system. It not only has a variety of motion control modes, such as speed, position, return to zero and so on. It can also support complex

advanced position interpolation modes, such as PT (Position) speed time interpolation, ECM (Electronic Counter Measure) electronic cam, PVT (Process Verification Test) position time velocity interpolation, etc. At the same time, the CAN bus port of Emlo's digital servo driver is an important part of the whole control network. As a slave station of CAN bus in the control network, it can timely receive control instructions and send feedback information.

In the servo system, the standard three closed loop control system is adopted, including the position loop of the outer loop, the speed loop of the middle loop and the current loop of the innermost loop, as shown in Figure 7.

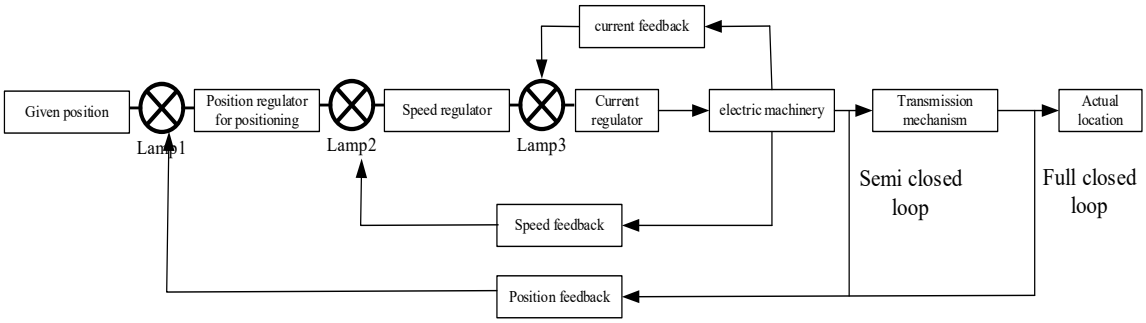

Figure 7. Structure of servo three loop control system

2.2. Software of control system

Combined with the discrete snake like robot gait, the hybrid programming method of C++ and TwinCAT soft PLT is used to integrate the gait coordination algorithm and operation interface in this system, so the interface function of ADS-DLL is selected. The specific process of quoting TcAdsDll is divided into the following parts.

(1) Add TcAdsDll header file

Install TwinCAT in the directory "C: \ TwinCAT \ ADSApi \ TcAdsDll \ Include" and "TcAdsDef.h" in the project file of VC++.

(2) Adding library function TcAdsDll.lib in VC++ Project

Add TcAdsDll.lib to linker input additional dependency in property configuration.

According to the above method, add TcAdsDll.hb, and the specific steps of how to open ads communication port are as follows: Firstly, define port variables and address variables, and then open ads communication port, then different discrete gait data types can be transmitted.

LongnErr,nPort; / / Define the port variables

AmsAddrAddr; / / Define AMS address variable

PAmsAddrpAddr = Addr; / / Define the port address variable

nPort = ADSPortOpen(); / / Open ads communication port

nErr = ADSGetLocalAddress(pAddr); / / Get the local port address

pAddr- > port = 805; / / point the pointer to port 805. The user's port number is defined according to his own definition. The following is the data function that sends the position data in the gait algorithm to the motor in the first section. The function of the position data sent to other motors is similar.

Where paddr is the address of ads device; 0x4020 is the base address, corresponding to the M register address in PLC; 0x00 is the offset address; 0x10 is the offset; FLOAT1-1 is the cache address of received data.

Then, the corresponding variables of FLOAT1-1are compiled in TwinCAT software PCL to save the position data sent and send to the servo driver at the same time, so as to drive the motor to move and realize the control of the snake like robot's gait coordination.

2.3. Development of control program

In the upper computer, the human-computer interaction function is mainly reflected in that it CAN switch different movement gait coordination modes according to different work needs and send them to the lower computer to realize the overall movement of the snake like robot. At the same time, the upper computer can also display the position of each joint in different states and the angle in the overall coordinate system. It can reflect the safety of snake-like robot in real time. There are three main motion modes of snake-like robot. Median mode: The initial state of the snake-like robot is in the neutral state; Follow mode: The head joint of the robot moves first, and then the gait of each joint moves along the path of the head joint; The backward mode: The snake-like robot can return according to its forward path. In the following mode and back mode, the actuator adopts position interpolation motion mode. In the lower computer, various motor running instructions are written by TwinCAT soft PCL program. In the middle mode, the middle position of the rope and lead screw is determined by the return value of the sensor. Under the premise of single motor movement, different movement gait coordination modes of the upper computer are implemented by using the motion function block in the soft PCL. Different modes of gait coordination control are realized by motor motion control, and the gait algorithm process is shown in Figure 8.

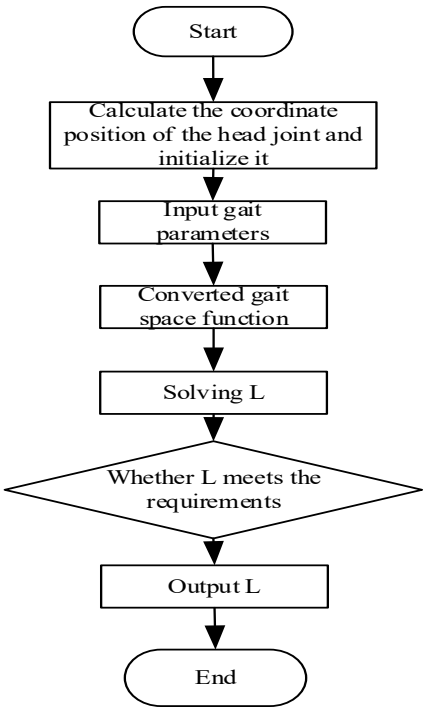

Figure 8. Flow chart of gait algorithm

In this way, the coordinated control of snake-like robot gait based on electromechanical tracking is realized, and the gait selection under environmental conditions is realized through the development of control program.

3. Experiment

In order to verify the effectiveness of the proposed method, the snake-like robot is controlled by a hierarchical control system on the experimental platform. The snake-like robot is made to carry out winding motion and plane rolling experiments, and the sensor data are collected to verify the reliability of the control system.

3.1. Construction of experimental platform

The computing rod and PCB board are installed in the head controller shell, and the camera is fixed at the front end of the head controller. The connection mode between the head controller and the joint is similar to that between the joints. The rear end of the head controller and one end of the joint has external threads. The two are connected through the connecting ring with internal thread, and the circumferential fixation is realized through the positioning pin and the positioning hole. External 28V DC power supply is required, and the power is supplied from the tail. The last joint can filter the power supply and provide current limiting protection, and provide matching resistance for PPSECO communication between joints. The snake like robot is equipped with 8 joints, each joint is distinguished by its own index number. The snake like robot prototype is shown in Figure 9.

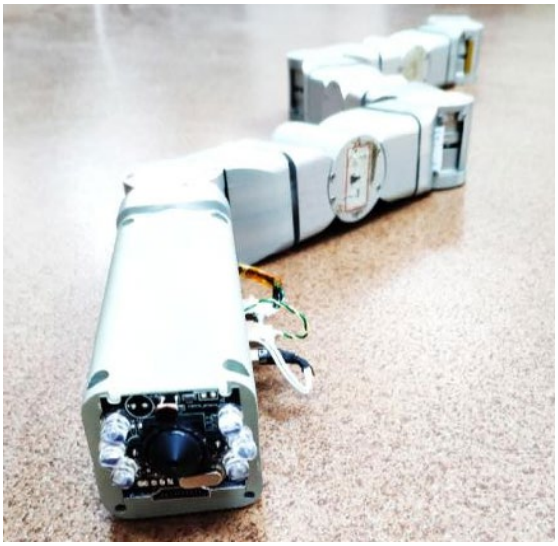

Figure 9. Prototype of snake-like robot

Figure 10 is the experimental platform. The system is composed of upper computer, router, DC power supply and snake like robot. The host computer and the snake robot establish a wireless connection, and the router establishes the local area network. The upper computer interface plays the role of human-computer interaction, which can be used to establish the connection and disconnection relationship with the snake like robot, select the robot's gait, and display the image observed by the snake robot's head in real time, display the sensor data and draw the curve. The DC power supply supplies 28V DC voltage to the snake like robot. According to the collected environmental data, the robot gait is planned and designed, and controlled by electromechanical tracking software.

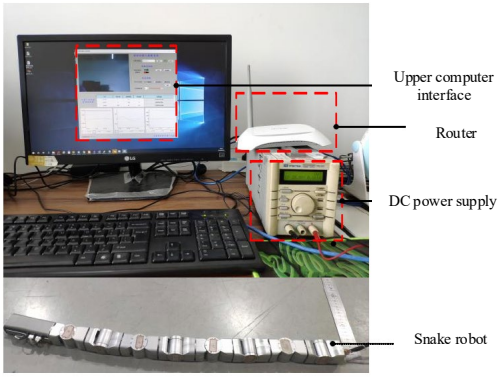

Figure 10. Experimental platform of snake like robot

The three-dimensional motion capture system used in this experiment is composed of eight infrared cameras, which are evenly distributed around the tested joint.

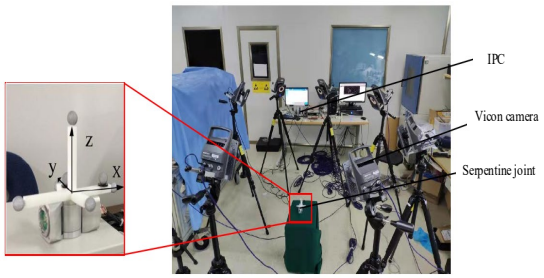

Figure 11. Measurement platform of vicon 3D motion capture system

3.2. Winding gait

Due to the snake like robot's sinuous motion, the whole body plane contacts with the ground, so it is required that the robot and the contact surface have large friction force to provide the motion power, and the normal friction force is greater than the tangential friction force. The surface of cloth with higher roughness is selected for the test. The movement process of the robot is shown in Figure 12, and the collected joint angle position information is shown in Figure 13.

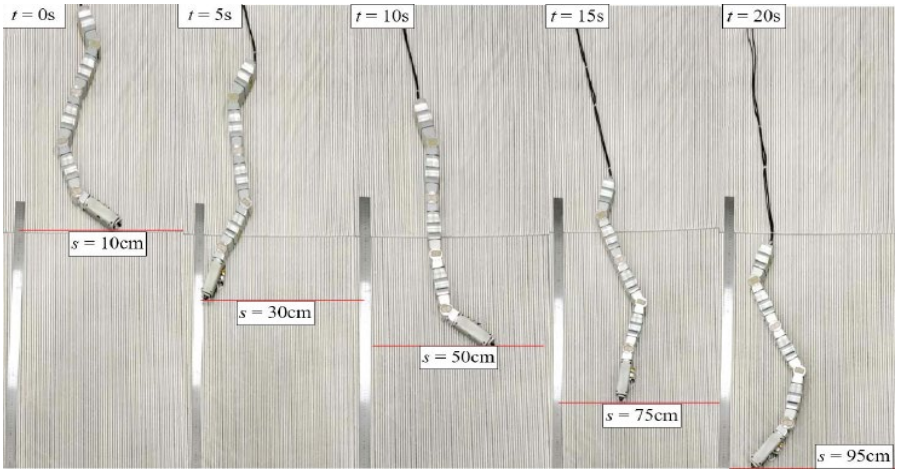

Figure 12. Serpentine robot winding motion

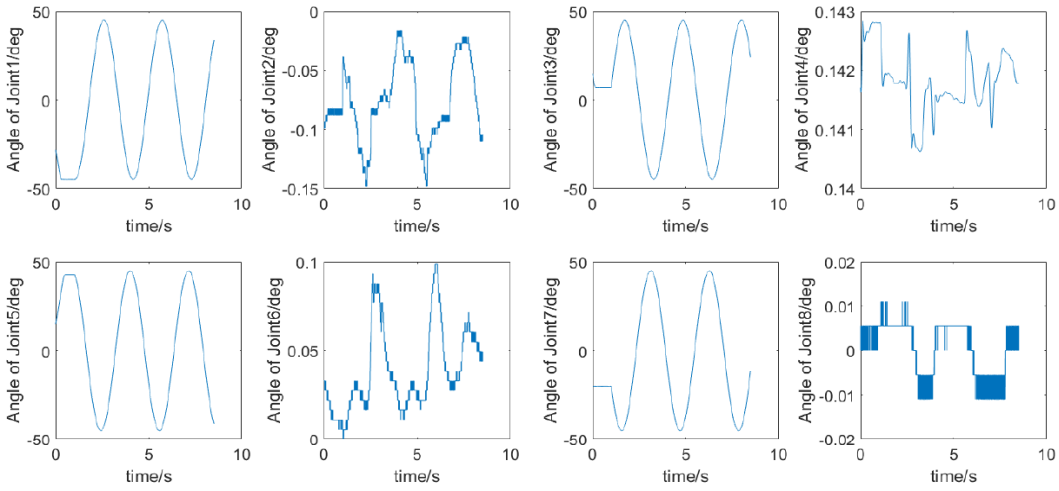

Figure 13. Angle of each joint in winding movement

Experimental results show that the average forward speed of the snake robot controlled by this method is 2.5 m/min. Based on the analysis of Figure 13, it can be seen that there is no sliding surface between the body of the robot and the friction force during the movement, which leads to better movement efficiency and faster movement speed. The results show that this method can effectively realize the coordinated control of robot gait in winding state.

3.3. Plane rolling gait

Take A = 20, ω = 0.5 to carry out the plane rolling gait experiment. The experimental process is the same as that of the winding gait experiment. The motion of each joint is shown in Figure 14. The upper computer reads the sensor data of the joint and saves it. The angle change curve of each joint during the movement process is shown in Figure 15. Take joint 2 as an example, the data of each sensor is shown in Figure 16.

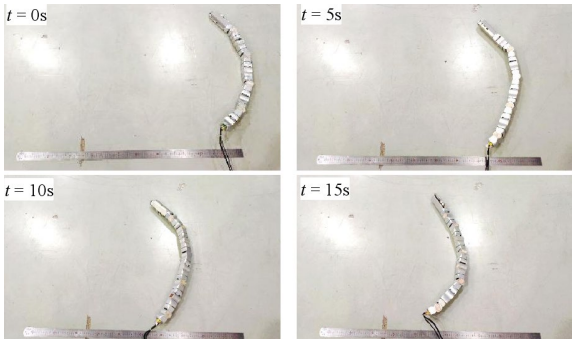

Figure 14. Planar rolling gait of snake like robot

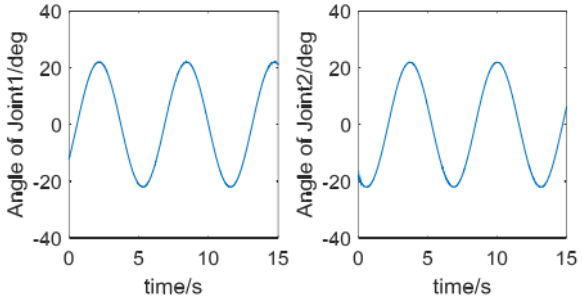

Figure 15. Variation curve of joint angle of snake like robot

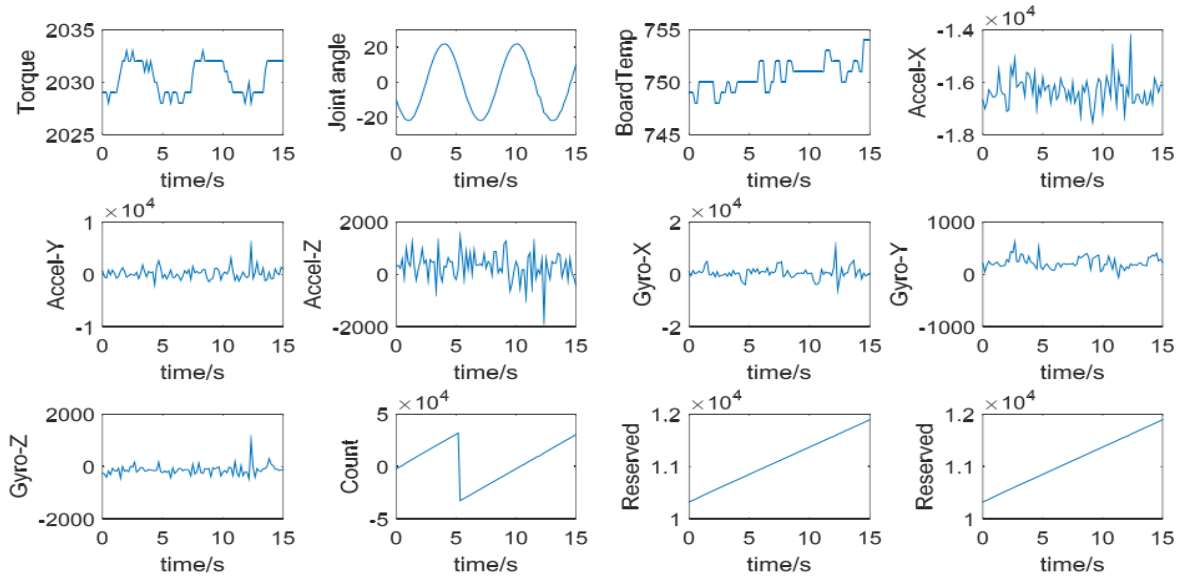

Figure 16. Joint 2 sensor information

It can be seen from the figure 16 that the speed of the snake like robot is positively correlated with the amplitude and period of the trigonometric function of each joint. When the amplitude is 20° and the frequency is the same as that of the meandering motion, the forward speed of the planar rolling gait is about 2.4 m/min, which is faster than that of the meandering motion. The reason is that the normal friction force is far greater than the tangential friction force when the snake-like robot with orthogonal joints is in planar meandering motion, and the friction performance improves the motion effect. The results show that the proposed method is effective and the control effect is stable.

4. Conclusions

In this paper, firstly, the motion planning of the snake like robot is carried out through the curve discretization, and then the coordinated control of the snake like robot gait is realized by the method of mechanical and electrical tracking combined with software design. The online motion control program of the snake like robot is compiled by using PLC and C++ mixed programming. The control system of hybrid programming is more intelligent, and all the work can be completed in a PC. It's more convenient to operate. The prototype of snake like robot is fabricated and assembled, and experiments are carried out to verify the stability and reliability of the proposed control method. The experimental results show that the robot can be controlled to travel at a speed of 2.4 m/min in the plane rolling motion and 2.5 m/min in the snake-like motion. By monitoring the change of each joint angle, it can be found that this method can periodically control the joint rotation, thus realizing the accurate and fast robot travel. In the future research, we can try to optimize the mechanism design of snake like robot to improve the effect of gait coordination control.

References

[1] Huq, N.M.L.; Khan, M.R.; Shafie, A.A.; Billah, M.M.; Ahmmad, S.M. Motion investigation of a snake robot with different scale geometry and coefficient of friction. Robotics, 2018, 7(2): 1-11.

[2] Koopaee, M.J.; Bal, S.; Pretty, C.; Chen, X.Q. Design and development of a wheel-less snake robot with active stiffness control for adaptive pedal wave locomotion. Journal of Bionic Engineering, 2019, 7(16): 593-607.

[3] Berthet-Rayne, P.; Leibrandt, K.; Gras, G.; Fraisse, P.; Crosnier, A.; Yang, G.Z. Inverse kinematics control methods for redundant snake-like robot teleoperation during minimally invasive surgery. IEEE Robotics and Automation Letters, 2018, 3(7): 2501-2508.

[4] Kano, T.; Yoshizawa, R.; Ishiguro, A. Snake-like robot that can generate versatile gait patterns by using tegotae-based control. Conference on Biomimetic &Biohybrid Systems. Springer, Cham, 2018, 7(7): 249-254.

[5] Ryo, A.; Ryota, T.; Motoyasu, T.; Toru, A. Head-trajectory-tracking control of a snake robot and its robustness under actuator failure. IEEE Transactions on Control Systems Technology, 2018, 11(6): 1-9.

[6] Malayjerdi, M.; Tootoonchi, A.A.Analytical modeling of a 3-D snake robot based on sidewinding. International Journal of Dynamics and Control, 2018, 6(1): 1-11.

[7] Mukherjee, J.; Roy, S.; Kar, I.N.; Mukherjee, S. A double layered artificial delay based approach for maneuvering control of planar snake robot. Journal of Dynamic Systems Measurement and Control, 2018, 141(4): DS-18-1323.

[8] Kaneguchi, A.; Ozawa, J.; Minamimoto, K.; Kaoru, Yamaoka. A rat model of arthrofibrosis developed after anterior cruciate ligament reconstruction without rigid joint immobilization. Connective Tissue Research, 2019, (2): 1-14.

[9] Wei, B.L.; Jiao, H.T. Fault status information monitoring technology for large complex electromechanical system. Jordan Journal of Mechanical and Industrial Engineering, 2021, 15(1): 105-112.

[10] Manzoor, S.; Cho, Y.G.; Choi, Y. Neural oscillator based CPG for various rhythmic motions of modular snake robot with active joints. Journal of Intelligent & Robotic Systems, 2019, (6): 127-132.

[11] Tang, J.G.; Li, B.; Chang, J.; Zhang, A.Q. Unscented Kalman-filter-based sliding mode control for an under water gliding snake-like robot. Chinese Science, 2020, 63(1): 209-221.

[12] Omisore, O.M.; Han, S.P.; Ren, L.X.; Zhao, Z.C.; Wang, L. A teleoperated snake-like robot for minimally invasive radiosurgery of gastrointestinal tumors. International Conference on Autonomous Robot Systems and Competitions (ICARSC). IEEE, 2018.

[13] Takagi, Y.; Ishikawa, M.; Osuka, K. Development and control experiment of a snake-like robot with controllable side-thrust links. IFAC-Papers On Line, 2019, 52(15): 229-234.

[14] Mutawe, S.; Hayajneh, M.; BaniHani, S.; Qaderi, M.A. Simulation of trajectory tracking and motion coordination for heterogeneous multi-robots system. Jordan Journal of Mechanical and Industrial Engineering, 2021, 15(4): 337-345.

[15] Nouby, M. Analysis and realization of CAN bus technology in industrial conveyors. International Journal on Recent and Innovation Trends in Computing and Communication, 2020, 8(5): 20-24.

[16] Dear, T.; Buchanan, B.; Abrajan-Guerrero, R.; Kelly, S.D. Locomotion of a multi-link non-holonomic snake robot with passive joints. The International Journal of Robotics Research, 2020, 5(35): 598-616.

[17] Chen, C.L.; Tsai, M.C. Kinematic and dynamic analysis of magnetic gear with dual-mechanical port using block diagrams. IEEE Transactions on Magnetics, 2018, 1-5.

[18] Lim, J.; Yang, W.; Shen, Y.; Yi, J. Analysis and validation of serpentine locomotion dynamics of a wheeled snake robot moving on varied sloped environments. 2020 IEEE/ASME International Conference on Advanced Intelligent Mechatronics (AIM), 2020, 1069-1074.

JJMIE

Volume 16, Number 1, January. 2022
ISSN 1995-6665
Pages 97 - 104

Jordan Journal of Mechanical and Industrial Engineering

Trajectory Tracking Control Algorithm of Six Degrees of Freedom Industrial Robot

Zhenhua Meng*

Engineering Training Centre, Yantai University, Yantai 264005, China

Received 14 July 2021 *Accepted 22 December 2021*

Abstract

Because the robot system has the characteristics of time-varying, strong coupling, and nonlinear system, the influence of many factors, such as load change, friction, interference and so on, is inevitable when the robot system is running in the industrial field. Therefore, the adaptive ability of the control system is required to be better. This paper discusses the pose description of robot and the transformation between coordinate systems. Under the condition of satisfying various constraints, the shortest running time is used as the optimization objective function to optimize the motion trajectory of six degrees of freedom Industrial Robot. The purpose is to minimize the running time of six degrees of freedom Industrial Robot under the conditions of point-to-point motion or along the given trajectory, and improve the working efficiency of the robot. The experimental results show that the trajectory tracking control method can meet the speed and acceleration constraints of the robot in Cartesian space and joint space at the same time, realize the overall motion smoothness of six degrees of freedom Industrial Robot, and maintain high motion efficiency.

Keywords: Six degrees of freedom; Six degrees of freedom Industrial Robot; Trajectory; Tracking control algorithm.

1. Introduction

Trajectory tracking control is a key technical module in the design of 6-DOF Industrial Robot, which focuses on the research of various trajectory tracking control algorithms to meet the diverse needs of users [1, 2]. At present, trajectory tracking control is mainly designed for three aspects: running time, energy optimization and stability. It is always the focus of research to find a reliable and stable algorithm to keep the motion of six degrees of freedom Industrial Robot smooth and stable, avoid the sudden change of speed and acceleration, and reduce the vibration and impact of the machine. It is also the basis and guarantee of other trajectory tracking control algorithms. Trajectory tracking control can be carried out in both joint space and Cartesian space [3]. The trajectory tracking control in joint space is easy to calculate, which can make the trajectory of robot joint smooth and continuous, and avoid the problem of robot singularity. Therefore, the trajectory tracking control in joint space can make the robot move smoothly and safely, but the disadvantage is that it is unable to control the robot end effector to move according to the expected trajectory. However, the trajectory tracking control based on Cartesian space can make the robot move according to the expected Cartesian coordinate system, which can clearly reflect the needs of users, and it is intuitive and clear. However, the disadvantage is that it needs to repeatedly carry out inverse kinematics to obtain the required joint information and then transmit it to the robot controller. Due to the nonlinear structure of six degrees of freedom Industrial Robot, it is difficult to judge the joint space variables when tracking the trajectory in Cartesian space. Therefore, it is possible that the joint motion exceeds the upper limit of velocity or acceleration when the end effector satisfies the Cartesian space motion constraint [4]. To solve the above problems, this paper optimized the structure of six degrees of freedom Industrial Robot and used the actuator with high load capacity and speed to reduce friction resistance. However, from the perspective of trajectory tracking control, the current common method used by Industrial Robots is to limit the speed and acceleration of the end effector according to the actual situation, so as not to cause vibration and other undesirable phenomena of the robot joint movement because of the excessive speed and acceleration of the end effector.

A joint space trajectory optimization algorithm which can avoid singularity in the process of robot motion is designed and studied by You et al. [5]. Using the redundancy of a joint's function during a six-degree of freedom robot's task, the joint limitation and singularity of the robot are taken as constraints, and the time weighted average (TWA) method is used to optimize the calculation. The time optimal trajectory tracking control algorithm was first proposed by using the position velocity phase diagram [6]. Its central idea is to use the joint angle position on the path as the abscissa parameter to describe the dynamic equation of the Industrial Robot.

* Corresponding author e-mail: mzh02021080@163.com.

The dynamic programming algorithm is introduced by Campeau-Lecours et al. [7]. However, the trajectory tracking control algorithm introduced before ignores the change of driving torque when establishing the dynamic mathematical model. Therefore, the produced trajectory will have discontinuous joint torque and acceleration, which will lead to bad effect. Therefore, this paper proposes the research on motion trajectory tracking control algorithm of six degree of freedom Industrial Robot. Firstly, the position and pose of the robot and the transformation between the coordinate systems are described. Under the constraint conditions, taking the shortest running time as the optimization objective function, the motion trajectory of the 6-DOF Industrial Robot was optimized, so as to improve the working efficiency of the robot. The results show that the trajectory tracking control method can achieve the overall motion smoothness of six degrees of freedom Industrial Robot, and can maintain high motion efficiency.

2. Kinematics and Dynamics Analysis of Six Degrees of Freedom Industrial Robot

The kinematics of six degrees of freedom Industrial Robot mainly studies the way and nature of the robot's motion process, neglecting the external forces. In the kinematics of six degrees of freedom Industrial Robot, the calculations involved are the mathematical factors associated with the mode of motion [8]. So the kinematics research of the six degrees of freedom Industrial Robot includes all the time and geometric parameters related to the motion [9]. In the field of robot dynamics, the effect and influence of environmental dynamic factors and human dynamic factors on robot motion are studied.

2.1. Pose description

The position and attitude of the end-effector in the base coordinate system are described to represent the working attitude of the 6-DOF Industrial Robot. Therefore, it is necessary to customize the uniform standard to describe the posture and posture in the robot space, including work actuator and machining parts.

(1) Location description

By measuring the three-dimensional coordinate component of a location point in the base coordinate system, a position vector in the form of 3×1 describing the point can be obtained [10]. The motion space of six degrees of freedom industrial robots is very complex, so multiple coordinate systems are established to analyze and discuss the motion between the robot and the parts. In order to clearly represent the coordinate system of a part or a position point, the reference coordinate system is marked in the left front of the position vector to be represented. For example, P_A, which indicates that the value of P_A is represented by the distance along the axis $\{A\}$.

$$P_A = \begin{Bmatrix} P_x \\ P_y \\ P_z \end{Bmatrix} \tag{1}$$

where the elements of the vector are indicated by subscripts x, y, z, and a position vector is used to describe the position of the midpoint in space.

(2) Attitude description

In practical engineering applications, it is often necessary not only to represent the points in space, but also to describe the attitude of objects in space. As shown in Figure 1, vector X_A directly determines a certain point between the operating actuators. Only when the attitude of the actuator is known can the position of the actuator be fully determined [11]. In order to describe the pose of an object, a coordinate system can be fixed on the object and its representation relative to the reference system is given.

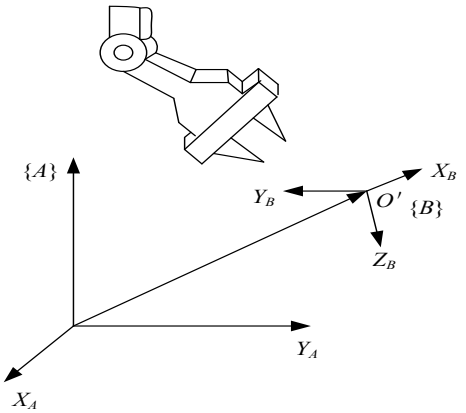

Figure 1. Pose of terminal actuator of Industrial Robot with six degrees of freedom

In Figure 1, the known coordinate system a $\{B\}$ is fixed to the end effector of six degrees of freedom Industrial Robot in some way. $\{B\}$ relative to the description in $\{A\}$ is enough to represent the attitude of the end of six degrees of freedom Industrial Robot. $\hat{X}_B$, $\hat{Y}_B$ and $\{B\}$ are used to represent the unit vector of the axis direction of coordinate system $\{B\}$ in coordinate system $\{A\}$. The three unit vectors are arranged in order into a 3×3 matrix, which is called rotation matrix. Since this special rotation matrix is the expression of $\{B\}$ relative to $\{A\}$, it is represented by the symbol R_B^A.

$$R_B^A = \left[X_B, Y_B, Z_B\right] = \begin{bmatrix} r_{11} & r_{12} & r_{13} \\ r_{21} & r_{22} & r_{23} \\ r_{31} & r_{32} & r_{33} \end{bmatrix} \tag{2}$$

(3) Combination of position and attitude

After getting the position and attitude of the terminal actuator of six degrees of freedom Industrial Robot. They can be combined in what is called a pose. In the kinematics of six degrees of freedom Industrial Robot mechanism, the position and attitude usually change together, so the position and attitude can be combined into a mathematical variable, which is recorded as the pose. R_B^A and P_{BORG}^A are used to describe the pose of coordinate system $\{B\}$ in coordinate system $\{A\}$.

$$\{B\} = \left\{R_B^A, P_{BORG}^A\right\} \tag{3}$$

where P_{BORG}^A is the position vector determining the origin of the coordinate system $\{B\}$.

2.2. Transformation of coordinates

In the application of six degrees of freedom Industrial Robots, it is often necessary to describe the same part in

different operating space. So the same quantity can be described in different space by the transformation between coordinate systems.

(1) Translation transformation of coordinate system

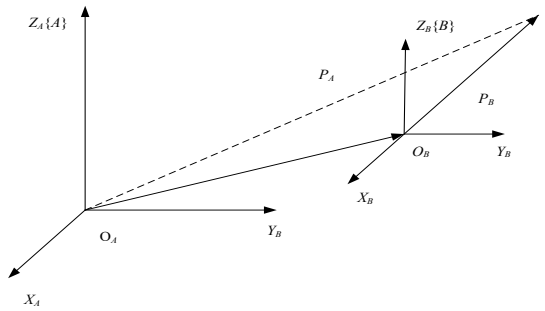

Figure 2. Translation transformation

As shown in Figure 2, it is a translation of the coordinate system. The 3D vector P_B refers to the position of P point in coordinate system $\{B\}$. If the coordinate system $\{A\}$ and $\{B\}$ have the same attitude, in this case, $\{B\}$ can obtain $\{A\}$ by translation. If $\{A\}$ coordinate system is needed to describe the space point, the position of the origin of coordinate system $\{B\}$ in $\{A\}$ can be expressed by vector P_{BORG}^{A} .Since the two vectors have the same attitude in the same space, we can use the offset plus the position of P in the coordinate system $\{B\}$ to obtain P_A :

$$P_A' = P_B + P_{BORG}^{A} \tag{4}$$

(2) Rotary transformation of coordinates

As shown in Figure 3, the rotation transformation of the coordinate system is realized by a 3×3 rotation matrix formed by three unit vectors arranged together. If this matrix refers to the description of $\{B\}$ relative to $\{A\}$, represented by the symbol R_B^A , then there is:

$$P_A'' = R_B^A \times P_B \tag{5}$$

By Equation (5), the description F of P_B point in space relative to $\{B\}$ is transformed into the description P_A of the point relative to $\{A\}$.

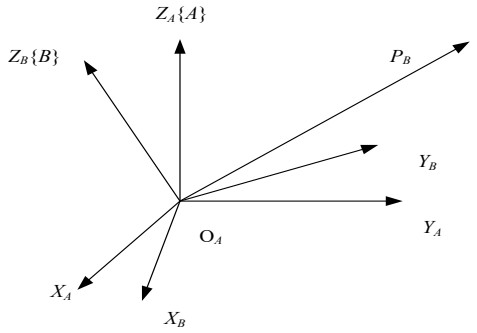

Figure 3. Rotation transformation

(3) Complex transformation of coordinates

As can be seen from Figure 4, the composite transformation graph is usually a transformation from one coordinate system to another, which requires translation and rotation. The origin of coordinate system $\{B\}$ and coordinate system $\{A\}$ do not coincide, there is a vector offset. The vector determining the origin of $\{B\}$ is represented by P_{BORG}^{A} , and the rotation of $\{B\}$ relative to $\{A\}$ is described by R_B^A . Given P_B , in order to find $\hat{P}_A$, first transform P_B into an intermediate coordinate system, which has the same attitude as $\{A\}$, and the origin coincides with the origin of $\{B\}$. Then the origin is translated by vector addition.

$$\hat{P}_A = R_B^A \times P_B + P_{BORG}^{A} \tag{6}$$

where $\hat{P}_A$ represents the composite transformation of a vector description from one coordinate system to another. A new concept is derived from Equation (6):

$$\tilde{P}_A = T_B^A \times P_B \tag{7}$$

In Equation (7), P_B is a homogeneous representation of four-dimensional vector, and T_B^A is a 4×4 -form homogeneous transformation matrix:

$$T_B^A = \begin{bmatrix} R_B^A & P_{BORG}^{A} \\ 000 & 1 \end{bmatrix} \tag{8}$$

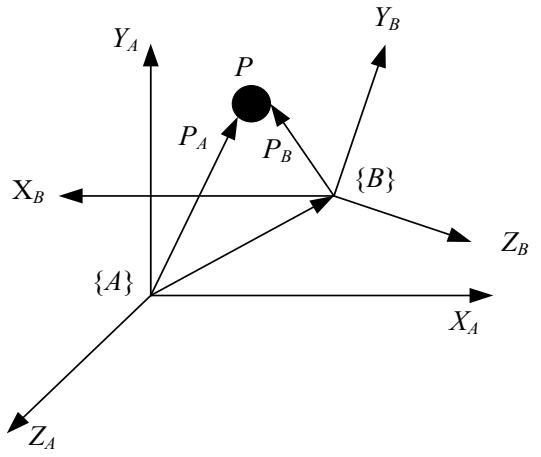

Figure 4. Composite transformation

3. General Trajectory Tracking Control Algorithm for Industrial Robots with Six Degrees of Freedom

In Cartesian space, it can also be done in joint space, but the trajectory curve functions must be continuous and smooth so that the end effector can move smoothly without large fluctuations [12, 13]. Trajectory tracking control in right angle space refers to the function that the position, attitude, velocity and acceleration of the terminal actuator are expressed as time, while that in joint space refers to the function that the angle of the joint is expressed as time, and it constrains its angular velocity, angular acceleration, force and torque.

Rectangular coordinate space trajectory tracking control in the workspace coordinate system, tracking control results are very intuitive, can clearly observe the end of the movement of the trajectory. However, the cartesian space trajectory requires a large amount of calculation, so it is necessary to ensure the accuracy of the trajectory by fast calculation speed. In addition, it is not guaranteed that there is no singular point, and the singular point can not be tracked. Under certain circumstances, the linear path in joint space is easy to realize, but the linear path in Cartesian space is impossible to realize. In addition, the motion between two points may cause a

mutation in the joint value of six degrees of freedom Industrial Robot [14]. In order to solve the above problems, six degrees of freedom Industrial Robot can be specified to pass through the intermediate points to avoid these singular points. Due to the problems mentioned above, most current six degrees of freedom trajectory tracking controllers can generate trajectory in both joint space and right angle space. Users usually apply the joint space tracking control method, and only apply the cartesian coordinate space tracking control when necessary.

3.1. Joint space trajectory tracking control

For trajectory tracking control in joint space, it is necessary to determine the arm pose of the Industrial Robot at the starting point and the ending point. When interpolating joints, a series of constraints should be satisfied. Under all constraints, different types of joint interpolation functions can be selected to generate different trajectories.

Now we consider the general problem that the terminal actuator of six degrees of freedom Industrial Robot moves from initial position to target position in a certain time. First of all, we need to use the inverse kinematics calculation to solve the joint position of a group of initial and final positions [15, 16]. Therefore, a smooth function $q(t)$ of joint angle can be used to describe the trajectory of the end effector. The value of $q(t)$ at time $t=0$ is the initial joint angle q_0, and the value of t_f at the terminal time is the terminal joint angle q_f. Obviously, there are many smooth functions satisfying this condition, and the cubic spline interpolation diagram is shown in Figure 5.

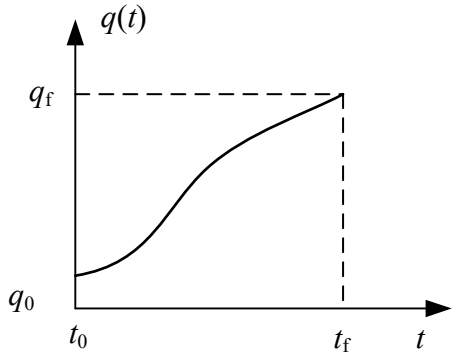

Figure 5. Cubic spline interpolation diagram

In order to ensure the smooth operation of the joint, the trajectory function $q(t)$ of each joint should meet at least four constraints: two end point position constraint and two end point velocity constraint.

The end position constraint contains the joint angles given by the start pose value and the end pose value respectively. The value of $q(t)$ at time $t_0=0$ is equal to the angle q_0 of the starting joint, and the value of t_f at the terminal time is equal to the angle q_f of the terminal joint, i.e.:

$$\begin{cases} q(0)=q_0 \\ q(t_f)=q_f \end{cases} \tag{9}$$

In order to meet the requirement of continuous joint velocity, the joint angular velocity at the starting and ending points can be simply set to zero:

$$\begin{cases} \dot{q}(0)=q_0 \\ \dot{q}(t_f)=q_f \end{cases} \tag{10}$$

A cubic polynomial can be uniquely determined by the above four constraints:

$$q(t)=a_0+a_1t+a_2t^2+a_3t^3 \tag{11}$$

3.2. Cartesian space trajectory tracking control

3.2.1. Linear trajectory tracking control

The trajectory tracking control of a straight line is to calculate the position and attitude of the middle point (interpolation point) on the trajectory of a straight line by knowing the position and attitude of the first and last points of the line, and to use the linear function of parabolic transition, which means to add a parabolic buffer curve segment within the neighborhood of two points when linear interpolation is used between the positions and attitudes of two points [17]. Because the second derivative of the parabola is a constant, that is, the acceleration is constant in the corresponding curve segment, the trajectory can be smoothly transferred, and the displacement and velocity can be continuous on the whole trajectory curve. A function consisting of two parabolic curves and a linear function connected smoothly is defined as a linear function transitioning to a parabolic curve. In order to design the trajectory curve, the same constant acceleration value is used in the transition line of the two parabolas, but the positive and negative values are opposite. The normalized factor can be solved in the following way.

Let the velocity of the straight line segment on the linear function of the parabola transition be v and the acceleration of the parabolic segment be a. Then the motion time and displacement of the parabolic line segment are:

$$T_b=\frac{v}{a} \tag{12}$$

$$L_b=\frac{1}{2}aT_b^2 \tag{13}$$

The total displacement and time of the linear motion are as follows:

$$L=\sqrt{(x_2-x_1)^2+(y_2-y_1)^2+(z_2-z_1)^2} \tag{14}$$

$$T=2T_b+\frac{L-2L_b}{v} \tag{15}$$

It is assumed that the linear segment velocity of the linear function of parabolic transition is v, and the acceleration of parabolic segment is a, rather than the total time of a given motion. The main consideration is that all six degrees of freedom Industrial robots have motion speed and acceleration constraints, and different six degrees of freedom Industrial robots have different constraint conditions, so velocity and acceleration are taken as input variables.

3.2.2. Trajectory tracking control of spatial arcs

In order to control the trajectory of circular arc in Cartesian space, it is necessary to use the coordinate system transformation, that is, to establish a new rectangular coordinate system on the plane where the circular arc is located, and obtain the values of the circular interpolation points in the new coordinate system, then to map these values back to the old coordinate system and find out the values of the interpolation points in the old coordinate system, and the displacement curve of circular interpolation also adopts linear function of parabola transition.

Three points can uniquely determine an arc. Suppose that the end effector of six degrees of freedom Industrial Robot passes through the intermediate point P_1 from the starting position P_2 to the terminal point P_2, if these three points are not collinear, there must be an arc from the starting point P_1 through the middle point P_2 to the end point P_3. This paper introduces the solving steps of arc trajectory tracking control.

The center $P_0(x_0, y_0, z_0)$ of the circle and the three points r, $P_1(x_1, y_1, z_1)$, $P_2(x_2, y_2, z_2)$ and $P_3(x_3, y_3, z_3)$ are calculated to determine the unique plane M, whose equation can be expressed as:

$$M = \begin{vmatrix} x - x_3 & y - y_3 & z - z_3 \\ x_1 - x_3 & y_1 - y_3 & z_1 - z_3 \\ x_2 - x_3 & y_2 - y_3 & z_2 - z_3 \end{vmatrix} \tag{16}$$

The equation of plane T passing through the midpoint of P_1 and P_2 and perpendicular to P_1 and P_2 is as follows:

$$T = \left[x - \frac{1}{2}(x_1 + x_2)\right](x_2 - x_1) + \left[y - \frac{1}{2}(y_1 + y_2)\right](y_2 - y_1) + \left[z - \frac{1}{2}(z_1 + z_2)\right](z_2 - z_1) \tag{17}$$

The equation of plane S passing through the midpoint of P_2 and P_3 and perpendicular to P_2 and P_3 is as follows:

$$S = \left[x - \frac{1}{2}(x_3 + x_2)\right](x_3 - x_1) + \left[y - \frac{1}{2}(y_3 + y_2)\right](y_3 - y_2) + \left[z - \frac{1}{2}(z_3 + z_2)\right](z_3 - z_2) \tag{18}$$

Combined with the three plane equations M, T and S, the elimination method can be used to solve the center $P_0(x_0, y_0, z_0)$ of the circle. However, attention should be paid to the situation when the denominator is zero in the process of elimination. Then the radius can be obtained as follows:

$$r = \sqrt{(x_1 - x_0)^2 + (y_1 - y_0)^2 + (z_1 - z_0)^2} \tag{19}$$

Based on the above results, the interpolation points on the arc can be obtained. The three attitude angles of each interpolation point can be calculated respectively according to the linear function of the parabolic transition of displacement curves. The joint angle of each interpolation point can be obtained by inverse kinematics solution of the position and pose of each interpolation point.

Trajectory tracking control in joint space and Cartesian space are discussed. Linear Trajectory tracking control and arc Trajectory tracking control are discussed in Cartesian space. The trajectory tracking control algorithm of space line and arc is the most basic and mature algorithm, which has been widely used in the six degrees of freedom Industrial Robots. But it is necessary to determine the velocity function according to the specific requirements, that is, to determine the normalized factor in the algorithm, and the normalized factor is a linear function with a parabolic transition.

4. Experimental Analysis

4.1. Parameter setting

In view of the fact that there is no specific dynamic parameters of the actuator, and the amount of dynamic calculation is huge, the error influence is more, and it is inconvenient to observe and analyze, so the moment constraint is not considered here, and the constraint conditions are simplified. The former three joints are taken as examples. In order to compare the data and prove the optimization of the algorithm, the set parameters can be selected according to the simulation results of trapezoidal acceleration and deceleration trajectory tracking control. According to the results of Cartesian trajectory tracking control by trapezoidal acceleration and deceleration of robot, it can be seen that the maximum velocity of the first to the third joint is about 0.4 rad/s, 0.1 rad/s, 0.25 rad/s, and the maximum acceleration is about 0.3 rad/s^2, 0.1 rad/s^2 and 0.2 rad/s^2 respectively. The six values are used as the constraints of the first three joints of the multi constraint trajectory tracking control algorithm. Given that the maximum acceleration and maximum velocity of the end effector in Cartesian coordinate system are $V_{\max}$=0.25 m/s, $A_{\max}$=0.25 m/s^2, and the error factor is g_p=0.0025 m, g_v=0.01 m/s. The starting and ending conditions of trajectory are P_0 = (0.5963, -0.1500, -0.0144) and P_1 = (0.3963, 0.3500, -0.0144), and the velocities of both start and end points are zero, and the interpolation period of trajectory tracking control is 0.1 s. The complete parameters are shown in Table 1.

Table 1 Simulation parameters table

Parameter name	Parameter value
Initial position	(0.5963, -0.1500, -0.0144)
Terminal position	(0.3963, 0.3500, -0.0144)
Initial joint velocity	$\dot{q}_t(t_0) = 0, i = 1, 2, ..., 6$
End joint velocity	$\dot{q}_t(t_f) = 0, i = 1, 2, ..., 6$
End effector speed and acceleration constraints	$V_{\max} = 0.25$ m/s, $A_{\max} = 0.25$ m/s
Joint velocity and acceleration constraints	$\dot{q}_{\max} = (0.4 \text{ rad/s}, 0.1 \text{ rad/s}, 0.25 \text{ rad/s})$ $\dot{q}_{\max} = (0.3 \text{ rad/s}, 0.1 \text{ rad/s}, 0.2 \text{ rad/s})$

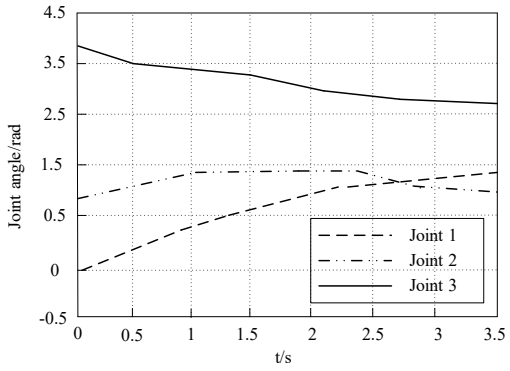

Figure 6. Joint angle

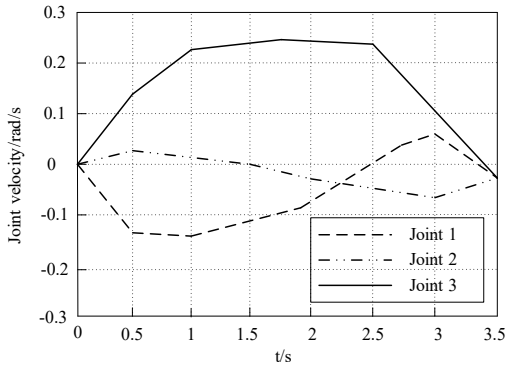

Figure 7. Joint velocity

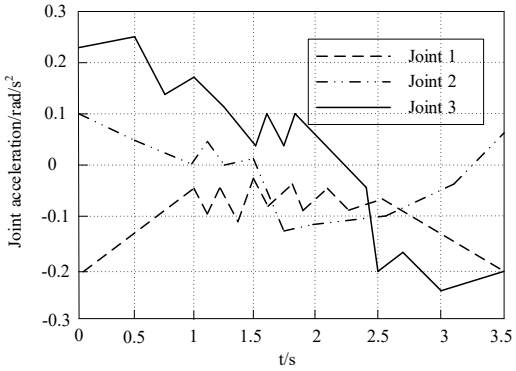

Figure 8. Joint acceleration

Figure 6 to Figure 8 are the curves of the first three joint angles of six degrees of freedom Industrial Robot. It can be seen from Figure 6 that the changes of the angles of the three joints are smooth and continuous during the whole movement period, and there is no sudden change. This is because the upper limit of joint velocity and acceleration is restricted in the trajectory tracking control algorithm. As shown in Figure 7 and Figure 8 are the curves of joint velocity and acceleration in the process of trajectory tracking control. It can be seen from the curve that the velocity and acceleration of the three joints are within the upper limit of the constraint from beginning to end, and the velocities and accelerations of these three joints are very close to their upper limits in some different periods of time, which is due to the nonlinear structure of six degrees of freedom Industrial Robot. The reason is that the time of acceleration or deceleration of each joint is different. Compared with the trapezoidal acceleration and deceleration algorithm with the same joint velocity and acceleration constraints, the Simulation results show that the 6-DOF Industrial Robot has shorter movement time.

In order to further verify the effectiveness of the trajectory tracking control algorithm for six degrees of freedom Industrial Robot, a simulation example is added to analyze and verify the algorithm. The initial position was taken as P_0 = (0.5963, -0.1500, -0.0144), and the end position was taken as P_2 = (4.7556, 0.6000, -2.5728). Except for the joint constraints, other parameters are consistent with the above simulation examples. Firstly, the trapezoidal acceleration and deceleration algorithm is used to track the trajectory of six degrees of freedom Industrial Robot in Cartesian space from P_0 to P_2, and the whole motion process is still maintained for 60 seconds. Figure 9, Figure 10 and Figure 11 show the angles, angular velocities and angular acceleration curves of joint 1, joint 2 and joint 3 respectively.

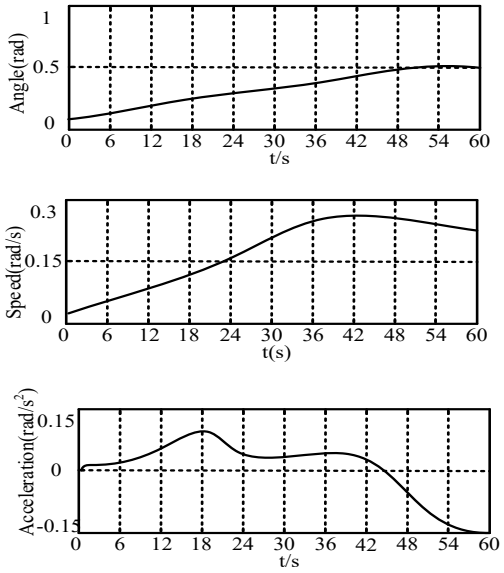

Figure 9. Joint 1 locus

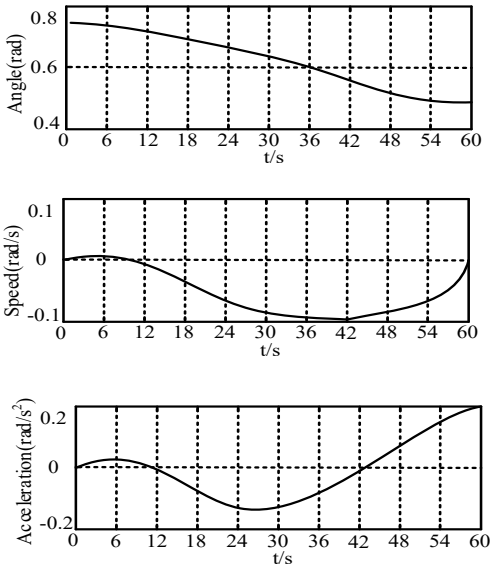

Figure 10. Joint 2 locus

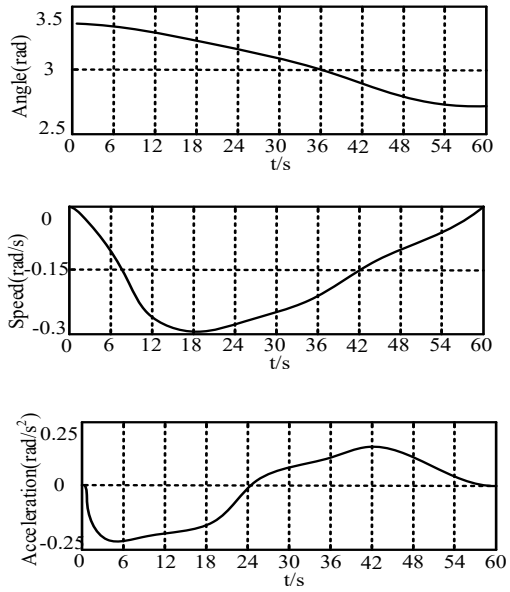

Figure 11. Joint 3 locus

As can be seen from Figures 9-11, the maximum angular velocity and acceleration of joint 1 are about 0.27 rad/s and 0.19 rad/s^2, respectively. The angular velocity increases with time and then tends to be stable, and the acceleration reaches the maximum value at 18 s. Joint 2 was about 0.18 rad/s and 0.2 rad/s^2, both of which decreased first and then increased. The joint angular velocity reached the maximum value of 0.28 rad/s at 18 s, and the acceleration dropped to the maximum value of 0.24 rad/s^2 at 42 s.

Compared with Cartesian space trajectory tracking control algorithm without joint velocity and acceleration constraints, this trajectory tracking control algorithm has the advantage of smooth and safe motion. Because the motor load capacity is limited, its speed, driving torque has an upper limit value, too high load may make the motor vibration or even damage the motor. The joint of six degrees of freedom Industrial Robot is driven directly or indirectly by motor, so the motion of joint is limited by motor. At the same time, this algorithm can make the six degrees of freedom Industrial Robots optimize the motion time as much as possible within the range of satisfying constraints, instead of sacrificing efficiency. Its multi-constraint characteristics are also limited, and the motion of six degrees of freedom Industrial Robots is always limited within these constraints. This trajectory tracking control method can be used in the situation that the six degrees of freedom Industrial Robot is required to work smoothly and at the same time has certain requirements for the motion speed of the robot.

5. Conclusion and Prospect

5.1. Conclusion

Point-to-point control only needs to control the accuracy and time of the starting point and the ending point, so most Industrial Robots can realize point-to-point control, such as spot welding, handling and assembling robots. Continuous trajectory control requires not only the accuracy and time of the start and end points, but also the time and position of each trajectory point, such as spraying and arc welding robot. However, most six degrees of freedom Industrial Robots are limited by their structure and control program, and can only follow a simple continuous trajectory. Their flexibility and intelligence are still deficient, and their trajectories are not smooth enough.

In the actual production of six degrees of freedom Industrial Robot, people pay more attention to its efficiency and precision. This paper studies the kinematics and dynamics of Industrial Robots. The description of robot pose, the transformation between coordinate systems and the linkage mechanism are discussed. Several trajectory tracking control methods are analyzed and discussed in view of the different working environment and smoothness of six degrees of freedom Industrial Robots. The experimental results show that the trajectory tracking control method can satisfy the requirements of velocity and acceleration constraints in Cartesian space and joint space, and achieve the smoothness of the whole robot, and maintain a high efficiency.

5.2. Prospects

In this paper, the kinematics and dynamics analysis and trajectory tracking control of six degrees of freedom Industrial Robot are carried out in an ideal environment, without considering the influence of the external environment and the friction, stiffness and other dynamic factors of six degrees of freedom Industrial Robot. And only in theory and program analysis and Simulation of robot trajectory tracking control, not in the actual robot verification, so the experimental verification can be used as a further research content.

References

[1] Kyrarini, M.; Haseeb, M.A.; Risti-Durrant, D.; Graser, A. Robot learning of industrial assembly task via human demonstrations. Autonomous Robots, 2019, 43(6): 239-257.

[2] Andrés, F.; Lars Toft, J.; Sebastian, R. Automating the incremental evolution of controllers for physical robots. Artificial Life, 2018, 23(2): 142-168.

[3] Lippi, M.; Marino, A. Human multi-robot safe interaction: A trajectory scaling approach based on safety assessment. IEEE Transactions on Control Systems Technology, 2020, 12(99): 1-16.

[4] Leali, F.; Pini, F.; Villani, V. Guest editorial note: Special issue on human-robot collaboration in industrial applications. Mechatronics, 2019, 58(6): 80-87.

[5] You, B.; Zhang, L.C.; Li, Z.; Ding, L. Fuzzy sliding mode trajectory tracking control of wheeled mobile robots. Computer Simulation, 2019, 36(2): 317-323.

[6] Yang, K.; Yang, W.; Wang, C. Inverse dynamic analysis and position error evaluation of the heavy-duty industrial robot with elastic joints: an efficient approach based on Lie group. Nonlinear Dynamics, 2018, 93(4): 1-18.

[7] Campeau-Lecours, A.; Cote-Allard, U.; Dinh-Son, V.; Routhier, F.; Gosselin, B.; Gosselin, C. Intuitive adaptive orientation control for enhanced human–robot interaction. IEEE Transactions on Robotics, 2018, 6(2): 1-12.

[8] Sommier, A.; Malvaut, J.; Delos, V.; Romano, M.; Bazire, T.; Batsale, J.C. Coupling pulsed flying spot technique with robot automation for industrial thermal characterization of complex shape composite materials. NDT & E International, 2019, 102(9): 175-179.

[9] Yan, Z.; Ouyang, B.; Li, D.; Liu, H.L.; Wang, Y.N. Network intelligence empowered industrial robot control in the F-RAN environment. IEEE Wireless Communications, 2020, 27(2): 58-64.

[10] Asar, M.F.; Elawady, W.M.; Sarhan, A.M. ANFIS-based an adaptive continuous sliding-mode controller for robot manipulators in operational space. Multibody System Dynamics, 2019, 47(1): 95-115.

[11] Santina, C.D.; Katzschmann, R.K.; Bicchi, A.; Daniela, R. Model-based dynamic feedback control of a planar soft robot: Trajectory tracking and interaction with the environment. The International Journal of Robotics Research, 2020, 12(2): 27-36.

[12] Hashlamon, I. Adaptive disturbance estimation and compensation for delta robots. Jordan Journal of Mechanical and Industrial Engineering, 2020, 14(4): 413-422.

[13] Guerrero, J.A.; Torres, J.; Creuze, V.; Ahmed, C. Adaptive disturbance observer for trajectory tracking control of underwater vehicles. Ocean Engineering, 2020, 200(12): 107-118.

[14] Coronel-Escamilla, A.; Torres, F.; Gómez-Aguilar, J.F.; Escobar-Jiménez, R.F.; Guerrero-Ramírez, G.V. On the trajectory tracking control for an SCARA robot manipulator in a fractional model driven by induction motors with PSO tuning. Multibody System Dynamics, 2018, 43(3): 257-277.

[15] Mutawe, S.; Hayajneh, M.; BaniHani, S.; Qaderi, M.A. Simulation of trajectory tracking and motion coordination for heterogeneous multi-robots system. Jordan Journal of Mechanical and Industrial Engineering, 2021, 15(4): 337-345.

[16] Baek, J.; Cho, S.; Han, S. Practical time-delay control with adaptive gains for trajectory tracking of robot manipulators. IEEE Transactions on Industrial Electronics, 2018, 65(7): 5682-5692.

[17] Andreev, A.; Peregudova, O. On global trajectory tracking control of robot manipulators in cylindrical phase space. International Journal of Control, 2019, 9(12): 1-27.

JJMIE

Volume 16, Number 1, January. 2022
ISSN 1995-6665
Pages 105 - 111

Jordan Journal of Mechanical and Industrial Engineering

Design of Multi Joint Integrated Control System for Non Driven Robot

Qian Zhang *

Department of Computer Science, Guangdong University of Education, Guangzhou 510303, China

Received 14 July 2021 *Accepted 29 December 2021*

Abstract

All joints of the non-driving robot have driving devices, but they can not be controlled effectively, which increases the difficulty of the robot control. In order to solve this problem, a multi joint integrated control system for non- actuated robot is designed in this paper. The research object is a two-degree of freedom non-actuated robot. After designing the basic structure of the robot, the dynamic characteristics of the robot are analyzed, and the integrated control system is designed from two aspects of current and position. The experimental results show that the design method can realize the accurate motion control of multi- joints of non-driven robot, which provides a reference for practical application.

Keywords: Non driven robot; Joint control; Integrated control system;

1. Introduction

Because the joint of ordinary robot is controlled and driven separately, the activity is relatively simple, while the actual control input of non-driven robot is less than the motion freedom of the robot, the underactuated part is generally set at the end of the robot. Compared with the conventional series robot, it has many advantages, such as light weight, small inertia, simple structure design and low system cost [1-3]. At the same time, the end joint of the non driven robot is driven by the cooperative action of multiple joints, so the fault tolerance rate of the non-driven robot is relatively high [4]. The robot with the number of independent control inputs less than the actual motion degree of freedom has good flexibility and light weight, and can be applied to some extreme environments. Therefore, the non-driven robot has always been one of the important fields of robot research. Wang et al. studied the multi arm concentric tube robot. The concentric tube robot has the advantages of small volume and strong shape control ability, which improves the shortcomings of most single arm robots. A four-degree of freedom vision arm and two six-degree of freedom mechanical arms are designed, and the end effector of CTR system is configured at the end to enable the robot to realize surgical operation, however, the positioning and tracking effect of control is general [5]. Wang et al. mainly studied the timed formation control of multi robot systems with time-delay constraints. Through the state transformation of the predictor to deal with the input delay caused by the network connection, a nonlinear fixed time formation protocol is proposed, and the corresponding stability time is calculated by Lyapunov function to realize the effective control of the robot, but the balance control effect of the driving arm is general [6]. Liu et al. studied the multi-objective control system based on DOB. The stability of the characteristic equation with uncertain time delay is analyzed by using the zero exclusion criterion, and the anti-interference performance and robustness of the system are studied. In the presence of uncertain time delay and disturbance, effective control is realized, but the response effect of the control system is poor [7]. Based on the above research, the design method proposed in this paper solves the problem of difficult motion control of non drive system. The control effect of the designed control system is studied, which provides a preliminary reference for the multi joint control of non driven robot.

2. Model Construction of 2-DOF Non Driven Robot

In the non driving robot system, the joints without driving ability can only be controlled by the driving joints, so the position control method is much more difficult than the general full driving system. In this paper, a multi joint robot is designed, which has one driving joint and one non-driving joint. The structure is relatively simple and has the basic characteristics of underactuated system. It is an ideal research object for us to study the multi joint integrated control problem of non driven robot.

2.1. Performance index of robot system

The planar 2-DOF robot has two parallel rotating joints, and the second joint is a non driving joint. Its main parameters and performance indicators are shown in Table 1.

* Corresponding author e-mail: zhqian020@126.com.

Table 1 Main parameters and performance indexes of robot

Freedom	2	DD motor drive + encoder
Structural form	Planar joint type	Encoder + brake
Base size (support foot)	1500 mm × 1500 mm	Unlimited rotation
Height	1350 mm	Torque control
Motion plane	The angle with the horizontal plane is 60 degrees	PC computer + motor driver
Arm length (wheelbase of two joints)	340 mm	

2.2. Mechanical structure design of robot

The structure of the first degree of freedom is shown in Figure 1.

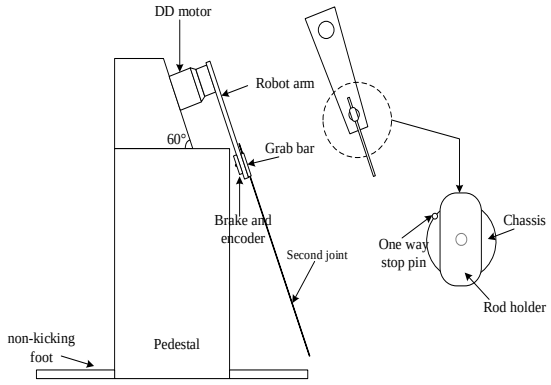

Figure 1. Structure of robot

Base and support foot: The base is the coordinate reference of robot motion, so it is necessary to keep the stability and balance of the base under the high-speed motion of robot arm. Since the reaction force of the arm to the base is quite large during the high-speed swing, a heavy block is added to the base to increase the stability (as shown in Figure 1). Meanwhile, the deployable support foot is designed to increase the support area and prevent the robot from overturning.

The first joint: driven by a DD motor. In our research, the control method is to give the driving torque directly to control the robot torque. In order to improve the control accuracy and reaction speed, the direct drive motor is used. The actual maximum output torque of the motor is 110 nm, which is limited to 100 nm in our experiment.

The second joint is a non-driving joint. In this joint, an encoder is used to measure the joint motion angle, and a brake device is used to provide the braking force after the action. A one-way stop pin is set on the joint of the robot to block the excessive clockwise rotation angle of the grab rod.

2.3. Kinematics equation of robot

The $x-y$ coordinate is established with the motion plane of robot arm as the coordinate plane, and the axis of the first joint is used as the coordinate origin. θ_1 and θ_2 are defined as the motion angles of the first joint and the second joint. Then the forward kinematics solution of the grab bar is as follows:

$$\begin{cases} x = l_1 \cos\theta_1 + l_2 \cos(\theta_1 + \theta_2) \\ y = l_1 \sin\theta_1 + l_2 \sin(\theta_1 + \theta_2) \end{cases} \quad (1)$$

l_1 and l_2 are the length of two connecting rods, l_1 is the distance from the axis of the first joint to the axis of the second joint, and the measured value is 0.34 M; l_2 is the distance from the axis of the second joint to the target point [8].

The inverse kinematics solution is as follows:

$$\begin{cases} \theta_1 = \arctan\left(\dfrac{(l_1 + l_2\cos\theta_2)y - l_2 x \sin\theta_2}{l_2 y \sin\theta_2 + (l_1 + l_2\cos\theta_2)x}\right) \\ \theta_2 = \arccos\left(\dfrac{x^2 + y^2 - l_1^{\,2} - l_2^{\,2}}{2l_1 l_2}\right) \end{cases} \quad (2)$$

According to the different arm shape, there are multiple solutions, that is, there are positive and negative solutions when solving θ_2 in the above equation.

2.4. Bottom control structure of robot

Since only one drive joint needs motor control, the underlying control hardware of the robot is relatively simple. However, since the grab bar action is a high-speed motion, the whole process only takes about 0.8 seconds, and there are complex torque changes in this process, so the requirements for the performance of the underlying hardware are also very high [9-12].

The hardware structure of the control system is shown in Figure 2.

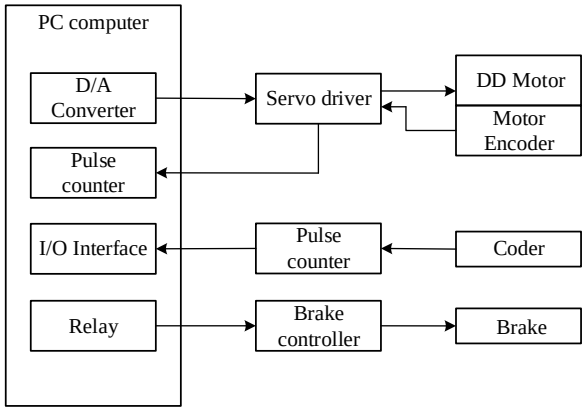

Figure 2 Robot control hardware

The control computer is nec pc-9801 microcomputer with DOS 6.0 operating system. The D / a converter converts the calculated control torque into analog quantity and outputs it to the motor driver to drive the motor to move. At the same time, a pulse counter is used to receive the signal of motor code disk. Due to the high precision of code disk of DD motor (319 488 pulses per revolution) and high frequency of code disk signal under high speed operation, qpg45 high-speed pulse counter is used, and the counting frequency can reach 1.8 mhz. For the non driven joint, an encoder is used to feedback the angle of the joint, and the brake is used for braking. The encoder signal is

read through the I/O interface of the computer after counting, and the brake is controlled by the computer through the relay. The reaction time of braking is 50 ms for braking, 20 ms for releasing braking, and the braking torque is 25 nm.

The sampling period of the whole control is 1 millisecond, and the timing interrupt is provided by 8 253 chip. In the bottom control, the current loop (torque) is controlled by the motor driver, and the speed loop and position loop are controlled by the computer in software mode, that is, the PID controller of software servo [13-16]. Since the non-driving joint has no control torque, the PID controller has two inputs and one output, that is to adjust the two joints at the same time. In fact, it is equivalent to the superposition of the output of the two PID controllers. The effect is Equation (3):

$$u = K_{p1}\Delta\theta_1 + K_{I1}\int\Delta\theta_1 + K_{d1}\Delta\dot{\theta}_1 + K_{p2}\Delta\theta_2 + K_{I2}\int\Delta\theta_2 + K_{d2}\Delta\dot{\theta}_2 \quad (3)$$

The coefficients are adjusted according to the experimental results. As explained in the introduction of the first chapter, such PID feedback controller can not guarantee the uniform convergence of the error. In fact, in the process of motion, the effect of the two joint errors on the controller will cancel each other. However, it can keep the balance between the errors of two joints, prevent one-sided increase of the error of one joint, and can effectively reduce the error when the effect of two joint errors is the same.

The control structure of the whole system is shown in Figure 3, in which the track generation part is calculated off-line, and the calculated track data is transmitted to the lower computer for the bottom control as a file. The lower computer controls the robot to complete the action. The dynamic feedforward + PID feedback control is used in the control. The feedforward control signal is the torque track calculated off-line. The PID controller is realized by the software of the lower computer. The motion track calculated offline is used as the reference signal of PID regulation.

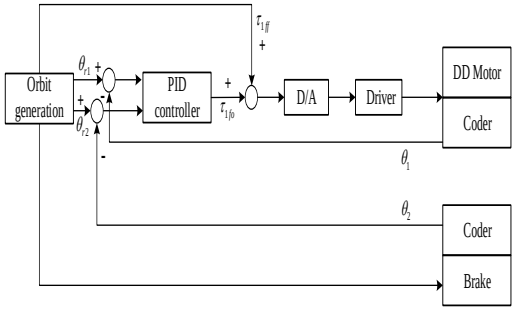

Figure 3. Overall control structure of robot

3. Design of Robot Integrated Control System

Based on the analysis of robot dynamics, the robot integrated control system is designed from two aspects: current controller and position controller. Differential feedforward and fuzzy control are introduced to improve the response effect of system position.

3.1. Design of current controller

The current controller consists of four parts: current feedback, PI controller, three-phase inverter and motor stator armature circuit. Its main function is to improve the rapidity of the system and suppress the internal interference of the current loop [17]. According to the overall block diagram of the system introduced in Section 2.3, the current loop consists of two non-interference loops, torque current i_q and excitation current i_d. In this paper, the control methods of the two loops are identical, so the design of torque current i_q loop is only introduced.

The current loop control loop is shown in Figure 4. $H(s)$, $G_p(s)$, $G_s(s)$ and $G_s(s)$ represent the transfer functions of current feedback, PI controller, three-phase inverter and motor stator armature circuit respectively.

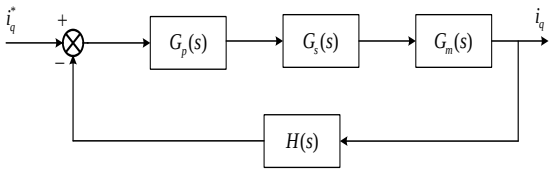

Figure 4. Current loop control loop

The current feedback link can be divided into three parts: detection, filtering and sampling. The detection part can be regarded as a proportion link. The filter is a hardware implemented RC filter, which can be regarded as a first-order inertial link, and its transfer function is $G_{RC}(s) = \frac{1}{RCs+1} = \frac{1}{\tau_{RC}s+1}$. Among them, $\tau_{RC} = RC$ is the time constant of RC filter circuit. The sampling part is realized by ad module in the controller, and its transfer function is $G_{AD}(s) = \frac{1}{\tau_{AD}s+1}$. Therefore, the transfer function of the current feedback link can be expressed as follows:

$$H(s) = K_1 G_{RC}(s) G_{AD}(s) G_s(s) = \frac{1}{(\tau_{AD}s+1)(\tau_{RC}s+1)}$$

Because τ_{AD} and τ_{RC} are relatively small, they can be replaced by a first-order inertial link with a time constant τ_{fb}. Equation (4) can be simplified as follows:

$$H(s) \approx \frac{K_1}{\tau_{fb}s+1} \quad (5)$$

Among them, $\tau_{fb} = \tau_{AD} + \tau_{RC}$ and K_1 are the magnification of the detection link.

The three-phase inverter can be regarded as an amplifier, which can amplify the output signal of the front current PI controller to the voltage signal of the direct control motor. However, due to the output delay of SVPWM algorithm, the delay is at least half of the PWM switching cycle. Therefore, the transfer function of the three-phase inverter can also be regarded as a first-order inertial link. The transfer function can be expressed as follows:

$$G_s(s)=\frac{K_2}{\tau_{pwm}s+1} \tag{6}$$

Among them, τ_{pwm} is half of PWM switching period and K_2 is voltage amplification factor of three-phase inverter.

The stator armature of the motor has stator resistance R_m and stator inductance L_m, which can be regarded as the first-order inertial link. The transfer function is as follows:

$$G_m(s)=\frac{1}{R_m(\tau_L s+1)} \tag{7}$$

where $\tau_L=\frac{L_m}{R_m}$ is the time constant of stator armature inductance.

The transfer function of PI controller can be expressed as follows:

$$G_p(s)=K_p+\frac{K_i}{s}=\frac{K_p(\tau_i s+1)}{\tau_i s} \tag{8}$$

K_p and K_i are the proportional constant and integral constant of PI controller respectively.

Figure 4 open loop transfer function of current loop can be expressed as follows:

$$G_i(s)=\frac{K_pK_1K_2(\tau_i s+1)}{R_m\tau_i s(\tau_{fb}s+1)(\tau_{pwm}s+1)(\tau_L s+1)} \tag{9}$$

Since the inductance time constant τ_L is generally much larger than the current feedback link time constant τ_{fb} and PWM switching period τ_{pwm}, the zero point and large time constant pole cancellation of the current regulator are selected:

$$\tau_i=\tau_L=\frac{L_m}{R_m} \tag{10}$$

Therefore, Equation (9) can be simplified as follows:

$$G_i(s)=\frac{K}{s(\tau_{fb}s+1)(\tau_{pwm}s+1)} \tag{11}$$

Among $K=\frac{K_pK_1K_2}{L_m}$.

The time constant τ_{fb} and switching period τ_{pwm} of the current feedback link are relatively small, so an inertial link can be used to replace the two inertial links, $\tau=\tau_{pwm}+\tau_{fb}$. Equation (11) is further simplified:

$$G_i(s)=\frac{K}{s(\tau s+1)} \tag{12}$$

The closed-loop transfer function of the current controller is a typical second-order system:

$$G_i(s)=\frac{G_i(s)}{1+G_i(s)}=\frac{K/\tau}{s^2+s/\tau+K/\tau} \tag{13}$$

By comparing the standard form of closed-loop transfer function of current controller, the damping coefficient ζ and undamped natural frequency ω_n can be obtained:

$$\begin{cases}\omega_n=\sqrt{\frac{K}{\tau}}\\ \zeta=\frac{1}{2\tau\omega_n}=\frac{1}{2}\sqrt{\frac{1}{K\tau}}\end{cases} \tag{14}$$

According to the characteristics of the second-order system, the damping coefficient is inversely proportional to the overshoot. When the damping coefficient is large, the overshoot of the system is small, but the response speed is slow; The smaller the damping coefficient, the greater the overshoot, but the faster the response speed. Therefore, it is necessary to select the damping coefficient ζ of the system reasonably. From the engineering test, $\zeta=0.707$ is the optimal index of the second-order system, so $K=1/2\tau$ can be obtained. The proportional constant K_p and integral constant K_i of PI controller are obtained:

$$\begin{cases}K_p=\frac{L_m}{2\tau K_1K_2}\\ K_i=\frac{R_m}{2\tau K_1K_2}\end{cases} \tag{15}$$

3.2. Design of position controller

People are most concerned about whether the robot arm can quickly and accurately move to the preset position. Therefore, in the design of the control algorithm of the joint servo driver, the design of the position controller is the most important. The control parameters of traditional PID controller have been fixed, which can only have the best control effect for one or several working conditions, and can not respond to the external real-time changes. Therefore, this paper introduces the fuzzy PID control algorithm in the design of position controller. In the design of position control algorithm, the most taboo is that the position control appears overshoot and static error. On the basis of fuzzy PID control algorithm, the differential feed-forward link is added to eliminate the overshoot of the control system.

3.2.1. Controller design based on Fuzzy PID algorithm

Fuzzy control theory is a kind of control theory based on language rules and fuzzy reasoning based on fuzzy set theory in modern control theory. Its mathematical basis is fuzzy set theory, which belongs to an important branch of intelligent control. The structure of fuzzy PID controller is shown in Figure 5. The fuzzy controller with two inputs and three outputs is adopted. The input is the error between the position feedback signal and the given quantity and the error change rate. The output is the three parameters ΔK_p, ΔK_i and ΔK_d of PID controller.

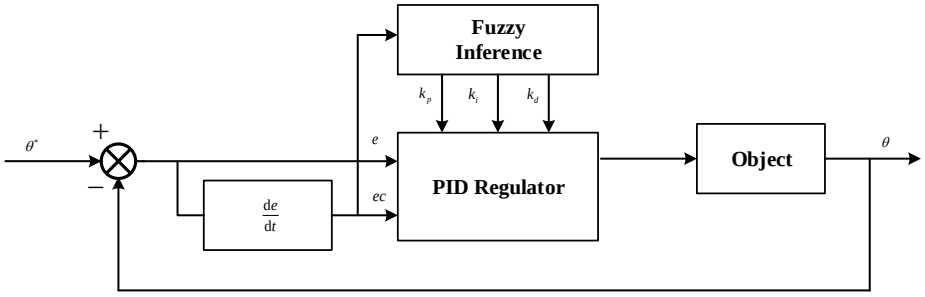

Figure 5 Schematic diagram of fuzzy PID

Firstly, the input signals E and EC, the output signals ΔK_p, ΔK_i, ΔK_d are transformed into fuzzy variables for input into fuzzy inference engine for processing. The input signal and output signal are divided into seven levels, corresponding to seven fuzzy subsets {positive big (PB), positive middle (PM), positive small (PS), zero (Zo), negative small (NS), negative medium (nm), negative large (NB)}. The fuzzy universe covering the input signal and the output signal is set as {-6, -5, -4, -3, -2, -1, 0, 1, 2, 3, 4, 5, 6}, and the input and output signals obey the triangular membership function.

Secondly, since the position servo system is not allowed to be out of calibration and overshoot, special attention should be paid to the adjustment of integral coefficient K_i in the process of adjustment. When the system error is large, the larger K_p and the smaller K_i and K_d should be selected to make the system response have better fast tracking performance and avoid integral saturation and large overshoot. When the system error is small, in order to make the system have good steady-state performance, K_i should be appropriately increased, but attention should be paid not to make the system overshoot.

Finally, the output of fuzzy reasoning is defuzzified, and the method of maximum membership degree is usually used, that is to select the domain element with the largest membership degree in the output fuzzy set as the judgment result. Finally, the calculation equation of three PID parameters is as follows:

$$K_p = K_{p0} + \Delta K_p \tag{16}$$

$$K_i = K_{i0} + \Delta K_i \tag{17}$$

$$K_d = K_{d0} + \Delta K_d \tag{18}$$

where, is the initial value of PID, is the output of fuzzy controller.

3.2.2. Design of differential feedforward controller

The position loop control system is composed of position controller, speed closed loop and permanent magnet synchronous motor. Since the cut-off frequency of the position loop is far less than the reciprocal of each time constant of the speed loop, the speed loop is approximately equivalent to the first-order inertial link $G_v(s) = \frac{k_v}{T_n s + 1}$, and the permanent magnet synchronous motor is approximately equivalent to the integral link $G_m(s) = \frac{k_m}{s}$. The feed-forward control structure diagram of the position loop is shown in Figure 6.

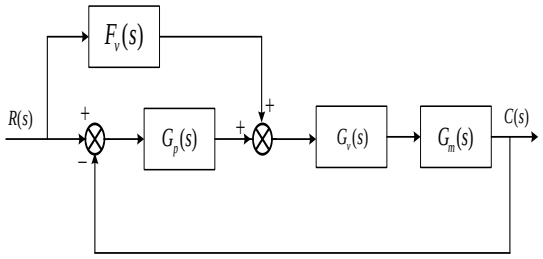

Figure 6. Structure diagram of position loop feedforward control

The closed-loop transfer function of the system is obtained from the structure diagram of position loop feedforward control:

$$\frac{C(s)}{R(s)} = \frac{\left[F_v(s) + G_p(s)\right] G_v(s) G_m(s)}{1 + G_p(s) G_v(s) G_m(s)} \tag{19}$$

From Equation (19), it can be concluded that:

$$F_v(s) = \frac{1}{G_v(s) G_m(s)} = \frac{s(T_n s + 1)}{k_v k_m} \tag{20}$$

The transient error and steady-state error of the system are both zero. Since the accuracy of the servo system depends on the low frequency part of the system, the high-order part in the equation can be ignored and simplified as follows:

$$F_v(s) = \frac{s}{k_v k_m} \tag{21}$$

In other words, the feedforward of the position loop is the differential of the given position, and the speed can be predicted according to the given position, and the predicted value can be compensated to the given speed so as to realize the early response.

4. Experimental Part

Matlab/Simulink is used for simulation experiment. The experimental system is windows 10, equipped with Core i7 processor and 8 g memory, which can meet the experimental requirements. Assuming that the initial angle of the non driving arm is $\theta_{20} = 0.8\left[rad\right]$ and the initial angular velocity is $\dot{\theta}_{20} = 0\left[rad/s\right]$, the expected points to be achieved by the control are: angle $\theta_{2d} = 0.5\left[rad\right]$, angular velocity $\dot{\theta}_{2d} = 0\left[rad/s\right]$.

4.1. Balance control test of drive arm

The initial angular velocity of the active arm and underactuated arm is 0, the maximum simulation step size is 1 ms, and the simulation time is 5 s. Test the free swing angle value of the active arm and underactuated arm near the vertical downward stable equilibrium position, as shown in Figure 7.

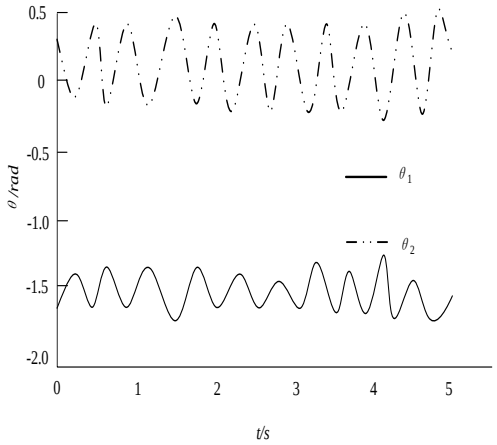

Figure 7. Free swing range of active arm and underactuated arm

By changing the position input parameters, balance control is carried out near the vertical unstable equilibrium position, and the balance control of the first joint and the second joint is tested. The experimental results are shown in Figure 8.

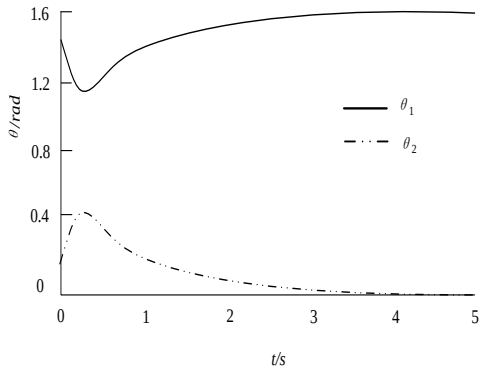

Figure 8. Angle value (LQR)

It can be seen from Figure 8 that the angle θ_1 of the active arm (the first joint) approaches π/2, and the angle θ_2 of the underactuated arm (the second joint) approaches to 0, which proves that the design method can be used for balance control.

4.2. Given position tracking test

A sine wave with an amplitude of 20° and a frequency of 1 Hz is given. The response of the control method in Reference [5] and Reference [6] and the control method designed in this paper are compared respectively, as shown in Figure 9.

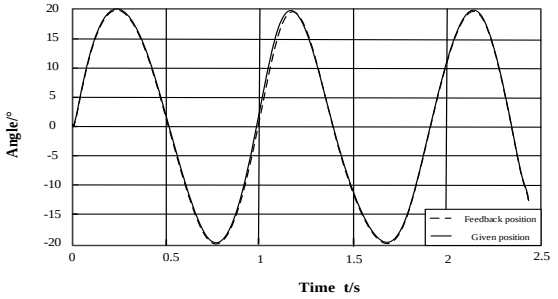

(a) The method of this paper

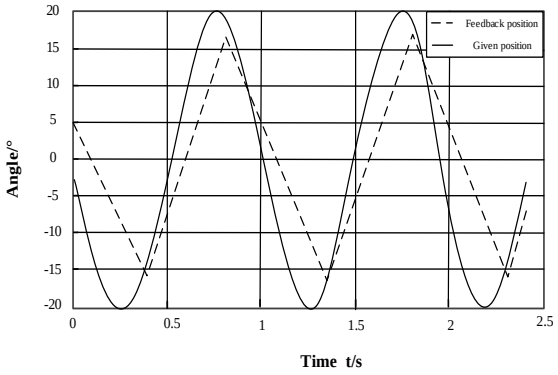

(b) Method of Reference [5]

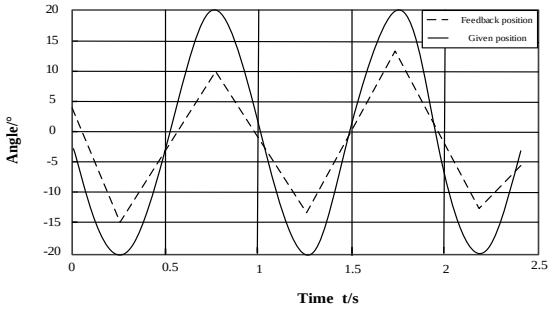

(c) Method of Reference [6]

Figure 9 Experimental results of given position tracking

From the observation of Figure 9, it can be seen that when the position is given as a real-time sine wave, the proposed method can track the given position well and has good dynamic response performance. However, the method in the literature has poor performance in tracking the given position with real-time changes. Therefore, the proposed method has good practical performance.

5. Conclusions

In order to solve the problem that the non-actuated joints can not be well controlled in the non-actuated robot system, a multi-joint integrated control system of the non-actuated robot is designed in this paper. Differential feedforward and fuzzy control are introduced to improve the response effect of the system position. Experiments show that the system designed in this paper can track the given position well. Additionally, the experiments also show that the effect of balance control is good, and good results are obtained. The system designed in this paper can solve some problems existing in the motion control of non-driving system. Such system has good applicability to the comprehensive control of non-driving multi joints, which

realizes accurate motion control of non-driving robot multi joints, and can also provide a scientific basis for non-driving robot to participate in more work.

Acknowledgements

The research is supported by: Computer Experimental Teaching Demonstrating Center (undergraduate teaching quality and teaching reform project of Guangdong education); Guangdong University of Education Network Engineering Key Subject (No. ZD2017004); The undergraduate teaching quality and teaching reform project of Guangdong University of Education (Experimental Teaching Demonstration Center of Computer Application) (No. 2018sfzx01).

References

[1] Kim, Y.J.; Park, S.W.; Yeom, H.G.; Bang, M.S.; Kim, J.S.; Chung, S.K.; Kim, S. A study on a robot arm driven by three-dimensional trajectories predicted from non-invasive neural signals. Biomedical Engineering Online, 2015, 14: 81.

[2] Rijk, R.D.; Rushton, M.; Khajepour, A. Out-of-plane vibration control of a planar cable-driven parallel robot using a multi-axis reaction system. IEEE/ASME Transactions on Mechatronics, 2018, (4): 1-1.

[3] Park, H.; Hutchinson, S. Robust rendezvous for multi-robot system with random node failures: An optimization approach. Autonomous Robots, 2018, 42(8): 1807-1818.

[4] Zhi, Z.; Huan, Z.; Swanson, A.R.; Weitlauf, A.S.; Warren, Z.E.; Sarkar, N. Design, development, and evaluation of a noninvasive autonomous robot-mediated joint attention intervention system for young children with ASD. IEEE Transactions on Human-Machine Systems, 2018, 48(2): 125-135.

[5] Wang, J.; Yang, X.; Li, P.; Song, S.; Liu, L.; Meng, M.Q.H. Design of a multi-arm concentric-tube robot system for transnasal surgery. Medical & Biological Engineering & Computing, 2020, 58(3): 497-508.

[6] Wang, C.Y.; Tnunay, H.; Zuo, Z.Y.; Lennox, B.; Ding, Z.T. Fixed-time formation control of multirobot systems: Design and experiments. IEEE Transactions on Industrial Electronics, 2019, 66(8): 6292-6301.

[7] Liu, Q.; Liu, M.; Jin, Q.B.; Liu, Y.J. Design of DOB-based control system in the presence of uncertain delays for low-order processes. IEEE Transactions on Control Systems Technology, 2020, 28(2): 558-565.

[8] Kasmuri, N.H.; Kamarudin, S.K.; Abdullah, S.R.S.; Hasan, H.A.; Som, A.M. Integrated advanced nonlinear neural network-simulink control system for production of bio-methanol from sugar cane bagasse via pyrolysis. Energy, 2019, 168: 261-272.

[9] Mutawe, S.; Hayajneh, M.; BaniHani, S.; Qaderi, M.A. Simulation of trajectory tracking and motion coordination for heterogeneous multi-robots system. Jordan Journal of Mechanical and Industrial Engineering, 2021, 15(4): 337-345.

[10] Chen, Y.F.; Zhao, H.C.; Mao, J.; Chirarattananon, P.; Helbling, E.F.; Hyun, N.S.P.; Clarke, D.R.; Wood, R.J. Controlled flight of a microrobot powered by soft artificial muscles. Nature, 2019, 575(7782): 324-329.

[11] Dong, C.Y.; Yang, S.F.; Jia, H.J.; Wang, P. Padé-based stability analysis for a modular multilevel converter considering the time delay in the digital control system. IEEE Transactions on Industrial Electronics, 2019, 66(7): 5242-5253.

[12] Kong, F.X.; Zhu, Y.H.; Yang, C.; Jin, H.Z.; Cai, H.G. Integrated locomotion and deformation of a magnetic soft robot: Modeling, control and experiments. IEEE Transactions on Industrial Electronics, 2021, 68(6): 5078-5087.

[13] Koyama, K.; Shimojo, M.; Ming, A.; Ishikawa, M. Integrated control of a multiple-degree-of-freedom hand and arm using a reactive architecture based on high-speed proximity sensing. The International Journal of Robotics Research, 2019, 38(14): 1717-1750.

[14] Yang, C.G.; Jiang, Y.M.; He, W.; Na, J. Adaptive parameter estimation and control design for robot manipulators with finite-time convergence. IEEE Transactions on Industrial Electronics, 2018, 65(99): 8112-8123.

[15] Hashlamon, I. Adaptive disturbance estimation and compensation for delta robots. Jordan Journal of Mechanical and Industrial Engineering, 2020, 14(4): 413-422.

[16] Li, S.H.; He, H.Y.; Dong, K.F.; Sheng, L.X. Research on real-time integrated control method of PV-SHAPWH. Solar Energy, 2019, 182: 213-224.

[17] Derakhshani, A. On the uncertainty analysis of uplift capacity of suction caissons in clay based on the fuzzy sets theory. Ocean Engineering, 2018, 170: 416-425.

JJMIE

Volume 16, Number 1, January. 2022
ISSN 1995-6665
Pages 113 - 121

Jordan Journal of Mechanical and Industrial Engineering

Temperature Field and Stress Field Distribution of Forged Steel Brake Disc for High Speed Train

Ruoqi Suo*, Xiaoling Shi

Department of Mining Engineering, Luliang University, Luliang 033000, China

Received 14 July 2021 *Accepted 22 December 2021*

Abstract

Thermal load plays a great role in brake disc failure, which seriously threatens the safety of train running. In this paper, the thermal elastic-plastic constitutive relation of the brake disc is obtained by experimental test, and the stress-strain response relationship of brake disc under different braking conditions is simulated by using the numerical calculation based on sequential coupling method. The temperature field and stress field are calculated under once 200 km/h emergency braking, once 300 km/h emergency braking, once 29 kN constant pressure braking and three times of 29 kN successive constant pressure braking. The results show that the worse the braking condition, the greater the temperature field and stress field. The temperature field decreases along the thickness direction; increases first and then decreases along the radial direction. During the braking process, the circumferential stress is the principal stress on the disc surface and the different residual tensile stress is formed after four braking conditions. The speed value has the greatest influence on the temperature field and stress field. These findings provide a reference for the thermal fatigue life evaluation of the high-speed train brake disc.

Keywords: Brake disc; Temperature field; Thermal stress; Residual stress; Thermal elastic-plastic;

1. Introduction

The thermal fatigue crack on the surface of the brake disc is closely related to the stress state in service, the structure and material [1-6]. The domestic and international researchers have conducted in-depth research on temperature field and stress field [7-13]. Yevtushenko and Greza, Anderson and Knapp found that thermal stress caused by high temperature can lead to disc surface crack or permanent deformation of brake disc [14, 15]. The friction, thermal deformation and elastic contact between brake disc and brake pad will also influence the change of contact pressure and surface temperature. Belhocine and Bouchetara simulated the coupling behavior between temperature field and stress field of automobile brake disc by thermal structure sequential coupling method [16]. It was found that stress concentration was easy to arise at the joint of brake disc and wheel, and cracks may occur after multiple braking. Ghadimi et al. found that the heat generated during friction between brake disc and brake pad has a lot of adverse effects on the brake system, such as braking performance, premature wear, thermal crack and brake disc thickness change [17]. Choj and Lee, Su et al., Gao et al. used the finite element method to analyze the thermo elastic contact between the brake disc and the brake pad [18-20]. Based on the theory of coupled heat conduction and elastic equation, the thermal stress under successive braking is calculated, and the influence of thermoelastic instability (TEI) on thermoelastic behavior is studied. Kim et al. established a three-dimensional ventilation brake disc model, and analyzed the distribution law of thermal stress of brake disc under two different conditions of uniform contact pressure and non-uniform contact pressure [21]. Adamowicz and Grzes, Li et al., Zhu et al., Chai et al. established two-dimensional and three-dimensional brake disc models [22-25]. By comparing the temperature field distribution of the two models under the action of non axisymmetric load, it is found that the temperature field calculation results based on the three-dimensional brake disc model are lower than those of the two-dimensional brake disc model, thus affecting the thermal stress field distribution of the brake disc. These results provide a theoretical basis for the development and design of brake disc [26-30]. In this paper, the elastic-plastic finite element method is used to analyze the temperature field and stress field distribution of brake disc under different braking conditions, so as to achieve a better heat and stress distribution on the surface [31].

2. Theoretical Analysis

When the expansion or contraction caused by the temperature change of the object is constrained, thermal stress will be generated inside the structure, and the thermal stress is $\alpha \times \left(T_\tau - T_0\right)$. Where α is the thermal expansion coefficient of the material, which changes with the change of temperature and material. T_τ is the temperature corresponding to the time τ, which T_0 is room temperature [32-35].

* Corresponding author e-mail: llxysrq@163.com.

When the stress function of material yield is set to f, the yield function is satisfied by $f=0$. Then the forged steel material meets Mises yield condition:

$$f = J_2 - K^2 = 0 \tag{1}$$

where, K is the yield stress under shear condition; J_2 is the second invariant of stress deviator.

Based on the theory of thermodynamics, thermal stress is mainly caused by temperature gradient. It is assumed that $t=t(r)$, for isotropic materials, the strain components in polar coordinates in the elastic range are:

$$\begin{aligned}
\varepsilon_r &= \frac{1}{E}[\sigma_r - \mu(\sigma_\theta + \sigma_z)] + at \\
\varepsilon_\theta &= \frac{1}{E}[\sigma_\theta - \mu(\sigma_r + \sigma_z)] + at \\
\varepsilon_z &= \frac{1}{E}[\sigma_z - \mu(\sigma_\theta + \sigma_r)] + at \\
\gamma_{zr} &= \frac{1}{G}\tau_{zr} = \frac{2(1+\mu)}{E}\tau_{zr} \\
\varepsilon_{r0} &= \varepsilon_{\theta 0} = \varepsilon_{z0} = at, \gamma_{zr0} = 0
\end{aligned} \tag{2}$$

The second invariant of stress deviation J_2 is:

$$\begin{aligned}
J_2 &= \frac{1}{6}\Big[(\sigma_\theta - \sigma_z)^2 + (\sigma_z - \sigma_r)^2 \\
&\quad + (\sigma_r - \sigma_\theta)^2 + 6\left(\tau_{\theta z}^2 + \tau_{zr}^2 + \tau_{r\theta}^2\right)\Big]^{1/2} \\
&= \frac{1}{6}\Big[(\sigma_1 - \sigma_2)^2 + (\sigma_2 - \sigma_3)^2 + (\sigma_3 - \sigma_1)^2\Big]^{1/2}
\end{aligned} \tag{3}$$

According to Formula (1), the plastic yield condition of forged steel material uses Mises criterion [36]. Considering the influence of strain during plastic deformation, the yield function can be expressed as:

$$\begin{aligned}
f = f\Big(&\sigma_r, \sigma_\theta, \sigma_z, \tau_{\theta z}, \tau_{zr}, \tau_{r\theta}, \varepsilon_r^p, \\
&\varepsilon_\theta^p, \varepsilon_z^p, \lambda_{\theta z}^p, \lambda_{zr}^p, \lambda_{r\theta}^p\Big) = 0
\end{aligned} \tag{4}$$

If the influence of temperature T is considered, the corrected yield function is:

$$f = f\left(\sigma_r, \sigma_\theta, \cdots, \varepsilon_r^p, \varepsilon_\theta^p, \cdots, T\right) = 0 \tag{5}$$

During the running of the brake disc, the mechanical stresses such as the brake pad pressure and friction force between the brake pad and the brake disc interact with the thermal stress during the braking process [37-40]. Hence, when mechanical stress and thermal stress work together, the relationship between stress and strain is:

$$[K]\{\delta\} = \{R\}_T + \{R\} \tag{6}$$

where $[K]$ represents the total stiffness matrix; $\{R\}$ represents the mechanical stress; $\{R\}_T$ represents the thermal stress; $\{\delta\}$ represents the node displacement.

It can be seen that the total structural deformation caused by mechanical stress and thermal stress can be obtained according to the superposition principle.

3. Modeling for Calculation

3.1. Finite element model

The braking process of high-speed train is the process of converting kinetic energy into heat energy. Relevant studies have shown that only about 20% of the heat generated by friction between the brake disc and the brake pad is consumed on the contact surface, and about 80% of the energy is transferred to the sub-surface material of the brake disc [41-44]. Therefore, the temperature field of the brake disc is not only unstable, but also the volume heat generated by the interface layer. The finite element grid and related parameters of the brake disc are shown in Figure 1 and Table 1.

Table 1. Related dimensions of brake disc and pad

Category	Outer diameter/mm	Inside diameter/mm	Thickness/mm	Coverage angle/°
Brake disc	36.0	22.3	53.3	64.5
pad	35.5	23.7	20.0	100

When dividing the three-dimensional finite element mesh, the friction surface part of the brake disc adopts a hexahedral mesh, the heat dissipation rib uses a tetrahedral mesh, and the brake pad adopts a hexahedral mesh. The divided finite element mesh has a total of 66948 elements. There are 15516 hexahedral meshes and 51432 tetrahedral meshes.

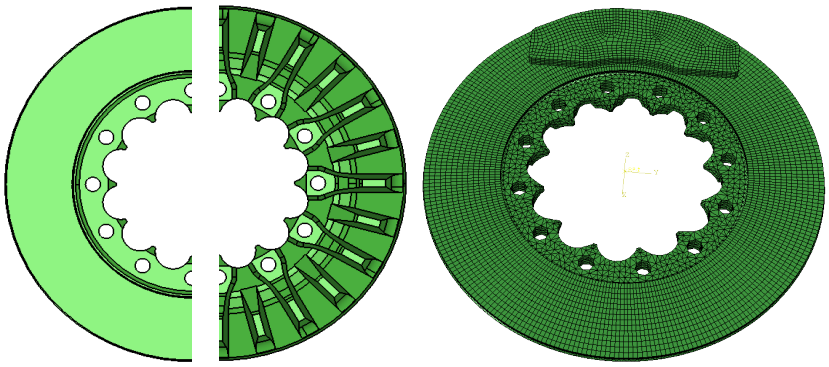

Figure 1. The geometric model and finite element model of brake disc and pad

3.2. Material parameters

The material is subjected to monotonic tensile tests at room temperature and high temperature, and the strain amplitude control method is adopted in the test and test temperatures are as follows: 25 °C, 100 °C, 200 °C, 300 °C, 400 °C and 500 °C. The stress-strain curve of monotonic tension is shown in Figure 2, which the test values are the average of three valid tests.

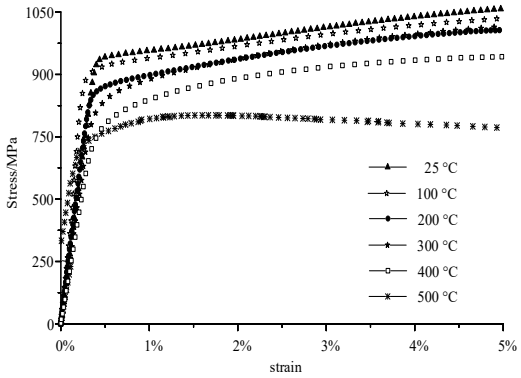

Figure 2. Monotonic tensile curve of $\sigma - \varepsilon$

Table 2 shows the material parameters at different temperatures. Considering that Poisson's ratio and density are not affected by temperature, they are regarded as constants. The yield strength, elastic modulus and thermal conductivity of the material decrease obviously with temperature, while the specific heat capacity and thermal expansion coefficient increase with temperature.

3.3. The boundary conditions

According to the technical requirements and actual operation curve of high-speed train foundation braking [45-48], four typical working conditions are calculated, including once emergency braking at 200 km/h, once emergency braking at 300 km/h, once 29 kN constant pressure braking at 200 km/h and three times of 29 kN successive constant pressing braking at 200 km/h. The bolt hole is fully constrained in the calculation process. Figure 3 illustrates the variation curves of brake pad pressure and braking speed with braking time under the speed levels of 200 km/h and 300 km/h. Figure 4 shows the variation curves of brake pad pressure and braking speed with braking time under one 29 kN constant pressure braking and three times of 29 kN successive constant pressure braking.

Table 2. Mechanical properties and thermophysical parameters at different temperatures

Temperature (°C)	Elastic modulus/E (GPa)	Yield strength (MPa)	Specific heat capacity (Cp/J/gK)	linear expansion coefficient (10^{-6}/°C)	Thermal conductivity /(W/m·°C)
25°C	228	790	0.485	10.9	45.2
100°C	224	710	0.485	10.9	45.0
200°C	223	670	0.515	11.7	42.7
300°C	207	590	0.550	12.3	40.5
400°C	177	450	0.555	12.8	37.6

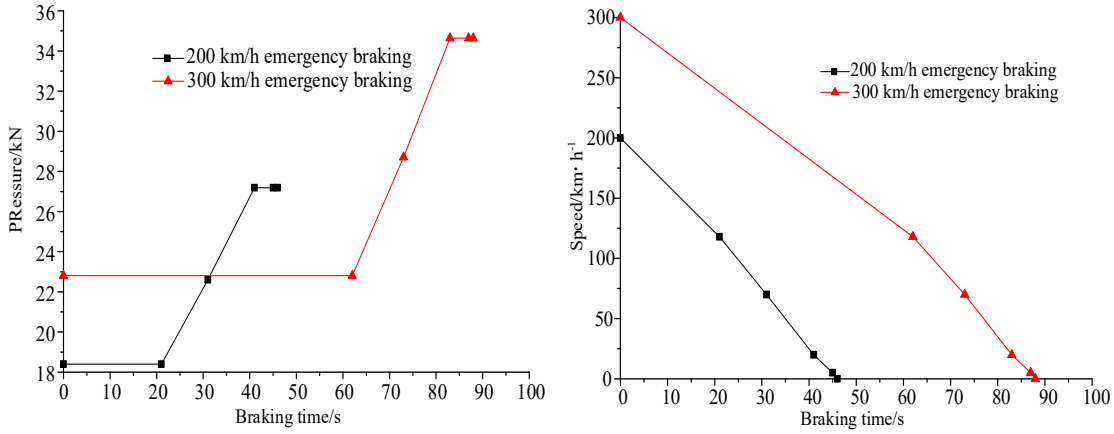

Figure 3. The emergency braking force curve

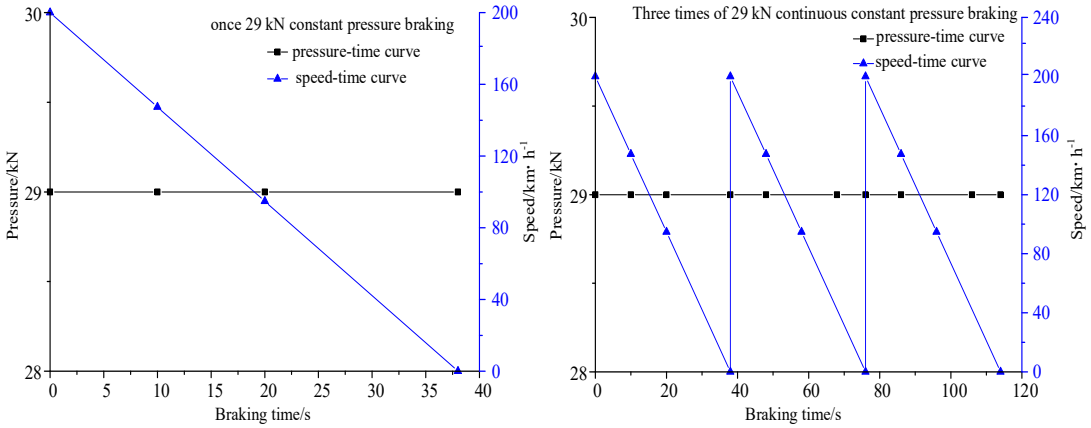

Figure 4. The constant pressure brake curve

As shown in Figure 3, the heat input is the highest under 300 km/h emergency braking. The maximum pressure under 200 km/h emergency braking and 300 km/h emergency braking is 27.18 kN and 34.64 kN respectively. It can be seen from Figure 4 that under the speed level of 200 km/h, there is a linear relationship between the speed curve of 29 kN constant pressure braking and the braking time. After braking, the natural convection and heat dissipation occur between brake disc and air. After 30 minters later, the surface temperature of 200 km/h emergency braking will return to room temperature.

3.4. Other calculation parameters

In this study, the ambient temperature is T (X, Y, Z) = 25 °C at time t = 0 s. The input heat flow is obtained by using the friction power method. The effective friction area of the brake disc is 0.21 m^2, the friction coefficient is 0.28, and the effective radius of the brake disc is 297.3 mm. During the braking process, the brake disc is in forced convection heat dissipation state, and the heat dissipation coefficient is taken as 120 $W/m^{2}\cdot°C$ at 200 km/h; After braking, the brake disc is in natural convection heat dissipation state, with the value of 28 $w/m^{2}\cdot°C$, and the linear value is taken during braking. In the braking process, the indirect coupling method is used for calculation. The bilinear isotropic strengthening criterion is adopted in the thermal stress calculation, and the structural analysis element solid 185 is used to replace the thermal analysis element solid 70 for nonlinear transient analysis.

4. Calculation Results

4.1. Temperature field results

In order to study the stress distribution of the brake disc, that is, the distribution law of the thermal stress of the brake disc with the thickness and radial direction, the temperature field distribution of the brake disc is first analyzed. Select five positions along the radial direction. The distances from the center of the brake disc are 223 mm, 243 mm, 263 mm, 283 mm, and 303 mm. The node numbers are 41487, 41431, 41430, 41353, 41379. Four positions are selected along the thickness direction, and their distances from the friction surface are 0 mm, 6 mm, 16 mm, 38 mm. The node numbers are 41430, 41960, 42233, 42242, as shown in Figure 5. Under different braking conditions, the temperature change curve along the thickness direction is shown in Figure 6, and the temperature change curve along the radial direction is shown in Figure 7.

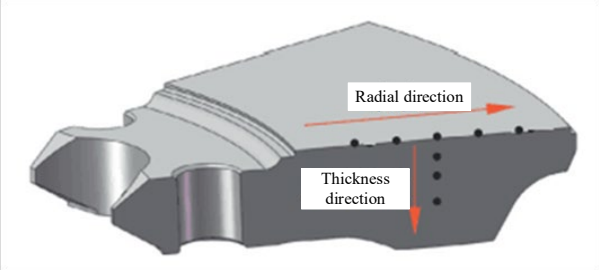

Figure 5. The temperature and stress measuring point of brake disc

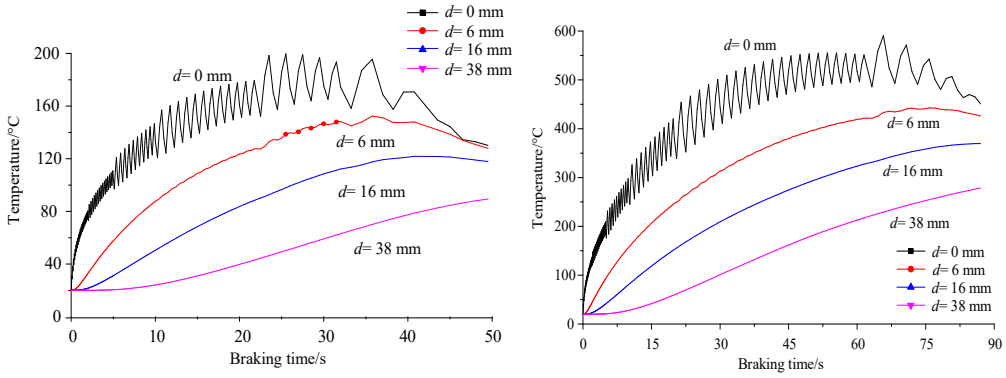

(a) 200 km/h emergency braking (b) 300 km/h emergency braking

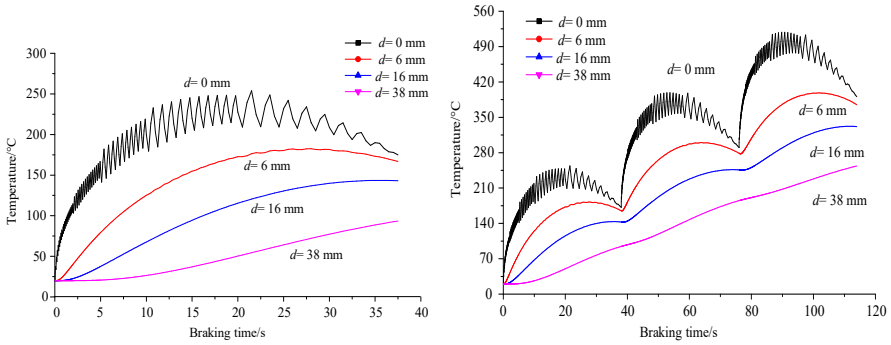

(c) Once 29 kN constant pressure braking (d) Three times of 29 kN successive constant pressure braking

Figure 6. The temperature curve of different thickness direction under different braking conditions

It is found that at the beginning of braking, with the successive input of strong heat flow, the surface heats up rapidly in a short time and reaches the peak point soon in Figure 6. Then, due to the effect of forced convection cooling, the surface gradually transfers heat to the disk body through heat conduction, thus the temperature gradually drops. At the same time, the temperature field of the brake disc gradually decreases along the thickness direction. This is because the strong friction between the brake disc and the brake pad that causes the surface temperature to rise sharply in a short time, while the temperature inside the brake disc is caused by heat conduction. Therefore, the greater the distance *d* from the friction surface, the lower the temperature.

Figure 7 shows that the temperature field of the disc surface increases first and then decreases in the radial direction. This is due to: (1) Limited by the geometric structure of the brake disc; (2) The friction ring is located at the center of the disc surface, closer to the center of the disc surface, the slower the heat dissipation, the higher the temperature. The cloud diagram of brake disc transient temperature field under different working conditions is shown in Figure 8.

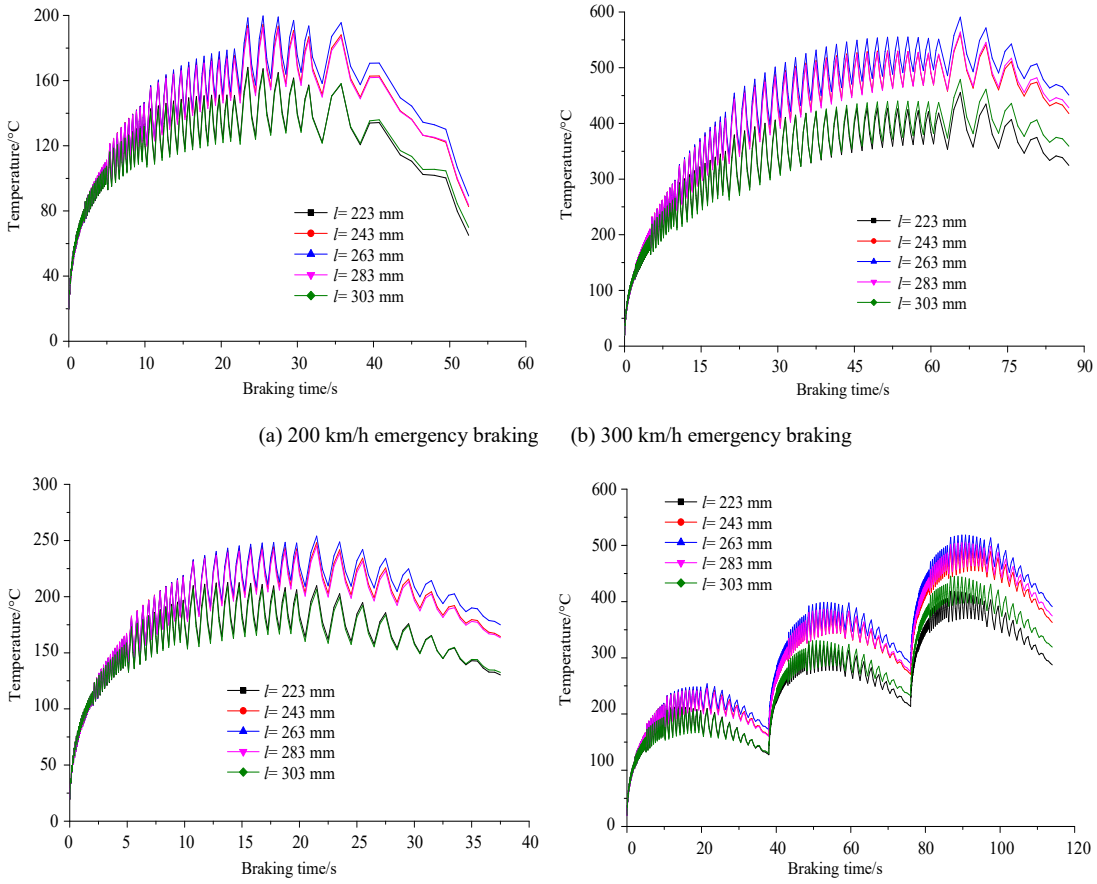

(a) 200 km/h emergency braking (b) 300 km/h emergency braking

(c) Once 29 kN constant pressure braking (d) Three times of 29 kN successive constant pressure braking

Figure 7. The temperature curve of different radial direction under different braking conditions

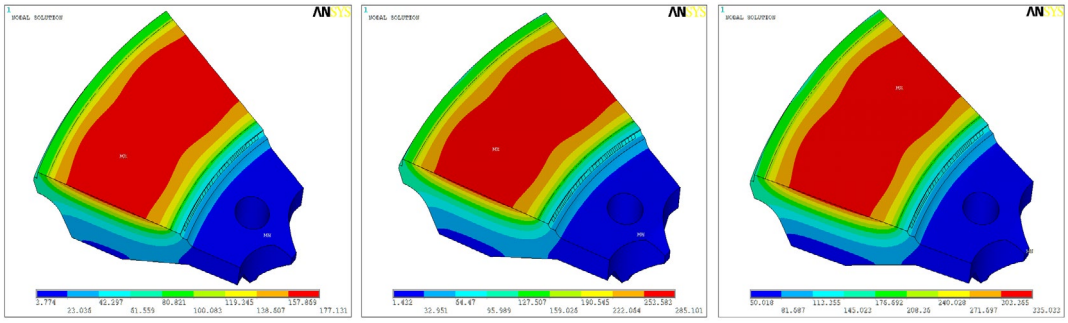

(a) 200 km/h emergency braking (b) 29 kN constant pressure braking (c) 300 km/h emergency braking

Figure 8. The cloud diagram of temperature field under different braking conditions

It can be seen from Figures 6-8 that the temperature field changes under different braking conditions are relatively similar. At the beginning of braking, the heat flux density is the largest, and during the braking process, the heat flux density gradually decreases as the braking time increases. The temperature field of the brake disc also shows a similar law under different braking conditions, that is, the temperature growth rate is getting smaller and smaller. After reaching the peak, the temperature of the disk gradually decreases. After braking, the temperature of the disc body gradually returns to room temperature.

4.2. Stress field results

Using the indirect coupling method, the analysis result of the temperature field is applied as a load to the simulation analysis of the thermal stress. The element type was also changed from SOLID70 to SOLID185, and full constraints were imposed on the bolt holes [49-50]. The nodes at d= 0 mm, 6 mm, 16 mm, and 38 mm from the disc surface position are selected in turn, and the change curves of circumferential stress, radial stress and equivalent stress with braking time are studied respectively. Figures 9-12 are once 200 km/h emergency braking, once 300 km/h emergency braking, once 29 kN constant pressure braking, and three times of 29 kN successive constant pressure braking curves of thermal stress along the thickness and radial directions. The cloud diagram of brake disc transient stress field under different working conditions is shown in Figure 13.

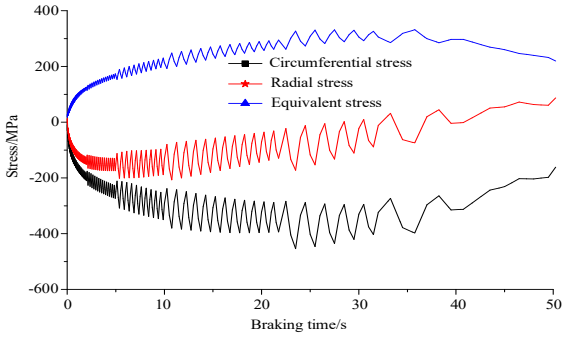

(a) Transient thermal stress change curve of the brake disk surface

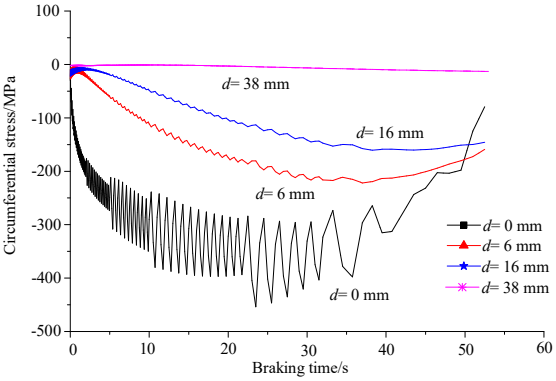

(b) Thermal stress variation curve of circumferential stress along the thickness direction

Figure 9. 200 km/h emergency braking

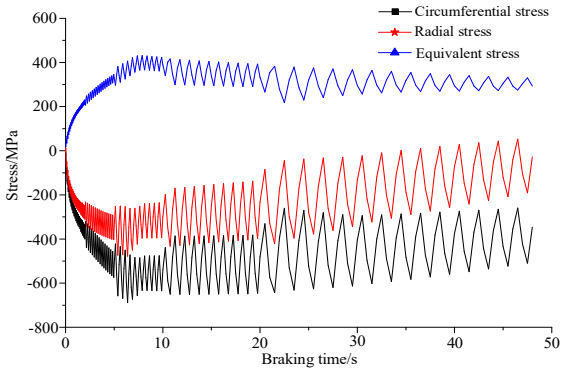

(a) Transient thermal stress change curve of the brake disk surface

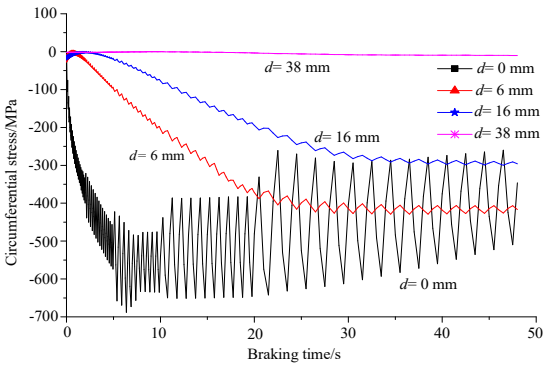

(b) Thermal stress variation curve of circumferential stress along the thickness direction

Figure 10. 300 km/h emergency braking

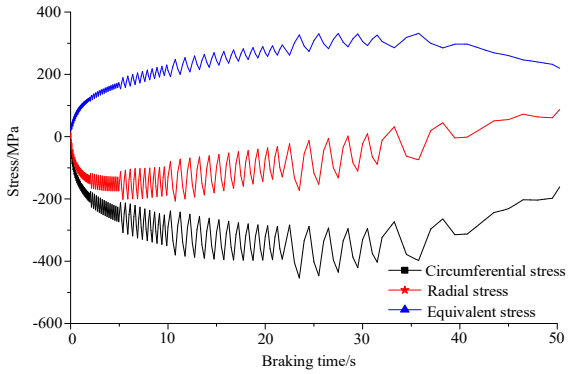

(a) Transient thermal stress change curve of the brake disk surface

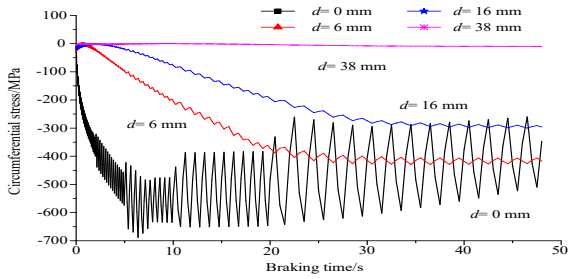

(b) Thermal stress variation curve of circumferential stress along the thickness direction

Figure 11. 29 kN constant pressure braking

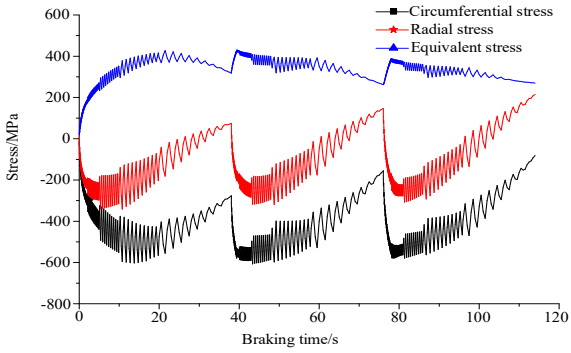

(a) Transient thermal stress change curve of the brake disk surface

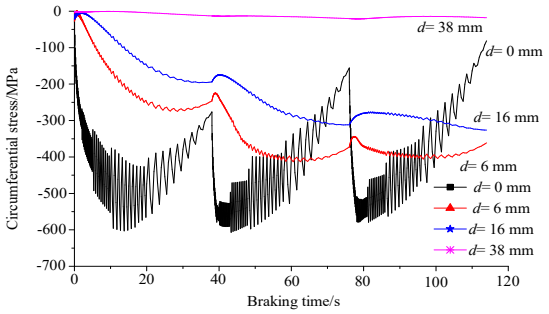

(b) Thermal stress variation curve of circumferential stress along the thickness direction

Figure 12. Three times of 29 kN successive constant pressure braking

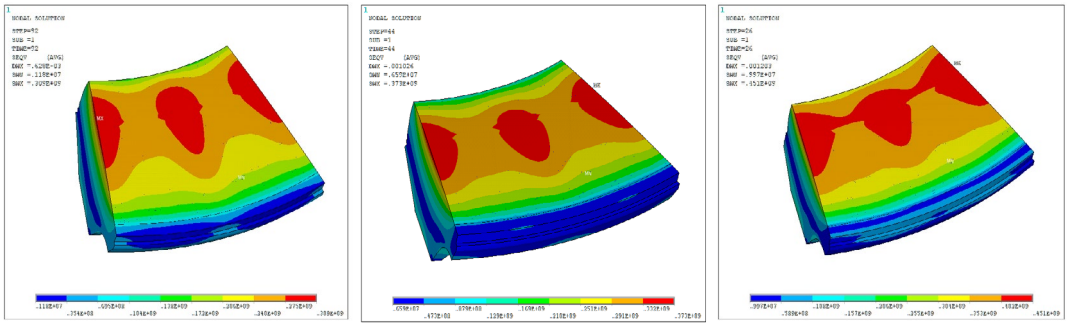

(a) 200 km/h emergency braking (b) 29 kN constant pressure braking (c) 300 km/h emergency braking

Figure 13. The stress field cloud diagram under different braking conditions

The main conclusions are as follows:

1. Under four different braking conditions, the circumferential stress of the disc surface is obviously greater than the radial stress.
2. During the braking process, the circumferential stress is dominant, which indicates that the surface is dominated by radial cracks; The rapid decline of the circumferential stress indicates that the radial cracks are mainly based on shallow cracks. When *d* is larger in the depth direction, the crack loses its driving force for growth. Radial cracks are one of the important reasons restricting train safety.
3. From the thermal stress curve of the brake disc, it can be seen that under four different working conditions, the stress is dominated by compressive stress during braking. After braking, a residual tensile stress of different magnitudes is formed under room temperature.
4. The change trend of the circumferential stress along the radial direction is similar to the change trend of the temperature field along the radial direction. The circumferential compressive stress reaches the maximum at about l = 263 mm (at the center of the friction ring); At l = 223 mm-263 mm and l = 263 mm-303 mm, the value gradually decreases; The circumferential stress values at l = 243 mm and l = 283 mm are not much different. It can be seen that the circumferential stress is almost symmetrical in the radial direction.
5. The thermal stress under 300 km/h emergency braking is greater than the thermal stress of three times of 29 kN successive constant pressure braking, once 29 kN constant pressure braking, and once 200 km/h emergency braking in turn.

It is found that there are three main reasons for the damage of the brake disc: (1) After the brake disc is heated

by friction, the temperature increases, resulting in the combined burning of the friction surface; (2) Abrasive wear caused by road dust and hard spots falling off the worn surface; (3) Fatigue damage caused by thermal stress caused by friction between brake disc and brake pad. To sum up, when the maximum temperature of the brake disc exceeds the maximum allowable temperature, or the maximum stress exceeds the yield stress, it will cause great damage to the brake disc. You can select better high-temperature and high-strength materials or optimize the heat dissipation structure of the brake disc, and add some grooves on the brake disc to reduce the temperature during the use of the brake disc, at the same time, the occurrence of severe working conditions such as emergency braking should be minimized, or the operating speed should be reduced to prolong the service life of the brake disc.

5. Conclusions

It can be inferred from simulation results that:

1. Although the braking conditions are different, the temperature change of the disk surface has similar laws from the temperature change curve. At the beginning of braking, with the continuous input of strong heat flow, the disk surface rises rapidly in a very short time and reaches the peak point soon. Then, due to the effect of forced convective cooling, the disk body gradually dissipates heat through radiation and convection, and the temperature decreases slowly.
2. The temperature of the brake disc surface is the highest. Along the depth direction, the farther away from the friction surface, the lower the temperature. The temperature in the center of the friction ring is the highest. Along the radius direction, the farther away from the center of the friction ring, the lower the temperature. The equivalent stress produced by the once 300 km/h emergency braking is the largest. It can be seen that speed has the greatest impact on the stress field of brake disc.
3. The three times of 29 kN successive constant pressure braking, the thermal stress in the second time is the largest and greater than the thermal stress formed during the first and third braking, while the temperature field is different. The maximum temperature in the latter time is greater than the previous. This is because the higher the temperature, the smaller the yield limit of the forged steel material, and the easier the material enters the plastic zone. The maximum equivalent stress produced by the third constant pressure braking is less than 10%, which shows that the damage caused by the third continuous braking is large.
4. According to the above research results, based on the bionic design concept, some new bionic heat dissipation ribs should be proposed to reduce the temperature field and stress field of the brake disc, so as to provide reference for the structural optimization and design of the brake disc.

Acknowledgments

The project supported by Scientific and Technological Innovation Programs of Higher Education Institutions in Shanxi (grant number: 2021L567); Luliang Development Zone High-Level Science and Technology Talent Introduction Program (grant number: Rc2020-116).

Reference

[1] Shi, X.L. Research on thermal fatigue life evaluation of high speed train on forging brake disc. PHD. Thesis, Beijing Jiaotong University, Beijing, 2016.
[2] Zhao, K.K., Jiang, P.F., Feng, Y.J., et al. Investigation of the characteristics of hydraulic fracture initiation by using maximum tangential stress criterion. Journal of Mining and Strata Control Engineering, 2021, 3(2), 023520.
[3] Jian, Q.F., Li, W., Yan, S. Thermal analysis of ventilated brake disc based on heat transfer enhancement of heat pipe. International Journal of Thermal Sciences, 2020, 155, 106356.
[4] Mori, K.S., Peng, H.M. Causes and countermeasures of thermal fatigue of brake disc. Foreign Rolling Stock Technology, 2009, (3), 38-41.
[5] Chen, G.B., Li, T., Yang, L., et al. Mechanical properties and failure mechanism of combined bodies with different coal-rock ratios and combinations. Journal of Mining and Strata Control Engineering, 2021, 3(2), 023522.
[6] Stepan, A., Mikhailenko, M.A., Sheremet. Impacts of rotation and local element of variable heat generation on convective heat transfer in a partially porous cavity using local thermal non-equilibrium model. International Journal of Thermal Sciences, 2020, 155, 106427.
[7] Wu, S.C, Zhang, S.Q, Xu, Z.W. Thermal crack growth-based fatigue life prediction due to braking for a high-speed railway brake disc. International Journal of Fatigue, 2016, 87, 359-369.
[8] Yevtushenko, A.A., Kuciej, M., Grzes, P., et al. Temperature in the railway disc brake at a repetitive short-term mode of braking. International Communications in Heat and Mass Transfer, 2017, 84, 102-109.
[9] Zhao, C., Wang, C.L., Wang, R.N., et al. Research on thermal performance simulation of ventilated brake disc based on ABAQUS. Drive System Technique, 2021, 35(3), 3-7.
[10] Srivastava, A.K., Arora, P.K., Kumar, H., et al. Numerical and experiment fracture modeling for multiple cracks of a finite aluminum plate. International Journal of Mechanical Sciences, 2016, 110, 1-13.
[11] Li, J., Li, L., Wu, J.P. Analysis of the temperature field during the sliding process of friction pair of brake disc. Journal of Beijing Information Science & Technology University, 2020, 35(6):43-49.
[12] Yang, Y., Ye, X.L., Ye, C. Analysis and optimization of thermal performance of brake disc of ultra deep mine hoist. Chinese Journal of Engineering Design, 2019, 26(1), 47-55.
[13] Collignon, M., Cristol, A.L., Dufrénoy, P., et al. Failure of truck brake disc: A coupled numerical-experimental approach to identifying critical thermomechanical loadings. Tribology International, 2013, 59(1), 114-120.
[14] Yevtushenko, A.A., Greza, P. Mutual influence of the velocity and temperature in the axisymmetric FE model of a disc brake. International Communications in Heat and Mass Transfer, 2014, 57, 341-346.
[15] Anderson, A.E., Knapp, R.A. Hot spotting in automotive friction systems. Wear 1990, 135(2), 319-337.
[16] Belhocine, A., Bouchetara, M. Investigation of temperature and thermal stress in ventilated disc brake based on 3D thermomechanical coupling model. Ain Shams Engineering Journal 2013, 4(3), 475-483.
[17] Ghadimi, B., Sajedi, R., Kowsary, F. 3D investigation of thermal stresses in a locomotive ventilated brake disc based on a conjugate thermo-fluid coupling boundary conditions.

International Communications in Heat and Mass Transfer, 2013, (49), 104-109.

[18] Choj, J.H., Lee, I. Finite element analysis of transient thermoelastic behaviors in disk brakes. Wear 2004, 257(1-2), 47-58.

[19] Su, S.L., Du, Y., Zhu, J.F., et al. Numerical study on bearing behavior of layered rock mass for deep roadway. Journal of Mining and Strata Control Engineering, 2020, 2(1), 013002.

[20] Gao, F., Wu, B.W., Yang, J.Y. Relationship of pad material parameters and brake disc temperature field. The Chinese Journal of Nonferrous Metals, 2020, 30(4), 837-846.

[21] Kim, D.J., Lee, Y.M., Park, J.S., et al. Thermal stress analysis for a disk brake of railway vehicles with consideration of the pressure distribution on a frictional surface. Materials Science and Engineering: A, 2007, 483, 456-459.

[22] Adamowicz, A., Grzes, P. Analysis of disc brake temperature distribution during single braking under non-axisymmetric load. Applied Thermal Engineering, 2011, 31(6-7), 1003-1012.

[23] Li, Y.M., Yang, J.Y., Han, X.M., et al. Influence of contact area and contact mode on temperature field of brake disc. Railway Locomotive & Car, 2020, 40(3), 23-28.

[24] Zhu, G., Huang, S.T., Xu, L.F., et al. Simulation and analysis of temperature field of SiCp/Al composite brake disc. Ordnance Material Science and Engineering, 2019, 42(6), 44-50.

[25] Chai, J., Ouyang, Y.B., Zhang, D.D. Crack detection method in similar material models based on DIC. Journal of Mining and Strata Control Engineering, 2020, 2(2), 023015.

[26] Chernyshov, E.A., Romanov, A.D., Romanov, I.D., et al. Evaluation of the Possibility of Replacement of an SCh24 Cast Iron of Detail of a "Brake Disc" of a Car by an Aluminum-Based Dispersion-Strengthened Composition Material Prepared by Internal Oxidation. Journal of Machinery Manufacture and Reliability, 2021, 50(1), 34-40.

[27] Chen, J.W. Analysis of road header's rotary table on vibration modal based on finite element method and tested data. Journal of Mining and Strata Control Engineering, 2020, 2(2), 026032.

[28] Chu, M.Z., Su, C., Mi, X.Z. Transient temperature field simulation analysis of high speed brake disc based on infinitesimal element method. Manufacturing Automation, 2020, 42(3),79-84.

[29] Wu, B., Sun, L. Study on transient temperature field of brake disc based on fluid-solid coupling heat transfer. Machinery Design & Manufacture, 2020, 6, 117-120.

[30] Sha, Z.H., Li, C.X., Liu, Y., et al. Effect of groove surface features on temperature field and stress field of brake disc in braking process. Machine Tool & Hydraulics, 2020, 48(11), 128-133.

[31] Zhang, B.L., Shen, B.T., Zhang, J.H., et al. Experimental study of edge-opened cracks propagation in rock-like materials. Journal of Mining and Strata Control Engineering, 2020, 2(3), 033035.

[32] Cai, Y.F., Li, X.J., Deng, W.N., et al. Simulation of surface movement and deformation rules and detriment key parameters in high-strength mining. Journal of Mining and Strata Control Engineering, 2020, 2(4), 043511.

[33] Ripley, M.I., Kirstein, O. Residual stresses in a cast iron automotive brake disc rotor. Physica B Condensed Matter, 2006, 385, 604-606.

[34] Yousuf, L.S. The effect of temperature on the stresses analysis of composites laminate plate. Jordan Journal of Mechanical and Industrial Engineering, 2019, 13(4), 265-269.

[35] Chiou, Y.J., Lee, Y.M., Tsay, R.J. Mixed mode fracture propagation by manifold method. International Journal of Fracture, 2002, 114(4), 327-347.

[36] Kheder, A.R.I., Jubeh, N.M., Tahah, E.M. Fatigue properties under constant stress/variable stress amplitude and coaxing effect of acicular ductile iron and 42 CrMo4 steel. Jordan Journal of Mechanical and Industrial Engineering, 2011, 5(4), 301-306.

[37] Teng, C.Q., Wang, L., Wei, P., et al. Parameter inversion of probability integral prediction based on shuffled frog leaping algorithm. Journal of Mining and Strata Control Engineering, 2020, 2(4), 047038.

[38] Zhou, S.X., Guo, Z.H., Bai, X.Y. Fatigue fracture analysis of brake disc bolts under continuous braking condition. Engineering Failure Analysis, 2020, 115, 104588.

[39] Khandakji, K.A. Analysis of hoisting electric drive systems in braking modes. Jordan Journal of Mechanical and Industrial Engineering, 2012, 6(2), 141-145.

[40] Alshyyab, A.S., Darwish, F.H. Three-dimensional stress analysis around rivet holes in a plate subjected to biaxial loading. Jordan Journal of Mechanical and Industrial Engineering, 2018, 12(4), 323-330.

[41] Tsay, R., Chiou, Y., Chuang, W. Crack growth prediction by manifold method. Journal of Engineering Mechanics, 1999, 128(8), 884-890.

[42] Li, Z.Q., Han, J.M., Yang, Z.Y., et al. Analyzing the mechanisms of thermal fatigue and phase change of steel used in brake discs. Engineering Failure Analysis, 2015, (57), 202-218.

[43] Wang, D.L., Hao, B.Y., Liang, X.M. Slurry diffusion of single fracture based on fluid-solid coupling. Journal of Mining and Strata Control Engineering, 2021, 3(1), 013038.

[44] Parameswaran, V., Sharma, S. Estimation of fracture parameters and stress field for edge cracks in finite elastically graded plates using boundary collocation. Acta Mechanica, 2006, 184(4), 159-170.

[45] Neimitz, A., Dzioba, I. The influence of the out-of- and in-plane constraint on fracture toughness of high strength steel in the ductile to brittle transition temperature range. Engineering Fracture Mechanics, 2015, 147, 431-448.

[46] Chen, A., Kienhöfer, F. The failure prediction of a brake disc due to nonthermal or mechanical stresses. Engineering failure analysis, 2021, 124, 105319.

[47] Yu, X.Y., Wang, Z.S., Yang, Y., et al. Movement rule of overburden in fully mechanized caving mining with thick depth and high mining height based on 3DEC. Journal of Mining and Strata Control Engineering, 2021, 3(1), 013533.

[48] Wallis, L., Leonardi, E., Milton, B., et al. Air flow and heat transfer in ventilated disc brake rotors with diamond and tear-drop pillars. Numerical Heat Transfer Applications, Part A, 2002, 41(6-7), 643-655.

[49] Duzgun, M. Investigation of thermo-structural behaviors of different ventilation applications on brake discs. Journal of Mechanical Science and Technology, 2012, 26(1), 235-240.

[50] Mcclung, R.C., Sehitoglu, H. On the finite element analysis of fatigue crack closure-1. Basic modeling issues. Edward Elgar, 1989, 33(2), 237-252.

JJMIE

Volume 16, Number 1, January. 2022
ISSN 1995-6665
Pages 123 - 131

Jordan Journal of Mechanical and Industrial Engineering

Mechanical Parts Pose Detection System Based on ORB Key Frame Matching Algorithm

Chun Liang*

School of Intelligent Manufacturing, Jiangsu Vocational Institute of Architectural Technology, Xuzhou 221000, China

Received 14 July 2021 *Accepted 28 December 2021*

Abstract

In order to solve the practical problem of accurate measurement of the position and posture of mechanical parts in the process of handling, a detection system for the position and posture of mechanical parts is designed. The improved Canny edge detection algorithm is used to recognize the contour of the mechanical part edge, and the scale invariant feature transformation method is used to extract the feature points and stereo matching of the mechanical parts. The mathematical model of the pose detection system is established, and the position and direction of the mechanical parts placed on the conveyor belt are calculated by solving the transformation relationship between coordinate systems. The shape and position of mechanical parts are recognized by compiling the pose recognition program. The experimental platform of pose test system is built and the test experiment is carried out. The experimental results show that the designed system can detect the position and orientation of parts quickly and effectively, and provide technical support for the realization of automatic pose detection of parts.

Keywords: ORB keyframe matching algorithm; Mechanical parts; Pose detection system; Canny edge detection.

1. Introduction

In the flexible automatic production line, robot is needed to carry, transfer and transport the mechanical parts. To grab a part, the robot first needs to measure the pose of the part [1]. It is the key technology of automatic feeding and unloading of parts to determine the placement, position and posture of the parts by the vision system. Machine vision is a kind of measuring and judging technology using machine instead of human eyes. In recent years, machine vision technology combined with robot technology has been widely used in industrial testing [2].

As a new non-contact technology, mechanical parts pose measurement technology can effectively make up for the shortcomings of the traditional 3D measurement, many experts at home and abroad have been widely concerned. The technology of measuring position and pose of mechanical parts has the advantages of real-time and high precision, which not only accords with the detection and positioning of intelligent factories, but also improves the automation and efficiency of industrial products [3]. The biggest advantage of non-contact position and pose detection is that the parts can be on-line detected and the following adaptive finishing can be carried out without reinstalling the parts. In the position and pose detection system of mechanical parts, the number of imaging pictures obtained by camera mainly includes many, binocular and monocular vision systems. Although the structure of monocular vision system is simple, it is difficult to measure the coordinate of depth in 3D coordinate. Binocular stereo vision is the use of two cameras in different positions to capture the same scene as a single camera after changes in position and pose [4]. Therefore, the study of binocular stereo positioning and pose detection is very meaningful, which can quickly and non-contact get the 3D coordinate information of parts, and calculate the pose.

In recent years, linear friction welding is an important method for machining and servicing aero-engine blades, and it can achieve better weld performance and integrated effect [5]. Because of the complex structure of the whole blisk, the machining technology is faced with great technical problems. Engine impeller is a kind of high precision machining product, and its machining quality affects engine performance. Therefore, the current disc processing technology has stopped the decentralized processing method, but adopted the overall processing method. At present, the way of machining integral blisk is concretely divided into welding and integral machining [6]. However, the overall processing of large quantities of materials and processing cycle is long, so linear friction welding is a good overall disk manufacturing means [7]. But after welding, the error detection of the position and attitude between blade and disk center is the key. After frictional linear welding, according to the position and posture obtained. At present, the visual inspection system is mainly used to detect the position of workpiece, but the research on the method of workpiece attitude inspection is less. Aiming at the actual demand of measuring the position and posture of mechanical parts in the process of transportation. This paper designs a position and posture detection system based on ORB (oriented fast and rotated brief) key frame matching algorithm.

* Corresponding author e-mail:liangchun1980@163.com

2. Conversion Scheme of Part Pose Detection System

2.1. Transformation of coordinate system of space coordinates

The system consists of 4 modules: image acquisition, image analysis and processing, dimension measurement and result output. The basic flow of the system is shown in Figure 1.

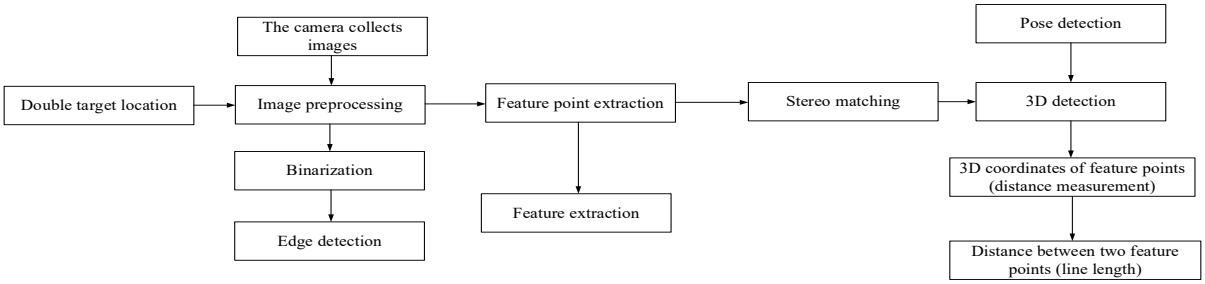

Figure 1. Work flow chart of pose detection system

In Figure 1, the position and attitude detection system is calibrated by using the calibration board, and then the image captured by the camera is binarized and edge detected, and the feature points are extracted from the image. Based on this, the points with the same features in the image are matched and the same name points are generated. Finally, the coordinates of the feature points, the external dimensions of the parts and the position and attitude information of the parts are measured through the 3D measurement module. The values of the coordinate system are represented by the position and orientation of the pixels. The origin is located at the top left corner of the pixel graph, the origin is located at the bottom of the V axis, and u axis is to the right, respectively representing the column pixels and row pixels. The coordinate conversion diagram of the spatial coordinate system is shown in Figure 2.

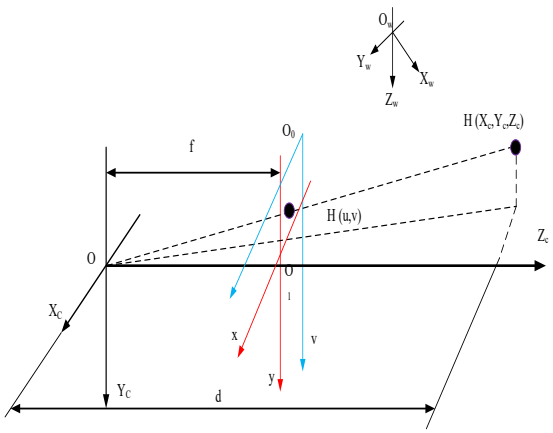

Figure 2. Transformation diagram of space coordinate system

2.2. Image gray level transformation

Mechanical part recognition needs to scan the part image by the camera first, and then transmit the acquired image to the PC through the image acquisition card. In the whole process of image collection, the quality of the collected image will be affected by various factors. Therefore, before the detection of mechanical parts, it is necessary to process the digital signal. In this way, the image distortion can be avoided as much as possible [8]. Therefore, it is very important to develop image preprocessing.

The general display consists of a finite number of points, and the points in this series are called pixels. The coloring device colors each pixel from left to right, and then colors all the pixels in the screen from top to bottom; people can feel the image information through the short visual effect of the eyes. Bitmaps display and save images through bitmaps [9]. Bitmaps include color bitmaps and grayscale images. Color bitmaps are formed by mixing red, green, and blue (R, G, B) colors, with different proportions of each color forming a variety of new colors. However, all pixels of all images are described by RGB components, which will eventually lead to the result that most of the computer storage space will be occupied by images. Grayscale image is a kind of non-color-table image described by different illumination intensity. It can express the grayscale image by quantifying the brightness value. Gray-scale map is generally divided into 0-255, where 0 represents pure black, 255 represents pure white.

Grayscale is one of the common ways of digital image information processing. There is an equal transformation relationship between image RGB color and gray value. In the RGB color mode of the image, a set of (RGB) values are used to represent the color information, which can be converted with the gray level of the image. After grayscale processing, the color and brightness of color image can be converted to the brightness of grayscale image. For RGB, the values are set to be equal, so the RGB value is changed from (0, 0, 0) to (255, 255, 255), (0, 0, 0) to pure black, (255, 255, 255) to pure white, and (0, 0, 0) to (255, 255, 255) to gray. In this way, we can use RGB value to describe the gray image.

Through image gray-processing, it can greatly reduce the workload of PC, shorten the image processing time, can get more detailed image information, greatly reduce the interference of external factors, and reduce the image processing difficulty [10]. Therefore, it is most reasonable to use gray-scale image in machine vision recognition and inspection.

There are three methods for gray scale transformation: maximum method, average method and weighted average method.

Maximum value method: the component with the largest value among RGB components is regarded as the gray value of the pixel. The formula is as follows:

$$R = G = B = \max(R, G, B) \tag{1}$$

The brightness of the image obtained by this method is high.

Average Value Method: Take the average of the three RGB components as the gray value of this pixel. The formula is as follows:

$$R = G = B = \frac{\max(R, G, B)}{3} \tag{2}$$

The images obtained by this method are more harmonious.

Weighted average method: to make certain proportional values of the three components of RGB according to certain rules, calculate the weighted average values of the three components and treat the values as gray values. The formula is as follows:

$$R = G = B = \frac{(W_R R + W_G G + W_B B)}{3} \tag{3}$$

where W_R, W_G and W_B are the weight values of RGB components. By changing the values of W_R, W_G and W_B, various gray images can be produced. It is found that people have the strongest light sensitivity to the green series, but the least sensitive to the blue series. In this study, weighted average method is used.

For the light between the green and blue series, according to the $W_R > W_G > W_B$ weight value, we can get the gray image which is more suitable for human eyes. In particular, in W_R=0.299, W_G=0.587, W_B=0.114 values, the human eye is more likely to feel the color of the light.

3. Image Preprocessing of Mechanical Parts Position and Pose Detection System

Due to the influence of external environment and internal parameters, such as illumination, lens, etc., in the process of image acquisition, the image of mechanical parts will be disturbed. If the angle of illumination causes the surface of the workpiece to be obscured by light from the environment, or to reflect light resulting in highlighting, or the workpiece is located on a platform showing signs of irregularity [11, 12]. Because the camera has a strong ability to capture images, these external effects will be captured by the camera and presented in the image, which is easy to cause image misjudgment, so image preprocessing is needed. There are three main steps in image preprocessing: image binarization, edge contour extraction, and mass processing (connected domain).

3.1. Image binarization

Because the principle of black-and-white image data is simple and reliable, it can be easily identified by computer. The binary method is used to process the image, and all the gray information of the image is converted into 0 and 255 binary values. Position and pose detection systems for mechanical parts minimize interference from object color properties [13]. In this paper, Otsu method is used to binarize the image. The idea of Otsu algorithm is to divide the image into background and target, and the larger the variance between the background and target, the greater the difference between the two parts. Therefore, maximizing the variance between classes means minimizing the probability of misdivision.

For the image gray value $K(x, y)$, the segmentation threshold of target and background is marked as H, then there are:

$$\begin{cases} w_0 = \dfrac{N_0}{M} \times N \\ w_1 = \dfrac{N_1}{M} \times N \\ N_0 + N_1 = M \times N \\ w_0 + w_1 = 1 \\ u = w_0 u_0 + w_1 u_1 \\ g = w_0 (u_0 - u_0)^2 + w_1 (u_1 - u_1)^2 \end{cases} \tag{4}$$

where: w_0 represents the proportion of target pixel points in the whole image; u_0 represents the average gray level; w_1 represents the proportion of background pixel points in the whole image; u_1 is the average gray level; u is the total average gray level of the image; g is the inter class variance; $M \times N$ is the size of the image when the background is dark; N_0 is the number of pixels whose gray value is less than the threshold T; N_1 is the number of pixels whose gray value is greater than the threshold T.

By simplifying Formula (4), the following can be obtained:

$$g = w_0 w_1 (u_0 - u_1)^2 \tag{5}$$

By using traversal method, the threshold T is obtained when the variance between classes is maximized. The optimal threshold value obtained by Otsu algorithm is 177. The ORB framework proposed in this study is an improved method based on graph optimization, and its overall framework is shown in Figure 3.

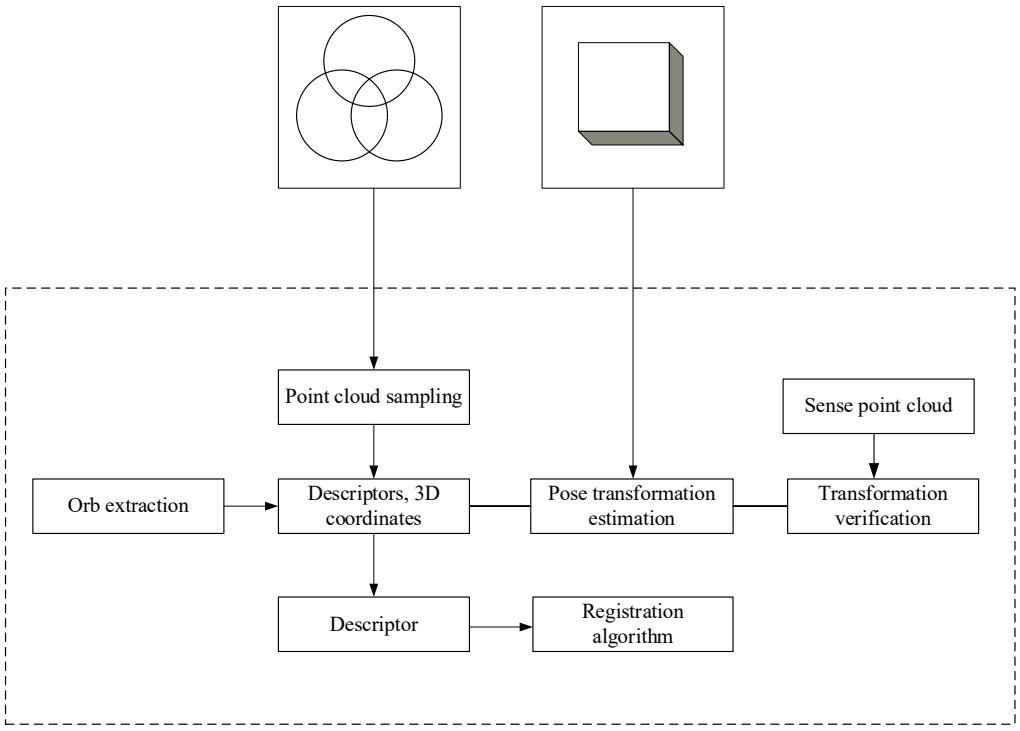

Figure 3. Improved ORB system framework diagram

The framework is divided into three parts: front-end construction, back-end optimization and map representation. According to the observation and constraint information, the system can construct the position and pose map and the 3D point cloud by feature point registration and position and pose transformation.

3.2. Extraction of part edge contour

Part edge reflects the structural characteristics of the part, so before the image recognition, image edge detection, effectively reduce the computer misjudgment of the measured parts [14].

In this paper, the improved Canny edge detection algorithm is used to detect the edge of parts, and the gradient amplitude calculation method is used to improve it.

The basic process is as follows: denoising the image by Gauss; interpolating all the pixels in the neighborhood along the gradient direction with the gradient amplitude, calculating the gradient direction and amplitude, detecting the maximum amplitude points, and then getting the edge points; then suppressing the non-maximum value, then connecting the edges through the double threshold algorithm to prevent false edges from appearing in the contour map, and improving the efficiency of part edge calculation [15].

3.3. Image block processing

Image agglomeration processing is to process the connected region of the image. The measurement system of the position and orientation of the parts remove the connected region that is smaller than the region value by setting the value of the area and the perimeter domain, and by successively removing the connected region through the processes of removing the noise of the perimeter, the area and the roundness domain [16, 17].

For example, in binarization image, the uneven part of the workpiece surface is displayed on binarization image because of the influence of the illumination angle.

***3.4.** Image preprocessing experiment*

After calibration by the calibration board, the system places the workpiece to be measured (in the middle of the camera picture). In this study, "Otsu binarization" method is used to preprocess the part image [18].

The Canny edge detection algorithm is used to detect the edge of parts. In this process, Gaussian filter is needed to filter out the interference information. In the Gaussian filter, the Gaussian kernel can be regarded as the weight negatively correlated with the center distance. During image smoothing, adjusting the standard deviation σ of Gaussian filter is actually adjusting the influence of surrounding pixels on the current pixel. Increasing σ increases the influence of distant pixels on the central pixel, and the smoother the image filtering result. The calculation process of spatial standard deviation σ of Gaussian filter is as follows:

$$\sigma=\frac{1}{2\pi\sigma_{\omega}} \tag{6}$$

where σ_{ω} represents the standard deviation corresponding to Gaussian in frequency domain. In this study, the standard deviation σ of Gaussian filter is set to 0.4, and the edge detection effect is shown in Figure 4.

(a) Left camera capture screen (b) Right camera capture screen

Figure 4. Edge detection image

4. Stereo Matching and Part Pose Detection

4.1. ORB feature point detection and matching

The ORB algorithm extracts feature points through FAST corner detection. Its principle description is as follows: for detecting the gray value of 16 pixels in a circle with any point p as the center and 3.4 pixels as the radius (referred to as the M16 template), if the gray value of consecutive n points in M16 is greater than Ip t or less than $I_p - t$ (among which: $I_p - p$ point gray value, t −threshold), p shall be determined as the feature point. In order to improve the speed and accuracy of feature point detection, the author adopts a segmentation test standard, namely 12 point detection method. Only the gray values of points 1, 5, 9 and 13 are detected first, and the remaining 12 points are detected only after at least 3 points meet the above threshold conditions [19]. The M16 test template is shown in Figure 5.

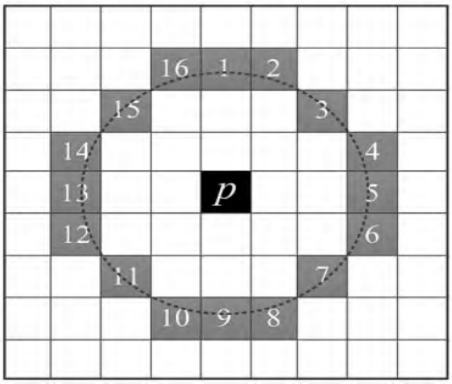

Figure 5. M16 test template

The above segmentation criteria only apply to the case of n = 12. In order to improve the accuracy and effectiveness of detection, the machine learning method is introduced into the FAST algorithm. The steps are as follows: for the specified pixel value n and threshold t, all feature points are detected from the image set by using the segmentation test criteria. The process needs to detect the M16 of each point, and the detected image is used as the training sample [20]. Then, according to the principle of maximum information gain, the ID3 algorithm is used to train the feature point classification decision tree. The points in the image are classified into feature points and non-feature points by decision tree.

The system backend is responsible for the optimization of the posture map, so that the output map model has global consistency. Sensor noise, cumulative error of depth value quantification and registration error will lead to the uncertainty of the system, and then pose and drift of 3D map will appear [21]. Through closed-loop detection, random closed-loop detection and trajectory optimization, the whole map is updated in real time in order to enhance the global consistency of the generated map model.

The fast corner detection based on machine learning only compares the pixel gray values, so that its matching efficiency is effectively improved. Machine learning can enhance the universality of the algorithm. If the intensity centroid is specified as the rotation direction, the rotation invariant of fast (oriented fast) descriptor can be obtained [22]. The process is as follows: take the feature point O as the origin of the coordinate system, calculate the centroid position B in the neighborhood P, and construct the vector OB with the feature point as the starting point and the centroid as the end point.

The matrix of a neighborhood can be expressed as:

$$R_{as} = \sum_{n \times m} x^a y^s K(x, y) \tag{7}$$

where: $K(x, y)$ is the gray value of the image, $x, y \in [-r, r]$, and r is the radius of the neighborhood P. Then the centroid position of the neighborhood is:

$$C_u = \left(\frac{R_{10}}{R_{00}}, \frac{R_{01}}{R_{00}} \right) \tag{8}$$

In order to detect the pose of workpiece in binocular stereo vision system, it is necessary to detect and match feature points. Stereo matching is to find the conjugate image points in the collected left and right images, and determine the corresponding relationship between the target points in the left and right images. Pose is the position and posture of the object, where the position is the coordinate value of X, Y and Z, and the posture is the rotation angle around X, Y and Z. Make the point set $P_{1i} = (x_{1i}, y_{1i}, z_{1i})$ at the ideal position before welding and $P_{2i} = (x_{2i}, y_{2i}, z_{2i})$ after welding. Therefore, the coordinate value of P point before welding is formed by a rotation matrix and a translation matrix, which is as follows:

$$\begin{bmatrix} x_{2i} \\ y_{2i} \\ z_{2i} \end{bmatrix} = R \begin{bmatrix} x_{1i} \\ y_{1i} \\ z_{1i} \end{bmatrix} + T \tag{9}$$

where vector T is a three-dimensional vector:

$$T = [tx, ty, tz]^T \tag{10}$$

The translation vector T is the position translation of two pieces before and after welding, and the R matrix is a 3×3 matrix, in which nine elements are trigonometric functions of three angles (R_x, R_y, R_z), and R_x, R_y and R_z are the three rotation angles around axis X, Y and Z of boss coordinate system respectively. The detailed rotation process is as follows: first, Z rotates around axis R_z, then rotates R_y around axis Y, and finally rotates R_x around axis X. the right hand rule is positive.

4.2. Extraction and stereo matching of feature points

The system utilizes the scale invariant feature transform (SIFT) based on feature point scale invariant feature transform for stereo matching. SIFT is a widely used feature point detection and description algorithm at present. The key of SIFT feature matching is to extract feature points. The extraction process of feature points is as follows: detecting the extreme value of scale space, determining the correct feature points and the main direction of feature points, and generating SIFT feature vectors. The specific steps are as follows:

(1) Computing the point-to-point test based on child windows in the neighborhood of a certain feature point;

(2) Sort all the test values in step (1) according to the difference between them and 0.5 to form a vector;

(3) Greedy search: (a) placing the first test point in the result vector R and removing it from the vector; (b) taking a test from the vector and comparing it with all the test values in the vector, and discarding it if the correlation is greater than a certain threshold, or adding it to the vector as a coordinate to generate the descriptor; and (c) repeating the above steps until there are 256 coordinates in the vector to form the final descriptor. Then the correlation threshold is increased, and the correlation of the selected test values is checked again to ensure that the final results have a smaller correlation.

The detection of the change of position and orientation of welding parts. Firstly, the technology structure of finishing square convex table on the blade blank is shown in Figure 6, which is used for blade positioning.

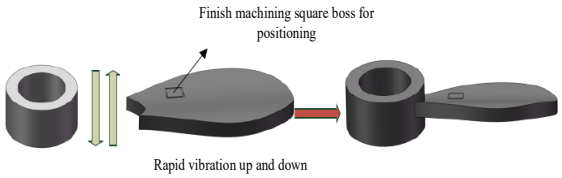

Figure 6. Sketch of linear friction welding of bladed disk

Before welding, fix the vane disc in the ideal position of the disc center with special fixture. Firstly, a mark circle is pasted on the convex platform, a vertex is selected, and three vertical boundaries are made as the coordinate system of X, Y and Z axis. After the welding, the images of the boss are taken and the 3D coordinates are calculated. Finally, we get the 3D coordinates and calculate the angle of the three translation parameters R_x, R_y and R_z in the convex coordinate system.

The position and posture detection system detects the coordinates of X, Y and Z of some key points by binocular stereo vision, and solves the displacements of three coordinate axes and the corners of three states according to the coordinates. Finally, the tool path is generated by NC programming and the blank parts are finished. The gray transparent portion is the extra margin in Figure 7.

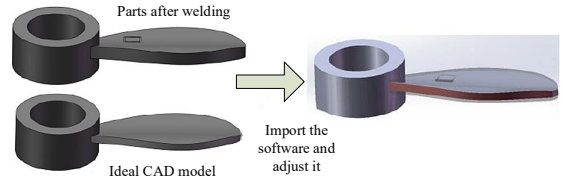

Figure 7. Comparison of parts and ideal part models after determination of welding pose

4.3. Modeling of pose detection system

In essence, the pose detection of parts is to solve the position relationship between two coordinate systems. There are two groups of parameters to describe the pose transformation of two coordinate systems: Euler angle and displacement. Firstly, a workpiece coordinate system is established on the part to be measured. The origin can be set at the space position on or near the part. The coordinate system is marked as OM and the world coordinate system is marked as Ow. The OM coordinate system is rotated around ZM axis. When XM axis (YM axis) is parallel to ow's XW axis (Yw axis), the rotation stops and the rotation angle γ is recorded. Suppose that the parallel axes are XM and Xw, then rotate the OM coordinate system around the XM axis until the second coordinate axis is parallel; assume that the second parallel axis is YM and Yw, record the rotation angle β; the last rotation makes OM parallel to Ow three axes, and then record the rotation angle α.

The coordinate system OM translates along the three directions of X, Y and Z, and finally completely coincides with Ow. The displacement of the translation is the three-dimensional coordinates XT, YT, ZT of the origin of the OM coordinate system in Ow. In fact, the pose of a part is the transformation of two coordinate systems.

The steps for measuring the pose of the part are as follows:

(1) Establishing the relationship between the reference coordinate system and the camera coordinate system. The space vectors of each axis of the coordinate system are obtained by using the method of plane fitting, and the space vectors of 3 axes in the camera coordinate system are constructed.

(2) Obtain the position relationship between the workpiece coordinate system and the camera coordinate system in real time. The coordinate values of the points in the coordinate system of the workpiece are obtained by identifying the feature points on the part, and the coordinate values of the points in the camera coordinate system are obtained by measuring the feature points.

(3) Obtain the position relationship between the workpiece coordinate system and the reference coordinate system. According to the relation obtained in step (2) and the relation between the reference coordinate system and the camera coordinate system, the position relation matrix of the two systems is obtained by matrix transformation.

(4) Solve the pitch angle, yaw angle and roll angle of the workpiece in the reference coordinate system.

The relationship between the workpiece coordinate system and the reference coordinate system determines the position of the partial angle of the part relative to the reference coordinate system, that is, the space attitude of the part. It is determined by three angles describing the relative relationship between the two coordinate systems, namely, the Euler angle, as shown in Figure 8.

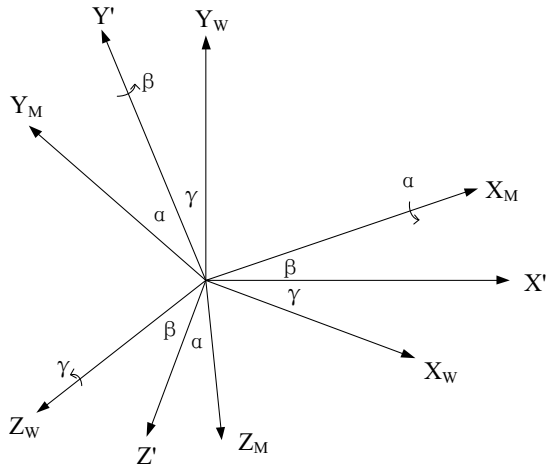

Figure 8. Relationship between reference coordinate system and moving body coordinate system

In Figure 8, the pitch angle alpha represents the angle of rotation of OYM 'around OXM to OYM, that is, the angle between OYM and the plane OXM Y'. The angle of yaw beta represents the angle of rotation of OX 'around OY' to OXM, that is, the angle between OXM and plane OZW X'. Roll angle γ represents the angle of rotation of the OXW axis around the OZW axis to the OXW axis in the reference coordinate system, that is, the angle between the OXW axis and the plane OXW ZW. The angle sign is determined by the right-hand rule.

5. Testing Experiment and Error Analysis of Parts Position and Pose

5.1. Parts and posture testing platform

In the simulation, the hardware environment: Celeron 2.4 GHz for the processor, 4GB of memory for the computer, Windows 7 for the software environment, using C + in the Visual Studio compiler. Testing experimental time was 30 min.

In order to verify the effect of part pose detection, a platform for part pose detection is built, as shown in Figure 9.

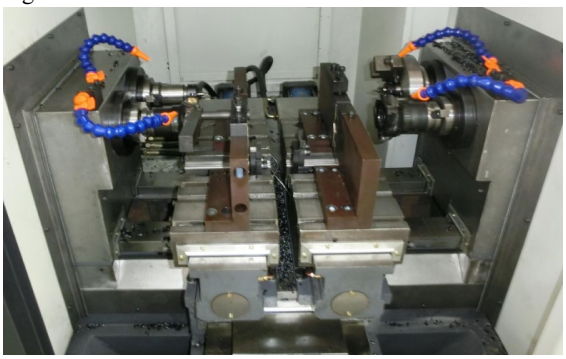

Figure 9. Binocular stereo vision measurement system platform

As can be seen from Figure 9, there are two parts of the instrument. Other specific platforms include: binocular calibration, binocular detection, stereo matching, binocular measurement, pose and angle measurement.

5.2. Part pose testing process

After actual measurement and parameter adjustment, the distance between each point of the calibration board and the left camera (the origin of the coordinate system coincides with the light center of the left camera) is approximately equal to the Z-direction value of the three-dimensional coordinates of the workpiece under measurement. Taking the six-hole workpiece as an example, the posture measurement is carried out. Select 5 feature points of the workpiece to measure, use 3 feature points to establish a workpiece coordinate system, and use 2 feature points for accuracy correction. The position and posture of the six-hole workpiece are tested by placing the workpiece in any of six positions. The specific flow is shown in Figure 10.

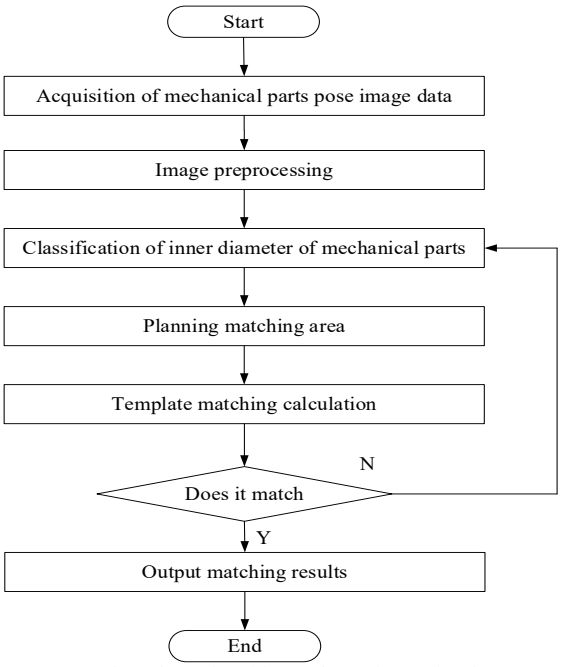

Figure 10. Flow chart of position and pose inspection for mechanical parts

5.3. Experimental error

The experiment is divided into two groups, the first group of tilted, the second group of vertical and horizontal direction of placement, left and right side of the detection of the screen as shown in Figure 11.

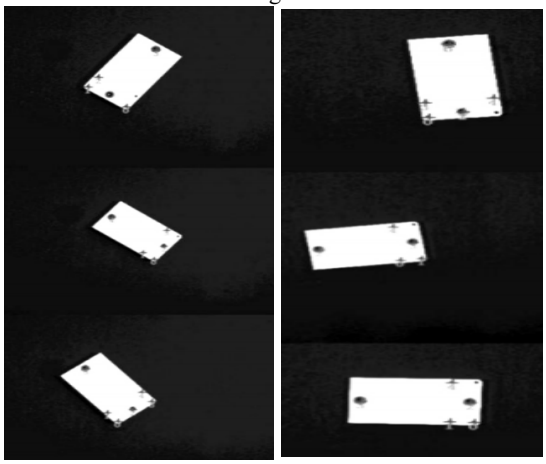

(a) Left instrument test drawing (b) Right instrument test drawing

Figure 11. Six hole workpiece placement posture

Measure the 6 positions of the parts, and get 6 sets of pose data, as shown in Table 1.

Table 1. Position and orientation data table of six holes

Position	Pitch angle (°)	Yaw angle (°)	Roll angle (°)
1	19.83	176.89	-106.25
2	36.44	-15.45	-155.45
3	84.82	-77.65	-99.45
4	84.26	54.26	170.69
5	52.36	8.89	115.28
6	58.14	-30.25	-127.65

In order to verify the accuracy of the position and pose measurement system, the position and pose of workpiece

No. 5 is repeated for 5 times. The results are shown in Table 2.

Table 2. Test data of position and pose of workpiece No. 5

Position	Pitch angle (°)	Yaw angle (°)	Roll angle (°)
1	53.25	8.95	115.25
2	53.26	8.54	115.89
3	53.12	9.01	114.15
4	53.30	9.52	114.69
5	53.45	8.90	117.86

In Table 2, the measurement of the angle of rotation of the workpiece around the X and Y axes has a slight fluctuation, with only a deviation of 0-0.54°and 0-1.03°; The measurement of the angle of rotation along the Z axis has a larger deviation, with a maximum of 3.42°. Generally, the parts are transported by adsorption, which requires high precision in X and Y direction and is insensitive to Z-axis deviation. Therefore, the system can meet the requirements of parts loading and blanking.

Using the same computer, we compare several common feature points extraction and matching algorithms by artificial rotation and Gaussian noise. The matching results can verify the rotative invariance of the improved ORB algorithm. As shown in Figure 12, the improved ORB algorithm proposed in this study has better anti-rotation performance than other algorithms.

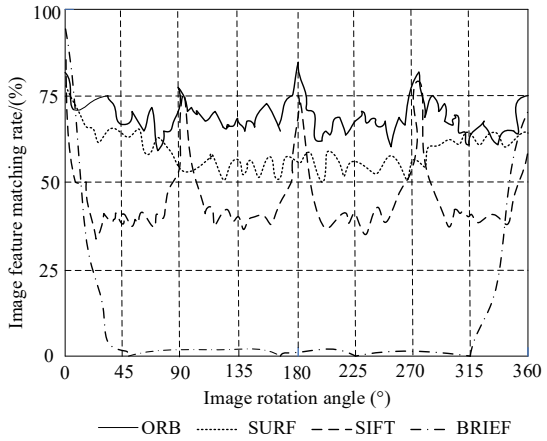

Figure 12 Comparison of various algorithms for rotation invariance

As can be seen from Figure 12, the execution time of the algorithm is an important indicator of the real-time performance of the algorithm. Under the same hardware conditions, using the atlas of data set can verify that the ORB operator has better real-time performance. The matching feature points are extracted by ORB algorithm, and the feature point descriptor D-R64 is stored in the form of Y-R3. The geometric relationship between the observed position (X-R6) and the observed information can be obtained. Through the inter-frame registration of ORB feature point image, the feature data in different observation coordinate system can be transformed into global coordinate system to detect the position and orientation of mechanical parts.

Finally, taking the pose detection accuracy as the index, the application performance of different methods is verified, and the results are shown in Table 3.

Table 3 Comparison results of pose detection accuracy of different methods (%)

Image rotation angle (°)	ORB	SURF	SIFT	BRIEF
90	93.26	87.89	75.24	82.36
180	94.27	88.55	75.88	83.41
270	94.13	89.02	74.14	83.60
360	95.31	89.50	74.64	84.14

By analyzing the results shown in Table 3, we can see that with the change of image rotation angle, the pose detection accuracy of different methods also changes. However, in contrast, the pose detection accuracy of this method can always be maintained at more than 90%, which is significantly higher than the three traditional methods, which proves that this method has better application effect.

6. Conclusions

Based on the ORB key frame matching algorithm, the position and pose detection system of mechanical parts is designed. According to the actual requirements of position and pose detection in the process of loading and unloading of mechanical parts, this paper designs a set of pose detection system for mechanical parts, establishes the mathematical model of pose detection system by using ORB key frame matching algorithm, and calculates the parts in the conveyor belt by solving the transformation relationship between coordinate systems The algorithm program of pose recognition is compiled to realize the recognition of the shape and pose of parts. The test experiment is carried out with a typical workpiece as an example. The experimental results show that the system can quickly locate and measure the parts and meet the requirements of loading and unloading of mechanical parts.

Acknowledgement

The research is supported by: Ministry of housing and urban rural development science and technology program (No. 2016-K4-063).

References

[1] Leicht A, Yu C H, Luzin V, et al. Effect of scan rotation on the microstructure development and mechanical properties of 316L parts produced by laser powder bed fusion. Materials Characterization, 2020, 163(5): 110-118.

[2] Vicente C M S, Martins T S, Leite M, et al. Influence of fused deposition modeling parameters on the mechanical properties of ABS parts. Polymers for Advanced Technologies, 2020, 31(3): 501-507.

[3] Sánchez-Safont E L, Arrillaga A, Anakabe J, et al. PHBV/TPU/cellulose compounds for compostable injection molded parts with improved thermal and mechanical performance. Journal of Applied Polymer Science, 2018, 28(5): 1-13.

[4] Azarniya A, Colera X G, Mirzaali M J, et al. Additive manufacturing of Ti–6Al–4V parts through laser metal deposition (LMD): Process, microstructure, and mechanical properties. Journal of Alloys and Compounds, 2019, 804(2): 15-26.

[5] Johnson L E. Chokepoints in mechanical coupling associated with allosteric proteins: the pyruvate kinase example. Biophysical Journal, 2019, 116(9): 1598-1608.

[6] Ramírez-Muñoz J E, Restrepo C J P, Vinck-Posada H. Indirect strong coupling regime between a quantum dot and a nanocavity mediated by a mechanical resonator. Physics Letters A, 2018, 382(15): 3109-3114.

[7] El-Zayat M M, Mohamed M A, Shaltout N A. Effect of maleic anhydride content on physico-mechanical properties of γ-irradiated waste polypropylene/corn husk fibers bio-composites. Radiochimica Acta, 2020, 108(2): 151-157.

[8] Wesierski D, Jezierska A. Instrument detection and pose estimation with rigid part mixtures model in video-assisted surgeries. Medical Image Analysis, 2018, 46(30): 244-265.

[9] Tejani A, Kouskourida R, Doumanoglou A, et al. Latent-class hough forests for 6DoF object pose estimation. IEEE Transactions on Pattern Analysis and Machine Intelligence, 2018, 40(1): 119-132.

[10] Sharma S, Ventura J, D'Amico S. Robust model-based monocular pose initialization for noncooperative spacecraft rendezvous. Journal of Spacecraft and Rockets, 2018, 55(6): 1414-1429.

[11] Li J G. Distributed multi-level inventory algorithms for automotive maintenance spare parts based on centralized control model. Jordan Journal of Mechanical and Industrial Engineering, 2020, 14(1): 89-99.

[12] Berrington A, Voets N L, Larkin S J, et al. A comparison of 2-hydroxyglutarate detection at 3 and 7T with long-TE semi-LASER. Nmr in Biomedicine, 2018, 31(5897): 25-31.

[13] Mademlis I, Tefas A, Pitas I. A salient dictionary learning framework for activity video summarization via key-frame extraction. Information Sciences, 2018, 432: 319-331.

[14] Seke E, Anagün, Y, Adar N. A new multi-frame super-resolution algorithm using common vector approach. IET Image Processing, 2018, 12(12): 2292-2299.

[15] Ferrari R, Cocchetti G, Rizzi E. Effective iterative algorithm for the limit analysis of truss-frame structures by a kinematic approach. Computers & Structures, 2018, 197(1): 28-41.

[16] Xu Q S, Zheng H D, Hu Z, et al. High-precision parts image defect feature fast positioning retrieval simulation. Computer Simulation, 2019, 36(4): 413-417.

[17] Ning P F. An adaptive scheduling method for resources in used automobile parts recycling. Jordan Journal of Mechanical and Industrial Engineering, 2020, 14(1): 53-60.

[18] Sathya S P A, Srinivasan R. Non-redundant frame identification and keyframe selection in DWT-PCA domain for authentication of Video. IET Image Processing, 2019, 14(2): 26-32.

[19] Bommisetty R M, Prakash O, Khare A. Keyframe extraction using Pearson correlation coefficient and color moments. Multimedia Systems, 2020, 116(26): 1-33.

[20] Sathya S P A, Ramakrishnan S. Non-redundant frame identification and keyframe selection in DWT-PCA domain for authentication of video. IET Image Processing, 2020, 14(2): 366-375.

[21] Ferrari R, Cocchetti G, Rizzi E. Effective iterative algorithm for the limit analysis of truss-frame structures by a kinematic approach. Computers & Structures, 2018, 197(12): 28-41.

[22] Oyebode O A, Erukainure O L, Ibeji C, et al. Crassocephalum rubens, a leafy vegetable, suppresses oxidative pancreatic and hepatic injury and inhibits key enzymes linked to type 2 diabetes: An ex vivo and in silico study. Journal of Food Biochemistry, 2019, 43(8): 129-135.

JJMIE

Volume 16, Number 1, January. 2022
ISSN 1995-6665
Pages 133 - 139

Jordan Journal of Mechanical and Industrial Engineering

Design of Visual Monitoring Software for Micro-Drive Debugging in Electromechanical System

Qian Wang, Yuqing Zhao*, Hongjun Shi

Department of Mechanical and Electrical Engineering, Xingtai Polytechnic College, Xingtai 054035, China

Received 14 July 2021 *Accepted 28 December 2021*

Abstract

Aiming at the problems of low monitoring accuracy and large memory consumption of traditional monitoring software, a visual monitoring software for MEMS micro-drive debugging is designed in this paper. According to the characteristics of MEMS system and the driving principle of micro actuator, the functional module of visual monitoring software for micro actuator debugging is designed. It includes monitoring pause button module program, visual display module program, monitoring quadrature signal module program and monitoring signal communication module program. Improve the monitoring accuracy through the connection between various modules. Select the material of the micro-drive and set its structural parameters, connect and debug the hardware of the drive, and test the performance of the designed software. The experimental results show that the software designed in this paper has high accuracy and low memory loss, the average accuracy is more than 90%, and the memory consumption is only 156 kb. It shows that this method can effectively monitor MEMS micro actuator, and the monitoring results are reliable.

Keywords: MEMS; Micro actuator; Function module; Connect and debug; Visual monitoring.

1. Introduction

So-called MEMS (Micro company Mechanical Systems, MEMS), refers to the micro structure of the sensors, actuators and signal processing of small and integration in the integration of control circuit and other components, which can give and send the order information or information acquisition and processing according to the obtained information to work independently or in accordance with the outside world commands a micro computer electric parts, gear, or the micro system [1]. The devices developed by using MEMS technology can be applied in the fields of aerospace, aviation, military, biomedical, environmental monitoring and electronic consumption, etc., with a very broad prospect [2]. MEMS technology is gradually developing into a huge industrial cluster, and at the same time is pregnant with a very profound technological change, which will bring a new round of impact on human production and life [3, 4]. As a key part of MEMS, micro-drives have been studied in many countries since the 1980s, and some achievements have been made in China.

Yu and Tan designed a laser processing system monitoring software based on DEA control module [5]. The system is divided into different modules, mainly: identity verification module, monitoring module, data management module, etc. It is built on the basis of OEF graphics algorithm DEA control model, adding DEA control model to the laser processing system can better control the system. The operator uses the above modules to complete the monitoring, data management and other functions of the laser processing system, and the interface of each module is very clear, which provides a guarantee for the smooth operation of the system. The monitoring software in the system mainly includes: port settings, converter configuration, motor status request, user request response, etc. These software have data collection, processing, analysis and other functions, which can ensure the stable operation of the laser processing system monitoring function. The software processes the program hierarchically, but ignores the overall function of the software, which has the problem of low accuracy of monitoring results. Li and Liu designed an upper computer monitoring software in the hydrological monitoring system [6]. The monitoring software is a software system that can be built on the hardware of the Internet of things, which will be a software innovation on the application layer of the Internet of things. Experiments show that the monitoring software designed on the host computer can not only complete the basic collection and management of hydrological information, but also continue the secondary development, and realize the advanced applications, such as statistical analysis of basic data, data mining and decision support. The functional design of the software is comprehensive, but there is a problem of large memory consumption.

In order to solve the problems of low monitoring accuracy and large memory consumption of traditional monitoring software, a MEMS micro drive debugging visual monitoring software is designed in this paper. The following is the main research content of this paper:

(1) According to the characteristics of MEMS system and the driving principle of micro actuator, the functional

* Corresponding author e-mail: hbxtzhaoyuqing@163.com

module of micro actuator debugging visual monitoring software is designed.

(2) Select the material of the micro drive and set its structural parameters, connect and debug the hardware of the drive.

(3) The monitoring results of the designed software verify that the visual monitoring software designed in this paper has ideal application effect.

2. Micro-Drive Debugging of Electromechanical System

The composition of the MEMS system in this paper is shown in Figure 1.

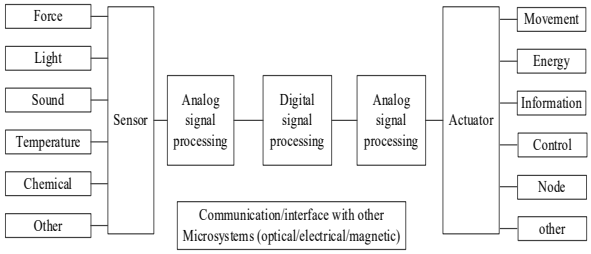

Figure 1. The composition of the MEMS system

In the debugging process of the micro-drive, the axial length of the internal micro beam is larger than the inner wall length of the external frame of the drive [7, 8], which is intended to provide certain axial extrusion pressure to the micro beam [9]; The drive structure also includes sixteen adjusting electrode pairs and a pair of driving electrode pairs. The adjusting electrode pair is realized to control both ends of the micro beam synchronously by adjusting the external adjusting circuit. The axial force on the micro beam is regulated, and the voltage provided by the external regulating circuit is driven laterally by the driving electrode to the micro beam. Thus, the micro-drive produces transverse displacement [10]. In MEMS, the micro-drive is a very important component. Micro actuator has the advantages of small size, high precision and low energy consumption. At present, compared with foreign countries, domestic researches on micro-drives are still in the laboratory stage, with only a small part of micro-drives products. But these products can only be used in some special fields, has not formed a complete industry group. So now, our country urgent problems for micro-drive is to keep up with the pace of the international as soon as possible, shorten the gap, improve research level, and then let the micro-drive to realize industrialization. Micro-drive refers to the micro electrical parts that enable micro devices to realize movement. It is a very important component of MEMS [11]. Electromagnetic drive When the electromagnetic coil and magnetic medium (permanent magnet or soft magnet) interact with each other will produce mutual attraction or mutual repulsion force. Under the action of this force, a certain displacement will be generated, so as to realize the electromagnetic drive of MEMS drive. The drive consists of a movable silicon film, a permanent magnet, and an electromagnetic coil, where the permanent magnet is above the movable silicon film and the electromagnetic coil. When ac voltage is applied to both ends of the coil, an electromagnetic field is generated under the action of ac voltage. The permanent magnet is driven by the electromagnetic coil to do up and down vibration, so the silicon film is also driven to do up and down vibration.

The advantages of electromagnetic drive include simple structure, sensitive action, easy to control, high reliability, low price, etc., but it also has shortcomings, such as high energy consumption, large volume, large noise, high manufacturing difficulty and so on. The S120 drive control system adopted in this paper adopts modular structure design [12]. In terms of hardware structure, it can be divided into two parts: power module and motor module, which are connected by DC bus, and each motor module shares the power source module. The S120 integrates a new communication interface DRIVE-CLiq, through which the S120 can be connected to motors and encoder and other components. Each component has an electronic nameplate, and all components can be automatically identified by the DRIVE-CLiq cable.

The power module converts three-phase ALTERNATING current into direct current, and supplies power to subsequent motor modules through DC bus. There are two types of power supply modules: Active Line Module (ALM) and Smart Line Module (SLM). ALM is equipped with DRIVE-CLiq interface (X200-X202). The DRIVE cable derived from the DRIVE-CLiq interface of the NUMERICAL control system is connected to the X200 interface of ALM, and the X201 interface of ALM is connected to the adjacent motor module. SLM does not have DRIVE-CLiq interface. The DRIVE cable derived from the DRIVE-CLiq interface of the CNC system is connected to the X200 interface of the first motor module. First, connect the motor module X201 to the next adjacent motor module, and so on. It should be noted that the more powerful motor module should be installed adjacent to the power module.

Use one SLM power module and two biaxial motor modules. The communication cable derived from the X1 interface of the CNC system is connected to the X200 (DRIVE-CLiq) interface of the first biaxial motor module. The X201 (DRIVE-CLiq) interface of the first biaxial motor module is connected to the X200 (DRIVE-CLiq) interface of the second biaxial motor module. The X202 and X203 (DRIVE-CLiq) interfaces of the two motor modules are used to connect the encoder on the servo motor.

After the hardware wiring is connected, the CNC system needs to be debuggable first, and then the S120 drive can be debuggable.

The debugging process consists of the following main steps:

(1) Check CNC system before power on

The inspection before electrification includes four aspects: 1) Check whether the power module of the drive and the 24 V DC power supply of the motor module are connected correctly. 2) Check that the power module of the drive and the DC bus of the motor module are connected correctly. 3) Check whether the DRIVE-CLiq cable is connected correctly. 4) Check whether the PROFIBUS cable is connected correctly and whether the terminal resistance is set correctly.

(2) Numerical control system electrification

If no errors are checked before energizing, the system can be energized. Close the system main power switch, 802Dsl host, PP72/48, and drive are powered on. The two green lights on PP72/48 marked "POWER" and "EXCHANGE" indicate that the PP72/48 module is ready and data is exchanged by the bus. The indicator light on the power module and motor module of the drive. The READY light if it is color means that the drive has not set parameters, and if it is red, it is faulty. DC LINK lamp if it is orange means normal, if it is red means incoming power failure. If there is no indicator light, it means there is no DC 24V power supply.

(3) Nc system initialization

After the 802Dsl is powered on, the system initialization should be performed first, and the required initialization files should be passed into the 802Dsl system using Siemens tooling software RCS802 or CF card. After the components of the 802Dsl are properly connected, the PLC control logic should be designed and debugged. The drive and 802Dsl parameters can only be debugged after all the safety functions of the PLC are correct.

(4) S120 drive debugging

Only after the PLC application program is correct, the drive can then be debugged. In order to simplify the debugging of the S120 drive, Siemens 802Dsl has specially designed a graphical drive debugging wizard, which can easily realize the fast debugging of the drive. The process is as follows: 1) Load S120 drive firmware. Ensure that all components of the drive have the same firmware version. 2) Load S120 drive factory settings. Activate the factory parameters of each drive component. 3) Topology identification and confirmation. Read the structure of the drive connection and the control parameters of the actual motor, and set the topological structure comparison level.

Complete the debugging of the micro-drive through the above steps. Based on this, the debugging result monitoring software is designed below.

The debugging process of S120 drive is shown in Figure 2.

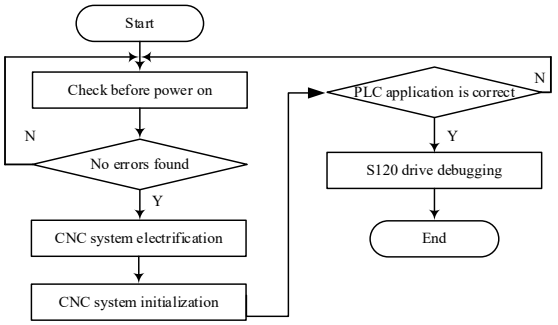

Figure 2. S120 drive debugging flow chart

3. The Design of the Function Module of the Visual Monitoring Software for Micro-Drive Debugging

Introduction to Software Development Environment Code Warrior (CW) is a software integrated development environment developed by Metrowerks. It provides a series of tools for software development, including the Integrated Development Environment (IDE), compiler, connector, Debugger etc. [13]. Processor Expert (PE) is an internal sub-module of CW, which encapsulates embedded internal function modules and peripheral function modules into independent modules. With the support of hardware circuits, you only need to configure the corresponding modules to use its functions without writing the underlying program. PE mainly completes the initialization of modules, and CW completes project integration, editing, compilation and downloading, etc. The cooperation of PE and CW effectively improves the development speed based on Freescale chip systems. CW has cutting-edge debugging technology and a sound development environment, that brings embedded development to a new level of development [14, 15], and also provides developers with a highly visual and automated framework. It greatly improves the speed of project development, and creates applications for users of various development levels that are simple and convenient. The powerful compiling function of CW can check out obvious syntax format errors in the code. After the compiling software is passed, use USB TAP to burn the program, and it can be debugged online. The development environment of CW is shown in Figure 3.

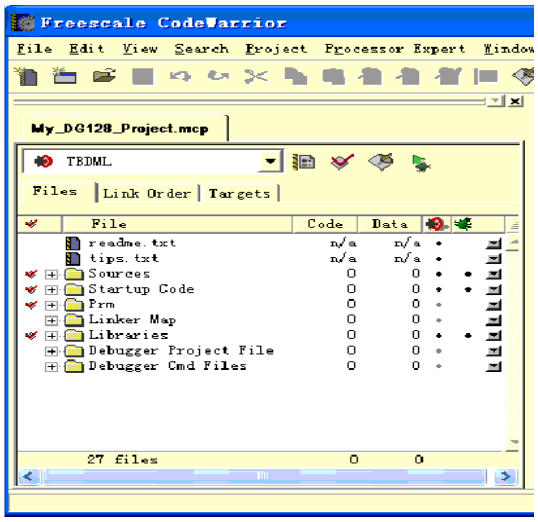

Figure 3 Code Warrior development environment

The main program of the system completes the initialization of the program and the selection of function modules. The initialization program is the operation of the MC56F84789 register after the terminal is powered on. It is an indispensable part of the program. In the terminal, it mainly initializes the ADC module, PWM module, IO status, timer module, etc. To ensure the normal operation of the system program. The terminal is divided into three functional modules: signal source, signal monitoring and digital signal. The signal source includes PWM, CLK, monitor quadrature signal, analog voltage signal and single-ended voltage signal; Signal monitoring includes CLK signal monitoring and encoder signal monitoring; digital commands are issued under RS232 and CAN communication respectively. After power-on, the system first initializes and enters the main menu interface. After the effective button is monitored, enter the corresponding secondary menu according to the button value. When the effective button is pressed again, the program jumps to the function module to work. The person presses the return

key, the program returns to the previous menu, and waits for the next key command [16, 17].

3.1. Monitoring pause button module program

In the process of debugging and monitoring the micro-drive, if an abnormal situation occurs, it must be paused in time to check the specific fault. This section designs the program of the monitoring pause button module. The button is used to realize the human-computer interaction function of the debugging terminal, and the corresponding function is entered through the button selection and parameter setting. The stability of the button program is the basic guarantee for the stable operation of the terminal. In the key hardware circuit, the debugging terminal uses the CH455 chip, which is connected to the I2C (Inter-Integrated Circuit) interface of MC56F84789, with an external interrupt IO port. In the process of software writing, configure the Internal I2C module and EINT module in the PE, and write the program in conjunction with the CH455 chip data manual. First, MC56F84789 sends a work start instruction to CH455 chip according to the instruction code of the data manual. CH455 chip starts to work according to the received digital instruction, and continuously scans the keyboard. The internal part of CH455 chip is divided into row scan and column scan to prevent misjudgment of keystrokes. In this case, CH455 chip uses double discrimination to be valid. When the two keyboard scan results are the same, the key is confirmed to be valid. Each key corresponds to a unique key code. The key code is determined by judging the position of the key pressed. When a key is pressed, MC56F84789 detects the interrupt signal and generates an effective low-level keyboard interrupt, and then reads the key code through the serial port. The key program flowchart is shown in Figure 4.

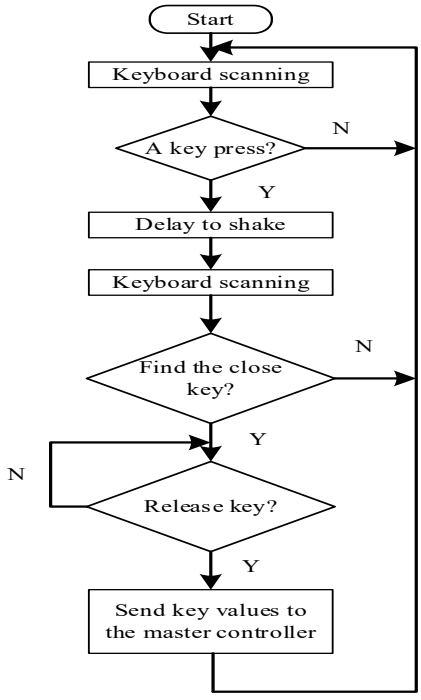

Figure 4. Keystroke program flowchart

3.2. Visual display module program

The LCD visual display screen visually displays the running status of the system in real time, and cooperates with the button function to realize the human-computer interaction function. The visual display module uses Jinpeng OCMJ44X8C-15 LCD visual display, and uses only 4 wires with MC56F84789 to realize data serial transmission, and combines the OCMJ44X8C-15 data manual for programming. The LCD screen of OCMJ44X8C-15 is a 128 × 64 dot matrix with an integrated font library chip, which can visually display 8192 Chinese characters and 126 symbol fonts, and users can also visually display drawings. OCMJ44X8C-15 provides basic and extended instruction set to meet the needs of developers, such as clear visual display, function setting, setting DDRAM address and other practical functions. Write and send a data function module according to the serial timing diagram of the data manual. First, set the PSB signal low to set the transmission mode to serial mode, set the chip select CS high, start transmitting the start byte, and receive 5 consecutive "1". As the starting byte, the transmission count is reset and the serial is synchronized to the serial transmission. The three bits received later are used as the transmission direction bit (RW), and the register selection is (RS) and "0". After receiving the start byte, each eight-bit instruction is divided into two parts. The upper four bits (DB7~DB4) are received in the LSB part of the first byte, and the lower four bits (DB3~DB0) are in the LSB part of the first byte. The LSB part of the second byte is received. The remaining bits of the first and second bytes are 0. In the LCD visual display function module, first write the sending data module according to the set time sequence, initialize the LCD screen with data manual instructions, set the visual display row and column position, and finally use the pointer to transfer the characters that need to be visualized to LCD module.

3.3. Monitor quadrature signal module program

The monitor quadrature signal is two rectangular waves with the same frequency, duty cycle, and amplitude, and a phase difference of 90°. Among the many signal sources of the micro-drive, the monitor quadrature signal is one of them. The micro-drive debugging terminal uses MC56F84789 internal integration.

The PWM module realizes the function of monitoring the quadrature signal. On the hardware circuit, only one output signal circuit is configured on the PWMA and PWMB ports, which can be realized by software programming. The PWM module is divided into center-aligned mode trigger and edge-aligned mode trigger. Using the different trigger mode characteristics of the PWM module, when channel A is 90° ahead of channel B, set PWMA module to edge-aligned mode trigger and PWMB module to configure center-aligned Mode trigger; vice versa. Figure 5 is the timing diagram of channel A ahead of channel B by 90°.

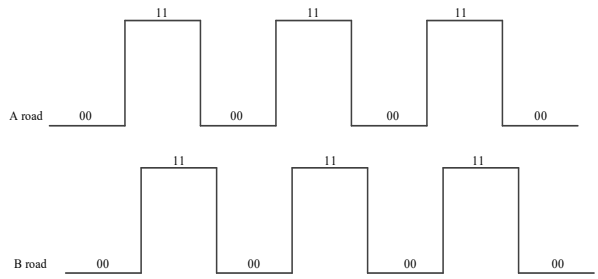

Figure 5. Timing diagram of channel A ahead of channel B by 90°

After the Code Warrior IDE compiler has configured the PWMMC module, the PE function automatically generates the underlying program. When the PWMMC module is configured in the center-edge alignment mode and the edge-aligned mode, the value written to the register will change, because the micro-drive debugging terminal In monitoring the quadrature signal source, it is required that the A and B signals can choose any one to lead the other. Therefore, both PWMA and PWMB can execute center-aligned mode programs and edge-aligned mode programs, but only one mode can be selected in the configuration. In the process of programming, it is found that the center-aligned mode program and the edge-aligned mode program are considered to be written in PWMMC In the bottom layer, and the PWMMC module is frozen to ensure that the bottom layer program does not change when the PWMMC module is changed next time. This method can solve the single use of center-aligned mode and edge-aligned mode. The program flow chart of monitoring quadrature signals is shown in Figure 6.

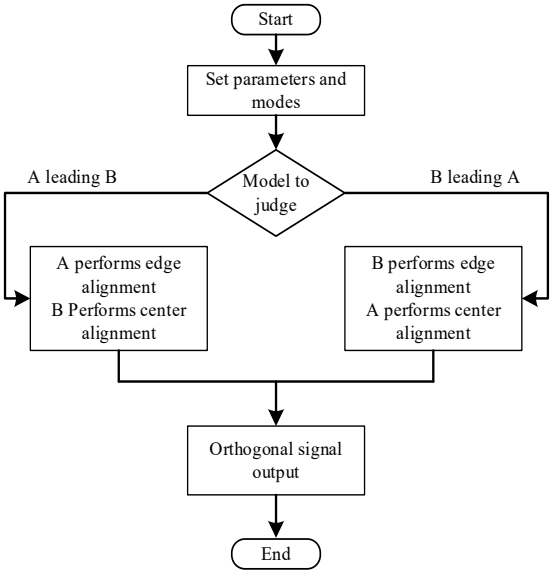

Figure 6. Program flow chart of monitoring orthogonal signal

3.4. Monitoring signal communication module program

RS232 communication and CAN communication are two widely used communication methods at present. The monitoring signal communication module program of the micro-drive debugging terminal uses a reasonable structure. When the function module program is written, RS232 communication and CAN communication are written together, through the flag bit Determine the communication method currently in use. The internal Asynchro Serial module and Freescale CAN module of MC56F84789 provide great convenience for the programming of monitoring signal communication module. Through the configuration of RS232 and CAN function module, PE generates such function functions as Send Char (), Recv Char (), Send Block (), Recv Blck (), etc., which are convenient for users to call. In this program preparation, three important parameters, namely flag bit, function code and value, are required to send a setting instruction. The communication mode at this time is determined by the flag bit, and then the function code and value are written into the corresponding buffer.

4. Software Performance Test

(1) Operational validity test of the designed monitoring software

In order to test the effectiveness of the visual monitoring software for micro-drive debugging, this experiment introduces a duty cycle indicator. The duty cycle of the signal is the ratio of the time occupied by the pulse to the total time during a period of continuous working time. The higher the duty cycle, the higher the effectiveness of the software. The monitoring signal is tested by connecting to an oscilloscope. The main test content is monitoring frequency and duty cycle. According to the comparison between the measurement and the setting value, it can be concluded whether the monitoring signal performance meets the standard. This project is designed to monitor if the frequency error range of 0.1% within 200K is qualified. Since the initial frequency is set to 500 Hz, the prescaler coefficient is automatically set to divide by 4, so operate the divider function to change the prescaler coefficient in different frequency ranges. Figure 7 shows the real-time waveform of the 500Hz oscilloscope measured by the oscilloscope.

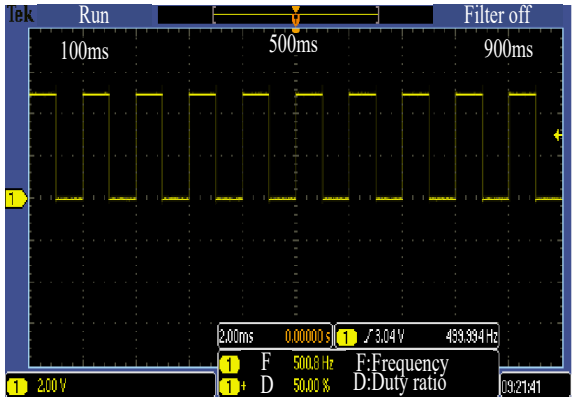

Figure 7. Monitoring signal waveform

The test of the monitoring waveform mainly focuses on the change of the duty cycle at different frequencies. Therefore, the design of the test data during the test is shown in Table 1. Each set frequency corresponds to three sets of duty cycle values, which can be clearly seen as high the error of the duty cycle increases under the frequency condition, which is consistent with the setting.

Table 1 Monitoring signal waveform data

Set monitoring frequency (Hz)	Read monitoring frequency (Hz)	Set monitoring duty cycle (%)	Read monitoring duty cycle (%)
12	12	20.00, 50.00, 70.00	20.00, 50.00, 70.00
500	500	20.00, 50.00, 70.00	19.99, 49.99, 69.00
1000	1000	20.00, 50.00, 70.00	19.98, 49.98, 69.97
5000	4999	20.00, 50.00, 70.00	19.97, 49.88, 69.99
10000	9996	20.00, 50.00, 70.00	19.98, 49.98, 69.97
20000	19980	20.00, 50.00, 70.00	19.33, 49.34, 69.75
30000	29970	20.00, 50.00, 70.00	19.05, 49.58, 69.99
40000	399300	20.00, 50.00, 70.00	19.90, 49.08, 69.17
50000	499000	20.00, 50.00, 70.00	18.76, 49.75, 69.73

(2) Comparison of accuracy of different monitoring software

The monitoring software is difficult to ensure that no errors will occur during the running process. In order to verify the effectiveness of the designed electromechanical system micro-drive debugging and visual monitoring software, the designed software is compared with the design in Reference [5] and Reference [6]. The monitoring accuracy rate of the micro-drive debugging monitoring software is compared, and the comparison result is shown in Figure 8.

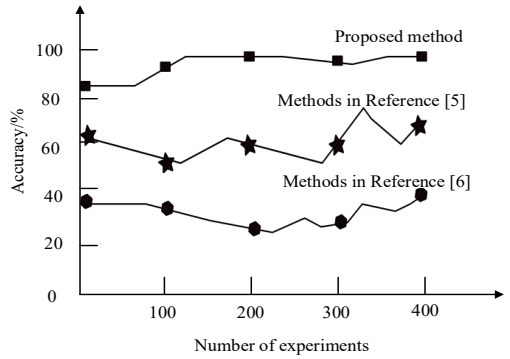

Figure 8 Comparison of monitoring accuracy of different methods

It can be seen from Figure 8 that the monitoring accuracy of different monitoring software is different. When the number of experiments is 100 times, the accuracy of the designed monitoring software is 88.29%, and the monitoring accuracy of the system designed in [5] is 65.27%. The monitoring accuracy rate of the system designed in [6] is 60.12%. Through data comparison, it can be seen that the monitoring accuracy of the designed monitoring software is much higher than other methods, and the average accuracy of the designed monitoring software is above 90%. It can be seen that the designed monitoring software has certain superior performance. Therefore, according to the characteristics of MEMS system and the driving principle of micro actuator, this paper designs the functional module of visual monitoring software for micro actuator debugging. It includes monitoring pause button module program, visual display module program, monitoring quadrature signal module program and monitoring signal communication module program. Through the connection between each module, the monitoring accuracy is improved.

(3) Comparison of memory loss between different monitoring software

Memory consumption (KB) was compared with the monitoring software designed in References [5] and [6], and the analysis results were shown in Table 2.

Table 2 Compares the memory consumption of different monitoring software

Software	Memory cost/kb
Software in this paper	156
Software in Reference [5]	3608
Software in Reference [6]	895

It can be seen from Table 2 that the memory consumption in the monitoring process using the designed system is relatively low. The memory consumption generated by software in Reference [5] is the highest, followed by that in Reference [6]. The experimental results show that the difference between the memory cost of Reference [5] and the memory cost of the designed software is 3456 kb. The difference between the memory cost of Reference [6] and that of the designed software is 739 kb. The lower memory loss effectively increases the applicability of the visual monitoring software for micro-drive debugging, and the application scope is wider. The data obtained from the experiment show that the applicability of the designed software is better than the other three traditional electromechanical system micro-drive debugging visual monitoring software.

(4) Test the packet loss rate of different monitoring software with or without queuing

Packet loss rate refers to the ratio of the number of monitoring packets lost in the monitoring test to the sent data group. In this experiment, it is divided into queued and non-queued cases. In the case of queuing for debugging of multiple micro-drives, queueing is required. In this case, visual monitoring requires better monitoring ordering. If there is no queuing, there is only one micro-drive debugging. The method in Reference [5] and the method in Reference [6] were compared with the proposed method, and the test results were shown in Figure 9.

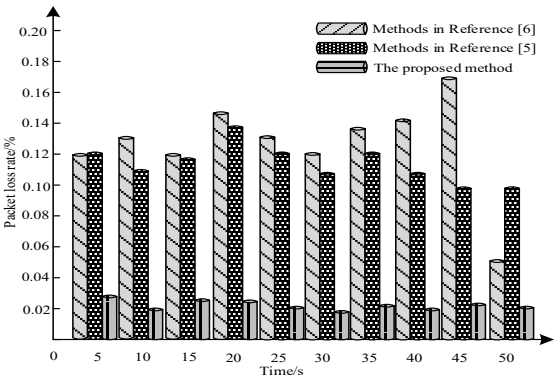

Figure 9 Comparison of packet loss rate of different software without queuing

In the case of queueing, three methods are adopted to visually monitor the packet loss rate of micro-drive

debugging. The comparison results are shown in Figure 10.

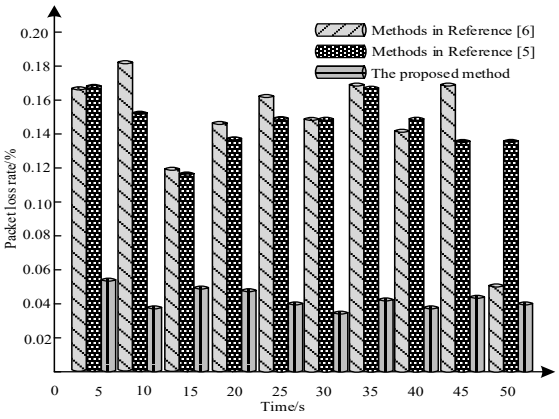

Figure 10. Comparison of packet loss rate of different software under queued conditions

Packet loss rate can effectively evaluate the micro actuators debugging visual monitor performance. It can be seen through Figure 9 and Figure 10 that the experimental results shown using this software to monitor the micro actuators debugging packet loss rate were significantly lower than the method of Reference [5] and the method of Reference [6], the experiment of using this software in the 50 s in the packet loss rate lower than 0.02%, and in the absence of any queue in case, having queued packet loss rate is kept below 0.16%. The packet loss rate meets the current technical requirements in this field, and ensures the data integrity of the visual monitoring process of micro-drive debugging, and verifies the monitoring reliability of the software designed in this paper. The reliability in this paper is the design software of the monitoring.

5. Conclusion

1. Electromechanical system drives are mainly debuted by computers as upper computers, and multiple signal sources need to be connected. Due to the uncertain on-site environment, it is difficult to visually monitor their operation status. Therefore, this paper designs a new visual monitoring software for micro-drive debugging.
2. The Design of the functional modules of the visual monitoring software for the micro-drive debugging, includes the monitoring pause button module program, the visual display module program, the monitoring orthogonal signal module program, and the monitoring signal communication module program.
3. Design software testing scheme. Select the material of the micro-drive and set its structural parameters. The designed software is used to monitor the debugging results visually.
4. Test results show that the designed software has higher accuracy, lower memory loss, ideal monitoring effect, and can be widely used.

Acknowledgement

The research is supported by Application innovation project of Xingtai Vocational and Technical College, Project name: Development of Automatic Multi-Functional Nursing Bed (No. 20180204).

References

[1] Hao L, Namuduri C S, Gopalakrishnan S, et al. PM-assisted synchronous reluctance machine drive system for micro-hybrid application. IEEE Transactions on Industry Applications, 2019, 55(5): 4790-4799.

[2] Mariano M, Bernardes J D S, Strauss M. Mold heat conductance as drive force for tuning freeze-casted nanocellulose foams microarchitecture. Materials Letters, 2018, 225: 167-170.

[3] Bahadori M, Gazman A, Janosik N, et al. Thermal rectification of integrated microheaters for microring resonators in silicon photonics platform. Journal of Lightwave Technology, 2018, 36(3): 773-788.

[4] Ashhab M, Talat N. Modeling of the MEMS reactive ion etching process using neural networks. Jordan Journal of Mechanical and Industrial Engineering, 2011, 5(4): 353-357.

[5] Yu Z, Tan A Z. Design of monitoring software for laser processing system based on DEA control model. Laser Journal, 2019, 40(4): 172-175.

[6] Li Q, Liu X F. The design of monitoring software for upper computer in hydrological monitoring system. Journal of Hunan University of Science & Technology (Natural Science Edition), 2020, 35(1): 98-103.

[7] Chen H, Zhao Q, Wang Y, et al. Near-infrared light-driven controllable motions of gold-hollow-microcone array. ACS Applied Materials & Interfaces, 2019, 11(17): 15927-15935.

[8] Qiu D, Chu Y, Zeng H, et al. Stretchable MoS_2 electromechanical sensors with ultrahigh sensitivity and large detection range for skin-on monitoring. ACS Applied Materials & Interfaces, 2019, 11(40): 37035-37042.

[9] Zhang X, Wang Y, Zhang J, et al. RINGLM: A link-level packet loss monitoring solution for software-defined networks. IEEE Journal on Selected Areas in Communications, 2019, 37(8): 1703-1720.

[10] Shahriar M R, Borghesani P, Tan A C C. Electrical signature analysis-based detection of external bearing faults in electromechanical drivetrains. IEEE Transactions on Industrial Electronics, 2017, 65(7): 5941-5950.

[11] Dubey A, Tzeferacos P, Lamb D Q. The dividends of investing in computational software design: A case study. Experimental Mechanics, 2019, 33(2): 322-331.

[12] Sievi-Korte O, Beecham S, Richardson I. Challenges and recommended practices for software architecting in global software development. Information and Software Technology, 2019, 106(52): 234-253.

[13] Zhu B, Yan S D, Zhao J, et al. Personalized lane-change assistance system with drive behavior identification. IEEE Transactions on Vehicular Technology, 2018, 67(11): 10293-10306.

[14] Ahumada C, Wheeler P. Modelling of reduced electromechanical interaction system for aircraft applications. IET Electric Power Applications, 2019, 13(7): 256-262.

[15] Wei B L, Jiao H T. Fault status information monitoring technology for large complex electromechanical system. Jordan Journal of Mechanical and Industrial Engineering, 2021, 15(1): 105-112.

[16] Kervinen M, Ramírez-Muñoz J E, Välimaa, A, et al. Landau-Zener-Stückelberg interference in a multimode electromechanical system in the quantum regime. Physical Review Letters, 2019, 123(24): 240401.

[17] Xu H, Yuan Q N, Xie Y K. Simulation of fault modeling and diagnosis of electromechanical system of palletizing. Computer Simulation, 2018, 35(12): 291-295.

JJMIE

Volume 16, Number 1, January. 2022
ISSN 1995-6665
Pages 141 - 152

Jordan Journal of Mechanical and Industrial Engineering

Design of Quantitative Risk Assessment System for Ship Longitudinal Motion Based on Analytic Hierarchy Process

Lixiao Jia, Jiantao Wang*, Lejun Rui, Jing Chu

School of Nautical Technology, Jiangsu Shipping College, Nantong 226010, China

Received 14 July 2021 *Accepted 29 December 2021*

Abstract

In order to ensure the normal operation of ship navigation and reduce the risk of ship longitudinal movement, a quantitative assessment system of ship longitudinal movement risk based on Analytic Hierarchy Process (AHP) is designed. Through the Beidou positioning module, external antenna, single-chip control module and power supply module, the hardware part of the ship's longitudinal movement risk quantitative assessment system is designed. Through the determination of the ship's longitudinal movement risk evaluation index, the analytic hierarchy process is used to determine the speed, heading, sea condition and frequency. The relative importance of each risk index is evaluated, and the weight of the evaluation index is calculated. On this basis, the ship was built. The quantitative model of ship longitudinal movement risk assessment uses genetic algorithm to calculate the optimal solution of the parameters, establishes the risk assessment interval, and determines the degree of risk. Using embedded Linux technology, the AHP-based quantitative assessment system design for ship longitudinal movement risk is realized on the C/S client. The experimental results show that the quantitative assessment system of ship longitudinal movement risk based on the analytic hierarchy process has high accuracy, and can improve the confidence of the evaluation, shorten the evaluation time, and stabilize the frequency and speed of the ship's longitudinal movement.

Keywords: Analytic Hierarchy Process (AHP); Ship Longitudinal Motion; Risk Quantification; Evaluation System.

1. Introduction

Sea transportation has always been the most important mode of transportation in world trade. The development of shipping industry has a direct impact on the stability of the global economy. With the rapid development of shipping industry and navigation science and technology, ships are developing towards large-scale, high-speed and specialization, and the navigation density of ships is also increasing. With the continuous improvement of transportation efficiency, the shipping industry also puts forward higher requirements for maritime navigation safety. When a ship navigates at sea, it will produce rolling motion with six degrees of freedom: pitch, roll, heave, pitch, roll and yaw [1]. The disturbance of external environment includes wind force, wave force and current force, and its mechanism is very complex. Due to the risk of longitudinal motion of the ship during navigation, the wind will produce additional power similar to the random walk process, and the waves will lead to additional high-frequency oscillation of the bow to other degrees of freedom, resulting in the motion deviation of the hull, reducing the stability of the ship and leading to the navigation of the ship. In order to improve the safety management level of ship transportation, it is necessary to quantitatively evaluate the ship navigation risk, so as to predict the longitudinal movement risk in the process of ship navigation in advance and take necessary safety measures.

On the basis of comprehensively considering the needs of domestic inland river traffic safety management departments and relevant laws and regulations, Zhang et al. constructed an inland river ship navigation safety state evaluation system based on Fuzzy evidential reasoning [2]. The risk levels of qualitative indicators are divided into high, medium and low. According to the target information, the fuzzy evaluation level distribution map of quantitative indicators is constructed by using fuzzy theory, and the fuzzy reliability distribution of evaluation indicators at the index level is calculated. However, the confidence of longitudinal motion risk assessment is low, resulting in poor evaluation effect. Ma et al. proposed and designed a ship navigation environment risk assessment system based on Improved TOPSIS method [3]. A certain channel section is selected as an evaluation example to evaluate its navigation environment risk. Compared with the evaluation results of entropy weight matter-element model, the effectiveness and practicability of the system are verified. However, the evaluation of the system takes a long time, resulting in low efficiency. Jiang et al. analyzed the influencing factors of ship navigation efficiency under traffic conflict, and defined the delay time of waterway traffic conflict, and put forward the concept of conflict threshold [4]. By collecting the channel data of a "t" intersection, a channel traffic safety evaluation system is established, and the quantitative evaluation results are obtained. However, the evaluation accuracy of the system still needs to be further improved. Li et al. extracted relevant data from the information of automatic

* Corresponding author e-mail: wjttk163@163.com.

identification system (AIS) and the evaluation index system of multi-objective and multi-layer fuzzy optimization theory [5], calculates from low level to high level through the optimal relative membership vector ranking, and selects the sea area with high navigation risk. However, due to the need to process more data, the final risk assessment efficiency is low. Bye and Aalberg introduced the statistical analysis results of maritime accident data and AIS data, to identify navigation related accidents (grounding and collision) and can be used as risk indicators [6]. The ships involved in the accident reported in the accident database have been tracked in the historical AIS records, and the data related to each ship have been converted into variables to obtain the risk assessment results. However, due to the long research data of the system, the accuracy of the assessment results is insufficient.

In order to solve the problems of the above-mentioned system and to better ensure the safe navigation of ships in the waters, this paper designs a quantitative risk assessment system for ship longitudinal movement based on the analytic hierarchy process. The use of this system improves the efficiency of quantitative assessment of ship longitudinal movement risks, and provides a basis for ship navigation safety.

2. Hardware Design of Quantitative Risk Assessment System for Ship Longitudinal Motion

The hardware structure of the system consists of Beidou positioning module, external antenna, MCU control module and power module, as shown in Figure 1.

2.1. Beidou Positioning Module

Through the external passive antenna, Beidou module can receive the satellite signal in real time. After processing and saving, it can generate navigation and positioning data, and then output the navigation and positioning data through the standard serial port according to the relevant protocol. At the same time, the MCU (Microcontroller Unit) reads the Beidou navigation and positioning information through the standard serial port, analyzes, processes and assembles the information, and then forwards the packaging information through the Beidou satellite system.

The system selects TM8620 Beidou positioning module, which has built-in RNSs (Radio Navigation Satellite System) & GPS (Global Positioning System) module, which can receive navigation signals from RDSS and RNSs/GPS satellites, ensuring the reliability and accuracy of information receiving. The RDSS here is equivalent to the Beidou first generation positioning system, which belongs to active positioning. If you want to locate, you need to apply first, and it mainly transmits the alarm message information through the Beidou satellite system; While the RNSs it mainly refers to the satellite system including the Beidou II positioning system, which is a passive and all-weather positioning system, that is, it can obtain the ship position information without application, and can receive the ship position information according to the service frequency. TM8620 Beidou positioning module is a module with transmission power of 10 W and output of TTL (Time to Live) level. It has the following main characteristics:

1. It has high integration, low power consumption, positioning and short message communication functions. It is very suitable for real-time and high-precision positioning and speed measurement of mobile carriers.
2. Small size, 54*60*8 mm, very suitable for the volume design requirements of small alarm terminal.
3. The positioning accuracy is less than 15 meters, and the speed accuracy is less than 1.0 m/s.
4. The mean time between failures (MTBF) is more than 5000 hours and the reliability is high.
5. The RDSS part of the interface protocol adapts to the active I/O 4.0 protocol and the RNSs part conforms to the input and output statement format of the Taidou navigation and positioning module.
6. The serial port can be directly connected with 3 V to 5 V logic level with RS-232 polarity standard without level conversion circuit.
7. It has strong environmental adaptability and anti multipath interference.
8. PA is built into the module, which modulates and amplifies the l-frequency signal, and then transmits it to the external passive antenna.
9. RNSs & GPS module is built in the module, and LNA (Low Noise Amplifier) is built into the RNSs part of the module, which can realize the filtering of RNSs frequency points and low noise amplification. Users can directly connect to the passive antenna of RNSs without external LNA. The principle block diagram is shown in Figure 2.

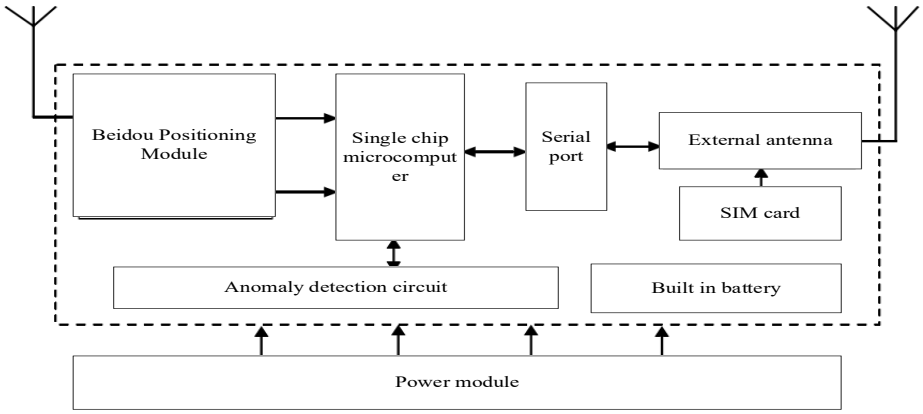

Figure 1. System hardware structure

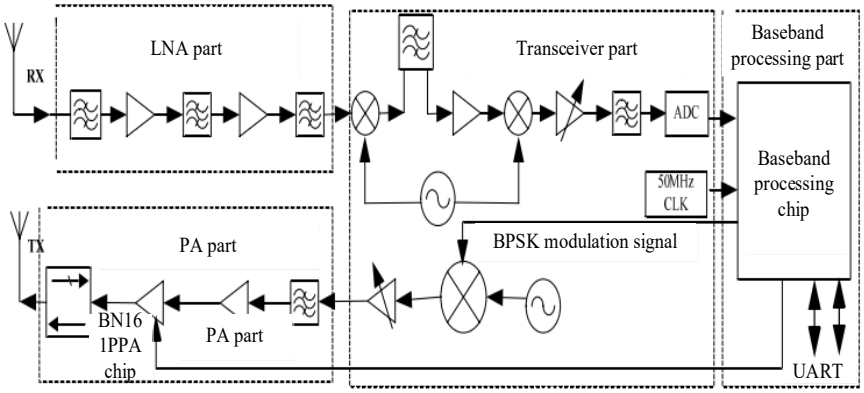

Figure 2. Principle block diagram of tm8620 Beidou Positioning Module

According to the principle of TM8620 Beidou positioning module, some important performance parameters of TM8620 are set, as shown in Table 1.

Table 1. Performance parameters of TM8620

RDSS parameters	Input VSWR	≤ 2.0
	Received signal sensitivity	-127.6 dBm
	Signal transmitting power	≥ 39 dBm
	Carrier suppression	≥ 30 dBc
	Modulation phase error	≤ 3°
	Positioning/communication	Positioning accuracy (continuous 24 hours): ≤ 100 m
RNSS parameters	Input frequency point	RNSS B1 + GPSL1
	Data update rate	≥ 1 Hz
	Horizontal position accuracy	≤ 5 m
	Vertical position accuracy	≤ 10 m
	Speed accuracy	≤ 1.0 m/s
	Capture sensitivity	-144 dBm

2.2. External antenna

Based on the satellite model received by Beidou module, and in order to improve the signal reception strength, the external antenna is designed.

When selecting external antenna, in order to match with TM8620 Beidou positioning module, at the same time, considering the signal-to-noise ratio and gain of antenna, TA-011 & GPS passive antenna is selected for receiving antenna in this paper. Its appearance and structure are shown in Figure 3.

During the circuit connection, the orientation of the antenna position may affect the sensitivity of the signal to a certain extent. According to the relevant test data, the antenna should be placed outdoors without obvious shielding to ensure that there is no obvious interference in the environment, and the receiving and transmitting direction is to the south, so the signal effect will be better. When connecting the antenna, it is necessary to ensure that the module interface is connected correctly and the antenna has been correctly connected before power on can be carried out. Special attention should be paid not to plug in and out the antenna with hot line, otherwise the module may be burnt out.

Figure 3. Ta-011 & GPS passive antenna

2.3. Single chip microcomputer control module

The single chip microcomputer control module is the core component of the hardware of the risk quantitative assessment system for ship longitudinal motion, which is equivalent to the “heart” of the system terminal. It mainly realizes the reading, parsing, comprehensive processing, packaging, evaluation and other control functions of Beidou positioning information, and finally controls the transmission of Beidou message data information. It also realizes the control and operation of abnormal power failure detection circuit, power battery switching circuit, built-in battery charging and discharging circuit and two serial interface data receiving and sending [7-10].

In this paper, STC12C5A60S2 single chip microcomputer is selected as the control chip of the system terminal. STC12C5A60S2 is a new generation of 8051 single-chip microcomputer, which is compatible with all functions of 8051 single-chip microcomputer, and has relatively unique functional characteristics. The MCU contains four 16 bit timers/counters, two universal full duplex asynchronous serial ports, and its RAM data memory is 1280 bytes. Its machine cycle is 1t, that is,

single clock, and the instruction code is fully compatible with the traditional 8051. Therefore, 803x/805x assembler and compiler can still be used in software development. The MCU integrates 2-channel PWM (Pulse Width Modulation), 8-Channel high-speed 10 bit A/D conversion (250 K/s), and has on-chip debug circuit and max810 special reset circuit. STC12C5A60S2 MCU circuit connection schematic diagram is shown in Figure 4.

2.4. Power module

Generally, the voltage of shipboard power supply system is 220 V, while the input voltage of tm8620 module used for receiving and transmitting is 5 V, the typical voltage for module transmitting is 12 V, and the power input of MCU and other components is 5 V. Therefore, it is necessary to transform the 220 V AC supplied by the ship longitudinal motion risk quantitative assessment system through transformer, and then use lm2576 integrated chip to stabilize the power supply. Power supply voltage stabilization is an important part of single-chip microcomputer system. If the power supply is unstable, it may affect the technical indicators of the system and produce signal interference. In order to ensure the stability of multi-channel power supply voltage, this paper selects LM2576 series voltage stabilizing chip to form DC/DC conversion control circuit. The 12 V or 24 V voltage output by transformer is reduced and stabilized through the circuit, and 5 V is output for the protection circuit [11-14].

LM2576 series voltage regulator chip is a single chip integrated circuit, which can drive 3 A load, realize many functions of voltage drop switch regulator, and its efficiency is higher than that of three line regulator, and its heat dissipation function is very good. With the increase of using time, the temperature of the chip will not be very high, which will not affect the normal operation of the system. The principle of power supply in this design is shown in Figure 5.

In order to make the assessment system work normally when the ship power supply is abnormal, the backup battery is built in during the design of this paper. The ship's power module supplies power to the terminal of the evaluation system and also charges the built-in battery. In case of power failure, the ship is powered by lithium battery, which can realize 96 hours continuous operation [15-17].

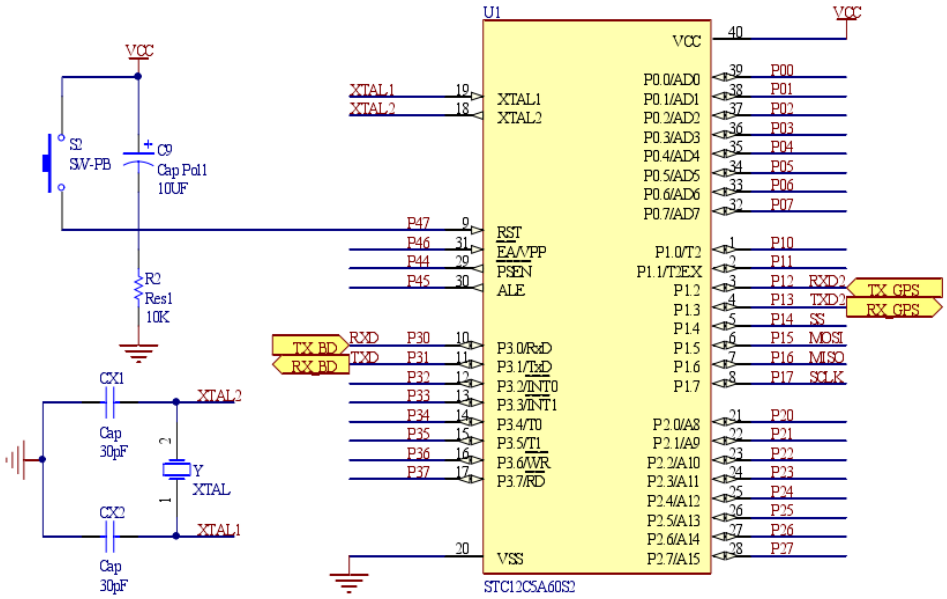

Figure 4. Circuit connection principle of STC12C5A60S2 single chip microcomputer

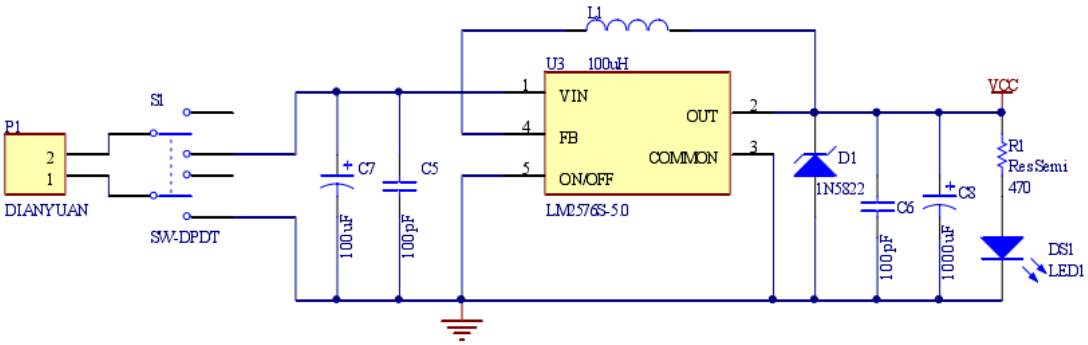

Figure 5. Power circuit principle

3. Software Design of Ship Longitudinal Motion Risk Quantitative Assessment System Based on AHP

3.1. Determine the risk assessment index of ship longitudinal motion

According to the ship hydrodynamic theory, the longitudinal motion equation of a ship sailing in waves can be expressed as follows:

$$\begin{cases}(a_{33}+D)z+b_{33}z+c_{33}z+a_{35}\theta+b_{35}\theta+c_{35}\theta=I_R+F_{w3}\\ a_{53}z+b_{53}z+c_{53}z+(I+a_{55})\theta+b_{55}\theta+c_{55}\theta=I_R X_R+F_{w5}\end{cases} \quad (1)$$

where z is the heave of the hull; D is the mass of the hull; θ is the pitch of the hull, F_{w3}, F_{w5} is the interference force of the wave heave and the interference moment of the sea pitch respectively. The wave force of a ship moving on the water surface is mainly composed of two parts, one is the linear inertial force generated by wave acceleration, the other is the nonlinear damping force generated by wave velocity. The disturbing moment is the tendency of the wave force to make the hull move up and down in the longitudinal motion of the ship; I_R is the horizontal rudder lift; X_R is the longitudinal distance from the rudder lift center to the center of gravity of the hull; $a_{ij}, b_{ij}, c_{ij}(i, j=3,5)$ is the hydrodynamic coefficient; I is the longitudinal moment of inertia.

By simulating the hydrodynamic coefficients of typical sea conditions, the hydrodynamic model which changes continuously with the course when the sea conditions and speed are constant can be expressed as follows:

$$w_{ij}(u,U,q)=au^2+bu+c \quad (2)$$

where u is the course, taking 30, 60, 90, 120, 150 and 180 degrees; U is the speed, taking 6 kN, 12 kN, 18 kN or 24 kN; q is the sea condition.

(1) When the speed U ≥ 8 kN:

$$w_{ij}(u,U,q)=(U-U_1)/(U_0-U_1)w_{ij}(u,18,q)+(U-U_0)/(U_0-U_1)w_{ij}(u,24,q) \quad (3)$$

where, $U_0=18, U_1=24$.

(2) When the speed U ≤ 18 kN:

$$w_{ij}(u,U,q)=w_{ij}(u,12,q)+\left[(U-U_2)(U-U_3)\right]/\left[(U_4-U_2)(U_4-U_3)\right]w_{ij}(u,18,q) \quad (4)$$

where, $U_2=6, U_3=12, U_4=18, q=3,4,5$.

According to Formula (3) and Formula (4), the hydrodynamic coefficient is related to the speed, course, sea condition and frequency. Therefore, the four indexes of speed, course, sea state and frequency can affect the risk of ship longitudinal motion.

3.2. Calculate evaluation index weight

On the basis of determining the risk assessment index of ship longitudinal motion, the weight of risk assessment index of ship longitudinal motion is calculated. When calculating the index evaluation weight, a judgment matrix is constructed. Before constructing the matrix, AHP is used to evaluate the relative importance of four risk indicators, namely speed, course, sea condition and frequency. The scale of the assessment set is 1 to 9. A judgment matrix is constructed according to the meaning of the evaluation set. The scale evaluation set used is shown in Table 2.

Table 2. Scale evaluation set

Serial number	Scale	Meaning
1	1	Indicates that two factors are equally important
2	3	Indicates that one factor is slightly more important than the other
3	5	One factor is more important than the other
4	7	It means that compared with two factors, one factor is obviously more important than the other
5	9	It means that compared with two factors, one factor is absolutely more important than the other
6	2, 4, 6, 8	The median value of the above two adjacent judgments
7	1, 1/2, ..., 1/9	The ratio of comparative judgment

By analyzing the assessment set in Table 2, it is assumed that the risk factor of longitudinal motion of ships of the same type is a risk layer, and n factor $C_1, C_2, ..., C_n$ in a certain layer is compared. The influence on a certain factor in another risk layer is assumed to be O. Two factors C_i and C_j are taken each time. a_{ij} is used to represent the ratio of the influence of C_i and C_j on O. The comparison matrix A formed is as follows:

$$A=\begin{bmatrix}a_{11} & \cdots & a_{1n}\\ \vdots & \ddots & \vdots\\ a_{n1} & \cdots & a_{nn}\end{bmatrix} \quad (5)$$

where $A=(a_{ij})_{n\times n}, a_{ij}>0, a_{ji}=1/a_{ij}$, $i, j=1,2,...,n$. In this case, Formula (5) is a positive reciprocal matrix. By using the positive reciprocal matrix, the largest eigenvalue of matrix A is marked as λ, and the eigenvector of eigenvalue is taken as the weight vector ω, then the weight coefficient is obtained:

$$A\omega=\lambda\omega \quad (6)$$

It can be seen from this formula that the eigenvalue and eigenvector of matrix a continuously depend on the factor a_{ij} of the matrix. Therefore, when a_{ij} meets the index consistency, the weight value of each index can be calculated, and the index weight value can be obtained by combining Formula (5) and Formula (6).

According to the weight coefficient obtained, AHP is used to evaluate the relative importance of four risk indicators, namely, speed U, course u, sea condition q and frequency p:

$$Q=s/A\omega(U,u,q,p) \quad (7)$$

In Formula (7), s represents the influence degree of influencing factors.

3.3. Construction of quantitative model for risk assessment

Based on the weight of the evaluation index, the quantitative model of ship longitudinal motion risk assessment is built to support the risk assessment system.

The basic model of ship longitudinal motion risk assessment is established:

$$R = F\left(V, T, C\right) \tag{8}$$

where R is the longitudinal motion risk of the ship; C is the existing risk control measures; V is the navigation efficiency of the ship; T is the risk control cycle.

In terms of the risk defined by ISO/IEC, it can be expressed by the vulnerability of the threat, the severity of the possibility, etc., then Formula (7) can be expressed as follows:

$$R = F\left(Pt, Pv, V\right) \tag{9}$$

where Pt is the probability of the threat and Pv is the severity of the vulnerability.

The value range of threat probability Pt is set as $\left[0,1\right]$ to reflect the possibility of risk events. The closer the probability of threat occurrence to 1, the greater the probability of ship longitudinal motion risk events; On the contrary, the probability of ship longitudinal motion risk events is smaller.

Vulnerability severity Pv is objective, but only when the threat is used, it will bring risks to the ship navigation. The greater the vulnerability, the greater the risk of longitudinal motion.

The effectiveness of risk control measures also determines the possibility of risk events and affects the accuracy of risk assessment. The more effective the risk control measures are, the smaller the risk of ship longitudinal motion is. The calculation formula of the effectiveness of risk control measures is as follows:

$$Sm = 1 - \frac{Nv}{NR} \tag{10}$$

where Nv is the number of times the risk of longitudinal motion of the ship occurs; N is the total number of times the ship's navigation is threatened.

According to the actual situation, the occurrence of risk events of ship longitudinal motion has randomness and statistical regularity.

Poisson distribution sets random variable x, its value is $\left[0,+\infty\right]$, and the formula is as follows:

$$P\left(X = k\right) = \frac{e^{-\lambda}\lambda^{x}}{Sm} \tag{11}$$

where λ is a constant, which means the average occurrence rate of random events per unit time. The range is $\left[0,+\infty\right]$. The random variable x obeys the Poisson distribution of parameter λ, abbreviated as $x * \Pi\left(\lambda\right)$.

When λ reaches the maximum value, Poisson distribution formula can be transformed into normal distribution formula, which is expressed as follows:

$$P\left(X = n\right) = \frac{1}{\sqrt{2\pi\lambda}} e^{\frac{(n-\lambda)^2}{2\lambda}} \tag{12}$$

When λ is equal to 10, the Poisson distribution curve is close to the normal distribution curve, as shown in Figure 6.

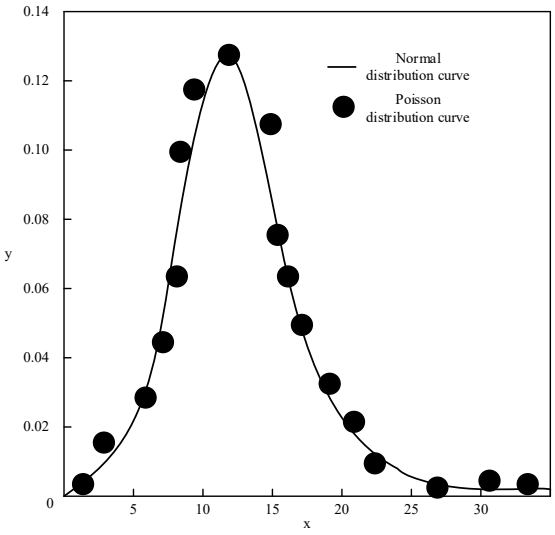

Figure 6. Poisson distribution curve and normal distribution curve of $\lambda = 10$

To sum up, Poisson distribution is used to quantify the risk assessment index. Combined with Formula (12), the quantitative model of ship longitudinal motion risk assessment is obtained as follows:

$$\begin{cases} Q = \sum_{k=1}^{k}\left(V \times \frac{e^{-\lambda}\lambda^{x}}{Sm} \times Pv\right), k < 10 \\ Q = \sum_{k=1}^{k}\left(V \times \frac{1}{\sqrt{2\pi\lambda}} e^{\frac{(n-\lambda)^2}{2\lambda}} \times Pv\right), k \geq 10 \end{cases} \tag{13}$$

3.4. Judgment of risk

Based on the above-mentioned quantitative model of ship longitudinal motion risk assessment, the genetic algorithm is used to calculate the optimal solution of the parameters, and the risk assessment interval is established to determine the risk degree, so as to realize the design of quantitative risk assessment system of ship longitudinal motion based on AHP.

According to Formula (12), it is necessary to calculate the values of Q and k. the specific solution process is as follows.

Set the initial population as

$$Chrom = \left\{\left(Rt1, k1\right), \cdots, \left(Rti, ki\right), \cdots \left(Rt20, k20\right)\right\},$$

where Rti and ki represent the real values in the range of Rt and k respectively.

The individual fitness of the population was calculated:

$$fitness = \left|V_j - V_i\right| \tag{14}$$

where V_j is the individual fitness value of the population; V_i is the expert evaluation value.

The smaller the $fitness$ value, the greater the chance that the individual will be retained in the new generation population. According to the calculation results of Formula (14), through selection, crossover and mutation operation, the optimal individual is obtained. The corresponding value is the optimal solution of model parameters. The optimal quantitative model of ship longitudinal motion risk assessment is obtained by substituting the corresponding value into Formula (12). The sample data is input into the

model to obtain the risk assessment value of ship longitudinal motion. On this basis, the risk degree is determined in Table 3.

Table 3. Risk degree judgment rule table

Degree of risk	The assessed value	Explanation
No risk	[0,60]	The ship sails normally and there is no possibility of risk
Low risk	[60,75]	Ship navigation is basically stable, there is a possibility of risk
Medium risk	[75,90]	The ship's navigation status fluctuates, and there is a possibility of obvious risks
High risk	[90,100]	The ship's sailing condition deteriorates and risks may occur

3.5. System software development

On the basis of the algorithm design of the ship longitudinal motion risk quantitative assessment system, the software development and design of the system are carried out. The software development of the system is carried out by using embedded Linux technology in C/S client. The system includes data processing module, information control module, program loading module, cross compiling module and human-computer interaction module Using SQL Server database as the data management engine of ship longitudinal motion risk quantitative assessment system, the equipment catalog table and equipment attribute table of ship longitudinal motion risk quantitative assessment model are established, and dma0 is configured_ START_ Addr register Dmax is implemented by cross compilation_ Y_ MODIFY, DMAx_ PERIPHERAL_ Map and other registers are configured, and the program loading module is used to load the quantitative assessment algorithm of ship longitudinal motion risk, and the software implementation diagram of the system is obtained, as shown in Figure 7.

Through the above process, the design and operation of the risk quantitative assessment system of ship longitudinal motion based on AHP is completed, which provides more effective guarantee for the safety of ship navigation.

4. Experimental Results and Analysis

In order to prove the application performance of the risk quantitative assessment system of ship longitudinal motion based on analytic hierarchy process (AHP) in actual ship navigation, the inland river ship navigation safety state evaluation system based on fuzzy evidence reasoning and the ship navigation environment risk assessment system based on Improved TOPSIS method are set as the contrast system of the experiment the risk of ship longitudinal motion is quantitatively evaluated.

4.1. Experimental preparation

According to the above software design, the software test of ship longitudinal motion risk quantitative assessment system is carried out. The buffer data word length is 16 bits, the length of sampling data of ship longitudinal motion risk is 1024, and dma0 of test set_ X_ Modify is 2.

(1) In this paper, the longitudinal motion of the ship as the research object, as shown in Figure 8.

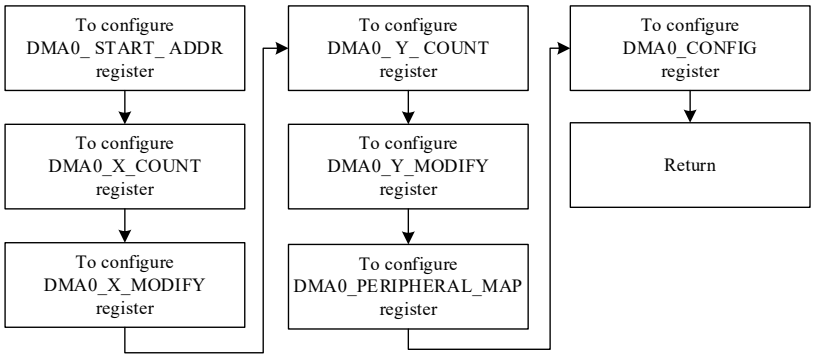

Figure 7. Software implementation diagram of the system

Figure 8. Ships in longitudinal motion

(2) The ship information is shown in Table 4

Table 4. Ship dimensions

Model ship name	Total length (m)	Width (m)	Mould depth (m)	Tail draft (m)	Full load tonnage (t)	Age of vessel (years)
200 seats	35.3	6.6	2.8	2.2	145	4

(3) Navigation route: from the south side of Jinxianding tourist wharf to the berth of Liugong Island tourist wharf.

(4) Expected working environment:

Visibility: 1500 m

Wind force: 4

Maximum flow rate: 2.0 knots

Channel width: minimum 100 m

Minimum channel depth: 5.0 m

Ship type composition: fishing boats and other passenger ferries

Traffic flow: dense traffic flow

Navigation aids: general

The nearest distance to the obstruction: 110 m.

Speed: 10 knots

Age of crew: 7 years

After selecting the route and inputting the estimated sailing time and speed, the system can calculate the position of the ship once an hour and the risk level of the ship's longitudinal movement at sea in the whole route from the port of departure to the port of destination.

The sensor is used to collect the longitudinal motion pose data of the ship, as shown in Figure 9.

4.2. Confidence level

The data of the quantitative assessment of the longitudinal motion risk of the ship is collected, and the results are shown in Figure 10.

Taking the data in Figure 10 as the research object, the ship's longitudinal motion risk assessment is carried out, and the level set of risk characteristic distribution is obtained as shown in Figure 11.

Based on the horizontal value of the ship's longitudinal motion risk characteristic distribution, the quantitative risk assessment system of ship's longitudinal motion based on analytic hierarchy process, the evaluation system of navigation safety status of inland ships based on fuzzy evidence reasoning, and the ship's navigation environment risk based on improved TOPSIS method are adopted. The evaluation system tests the confidence level of the ship longitudinal motion risk assessment, and the results are shown in Table 5.

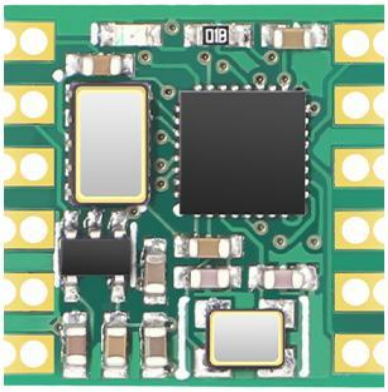

Figure 9. Sensor

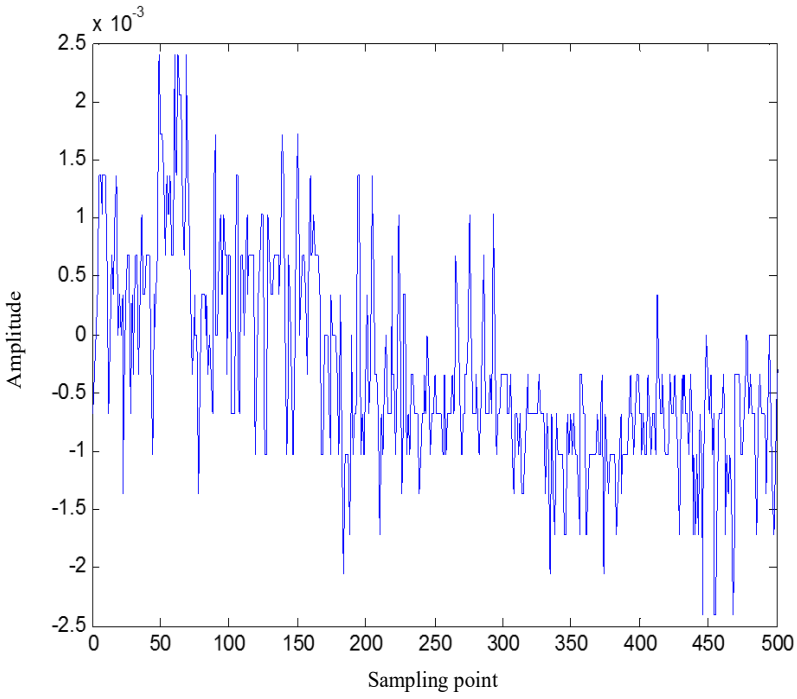

Figure 10. Data collection results

Based on the horizontal value of the ship's longitudinal motion risk characteristic distribution, the quantitative risk assessment system of ship's longitudinal motion based on analytic hierarchy process, the evaluation system of navigation safety status of inland ships based on fuzzy evidence reasoning, and the ship's navigation environment risk based on improved TOPSIS method are adopted. The evaluation system tests the confidence level of the ship longitudinal motion risk assessment, and the results are shown in Table 5.

Table 5. Confidence level of ship longitudinal motion risk assessment

Number of tests	Risk quantitative assessment system of ship longitudinal motion based on Analytic Hierarchy Process	Evaluation system for navigation safety status of inland river ships based on Fuzzy evidential reasoning	Shipping navigation environmental risk assessment system based on Improved TOPSIS method
100	0.963	0.871	0.811
200	0.983	0.891	0.872
300	0.992	0.901	0.881
400	0.998	0.912	0.913

Table 5 shows that the level of confidence in the ship's longitudinal motion risk assessment system based on the analytic hierarchy process method designed in this paper is higher than the confidence level based on fuzzy evidence inference for the inland river navigation safety assessment system and the improved TOPSIS method. The ship navigation environment risk assessment system has a high level of confidence.

4.3. Evaluation accuracy

In order to further verify the effectiveness of the design system in this paper, a quantitative assessment system for ship longitudinal motion risk is based on the analytic hierarchy process, and an inland ship navigation safety assessment system is based on fuzzy evidence reasoning, and a ship navigation environment risk assessment based on improved TOPSIS. The accuracy of the ship's longitudinal motion risk assessment system is compared and analyzed. The analysis results are shown in Figure 12.

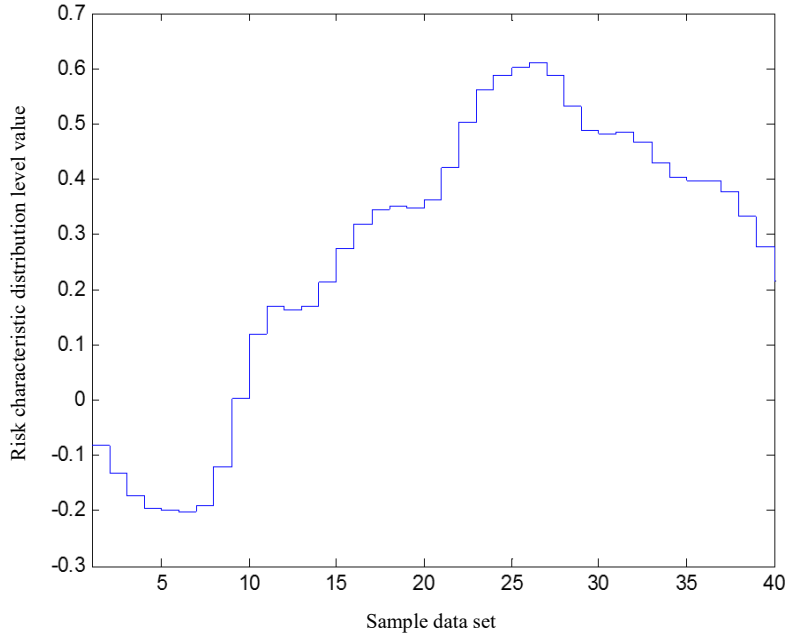

Figure 11. Horizontal values of risk distribution of ship longitudinal motion

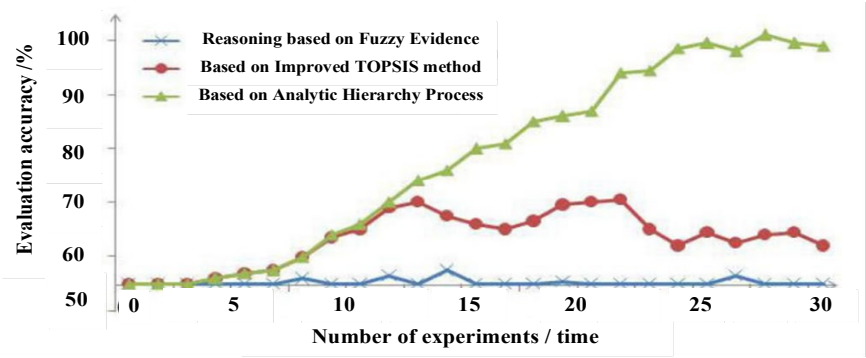

Figure 12. Comparison results of ship longitudinal motion risk assessment accuracy

According to Figure 12, the ship longitudinal motion risk quantitative assessment system based on the analytic hierarchy process has a ship longitudinal motion risk assessment accuracy of up to 100%, while the inland river navigation safety assessment system based on fuzzy evidence reasoning and the ship based on the improved TOPSIS method. The risk assessment accuracy of the longitudinal movement of ships in the general navigation environmental risk assessment system is only 59% and 70%. The method of this paper is better than the traditional method for the ship longitudinal motion risk assessment.

4.4. Assess efficiency

In order to verify the effectiveness of the system in this paper, the quantitative evaluation system of ship longitudinal motion risk based on the analytic hierarchy process, the evaluation system of inland ship navigation safety based on fuzzy evidence reasoning, and the ship navigation environment risk evaluation system based on improved TOPSIS. The time cost of the longitudinal motion risk assessment of the ship is compared and analyzed. The comparison results are shown in Figure 13.

Figure 13 shows that the time cost of using this system for quantitative assessment of ship's longitudinal motion risk is higher than that of inland river navigation safety assessment system based on fuzzy evidence reasoning and ship's longitudinal motion risk assessment system based on improved TOPSIS method of ship navigation environment risk assessment system. The short time overhead indicates that the system's responsiveness is better.

4.5. Risk index testing

The quantitative risk assessment system for ship longitudinal motion based on AHP designed in this paper, the navigation safety assessment system for inland ships based on fuzzy evidence reasoning and the ship navigation environment risk assessment system based on improved TOPSIS method are used to speed the ship's longitudinal motion. And frequency is tested. The test results are shown in Figure 14 and Figure 15.

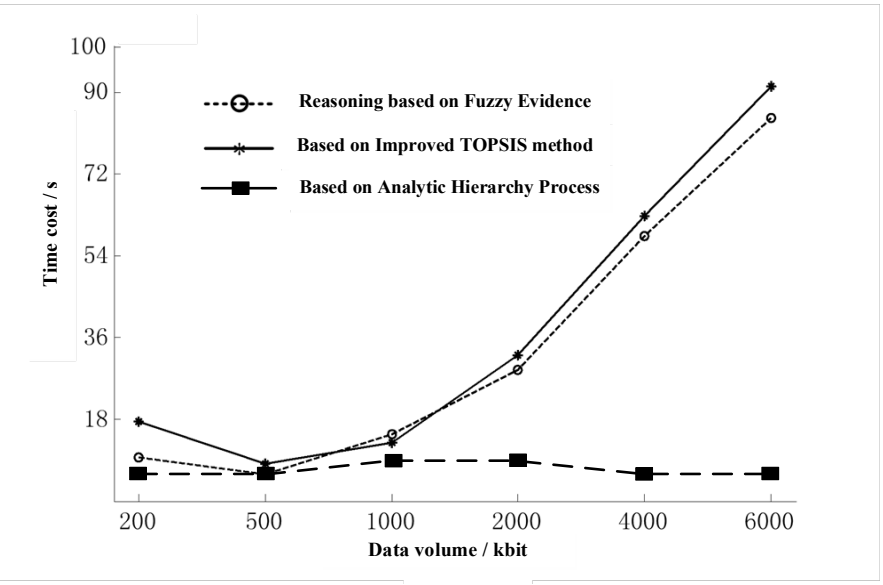

Figure 13. Time cost of ship longitudinal motion risk assessment

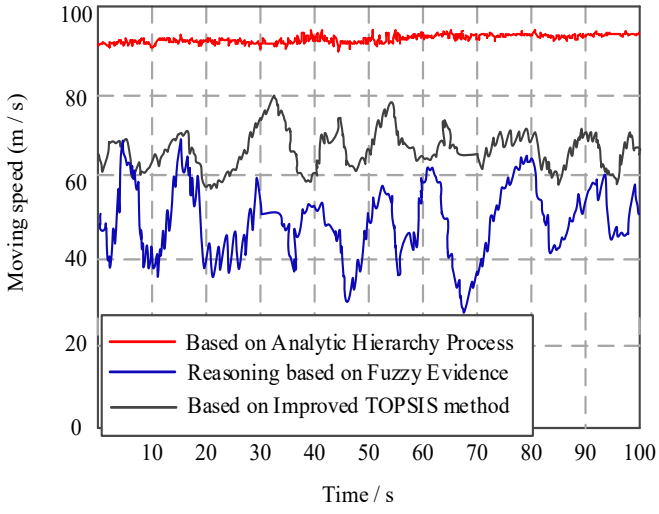

Figure 14. Ship longitudinal motion speed test

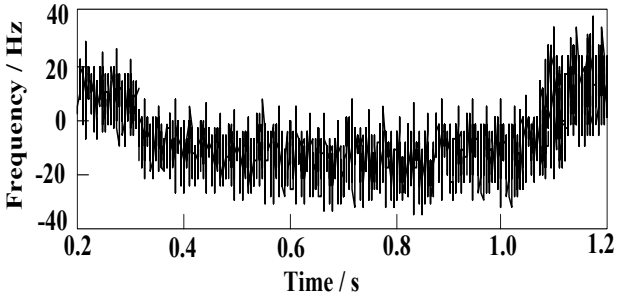

(a) Motion frequency based on fuzzy evidence reasoning

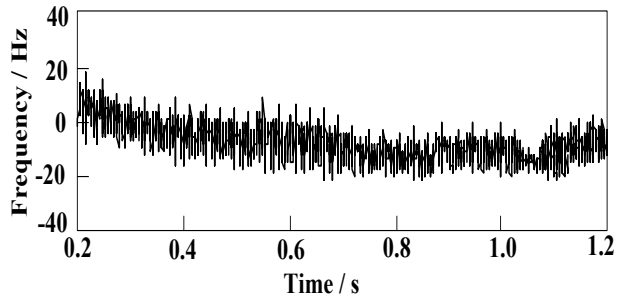

(b) Movement frequency based on improved TOPSIS method

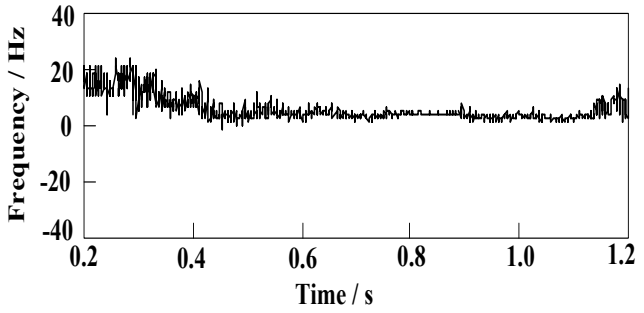

(c) Movement frequency based on AHP

Figure 15. Frequency test of ship's longitudinal motion

According to the data in Figure 14 and Figure 15, the quantitative evaluation system of ship longitudinal motion risk based on the analytic hierarchy process designed in this paper is more efficient than the ship's longitudinal motion speed and frequency based on fuzzy evidence reasoning. The improved ship navigation environment risk assessment system of TOPSIS method has stable speed and frequency of ship's longitudinal movement, and has high effectiveness.

5. Conclusion

Aiming at the problems of low confidence, poor evaluation effect and long time-consuming in the traditional ship longitudinal motion risk assessment system, a method based on analytic hierarchy process is proposed and designed (AHP). The system hardware is mainly composed of Beidou positioning module, external antenna, single chip microcomputer control module and power supply module. The risk assessment index is determined, the relative importance of the four risk indexes of speed, heading, sea state and frequency is evaluated by analytic hierarchy process. The weight of the evaluation index is calculated, and the risk assessment model of ship longitudinal motion is established. The risk degree is determined, and the design of ship longitudinal motion quantitative risk assessment system based on analytic hierarchy process is realized. The experimental results show that the system designed in this paper has high reliability, good evaluation effect, short evaluation time, feasibility and rationality. It lays a foundation for the analysis and research of ship navigation risk and the effective control of ship risk, and is of great significance to improve the safety of ship navigation. In the future research work, it is necessary to conduct a comprehensive analysis on other factors affecting the safety of ship operation, so as to improve the effectiveness of risk assessment and provide practical guarantee for the safe operation of ship.

Acknowledgement

The research was supported by Nantong Science and Technology Project of China (No. MS12021011 and No. JCZ20184).

References

[1] Xu XJ, Li Z, Wang LQ, et al. Modeling and simulation analysis of offshore lifting operation process. Computer Simulation, 2019, 36(6): 236-241,325.

[2] Zhang D, Yao HJ, Wan CP, et al. On the inland river navigation-safety assessment approach based on the fuzzy evidence reasoning approach. Journal of Safety and Environment, 2018, 18(4): 1272-1277.

[3] Ma QD, Jiang FC, Wang QP, et al. Improved TOPSIS based model for risk assessment on ship navigation environment. Navigation of China, 2018, 41(2): 86-90.

[4] Jiang FC, Cao WL, Yang JY, et al. Navigation safety evaluation method for junction waterway based on conflict threshold. Marine Engineering, 2017, 46(1): 177-180.

[5] Li L, Lu W, Niu J, et al. AIS data-based decision model for navigation risk in sea areas. Journal of Navigation, 2018, 71(3): 664-678.

[6] Bye RJ, Aalberg AL. Maritime navigation accidents and risk indicators: An exploratory statistical analysis using AIS data and accident reports. Reliability Engineering & System Safety, 2018, 176: 174-186.

[7] Wood MD, Collier ZA, Bridges TS, et al. Mental models of navigation safety to inform risk management decisions: case study on the Houston ship channel. ASCE-ASME Journal of Risk and Uncertainty in Engineering Systems, Part A: Civil Engineering, 2018, 4(3): 05018001.

[8] Li ZQ. On the navigation risk modeling of Gezhou Dam waters by using the ERA/AHP-BN theory. Journal of Safety and Environment, 2018, 18(4): 1265-1271.

[9] Deng X, Zhu Y. Analysis on navigation risk causes of large ships based on system dynamics and risk assessment. Revista de la Facultad de Ingenieria, 2017, 32(13): 143-147.

[10] Jung CY, Yoo SL. Analysis on the navigation risk factors in Gunsan coastal area (1). Bulletin of the Korean Society of Fisheries Technology, 2017, 53(3): 286-292.

[11] Al-Hawari T, Al-Bo'ol S, Momani A. Selection of temperature measuring sensors using the analytic hierarchy process. Jordan Journal of Mechanical and Industrial Engineering, 2011, 5(5): 451-459.

[12] Zhang S, Jing Z, Li W, et al. Navigation risk assessment method based on flow conditions: A case study of the river reach between the Three Gorges Dam and the Gezhouba Dam. Ocean Engineering, 2019, 175: 71-79.

[13] Qiu WQ, Tang CB, Tang QR. Navigation environment risk assessment of uncertain inland waterway. China Navigation, 2019, 42(1): 52-55,67.

[14] Ito S, Koji Z. Assessing a risk-avoidance navigation system based on localized torrential rain data. MATEC Web of Conferences, 2020, 308: 03006.

[15] Aumont É, Blanchette CA, Bohbot VD, et al. Caudate nucleus-dependent navigation strategies are associated with increased risk-taking and set-shifting behavior. Learning & Memory, 2019, 26(4): 101-108.

[16] Wang H C. Deep drainage detection system for inland vessels based on machine vision. Jordan Journal of Mechanical and Industrial Engineering, 2020, 14(1): 119-128.

[17] Pandey A. Tactical voyage planning in ice: Risk mitigation through e-navigation. The Journal of Ocean Technology, 2017, 12(3): 28-34.

JJMIE

Volume 16, Number 1, January. 2022
ISSN 1995-6665
Pages 153 - 162

Jordan Journal of Mechanical and Industrial Engineering

Multi-Layer and Multi-Channel Welding Trajectory Control Method of Welding Robot

Baiyang Zhao*

Department of Railway Vehicle, Liaoning Railway Vocational and Technical College, Jinzhou 121000, China

Received 14 July 2021 *Accepted 29 December 2021*

Abstract

In order to solve the problems of low productivity and poor quality stability of manual welding production mode, a multi-layer and multi-channel welding trajectory control method for welding robot is proposed. Firstly, the relationship between the welding current and the forming size of V-groove multi-layer multi pass welding was established by welding process test. At the same time, the starting point of the welding torch can be determined by using the feature point information. In order to verify the feasibility of the above method, V-groove medium and heavy plate workpiece is taken as the test object, and the weld bead is preplanned based on the self-defined filling scheme. The welding parameters are corrected by the above method, and the calculated starting point position of welding gun is compared with the actual welding gun position to verify its accuracy. The results show that the welding parameters of the weld bead can be modified effectively and the position of the welding gun of each pass can be accurately determined by this method, and the error is small. The maximum error of feature point extraction is 9 pixels, and the average error is 5.83 pixels

Keywords: Welding robot; Multi-layer and multi-channel welding; Welding track control.;

1. Introduction

Welding robot have the advantages of a stable welding quality, an improved welding labor productivity, and an improved welding working environment [1]. Since the first emergence of the industrial robot, welding robot has been developed vigorously. Single-side welding robot servo integrated workbench has several advantages, such as convenience, economic structure, compact space, stability and durability. It has significant advantages in ensuring the zero position accuracy of welding gun quality, electrode cap mold, welding quality and so on. It plays an important role in the equipment maintenance process, and has been successfully applied to FANUC robot. However, the current welding robot system is the first generation or quasi second generation robot, only according to the traditional teaching online way to carry out welding work, the trajectory of the welding process can not be well controlled. In the actual welding, there are often deformation, clearance and misalignment. In order to avoid the negative impact of these factors on the quality of the workpiece, the industrial robot is urgently required to have the ability of information feedback and intelligent control. The application of machine vision in industrial robot is a hot spot in robot research. The robot uses a six degree of freedom manipulator to reach the welding point conveniently and flexibly, while avoiding the singularity of its motion trajectory and fully ensuring the stability of the mechanism. Because the precision industrial camera can capture the optical characteristics of the workpiece and reflect it in the CCD lens of the camera, through the visual pattern recognition algorithm based on gray processing, the workpiece can be recognized and located in the gradient direction of edge pixels or geometric elements, so as to realize high-speed visual acquisition, and integrate the functions of image preprocessing, feature extraction and recognition, target positioning, etc., and high hardware processing capacity. Another task is to plan the control strategy of the control system, compile the upper computer software, optimize the multi axis trajectory, and realize the servo control. Finally, a prototype is developed and the verification experiment is carried out. The results show that the welding robot has the characteristics of high stability, high efficiency and high precision when the welding joints are random and the workpiece contour is irregular [2]. The method of quantifying and compensating the path deviation of intersecting curve determined by robot welding path. Weld location is a technical means, which can be used to determine the position of some key points on the intersection curve. The welding sequence has an important influence on the formation of stress and deformation in multi pass welding [3, 4]. At present, most of the artificial sensing navigation methods for service robots focus on the improvement of local path planning and reactive navigation, without considering the global environment. Then, a global path planning method based on pedestrian perception global range and multi-level cost graph is proposed [5]. The robot moves smoothly along the welding path to obtain higher position accuracy. This can be achieved by limiting the motion and dynamic changes of the robot joints, such as joint jitter, acceleration square sum torque when the robot moves along the welding path. In addition, robot walking should be completed in the

* Corresponding author e-mail: zhaobaiyang2020@126.com.

shortest possible time to maintain productivity [6]. Considering the external disturbance and dynamic uncertainty in the process of welding robot trajectory tracking, the controller can effectively suppress the chattering caused by sliding mode control algorithm, effectively realize the trajectory tracking of welding robot, and improve the robustness of the robot [7].

However, the key to solving the above problems is welding robot planning technology, including welding task planning, welding process parameters planning, welding robot path and trajectory planning and control. In this paper, according to the law of the influence of welding process parameters on the weld shape, the functional relationship between the weld cross-section area and wire feeding speed and welding speed is established to realize the welding parameter planning. Through the equal section method, the multi-layer and multi pass welding path planning of double-sided V-groove workpiece is carried out, and the spatial position and posture of welding gun are predicted, and the arrangement law of multi-layer and multi-pass welding of thick plate is established. Then, according to the D-H parameter method, the welding robot model is established in MATLAB, and the welding path is simulated to verify the feasibility of road force planning. Finally, through robot art, the off-line programming software establishes the three-dimensional model of the workpiece and the robot [8], analyzes the spatial position and posture of the welding seam according to the workpiece groove, carries out the trajectory planning and simulation analysis of the workpiece by using the optimization law of the welding process parameters and the multi-layer and multi-channel arrangement law of the thick plate, and then carries out the post-processing of the program, and imports the program into the robot control cabinet to guide the robot to automatically weld the workpiece. Experiments are carried out to verify the feasibility of the program and realize the track control of multi-layer and multi-channel automatic welding of welding robot.

2. Multi-Layer and Multi Pass Welding Path Planning

2.1. Robot motion path

The robot's motion path is composed of target points, and the motion modes between target points are mainly linear interpolation (MOVL), arc interpolation (MOVC) and joint interpolation (MOVJ). The pose information of robot target points recorded by teaching box or offline programming software can be solved by inverse kinematics of robot to calculate the robot joint angles corresponding to different target points [9].

In the process of thick plate multi-layer multi pass welding, there are many welding seams, each welding seam contains multiple paths, and each path contains multiple target points, as shown in Figure 1. The more the target points, the higher the motion accuracy of the robot. However, if there are too many targets, the efficiency will be reduced. If the arc is too long and the amount of filler metal is too much, it will overflow to the base metal, which is easy to cause overflow. The welding sequence of each weld bead in metal welded joints is different, resulting in different residual stresses. The weld is the part piled up or filled with welding materials on the surface or between the base metals. Weld bead refers to the number of specific welds in a layer of weld. If a thin workpiece is welded, only one layer is required, which is a single-layer single pass weld.

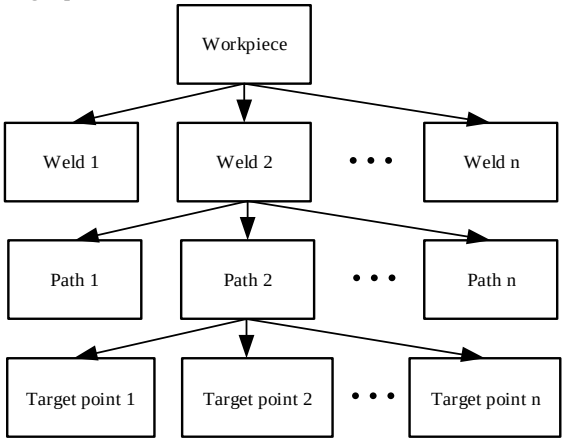

Figure 1. Relationship between weld, path and target point

2.2. Welding parameter planning

When the wire diameter D is constant, the wire feeding speed V1 and welding speed V2 determine the cross-sectional areas of weld bead filling. The equation is as follows:

$$S=\frac{\eta\pi D^2V_1}{4V_2} \tag{1}$$

Among them: η is deposition efficiency. The deposition efficiency η of MAG robot automatic welding used in this paper can reach 90-98%. According to Equation (1), when the welding conditions are determined, the cross-sectional area of weld bead filling can be controlled by adjusting the wire feeding speed and welding speed.

2.3. Weld bead section planning

Asymmetric x-groove is generally used for spherical tank assembly welding, taking V-groove as an example, this paper studies the section planning of multi-layer and multi pass welding path.

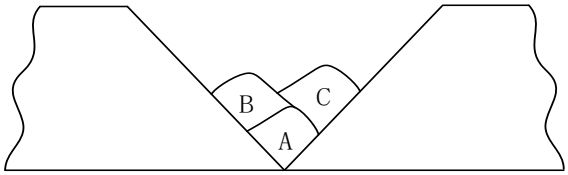

Figure 2. Actual section of V-shaped weld filling

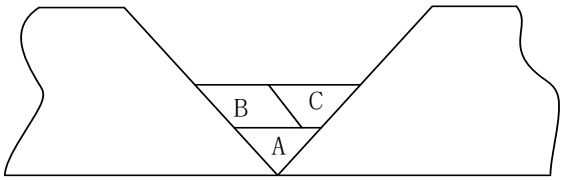

Figure 3. Theoretical section of V-weld filling

Figure 2 shows the actual section of V-shaped weld filling process. The first layer a weld bead is backing weld, which can be approximately triangular. The second layer is composed of two weld passes B and C. The first B weld bead of the second layer can be approximately parallelogram, and the second C weld bead of the second layer can be approximately trapezoidal or triangular.

Figure 3 shows the results of approximate treatment for each pass of V-shaped weld.

When planning the V-groove multi pass welding path, the shape of each groove section perpendicular to the weld bead can be approximately treated as the same, so the position distribution of each weld bead in each section is the same [10]. After simple regularization of the weld bead section shape, the spatial position information of each weld bead in the groove section can be obtained, thus the arrangement rules of multi-layer and multi pass welding can be established [11].

In order to simplify the study, the equal section planning method is adopted in this paper. The cross-sectional area of each weld bead is required to be the same, and the number of passes per layer is also required to be the same as the layer number of the layer.

Assuming that the number of filling layers of V-groove is n, then the total number of passes of filling groove Cn is:

$$C_n = \frac{n(n-1)}{2} + 1 \tag{2}$$

As shown in Figure 4, given the height h and angle θ of groove, the cross-sectional areas of V-groove can be calculated as follows:

$$S = \mathrm{H}_2 \tan\frac{\theta}{2} \tag{3}$$

In the actual welding process, there will be 1-2 mm reinforcement C. According to Equations (2) and (3), the cross-sectional area Sn of the weld bead can be calculated as follows:

$$S_n = \frac{S(2H + C)\tan\frac{\theta}{2}}{C_n} \tag{4}$$

According to Equation (1), when the welding conditions are constant, the wire feeding speed and welding speed can be adjusted by the cross-sectional area of the weld bead.

Set up a coordinate system with point o as the origin, as shown in Figure 4, the upward direction of vertical weldment is z axis, the inward direction of vertical groove section is x axis, and the horizontal right direction is y axis. After regularization of each V-groove section perpendicular to the weld bead, the change of x-axis coordinate value of the target point of the vertical weld bead section can be ignored. Let the height of the first layer of the weld bead is hi, the height of the i-layer is Δ hi, and the coordinates of the corresponding target points PI and j on the j-pass section of the i-layer are (yi, j, zi, J). There are:

$$\Delta h_i = \sqrt{\frac{i(i+1)}{\tan\theta} S_n} \tag{5}$$

$$h_i = \Delta h_i - \sum_{k=1}^{i} h_k \tag{6}$$

According to Equations (5) and (6), the coordinates of the corresponding target points Pi and j on the j-pass section of the i-layer are (yi, j, zi, J):

$$y_{i,j} = y_{i-1,1} - h_i \tan\theta + \frac{(j-1)}{h_i} S_n \tag{7}$$

$$z_{i,j} = z_{i-1,1} + \Delta h_i \tag{8}$$

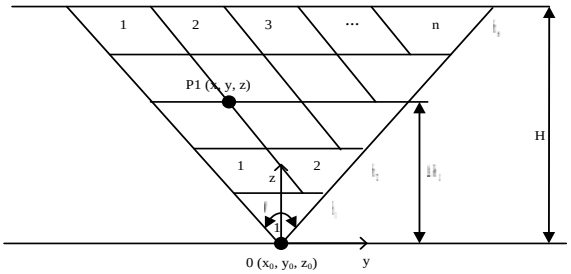

Figure 4. V-groove equal section planning

2.4. Position determination of welding gun

After welding bead layout planning, the position and posture of welding gun should be planned. In order to facilitate welding, the origin of the coordinate system between the weld and the welding gun is usually set as the same. The position of the welding torch is determined by the spatial position of the welding seam Pi, j. the posture of the welding torch needs to be determined according to the geometric characteristics of the weld. In order to prevent the collision between the welding gun and the two sides of the groove, it is necessary to adjust the welding gun posture to ensure that the welding gun is always on the bisector composed of the target point and the groove [12-14].

The coordinate system is established with point o as the origin. The z axis is vertical workpiece upward, x axis is vertical groove section inward, and y axis is horizontal right, as shown in Figure 5. Suppose the deflection angle of welding gun is Δα, and the angle between adjusted welding gun and groove is β. $P_{i,j}$ ($y_{i,j}$, $z_{i,j}$) represents the fixed-point position coordinates of the weld, and H is the groove height. Given the groove height h and angle θ, the relationships (9) and (10) between Δα and β can be established from the geometric relationship of graphs.

$$\tan(\beta - \Delta\alpha) = \frac{H\tan\theta + y_{i,j}}{H - z_{i,j}} \tag{9}$$

$$\tan(\beta + \Delta\alpha) = \frac{H\tan\theta - y_{i,j}}{H - z_{i,j}} \tag{10}$$

From Equations (9) and (10), the deflection angle Δα of welding torch can be calculated as follows:

$$\Delta\alpha = \arctan\left(\frac{H\tan\theta - y_{i,j}}{H - z_{i,j}}\right) - \arctan\left(\frac{H\tan\theta + y_{i,j}}{H - z_{i,j}}\right) \tag{11}$$

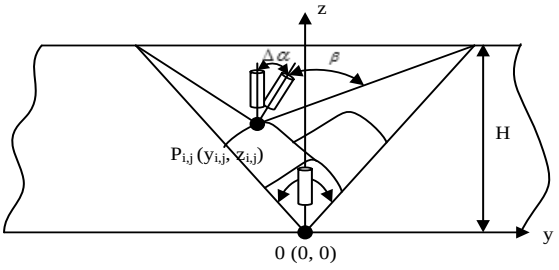

Figure 5. Welding torch posture planning

2.5. Multi pass welding path

In order to improve the welding quality and efficiency, offline programming is used to extract the welding reference path of the workpiece in the multi-layer and multi-pass welding path planning [15-17], and the matrix transformation (translation on the Y-Z plane and deflection transformation around the Z-axis) is performed on the target points on the welding reference path to obtain the pose information of the target points in other welding paths.

It is assumed that the pose matrix of the welding gun at point O is a and that at point Pi and j is B, as shown in Figure 5. From the coordinates of Pi and j and the deflection angle of welding torch Δα, the transformation matrix t of pose matrix A and B can be obtained as follows:

$$\mathbf{T}=\begin{bmatrix} 1 & 0 & 0 & 0 \\ 0 & \cos\Delta\alpha & -\sin\Delta\alpha & y_{i,j} \\ 0 & \sin\Delta\alpha & \cos\Delta\alpha & z_{i,j} \\ 0 & 0 & 0 & 1 \end{bmatrix} \quad (12)$$

$$\mathbf{B}=\mathbf{A}\times\mathbf{T} \quad (13)$$

According to Equation (13), the torch pose matrix B of each weld bead can be obtained by multiplying the torch origin pose matrix A by the transformation matrix T.

2.6. Welding sequence

The welding sequence planning of V-groove is shown in Figure 6, and the number represents the welding sequence [18, 19]. Figure 6(a) shows that each layer is sequentially welded from left to right, and Figure 6(b) shows that each layer is sequentially welded from both sides to the middle.

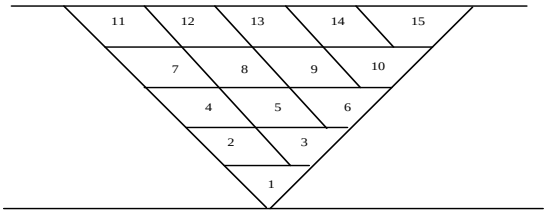

(a) Welding from left to right

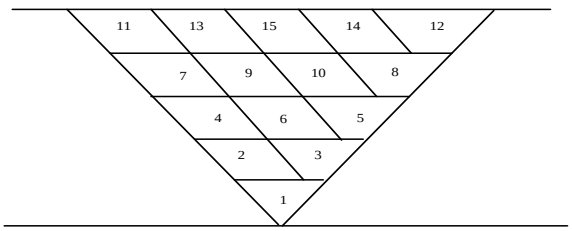

(b) Sequential welding from both sides to the middle

Figure 6 Welding sequence of V-groove

As for the welding layer sequence planning, each welding layer can be sequentially welded from left to right, or each welding layer can be welded alternately, as shown in Figure 7.

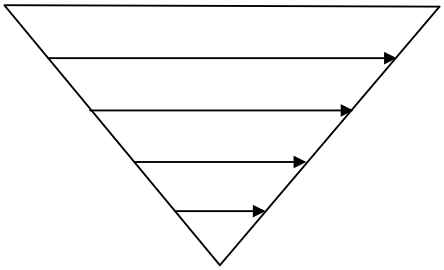

(a) The welding sequence is the same

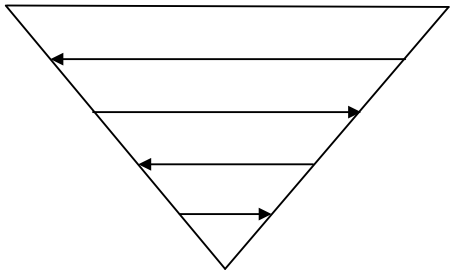

(b) Alternate welding sequence

Figure 7. Schematic diagram of welding layer sequence

In the alternate welding of weld bead and welding layer sequence, due to the imbalance of heat at the arc starting and extinguishing parts of the weld bead, the workpiece deformation is too large and the welding quality is reduced. Therefore, the multi-layer and multi pass welding of spherical tank thick plate is generally selected from left to right welding bead sequence and welding layer sequence welding.

3. Experimental Results

In order to verify the feasibility and accuracy of the multi-layer and multi pass welding adaptive planning method, V-groove workpiece of medium and heavy plate was used for welding test. Firstly, the number of welding passes and welding parameters are preplanned by using self-defined filling strategy and artificial experience. Then, the laser stripe image of each weld bead is collected at the same position. After image processing and feature extraction algorithm, the image feature points are obtained. After coordinate transformation, the actual 3D coordinates under the robot base coordinates are obtained. The actual coordinates of feature points are used to get the width of the weld bead to be filled, and the relationship between the welding parameters and the weld bead forming size is used to modify the preplanning welding parameters. At the same time, the position information of welding torch is calculated by feature point information, and compared with the actual welding torch coordinate point, the error range is analyzed.

3.1. Test conditions and equipment

As shown in Figure 8 which represents the test system diagram, the whole test system is composed of robot system, welding equipment system and laser vision sensing system. The schematic diagram of the test workpiece used is shown in Figure 9. The angle of the bilateral groove of the weld is 90°, the blunt edge is 2 mm, the gap is 2 mm, and the thickness is 16 mm. During the welding process, the welding current and welding torch swing amplitude of each weld bead are different, and the other welding parameters are the same. The number of welding passes and the welding parameters of each weld bead are preplanned by using custom weld bead filling and manual process experience, with a total of 4 layers and 7 passes. The welding process parameters of each weld bead are shown in Table 1. The welding sequence and sequence arrangement of two sides first and then the middle is adopted respectively, as shown in Figure 10.

3.2. Accuracy of image feature extraction

Figure 11 shows the outline of each weld bead groove collected by laser vision sensor. In order to see the groove image of the weld, the original image is rotated to the left by 90° and the coordinate value marked in the figure is the position information of the original image feature points. Table 2 is the coordinates of image feature points obtained by using the related algorithms of image processing and feature extraction in this paper. The coordinates of image feature points are manually marked by drawing software, and compared with the extracted coordinates. The results are shown in Table 2. Therefore, the maximum error of feature points extraction is 9 pixels, and the average error is 5.83 pixels, which can be used for the subsequent coordinate transformation.

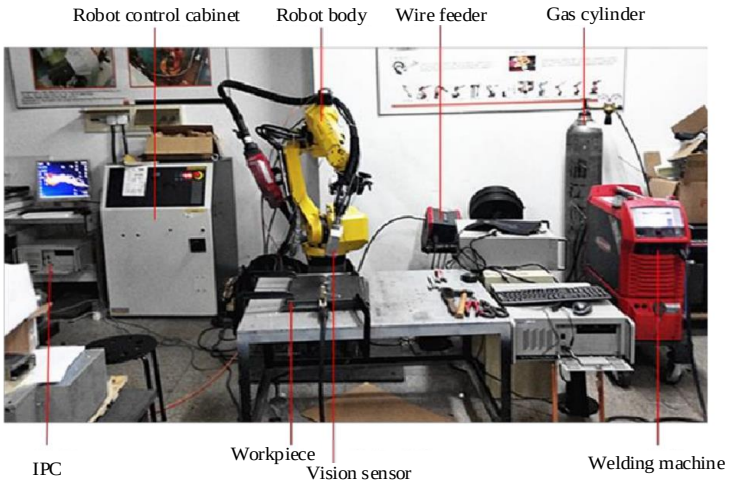

Figure 8. Test system diagram

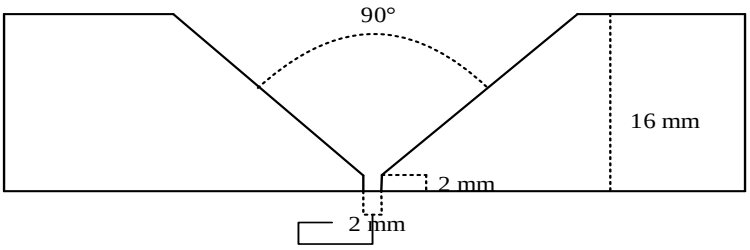

Figure 9. Schematic diagram of test workpiece

Table 1. Welding parameters of each weld bead pre planning

	Current value/A	Swing/mm	Welding speed cm/min	Dip angle/o	Swing frequency/Hz	Left stop/s	Right stop/s
1	180	0	24	0	0	0	0
2	290	4.0	24	0	1.2	0.1	0.1
3.1	220	3.5	24	15	1.2	0.1	0.1
3.2	220	3.5	24	0	1.2	0.1	0.1
4.1	240	4	24	15	1.2	0.1	0.1
4.2	240	4	24	15	1.2	0.1	0.1
4.3	240	4	24	0	1.2	0.1	0.1

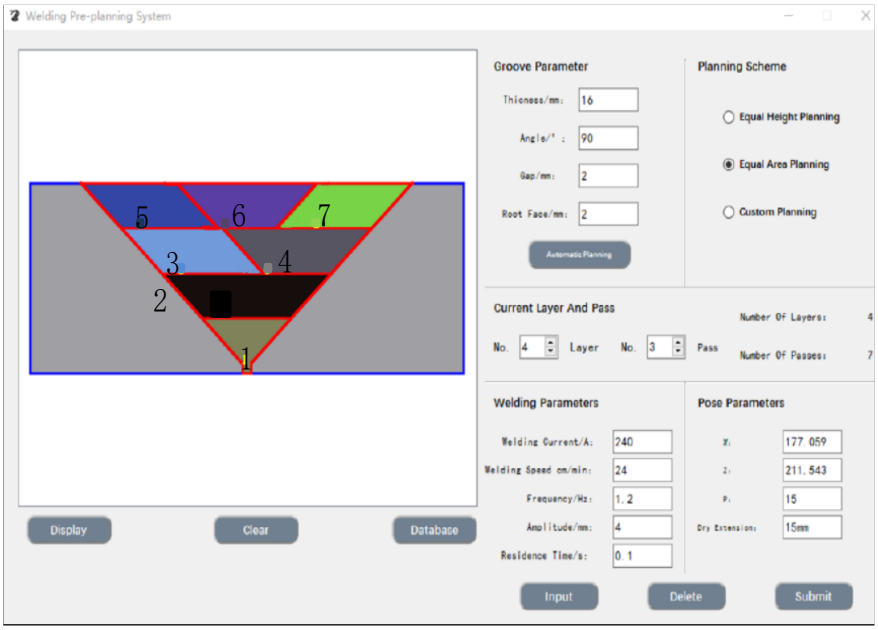

Figure 10. Weld bead layout

(a) the first line

(b) the second way

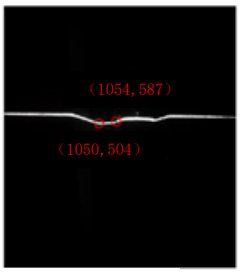

(c) the third way

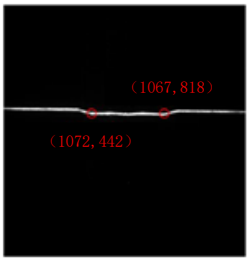

(d) the fourth line

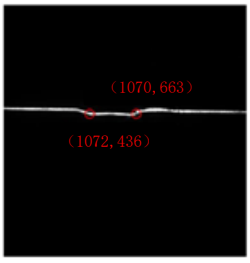

(f) the fifth line

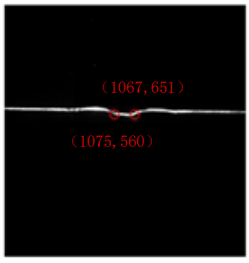

(e) the sixth line

Figure 11. Groove outline and characteristic points after welding

Table 2. Extraction results of image feature points

Number of passes	The first point		Errors/pixels	Second point		Errors/pixels
	Identified image coordinates	Actual coordinates		Identified image coordinates	Actual coordinates	
1	(1035, 572	(1075, 560)	2	(1034, 694)	(1032, 696)	4
2	(1052, 519)	(1054, 517)	4	(1050, 758)	(1055, 755)	8
3.1	(1050, 504)	(1055, 501)	8	(1054, 587)	(1056, 589)	4
3.2	(1072, 442)	(1075, 443)	4	(1067, 818)	(1062, 815)	8
4.1	(1072, 436)	(1074, 431)	7	(1070, 663)	(1076, 666)	9
4.2	(1075, 560)	(1076, 565)	6	(1067, 651)	(1069, 655)	6

3.3. Finished weld

Figure 12 shows the physical picture of each weld bead after welding, and Figure 13 corresponds to the collected weld bead contour map. In order to see the arrangement sequence and the general cross-section shape of the weld bead, the end length of the current weld bead is intentionally shortened by about 2 cm compared with the previous one. It can be seen from Figure 12 that each weld bead is well formed and the workpiece has a good forming appearance after welding. This is because this method performs matrix transformation on the target points on the welding reference path, and adjusts the welding gun attitude to prevent the collision between the welding gun and both sides of the groove.

(a) backing weld (b) the second way (c) the third way (d) the fourth line

(e) the fifth line (f) the sixth line (g) the seventh line

Figure 12. Physical picture after welding

As can be seen from Figure 14, According to Equation (2), if the number of filling layers of V-groove is 4, the total number of filling passes of V-groove is 7. The welding sequence of each weld is 4 layers and 7 passes. At the same time, through Equation (5), Equation (6) and Equation (12). The laser profile of each weld section is converted into coordinates, and the three-dimensional coordinates of the actual laser stripe points are calculated. The coordinates of Y-axis and Z-axis are represented by coordinate diagram, as shown in Figure 15, the actual restoration map of weld cross-section can be obtained. It can be concluded that in the actual welding, the shape of weld bead is irregular, we can simplify it in theory, but in the actual situation, we should use the characteristic points of weld bead to make corresponding correction measures according to different purposes.

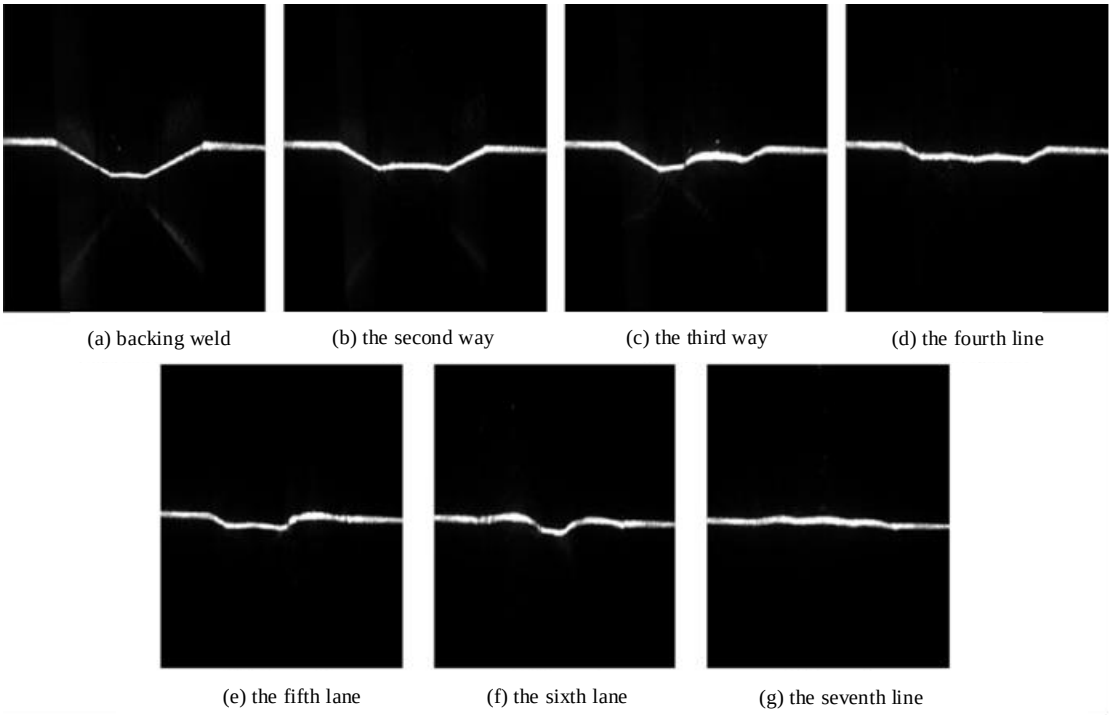

Figure 13. Laser outline of each pass

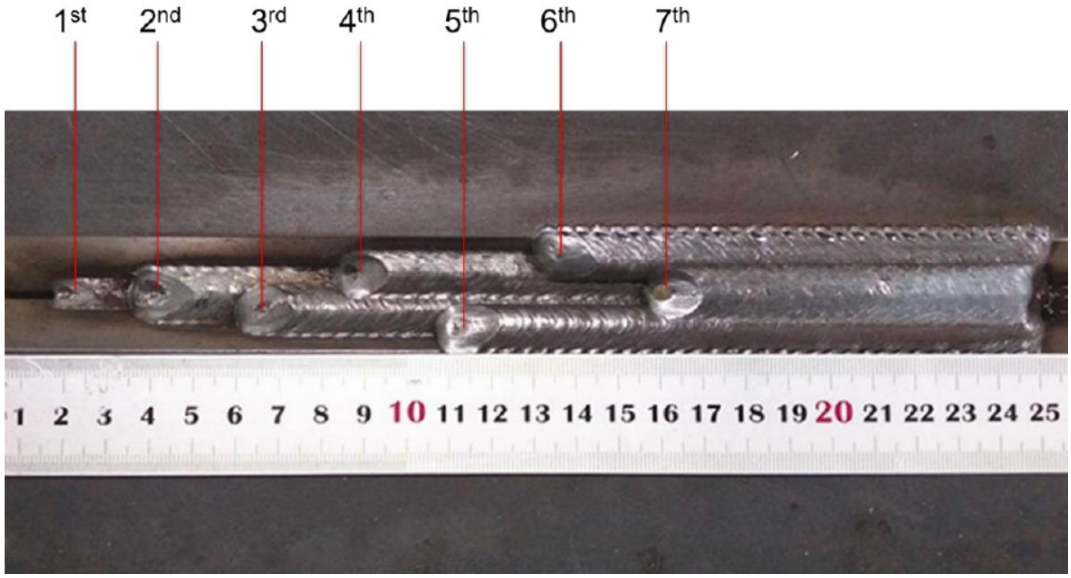

Figure 14. Final physical picture after welding

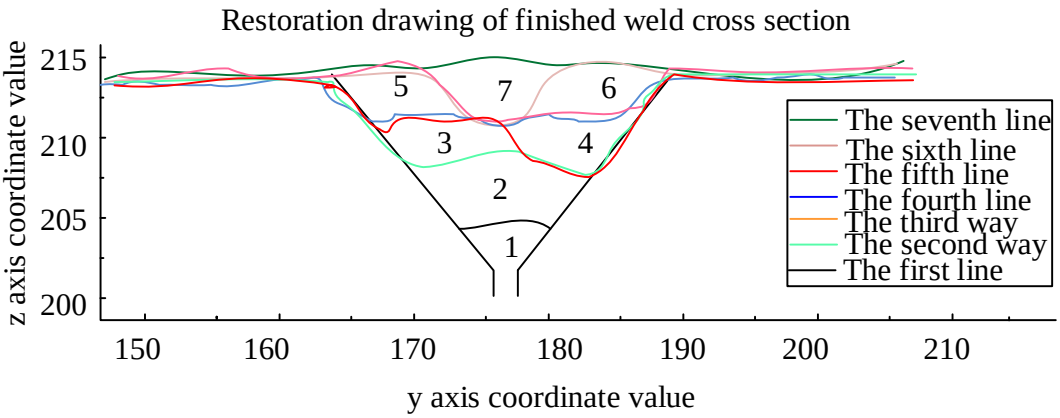

Figure 15. Weld bead section restoration

According to the test results, the filling effect of multi-layer and multi pass welding is basically the same as the planning result. The cross-sectional area of each weld bead is uniform and the welding parameters are not changed too much. It overcomes the problems of low production efficiency and poor-quality stability under the manual welding production mode of the existing welding robot, and improves the welding quality and makes the workpiece have a good forming appearance after welding. This is because that this method adopts the equal section planning method to simplify the research of weld section planning. The off-line programming method is used to extract the welding reference path of workpiece in multi-layer and multi pass welding path planning which improves welding quality and efficiency.

4. Conclusion

In this paper, the multi-layer and multi-channel welding process and trajectory of robot are studied. The results show that the planning path is basically accurate, which can effectively modify the welding parameters of the weld, and accurately determine the position of each welding gun. The results also show that the error is small, and that the multi-layer and multi-pass welding path basically achieves the expected effect.

1. With the welding process, the cross section of the weld bead is closer to the parallelogram.
2. The bottom diamond weld bead welding needs to reduce the welding angle properly to avoid wall collision.
3. Each weld is well formed, and the workpiece has a good forming appearance after welding. It overcomes the problems of low production efficiency and poor quality stability in the manual welding production mode of the existing welding robot.

Acknowledgement

The research is supported by: Scientific Research Project with Funding from Liaoning Education Department (No. LJKY2020113).

References

[1] Wei, J.Y. A servo unilateral spot welding robot integrated workbench. Equipment Manufacturing Technology, 2018, (4): 108-111.
[2] Hendriko, H. Development of invers kinematic method for 6-dof parallel robot using analytical approach. Procedia Manufacturing, 2019, 38: 203-208.
[3] Yan, L.; Jiang, L.; Tian, X.C. An approach to the path planning of intersecting pipes weld seam with the welding robot based on non-ideal models. Robotics and Computer-Integrated Manufacturing, 2019, 55PA: 96-108.
[4] Gao, Q.; Zhan, X.; Shen, H.; Ling, W.; Bu, H. Effect of welding sequence on stress and deformation field of Invar alloy multi-layer and multi-pass welding: A simulation study. Modern Physics Letters B, 2020, (4): 2050129.
[5] Fang, F.; Shi, M.; Qian, K.; Zhou, B.; Gan, Y. A human-aware navigation method for social robot based on multi-layer cost map. International Journal of Intelligent Robotics and Applications, 2020, 4(3): 308-318.
[6] Rout, A.; Bbvl, D.; Biswal, B.B. Optimal trajectory generation of an industrial welding robot with kinematic and dynamic constraints. Industrial Robot: The International Journal of Robotics Research and Application, 2019, 47(1): 68-75.
[7] Wang, P.; Zhang, D.; Lu, B. Robust fuzzy sliding mode control based on low pass filter for the welding robot with dynamic uncertainty. Industrial Robot, 2020, 47(1): 111-120.
[8] Zhang, X.H. Teaching design of ABB robot palletizing workstation based on Robot Art. Electronic Test, 2019, (22): 112-114.
[9] Jiang, L.; Zhu, Z.; Liu, H.; Zhu, J. Analysis of dynamic characteristics of water hydraulic rotating angle self-servo robot joint actuator. Journal of Intelligent & Robotic Systems, 2018, 92(2): 279-291.
[10] Ginzburg, S.; Morozova, L.; Kloshek, A.; Ossenbrink, R.; Michailov, V.; Bobrynina, E.; Koltsova, T.; Tolochko, O.; Kocak, M.; OEzbek, S. Addition of nanoparticles to flux cored wires for the nucleation of acicular ferrite micro-structure in weld metals of the high-strength low-alloy steel. Welding and Cutting, 2020, 19(1): 48-53.
[11] Cho, D.W. Algorithms of mathematical models for fast multi-pass weld-bead drawing technique in V-groove welding. Journal of Mechanical Ence and Technology, 2019, 33(11): 5347-5352.
[12] Masoud, Z.; Nazzal, M.; Alhazza, K. Multimode input shaping control of flexible robotic manipulators using frequency-modulation. Jordan Journal of Mechanical and Industrial Engineering, 2016, 10(3): 179-188.

[13] Liu, Y.; Shi, L.; Tian, X. Weld seam fitting and welding torch trajectory planning based on NURBS in intersecting curve welding. International Journal of Advanced Manufacturing Technology, 2018, 95(1-4): 2457-2471.

[14] Shen, Z.B.; Zhang, X.X.; Zhang, B.; Wu, X.Q.; Zhu, X.G. Application of multi-function welding torch fixture in welding robot. Science & Technology Vision, 2019, (8): 144-145.

[15] Wei, A.G.; Chang, B.H.; Xue, B.C.; Peng, G.D.; Du, D.; Han, Z.D. Research on the Weld Position Detection Method for Sandwich Structures from Face-Panel Side Based on Backscattered X-ray. Sensors, 2019, 19(14): 3198.

[16] Dildin, A.N.; Gerasimov, V.Y.; Zaitseva, O.V. The structure of multi-layer composite material obtained by the method of diffusion welding. Materials Science Forum, 2019, 946: 139-144.

[17] Agarwal, S.; Chakraborty, S.; Prasad, K.; Chakraborty, S. A rough multi-attributive border approximation area comparison approach for arc welding robot selection. Jordan Journal of Mechanical and Industrial Engineering, 2021, 15(2): 169-180.

[18] Wei, W.; Yun, C.; Song, D.; Wang, W. Path planning for robotic multi-path/multi-layer welding. Jiqiren/Robot, 2014, 36: 257-262+270.

[19] Shan, Z.; Xu, X.; Tao, Y.; Xiong, H. A trajectory planning and simulation method for welding robot. 2017 IEEE 7th Annual International Conference on CYBER Technology in Automation, Control, and Intelligent Systems (CYBER), 2017, 510-515.

المملكة الأردنية الهاشمية

الجامعة الهاشمية

المجلة الأردنية
للهندسة الميكانيكية والصناعية

JJMIE

مجلة علمية عالمية محكمة

تصدر بدعم من صندوق البحث العلمي

http://jjmie.hu.edu.jo/

ISSN 1995-6665

المجلة الأردنية للهندسة الميكانيكية والصناعية

المجلة الأردنية للهندسة الميكانيكية والصناعية: مجلة علمية عالمية محكمة تصدرعن الجامعة الهاشمية بالتعاون مع صندوق دعم البحث العلمي والابتكار- وزارة التعليم العالي والبحث العلمي في الأردن.

هيئة التحرير

فريـق الدعـم

ترسل البحوث إلى العنوان التالي

رئيس تحرير المجلة الأردنية للهندسة الميكانيكية والصناعية

الجامعة الهاشمية
كلية الهندسة
قسم الهندسة الميكانيكية
الزرقاء - الأردن

هاتف : 3903333 5 00962 فرعي 4147

Email: jjmie@hu.edu.jo

Website: www.jjmie.hu.edu.jo